Probing Polaron Design Principles in Iron Oxides with Transient Extreme Ultraviolet Spectroscopy

Thesis by
Jocelyn L. Mendes

In Partial Fulfillment of the Requirements for
the Degree of
Doctor of Philosophy

CALIFORNIA INSTITUTE OF TECHNOLOGY
Pasadena, California

2026
(Defended May 11th, 2026)

Jocelyn L. Mendes
ORCID: 0000-0003-3850-0724

ACKNOWLEDGEMENTS

"Science is just magic that works." – Kurt Vonnegut

I am deeply grateful for the support, kindness, and enthusiasm that I have received from so many people during the course of my PhD. Moving cross-country to California made me grow in many ways and I truly could not have done it without my fantastic support system.

One common thread through my academic career thus far has centered around being lucky enough to find enthusiastic and caring mentors. To that end, I first want to thank my PhD advisor Professor Scott Cushing, who brings such an infectious positivity to science that has kept me going, even when nothing is working and all of the equipment is broken (as is characteristic of physical chemistry research). I am especially appreciative of the opportunities he has given me to grow as a scientist, both inside and outside of the lab. And above all else, I feel so fortunate to have had such a compassionate, understanding advisor.

I next need to express my deepest gratitude to my incredibly enthusiastic undergraduate advisor Professor Ronald Grimm. He is the reason why I chose to pursue graduate school and his hands-on mentorship throughout my undergraduate studies made me fall in love with experimental chemistry research. I am so profoundly grateful to him for always believing in me and being such an encouraging, caring advisor. And beyond my undergraduate training, he has remained a mentor and friend, for which I am deeply grateful.

I would also like to express my heartfelt thanks to my thesis committee members, Professors Geoff Blake, Karthish Manthiram, and Joseph Falson. Their research and career guidance has been invaluable. Their breadth of experiences and knowledge has challenged my thinking beyond physical chemistry to push me to grow as a scientist.

Next, I owe so much thanks to my postdoc and graduate student mentors in the Cushing lab, Professor Hanzhe Lui and Dr. Jonathan Michelsen. I had never touched an optic or a laser prior to joining the XUV setup, and you both accepted my questions with endless patience and excitement to share your science with someone new. I am so incredibly grateful to have you two as mentors that taught me how to be an incredibly thorough scientist, but also to not be such a perfectionist that I was held back from using duct tape here and there. As far as mentors within the Cushing group go, I also need to thank Dr. Levi Palmer for being so incredibly organized and truly always having an answer when I need one. I am also incredibly appreciative of all of the Cushing group members who have been

shoulders to cry on when experiments go wrong, friends to gossip with, and people who are always willing to help each other with disparate and wide-reaching scientific side quests.

Next, I need to thank my friends outside of the Cushing lab that have made my time at Caltech even more enjoyable. Dr. Danika Nimlos, Dr. Katie Luedecke, and Megan Dallas, thank you for always being my run club, hiking, and general outdoorsy buddies. Jax Dallas, thank you for many a walk by the turtles when one of us is on the verge of a crash out (and for the scientific advice and support). I also owe a huge thanks to Vera Beilinson. I am so incredibly lucky that Caltech brought us together. You have been my most enthusiastic cheerleader at Caltech, and have been such a supportive and caring bestie, and I am so incredibly excited that we will get to continue our boba trips in New York. Ryan and Dr. Bryan, I will miss our grill sessions and am lucky to have such a great LA friend group.

A recurring theme in my PhD was exiting the sub-basement to see the wonderful SoCal sun, the mountains, and to walk around Caltech's beautiful campus. Whether that was through walks to see the turtles with Jax, boba trips with Vera and Grace, or the many many phone calls I have made to several individuals. For example, I need to thank my fellow academic friends from WPI, Dr. Julia Nöel and Madison Durgin, for their long phone calls about our respective research lives. I also want to thank my mom, Sharon, and my sister, Karissa, whom I call several times a week while walking around campus to take a break from work and just generally catch up. You guys are the best.

I am so grateful for my whole family for so enthusiastically supporting me throughout my PhD and always being there to chat when I needed a break. My family's visits to CA and my visits to MA have been bright spots through the past five years. I am also incredibly lucky to be gaining some very supportive in-laws that have cheered me on throughout this process.

Finally, I am so incredibly lucky to have a partner who is so incredibly driven, motivated, and supportive. Alex, firstly, thank you for letting me drag you across the country. Having your unyielding support in everything I do is an incredible privilege. You have been so generous and supportive of me throughout my PhD and having you as a support system during has gotten me through it. You are always willing to listen about my science, going so far as to let me practice presentations on you, and taking notes with your questions. You have also pushed me to have a bright life outside of my work, always wanting to go on an adventure in LA, make new friends, or try new things. Your sheer willpower to do legitimately anything you put your mind to has been an inspiration and motivator throughout my PhD, and I am so lucky to have found a partner who is so similar to me and who pushes me to grow, take risks, and try new things.

ABSTRACT

Long timescale charge separation and high carrier mobilities are necessary for efficient devices. In highly polar transition metal oxide materials, photoexcited polarons remain a bottleneck to realizing highly mobile carriers, while also offering an exciting route for long timescale charge separation. Controlling photoexcited polaron formation in transition metal oxides is therefore necessary. This thesis uses transient extreme ultraviolet (XUV) reflection-absorption spectroscopy and ab initio density functional theory (DFT) and the Bethe–Salpeter equation (BSE) to elucidate photoexcited polaronic dynamics in a series of iron oxide photocatalysts. By systematically varying structure, on-site repulsions, electron–phonon coupling, and exchange interactions, this work identifies the fundamental materials parameters that govern ultrafast polaron formation. The results demonstrate that photoexcited polaron formation can be tuned and, in some cases, suppressed. In $CuFeO_2$, small polarons form on ~100 fs timescales, followed by dynamic delocalization mediated by coherent lattice expansion and charge sharing with surrounding Fe sites. In $ErFeO_3$, frustrated iron-centered octahedra enable favorable exchange pathways, where exchange-mediated charge hopping thermalizes carriers prior to localization as polarons. In $GdFeO_3$, excitation-wavelength-dependent XUV spectroscopy reveals that ligand-to-metal and metal-to-metal charge transfer pathways modulate polaron formation, demonstrating that strong electronic and spin correlations can either suppress or enable polaron formation. In Fe_2SiO_4 polaron formation is present following metal-to-metal charge transfer. These experimental observables are then mapped onto the Holstein, Hubbard–Holstein, and t-J–Holstein models to define a parameter space for polaron control. These ground-state Hamiltonians act as a ground-state calculable roadmap for materials design parameters based upon measured excited state polaronic dynamics. Together, these studies provide design principles for controlling polaronic behavior in transition metal oxides for photocatalytic, electronic, and quantum materials applications.

PUBLISHED CONTENT AND CONTRIBUTIONS

(1) **Mendes, J. L.***; Bhattacharyya, S.*; Huang, C.; Michelsen, J. M.; Klein, I. M.; Babbe, F.; Sayer, T.; Li, T.; Cooper, J. K.; Liu, H.; Ginsberg, N.; Montoya-Castillo, A.; Cushing, S. K. Coherent and Dynamic Small Polaron Delocalization in $CuFeO_2$. *J. Phys. Chem. Lett.* **2026**, *17* (2), 656–664. https://doi.org/10.1021/acs.jpclett.5c03430

J.L.M. participated in transient extreme ultraviolet spectroscopic measurements, spectral analysis, density functional theory and Bethe–Salpeter equation calculations, and contributed to writing and editing the manuscript.

* denotes equal contributions

(2) Kim, Y.-J.; **Mendes, J. L.**; Michelsen, J. M.; Shin, H. J.; Lee, N.; Choi, Y. J.; Cushing, S. K. Coherent Charge Hopping Suppresses Photoexcited Small Polarons in $ErFeO_3$ by Antiadiabatic Formation Mechanism. *Sci. Adv.* **2024**, *10* (12), eadk4282. https://doi.org/10.1126/sciadv.adk4282

J.L.M. participated in transient extreme ultraviolet spectroscopic measurements and contributed to writing and editing the manuscript.

(3) **Mendes, J. L.**; Shin, H. J.; Seo, J. Y.; Lee, N.; Choi, Y. J.; Varley, J. B.; Cushing, S. K. Dynamic Competition Between Hubbard and Superexchange Interactions Selectively Localizes Electrons and Holes Through Polarons. *J. Am. Chem. Soc.* **2025**, *147* (19), 16018–16026. https://doi.org/10.1021/jacs.4c16837

J.L.M. conceived the project, collected transient extreme ultraviolet spectra, conducted spectral analysis, density functional theory and Bethe–Salpeter equation calculations, and led the writing and editing of the manuscript.

(4) **Mendes, J. L.**; Cushing, S. K. Experimentally Mapping the Phase Diagrams of Photoexcited Small Polarons. *Under review.* **2025**. https://doi.org/10.48550/arXiv.2512.17869.

J.L.M. participated in the conception of the project, spectral analysis, model Hamiltonian approximations, and led the writing and editing of the manuscript.

TABLE OF CONTENTS

LIST OF FIGURES

NOMENCLATURE

BSE. Bethe–Salpeter equation.

CBM. Conduction band minimum.

CTM4XAS. Charge transfer multiplet for X-ray absorption spectroscopy.

DFT. Density functional theory.

DOS. Density of states.

GGA. Generalized gradient approximation.

HHG. High harmonic generation.

LMCT. Ligand-to-metal charge transfer.

MMCT. Metal-to-metal charge transfer.

PBE. Perdew–Burke–Ernzerhof.

PDOS. Projected density of states.

SHG. Second harmonic generation.

VBM. Valence band maximum.

XUV. Extreme ultraviolet.

Chapter 1

INTRODUCTION

Understanding the fundamental physical phenomena that dictate device efficiency in materials is necessary for rational design. Ultrafast femtosecond to nanosecond processes between charge carriers and the crystal lattice dictate properties such as transport, reactivity, and magnetism. One such process is carrier self-trapping induced by polaron formation. While polaron formation occurs on femtosecond to picosecond timescales, this phenomenon has been demonstrated to localize carriers out to their lifetimes and results in limited charge mobility and transport. While this results in long timescale charge separation necessary for chemical reactions, it also reduces carrier mobility needed for facile charge transport within electronic devices. Time-resolved spectroscopic methods aim to characterize these types of phenomena across representative timescales, from initial charge trapping in the form of polarons on the order of hundreds of femtoseconds, out to nanosecond and microsecond carrier diffusion and recombination. This thesis focuses on the characterization of photoexcited polaron formation on ultrafast timescales using core-level extreme ultraviolet (XUV) spectroscopy. A particular focus centers on understanding the nature of electron–phonon coupling and how electron–phonon coupling might be tuned. A range of materials have been characterized to extract meaningful parameters by which design principles might be developed to inform rational design of polaron-forming materials. Ultimately, fundamentally understanding and controlling these types of charge-trapping phenomena can be leveraged to design efficient devices.

1.1 Semiconductor and Insulator Physics

Unlike molecular systems, condensed matter systems have a periodic repeating structure.[1] Due to the periodicity of crystal lattices, rather than having distinct orbitals and distinct energy levels for those orbitals, the overlapping orbitals of these periodic atoms are delocalized. The degeneracy of many of these overlapping orbitals gives rise to energy bands. In semiconductors and insulators, these bands are separated by some energy, which is

referred to as a band gap. Excitation of electrons from the valence band (VB) into the conduction band (CB) of a semiconductor or insulator requires energy greater than or equal to the band gap and creates holes in the VB.[2]

Several types of insulators are investigated in this thesis in transition metal oxide systems, specifically iron oxides. They can be understood by considering their band gaps, where the charge transfer energy (Δ_{CT}) and on-site repulsion (U) of the d orbitals compete to dictate the orbital character of the valence and conduction bands.[3,4] In the case of a charge-transfer insulator, $\Delta_{CT} < U$, as shown in **Figure 1.1A**. It is more energetically favorable for electrons in charge-transfer insulators to transfer between ligand p orbitals and metal d orbitals in transition metal oxides. This results in a projected density of states that has ligand p orbitals at its valence band maximum (VBM) and metal d orbitals at its conduction band minimum (CBM), meaning that the lowest energy charge transfer possible is a ligand-to-metal charge transfer (LMCT). On the other hand, Mott insulators have $U < \Delta_{CT}$, such that the lowest possible electronic transitions across the band gap are from electron transfer between adjacent metal sites.[5–8] This is because U is sufficiently small to enable this transfer, and results in metal-to-metal charge transfer (MMCT) transitions being the lowest energy above band gap charge transfer possible (**Fig 1.1C**). In the case where $\Delta_{CT} \approx U$, the insulator is considered an intermediate insulator (**Fig 1.1B**) and has MMCT and LMCT transitions accessible as the lowest energy above band gap excitation.

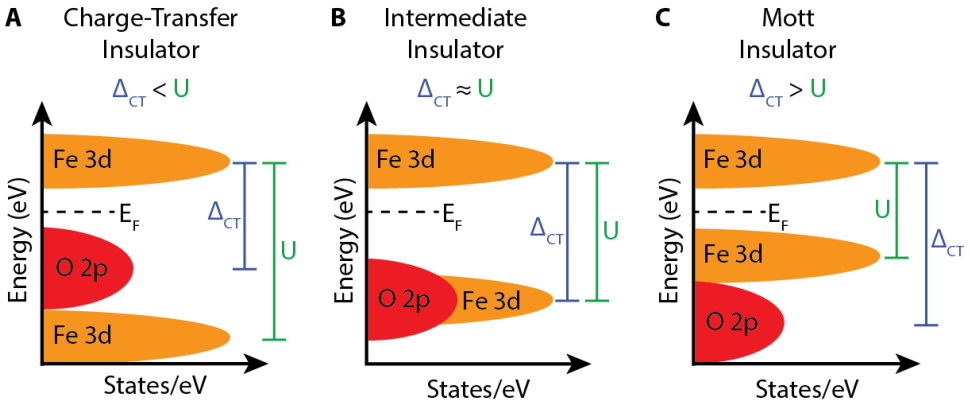

Figure 1.1 Schematic depiction of charge transfer **(A)**, intermediate **(B)**, and Mott **(C)** insulators in iron oxide systems. The balance between charge transfer energy and on-site Coulombic repulsions dictates insulator character.

Following above band gap excitation of these insulators, several pathways exist for carriers to relax and recombine, and the duration of such dynamics can play a great role in device efficiency. For example, the formation of polarons, which is when a charge carrier couples to lattice vibrations, reduces carrier mobility resulting in poor performance of photoelectrodes.[9,10] Generally, long carrier lifetimes and limited charge trapping give rise to highly efficient devices. Engineering materials to have these properties is possible, but only if the properties that reduce device efficiency, such as small polaron formation and charge trapping, are well understood.

1.1.2 Polarons

Excited charge carriers interact with lattice vibrations to dissipate excess energy in solid crystals through electron–phonon interactions.[11] Polaron formation occurs in polarizable crystal lattices when these excess charge carriers couple to vibrational modes. This coupling results in localization of the carrier as it generates a potential energy well.[12] Polarons have been demonstrated in a wide range of materials including semiconductors,[13] insulators,[14] organic crystals,[15] and superconductors.[16–18] The properties of this quasiparticle have been extensively studied experimentally and theoretically in both the ground and excited states.

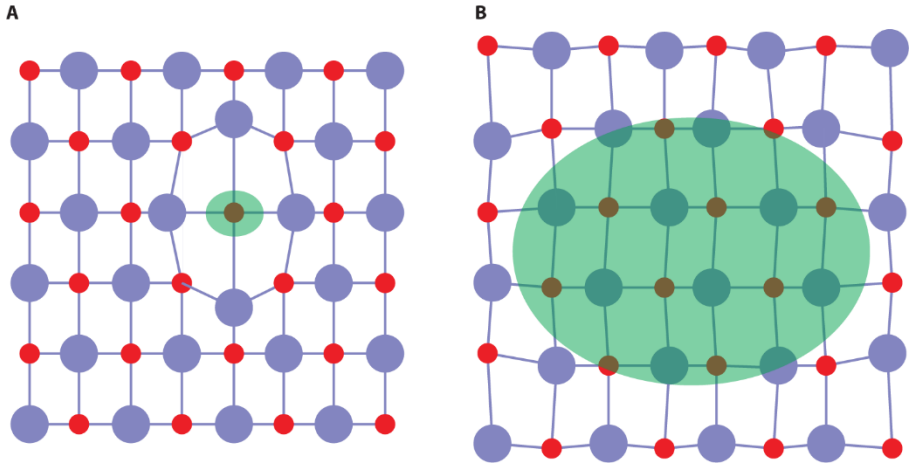

Figure 1.2 Schematic depiction of small **(A)** and large **(B)** polaron charge localization and lattice deformation in a crystal lattice. The carrier's localized wavefunction is denoted in green. In the case of small polarons **(A)**, the carrier is localized to a unit cell or less, often a single atomic site, and thus, the lattice distortion is highly anisotropic around the site of the polaron. In the case of large polarons, the carriers are localized over a larger area.

The extent of carrier localization has historically been separated into two theoretical frameworks dependent upon the coupling regime being considered and marks a distinction in polaron size, or the spatial extent of the localized carrier wavefunction. **Figure 1.2** shows a schematic depiction comparing small and large polarons and visualizes the localization of their carrier wavefunctions. The Fröhlich model considers long-range electron–phonon interactions typically applied in a large polaron regime that describes polaronic carrier wavefunctions localized over an area greater than a unit cell.[19,20] The Fröhlich Hamiltonian can be described by **Equation 1.1**:[21,22]

$$H = \sum_k \varepsilon_k c_k^\dagger c_k + \omega_{LO} \sum_q b_q^\dagger b_q + \sum_{k,q} V_q c_{k+q}^\dagger c_k (b_q + b_{-q}^\dagger) \qquad \textbf{(1.1)}$$

where ε_k is the band energy, and k and q are electron and phonon momentum, respectively. $c_k^\dagger$ (c_k) and $b_q^\dagger$ (b_q) are the electron and phonon creation (annihilation) operators, respectively. ω_{LO} refers to the dispersionless longitudinal optical phonon frequency in the continuum limit. $V_q = i(2\sqrt{2}\alpha\pi)^{1/2}\frac{1}{q}$ represents the electron–phonon coupling term which is dependent upon a dimensionless electron–phonon coupling constant, α. This Hamiltonian considers an approximation based upon a charge carrier in continuous polarizable medium and as such does not consider a discrete crystal lattice symmetry, but rather long-range optical phonons in a continuum limit.

On the other hand, the Holstein model describes short-range electron–phonon interactions.[12,23] This model best describes small polarons that are localized to a unit cell or smaller, often a single atomic site. However, because the Holstein model treats the lattice discretely, it can be applied to describe the transition between small to large polarons, while the Fröhlich model best describes large polarons in a continuum limit due to the fact that the carrier's wavefunction is localized over multiple unit cells. While the Fröhlich model does not have an exact solution, the Holstein model has an exact analytic solution in specific cases, including a two-site model, shown in **Equation 1.2**:[24]

$$H = -t \sum_{\langle ij \rangle \sigma} \left(c_{i\sigma}^\dagger c_{j\sigma} + c_{j\sigma}^\dagger c_{i\sigma} \right) + \omega_0 \sum_i b_i^\dagger b_i + g \sum_{i,\sigma} n_{i\sigma} (b_i + b_i^\dagger) \qquad \textbf{(1.2)}$$

where t is the hopping integral, $c_{i\sigma}^{\dagger}$ and $c_{j\sigma}$ are the electron creation and annihilation operators, respectively, with spin, σ, for an electron at sites i and j. $n_{i\sigma}$ is the number operator for electron spin, g corresponds to the electron–phonon coupling strength, and ω_0 refers to the phonon frequency. $b_i^{\dagger}$ and b_i are the creation and annihilation operators, respectively, for phonons at site i. Both models consider how electron–phonon coupling dictates polaron formation, localization, and transport. In this thesis, we consider the short-range electron–phonon effects of small polaron formation in highly polar transition metal oxide species. This class of materials is best described by Holstein-based models.

While these model Hamiltonians have provided a simplified framework under which polaronic localization and transport may be modeled, they require further information to accurately predict polarons across a range of solid crystals.[25] To that end, much ab initio theory development has been undertaken since Landau and Pekar's first studies of polarons.[26] For example, Feynman's path integral approach has been numerically integrated into diagrammatic Monte Carlo simulations to predict polaronic ground state energies and effective masses.[27] Dynamical mean-field theory can be extended beyond predicting ground state energies and effective masses to modeling spectral and transport properties of polarons.[28] Molecular dynamics simulations can predict the lattice distortions and configurations of localized polarons ab initio.[29] These theories have been compared to experiments to advance the field of polarons; however, most are limited to ground state modeling. While a few methods have been extended into the excited state, they remain computationally challenging and method dependent.

Spectroscopic experiments have also been advanced since the conception of polarons. These experiments aim to directly measure carrier localization, subsequent lattice deformation, and polaron-hopping-limited transport. For example, time- and momentum-resolved photoemission electron microscopy (PEEM) has been employed to directly image polaronic lattice distortions and subsequent changes in carrier effective mass in BiOI nanoplatelets.[30] Transient absorption spectroscopies leveraging photon probe energies from infrared to X-ray have been used to establish photoexcited polaronic binding energies and formation [12,31–34].

This range of spectroscopic experimentation aimed at elucidating all aspects of polaron formation and localization from the ground- to excited-states has enabled a deep understanding of polaron properties. However, the study of polaron properties remains an ongoing area of interest. Particularly, while spectroscopic and theory technique development have both been advanced greatly in the past fifty years, there are few studies that combine the two approaches. The work presented in this thesis aims to couple ultrafast experimental insights into polaron formation and localization with ground-state models that enable more facile prediction of polaronic properties.

1.2 Core-Level Spectroscopy

X-rays span tens to thousands of electron volts (<100 nm) and upon interacting with matter they induce core-level electronic transitions. Most elements have multiple core-level transitions, called edges, which correspond to the orbital being probed. These transitions are element and edge specific in energy. **Figure 1.3** shows a schematic diagram of the core-valence transitions induced by an X-ray photon. A core-hole is left behind when an electron transitions from a core to valence orbital and this core-hole perturbs the final X-ray absorption spectrum.[35] A distinct absorption peak will occur in the absorption spectrum at the energy of the core-level transition being probed and at energies above the edge.

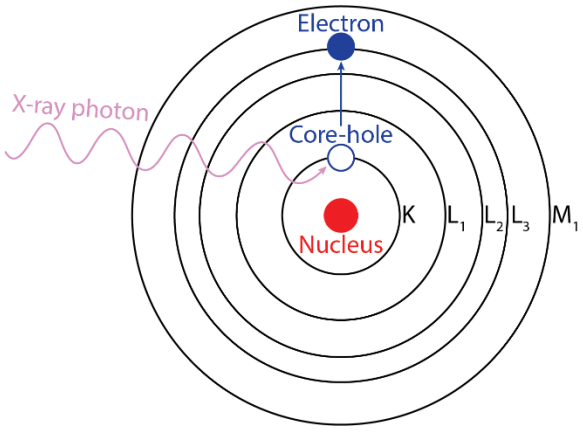

Figure 1.3 Schematic depiction of an electronic transition induced by an X-ray photon between a 1s orbital and a 2p orbital, probing a K edge.

In this thesis, transient extreme ultraviolet (XUV) spectroscopy is employed to measure photoexcited polaron dynamics in transition metal oxide semiconductors at their metal M edges. The XUV probe photons induce core-to-valence transitions of electrons that have element-specificity and are dependent upon which core-level orbitals are being probed, much like X-rays. The XUV photons are absorbed if the core-valence transitions occur. A change in probe absorption is subsequently measured.

To understand the origins of these M edge core-level transitions and subsequent XUV absorption, we must first consider the X-ray interaction Hamiltonian, approximated under first order perturbation theory, that describes the interactions of the XUV photons with electrons in the atoms being probed:

$$H_{int} = \frac{e}{mc}\sum_i p_i \cdot A(r_i) \quad \textbf{(1.3)}$$

where e is the electron charge, m is electron mass, and c is the speed of light. p_i is the momentum operator of an electron and $A(r_i)$ is the vector field that describes the plane wave of the interacting XUV photons.[35,36] If we apply the interaction Hamiltonian in **Equation 1.3** to Fermi's golden rule to predict the probability of an X-ray transition occurring, we have the form of **Equation 1.4**:

$$W_{fi} = \frac{2\pi}{\hbar}\sum_{fi}\left|\langle\Phi_f|T|\Phi_i\rangle\right|^2 \delta(E_f - E_i - \hbar\omega) \quad \textbf{(1.4)}$$

where W_{fi} is the transition probability between final and initial states and Φ_f (Φ_i) are the wavefunctions of the final (initial) state. The delta function considers conservation of energy and momentum, and a transition will occur if the energy of the final state is equal to the energy of the initial state plus the XUV photon energy.[37] T is the transition operator, considers all possible transitions, and to a first approximation its first term (T_1) is equal to the first term of the interaction Hamiltonian (H_1).

Figure 1.4 schematically depicts a transient XUV experiment in which an above band gap excitation prepares an excited state and changes in the XUV probe absorption are measured

to observe the changes in accessible, dipole-allowed electronic transitions following changes in state-filling. The dipole selection rules associated with these transitions conserve angular momentum and parity. Orbital angular momentum (l) follows the dipole selection rule $\Delta l = \pm 1$. Total angular momentum (j) must follow the dipole selection rule $\Delta j = 0, \pm 1$. And spin (ΔS) = 0 because the X-ray and XUV photons do not directly affect electronic spin. In this regard, because of orbital angular momentum selection rules, electrons originating from s orbitals can transition to p orbitals, while those originating in p orbitals could transition to either s or d orbitals. In this work, we mostly consider $M_{2,3}$ edges, which according to X-ray dipole selection rules typically probe 3p to 3d transitions.

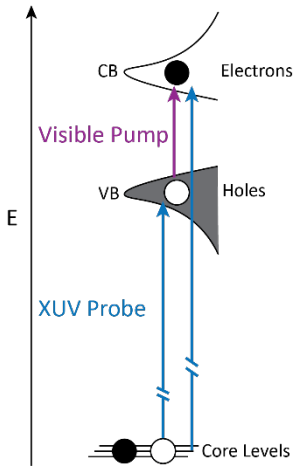

Figure 1.4 Schematic depiction of a transient XUV experiment in which an above band gap pump promotes electrons into the CBs, creating holes in the VBs. In a typical transient XUV experiment, the core-valence probe would probe dipole-allowed XUV transitions both before and after the photoexcitation arrives to differentiate between the ground and excited state.

1.2.1 Extreme Ultraviolet Reflection-Absorption Spectroscopy

Transient extreme ultraviolet (XUV) spectroscopy is a pump-probe spectroscopy that can resolve element-specific carrier and structural dynamics on the femtosecond (fs) to nanosecond (ns) time scale.[38–41] The energy range of XUV light is lower than that used in XAS (10–150 eV).[42] When a pump pulse photoexcites electrons from the conduction band to the valence band, transitions from the core level are either newly allowed (valence band holes) or blocked (conduction band electrons). XUV spectroscopy in a transmission mode provides bulk-sensitive material information, however, it requires sample thicknesses on the

order of hundreds of nanometers (nm) because of the attenuation length of XUV light.[43] On the other hand, XUV reflection-absorption spectroscopy provides surface-sensitive information (1–10 nm), where the penetration depth depends on the angle of reflection, though samples must be optically smooth to maximize reflected signal.

Transmission and reflection spectroscopies differ fundamentally in terms of the information being collected. Let us first consider the complex refractive index, $\tilde{n}(\omega)$, and dielectric function, $\varepsilon(\omega)$, of a material:

$$\tilde{n}(\omega) = n(\omega) + ik(\omega) = \sqrt{\varepsilon(\omega)} \quad \textbf{(1.5)}$$

where the real part of the complex refractive index (n) is dominated by refraction and indicates phase shift, the imaginary component contains the extinction coefficient (k), which is dominated by light attenuation and can be directly mathematically related to the absorption coefficient of a material as a function of frequency (ω).[44–47] When light hits a sample the light can be reflected, absorbed, scattered, or transmitted.[45,48] If we consider the Fresnel equations for transmitted light at normal incidence, the cos(θ) terms go to zero and we can simplify to:

$$t_{s0} = \frac{2n_1}{n_1+n_2} \quad \textbf{(1.6)}$$

$$t_{p0} = \frac{2n_1}{n_2+n_1} \quad \textbf{(1.7)}$$

where n_1 and n_2 are the refractive indices of the vacuum and sample, respectively. In **Equation 1.6**, t_{s0} describes the transmission of *s* polarized light at normal incidence and in **Equation 1.7** t_{p0} represents the transmission of *p* polarized light at normal incidence. For all positive values of complex refractive index, the Fresnel equations for both polarizations of transmitted light are equivalent, which indicates that phase differences are negligible at normal incidence in transmission and therefore the spectra will be dominated by k.[49] On the other hand, different angles of *reflected* light will have different contributions from the real

and imaginary parts of the complex refractive index, as seen in the Fresnel equations for reflected light:

$$r_s = \frac{n_1 cos\theta_i - n_2 cos\theta_t}{n_1 cos\theta_i + n_2 cos\theta_t} \quad \textbf{(1.8)}$$

$$r_p = \frac{n_2 cos\theta_i - n_1 cos\theta_t}{n_2 cos\theta_i + n_1 cos\theta_t} \quad \textbf{(1.9)}$$

The *s* and *p* polarized reflections (**Equations 1.8 and 1.9**) are not the same equation for positive refractive indices and as a result, transient XUV reflection-absorption spectroscopy measures both parts of the complex refractive index and both parts of the complex dielectric function, as the two are related. This has been both theoretically and experimentally verified for wavelengths in the XUV, as the complex refractive index is wavelength dependent.[9,46,48,50,51] This indicates that transient XUV measurements in a reflection geometry will provide different information than in a transmission geometry. As a result, the interpretation of reflection measurements can be complicated to deconvolve, as there are two parts of the complex refractive index contributing to transient signal.[46,48–50] In this thesis, we employ density functional theory (DFT) and the Bethe–Salpeter equation (BSE) to deconvolve our spectra.

1.2.2 Pump-Probe Spectroscopy

Pump-probe spectroscopy measures the ultrafast phenomena that determine electronic transport and optical properties of materials. This method relies on ultrafast laser pulses to maintain temporal control of the pump and probe. The pump pulse acts as an excitation to the sample. Changes to the probe pulse are then measured as a result of excitation after a time delay. This can mathematically be represented as:[48,52,53]

$$\Delta OD = -log_{10}\left(\frac{I_{pump\ on}}{I_{pump\ off}}\right) \quad \textbf{(1.10)}$$

In terms of the timing of pump-probe spectroscopy in the ultrafast regime, one of the two beams will be time delayed (Δt) with respect to the other. The pump beam arrives at the

sample before the probe beam and the two beams must be spatially overlapped to measure the excited area of the sample. The relative time delay in practice can be varied by changing the distance that the pump beam must travel to reach the sample with a mechanical delay stage or by electronically triggering the pulse. This method is invaluable to understanding the ultrafast dynamics of materials and has been broadly applied with different pump and probe wavelengths and expanded beyond the detection of light to instead the detection of photoelectrons.[54–57]

1.3 Thesis Overview

Transient XUV reflection-absorption spectroscopy is applied throughout this thesis to study the transient dynamics of carriers in iron oxide photocatalysts. Specifically, we probe photoexcited polaron formation on iron centers to understand the extent of electron–phonon coupling strength and carrier localization effects. In **Chapter 2**, we discuss the transient XUV experiment used in these studies. In **Chapters 3-6** we consider measurements of several iron oxides, systematically tuning structure, on-site repulsions, electron–phonon coupling strength, and exchange interactions to tune and even suppress photoexcited polaron formation. Finally, in **Chapter 7** we relate the result of systematically tuning materials parameters and measuring the resulting ultrafast polaron dynamics to several ground-state model Hamiltonians to provide design parameters that could aid in control of polaronic behavior in polaron forming materials. This work aims to present polaronic design principles that can be applied to device-relevant design rules for rational materials design.

1.4 References

(1) Ashcroft, N. W. *Solid State Physics*, 2nd ed.; Saunders College Publishing, 1976.

(2) Böer, K. W.; Pohl, U. W. *Semiconductor Physics*; Springer International Publishing: Cham, 2018. https://doi.org/10.1007/978-3-319-69150-3.

(3) Zaanen, J.; Sawatzky, G. A.; Allen, J. W. Band Gaps and Electronic Structure of Transition-Metal Compounds. *Phys. Rev. Lett.* **1985**, *55* (4), 418–421. https://doi.org/10.1103/PhysRevLett.55.418.

(4) Bu, X.; Li, Y. Optical Signature for Distinguishing between Mott-Hubbard, Intermediate, and Charge-Transfer Insulators. *Phys. Rev. B* **2022**, *106* (24), L241101. https://doi.org/10.1103/PhysRevB.106.L241101.

(5) Mott, N. F. The Basis of the Electron Theory of Metals, with Special Reference to the Transition Metals. *Proc. Phys. Soc. A* **1949**, *62* (7), 416

(6) Mott, N. F.; Peierls, R. Discussion of the Paper by de Boer and Verwey. *Proc. Phys. Soc.* **1937**, *49* (4S), 72. https://doi.org/10.1088/0959-5309/49/4S/308.

(7) Böer, J. H. de; Verwey, E. J. W. Semi-Conductors with Partially and with Completely Filled 3d-Lattice Bands. *Proc. Phys. Soc.* **1937**, *49* (4S), 59. https://doi.org/10.1088/0959-5309/49/4S/307.

(8) Mott, N. F. Metal-Insulator Transition. *Rev. Mod. Phys.* **1968**, *40* (4), 677–683. https://doi.org/10.1103/RevModPhys.40.677.

(9) Chen, W.; Xiong, W. Polaron-Formation Revealed by Transient XUV Imaginary Refractive Index Changes in Different Iron Compounds. *Phys. Chem. Chem. Phys.* **2021**, *23* (8), 4486–4490. https://doi.org/10.1039/D1CP00103E.

(10) Bandaranayake, S.; Hruska, E.; Londo, S.; Biswas, S.; Baker, L. R. Small Polarons and Surface Defects in Metal Oxide Photocatalysts Studied Using XUV Reflection–Absorption Spectroscopy. *J. Phys. Chem. C* **2020**, *124* (42), 22853–22870. https://doi.org/10.1021/acs.jpcc.0c07047.

(11) *Polarons in Advanced Materials*; Alexandrov, A. S., Ed.; Hull, R., Osgood, R. M., Parisi, J., Warlimont, H., Series Eds.; Springer Series in Materials Science; Springer Netherlands: Dordrecht, 2007; Vol. 103. https://doi.org/10.1007/978-1-4020-6348-0.

(12) Franchini, C.; Reticcioli, M.; Setvin, M.; Diebold, U. Polarons in Materials. *Nat. Rev. Mater.* **2021**, 1–27. https://doi.org/10.1038/s41578-021-00289-w.

(13) Puppin, M.; Polishchuk, S.; Colonna, N.; Crepaldi, A.; Dirin, D. N.; Nazarenko, O.; De Gennaro, R.; Gatti, G.; Roth, S.; Barillot, T.; Poletto, L.; Xian, R. P.; Rettig, L.; Wolf, M.; Ernstorfer, R.; Kovalenko, M. V.; Marzari, N.; Grioni, M.; Chergui, M. Evidence of Large Polarons in Photoemission Band Mapping of the Perovskite Semiconductor $CsPbBr_3$. *Phys. Rev. Lett.* **2020**, *124* (20), 206402. https://doi.org/10.1103/PhysRevLett.124.206402.

(14) Zhang, L.; Chu, W.; Zhao, C.; Zheng, Q.; Prezhdo, O. V.; Zhao, J. Dynamics of Photoexcited Small Polarons in Transition-Metal Oxides. *J. Phys. Chem. Lett.* **2021**, *12* (9), 2191–2198. https://doi.org/10.1021/acs.jpclett.1c00003.

(15) Ghosh, R.; Spano, F. C. Excitons and Polarons in Organic Materials. *Acc. Chem. Res.* **2020**, *53* (10), 2201–2211. https://doi.org/10.1021/acs.accounts.0c00349.

(16) Mott, N. F. Polaron Models of High-Temperature Superconductors. *J. Phys. Condens. Matter* **1993**, *5* (22), 3487. https://doi.org/10.1088/0953-8984/5/22/003.

(17) Mihailovic, D. Insights into the Polaron Physics of High Temperature Superconductors from Optical and Time-Domain Spectroscopy. *Phys. C Supercond. Its Appl.* **2023**, *615*, 1354385. https://doi.org/10.1016/j.physc.2023.1354385.

(18) Zhang, C.; Sous, J.; Reichman, D. R.; Berciu, M.; Millis, A. J.; Prokof'ev, N. V.; Svistunov, B. V. Bipolaronic High-Temperature Superconductivity. *Phys. Rev. X* **2023**, *13* (1), 011010. https://doi.org/10.1103/PhysRevX.13.011010.

(19) Fröhlich, H. Electrons in Lattice Fields. *Adv. Phys.* **1954**, *3* (11), 325-361. https://www.tandfonline.com/doi/abs/10.1080/00018735400101213.

(20) Alexandrov, A. S.; Devreese, J. T. *Advances in Polaron Physics;* Springer Series in Solid-State Sciences, Vol. 159; Springer: Berlin, Heidelberg, 2010.

(21) Devreese, J. T. Polarons. In *Encyclopedia of Applied Physics*; Wiley-VCH Verlag GmbH & Co. KGaA: Weinheim, Germany, 2003; DOI: 10.1002/3527600434.eap347.

(22) Guster, B.; Melo, P.; Martin, B. A. A.; Brousseau-Couture, V.; de Abreu, J. C.; Miglio, A.; Giantomassi, M.; Côté, M.; Frost, J. M.; Verstraete, M. J.; Gonze, X. Fröhlich Polaron Effective Mass and Localization Length in Cubic Materials: Degenerate and Anisotropic Electronic Bands. *Phys. Rev. B* **2021**, *104* (23), 235123. https://doi.org/10.1103/PhysRevB.104.235123.

(23) Holstein, T. Studies of Polaron Motion: Part II. The "Small" Polaron. *Ann. Phys.* **2000**, *281* (1), 725–773. https://doi.org/10.1006/aphy.2000.6021.

(24) Berciu, M. Exact Green's Functions for the Two-Site Hubbard-Holstein Hamiltonian. *Phys. Rev. B* **2007**, *75* (8), 081101. https://doi.org/10.1103/PhysRevB.75.081101.

(25) Sio, W. H.; Verdi, C.; Poncé, S.; Giustino, F. *Ab Initio* Theory of Polarons: Formalism and Applications. *Phys. Rev. B* **2019**, *99* (23), 235139. https://doi.org/10.1103/PhysRevB.99.235139.

(26) Landau, L. D.; Pekar, S. I. Effective Mass of a Polaron. *Zh. Eksp. Teor. Fiz* **1948**, *18* (5), 419–423.

(27) Prokof'ev, N. V.; Svistunov, B. V. Polaron Problem by Diagrammatic Quantum Monte Carlo. *Phys. Rev. Lett.* **1998**, *81* (12), 2514–2517. https://doi.org/10.1103/PhysRevLett.81.2514.

(28) Ciuchi, S.; de Pasquale, F.; Fratini, S.; Feinberg, D. Dynamical Mean-Field Theory of the Small Polaron. *Phys. Rev. B* **1997**, *56* (8), 4494–4512. https://doi.org/10.1103/PhysRevB.56.4494.

(29) Meggiolaro, D.; Ambrosio, F.; Mosconi, E.; Mahata, A.; De Angelis, F. Polarons in Metal Halide Perovskites. *Adv. Energy Mater.* **2020**, *10* (13), 1902748. https://doi.org/10.1002/aenm.201902748.

(30) Kestler, M. F.; Woo, K. C.; Lim, J. W. X.; Prins, L. M.; Feldmann, J.; Loh, Z.-H. Direct Observation of Fröhlich Polaron Formation in BiOI Nanoplatelets. *Phys. Rev. Mater.* **2026**, *10* (2), L022401. https://doi.org/10.1103/wcq2-gpmz.

(31) Mendes, J. L.; Shin, H. J.; Seo, J. Y.; Lee, N.; Choi, Y. J.; Varley, J. B.; Cushing, S. K. Dynamic Competition between Hubbard and Superexchange Interactions Selectively Localizes Electrons and Holes through Polarons. *J. Am. Chem. Soc.* **2025**. https://doi.org/10.1021/jacs.4c16837.

(32) Ahmad, J.; Uwe, H. Small-Polaron Excitations in $Ba_{1-x}K_xBiO_3$ Studied by Optical Reflectivity Measurements. *Phys. Rev. B* **2005**, *72* (12), 125103. https://doi.org/10.1103/PhysRevB.72.125103.

(33) Tian, L.; Sachs, M.; Verga, L. G.; Kunzelmann, V. F.; Kafizas, A.; Sharp, I. D.; Cushing, S. K.; Walsh, A.; Durrant, J. R. Optical Spectroscopic Determination of Photoexcited Small-Polaron Hopping in Transition Metal Oxide Photocatalysts. *Chem. Sci.* **2026**, *17* (8), 4203–4212. https://doi.org/10.1039/D5SC08101G.

(34) Carneiro, L. M.; Cushing, S. K.; Liu, C.; Su, Y.; Yang, P.; Alivisatos, A. P.; Leone, S. R. Excitation-Wavelength-Dependent Small Polaron Trapping of Photoexcited Carriers in α-Fe_2O_3. *Nat. Mater.* **2017**, *16* (8), 819–825. https://doi.org/10.1038/nmat4936.

(35) de Groot, F. Multiplet Effects in X-Ray Spectroscopy. *Coord. Chem. Rev.* **2005**, *249* (1), 31–63. https://doi.org/10.1016/j.ccr.2004.03.018.

(36) de Groot, F; Kotani, A. *Core Level Spectroscopy of Solids*; CRC Press: Boca Raton, 2008. https://doi.org/10.1201/9781420008425.

(37) *Neutron and X-Ray Spectroscopy*; Hippert, F., Geissler, E., Hodeau, J. L., Lelièvre-Berna, E., Regnard, J.-R., Eds.; Springer Netherlands: Dordrecht, 2006. https://doi.org/10.1007/1-4020-3337-0.

(38) Cushing, S. K.; Lee, A.; Porter, I. J.; Carneiro, L. M.; Chang, H.-T.; Zürch, M.; Leone, S. R. Differentiating Photoexcited Carrier and Phonon Dynamics in the Δ, *L* , and Γ Valleys of Si(100) with Transient Extreme Ultraviolet Spectroscopy. *J. Phys. Chem. C* **2019**, *123* (6), 3343–3352. https://doi.org/10.1021/acs.jpcc.8b10887.

(39) Cushing, S. K.; Zürch, M.; Kraus, P. M.; Carneiro, L. M.; Lee, A.; Chang, H.-T.; Kaplan, C. J.; Leone, S. R. Hot Phonon and Carrier Relaxation in Si(100) Determined by Transient Extreme Ultraviolet Spectroscopy. *Struct. Dyn.* **2018**, *5* (5), 054302. https://doi.org/10.1063/1.5038015.

(40) Biswas, S.; Husek, J.; Londo, S.; Fugate, E. A.; Baker, L. R. Identifying the Acceptor State in NiO Hole Collection Layers: Direct Observation of Exciton Dissociation and Interfacial Hole Transfer across a Fe_2O_3/NiO Heterojunction. *Phys. Chem. Chem. Phys.* **2018**, *20* (38), 24545–24552. https://doi.org/10.1039/C8CP04502J.

(41) Vura-Weis, J.; Jiang, C.-M.; Liu, C.; Gao, H.; Lucas, J. M.; de Groot, F. M. F.; Yang, P.; Alivisatos, A. P.; Leone, S. R. Femtosecond $M_{2,3}$-Edge Spectroscopy of Transition-Metal Oxides: Photoinduced Oxidation State Change in α-Fe_2O_3. *J. Phys. Chem. Lett.* **2013**, *4* (21), 3667–3671. https://doi.org/10.1021/jz401997d.

(42) Khalil, M.; Mukamel, S. Ultrafast Spectroscopy and Diffraction from XUV to X-Ray. *J. Chem. Phys.* **2020**, *153* (10), 100401. https://doi.org/10.1063/5.0026054.

(43) Henke, B. L.; Gullikson, E. M.; Davis, J. C. X-Ray Interactions: Photoabsorption, Scattering, Transmission, and Reflection at E = 50-30,000 eV, Z = 1-92. *At. Data Nucl. Data Tables* **1993**, *54* (2), 181–342. https://doi.org/10.1006/adnd.1993.1013.

(44) Sorensen, C. M.; Maughan, J. B.; Moosmüller, H. Spherical Particle Absorption over a Broad Range of Imaginary Refractive Index. *J. Quant. Spectrosc. Radiat. Transf.* **2019**, *226*, 81–86. https://doi.org/10.1016/j.jqsrt.2019.01.011.

(45) Lucas, P. Optical Materials | Measurement of Optical Properties of Solids. In *Encyclopedia of Modern Optics*; Elsevier, 2005; pp 466–474. https://doi.org/10.1016/B0-12-369395-0/00874-5.

(46) Kaplan, C. J.; Kraus, P. M.; Gullikson, E. M.; Borja, L. J.; Cushing, S. K.; Zürch, M.; Chang, H.-T.; Neumark, D. M.; Leone, S. R. Retrieval of the Complex-Valued Refractive Index of Germanium near the $M_{4,5}$ Absorption Edge. *JOSA B* **2019**, *36* (6), 1716–1720. https://doi.org/10.1364/JOSAB.36.001716.

(47) Bohren, C. F.; Huffman, D. R. *Absorption and Scattering of Light by Small Particles*; Wiley-VCH Verlag GmbH, 1998.

(48) Cirri, A.; Husek, J.; Biswas, S.; Baker, L. R. Achieving Surface Sensitivity in Ultrafast XUV Spectroscopy: $M_{2,3}$ -Edge Reflection–Absorption of Transition Metal Oxides. *J. Phys. Chem. C* **2017**, *121* (29), 15861–15869. https://doi.org/10.1021/acs.jpcc.7b05127.

(49) Kaplan, C. J. Ultrafast Dynamics in Condensed Matter Studied with Attosecond Extreme Ultraviolet Transient Reflectivity, UC Berkeley, 2019. https://escholarship.org/uc/item/3xh309qx (accessed 2023-02-17).

(50) Feuerbacher, B.; Skibowski, M.; Godwin, R. P.; Sasaki, T. Optical Constants of Germanium in the Region of the $M_{4,5}$ Edge*. *JOSA* **1968**, *58* (11), 1434–1440. https://doi.org/10.1364/JOSA.58.001434.

(51) Rustgi, O. P.; Nodvik, J. S.; Weissler, G. L. Optical Constants of Germanium in the Region 0-27 Ev. *Phys. Rev.* **1961**, *122* (4), 1131–1134. https://doi.org/10.1103/PhysRev.122.1131.

(52) Klein, I. M. Understanding the Origins of Photoexcited XUV Spectra. PhD, California Institute of Technology, 2023. https://doi.org/10.7907/s8qe-4s74.

(53) Liu, H.; Michelsen, J. M.; Mendes, J. L.; Klein, I. M.; Bauers, S. R.; Evans, J. M.; Zakutayev, A.; Cushing, S. K. Measuring Photoexcited Electron and Hole Dynamics in ZnTe and Modeling Excited State Core-Valence Effects in Transient Extreme Ultraviolet Reflection Spectroscopy. *J. Phys. Chem. Lett.* **2023**, 2106–2111. https://doi.org/10.1021/acs.jpclett.2c03894.

(54) Di Cicco, A.; Polzoni, G.; Gunnella, R.; Trapananti, A.; Minicucci, M.; Rezvani, S. J.; Catone, D.; Di Mario, L.; Pelli Cresi, J. S.; Turchini, S.; Martelli, F. Broadband Optical Ultrafast Reflectivity of Si, Ge and GaAs. *Sci. Rep.* **2020**, *10* (1), 17363. https://doi.org/10.1038/s41598-020-74068-y.

(55) de Groot, F. High-Resolution X-Ray Emission and X-Ray Absorption Spectroscopy. *Chem. Rev.* **2001**, *101* (6), 1779–1808. https://doi.org/10.1021/cr9900681.

(56) Mayer, D.; Lever, F.; Picconi, D.; Metje, J.; Alisauskas, S.; Calegari, F.; Düsterer, S.; Ehlert, C.; Feifel, R.; Niebuhr, M.; Manschwetus, B.; Kuhlmann, M.; Mazza, T.; Robinson, M. S.; Squibb, R. J.; Trabattoni, A.; Wallner, M.; Saalfrank, P.; Wolf, T. J. A.; Gühr, M. Following Excited-State Chemical Shifts in Molecular Ultrafast X-Ray Photoelectron Spectroscopy. *Nat. Commun.* **2022**, *13* (1), 198. https://doi.org/10.1038/s41467-021-27908-y.

(57) Zapolnova, E.; Golz, T.; Pan, R.; Klose, K.; Schreiber, S.; Stojanovic, N. THz Pulse Doubler at FLASH: Double Pulses for Pump–Probe Experiments at X-ray FELs. *J. Synchrotron Radiat.* **2018**, *25*, 39–43. DOI: 10.1107/S1600577517015442.

Chapter 2

TRANSIENT EXTREME ULTRAVIOLET SPECTROSCOPY

2.1 High Harmonic Generation

Extreme ultraviolet (XUV) light is generated using the high harmonic generation (HHG) process. HHG in noble gases generally follows semiclassical a three-step model, initially presented by Corkum.[1,2] **Figure 2.1** illustrates this process.

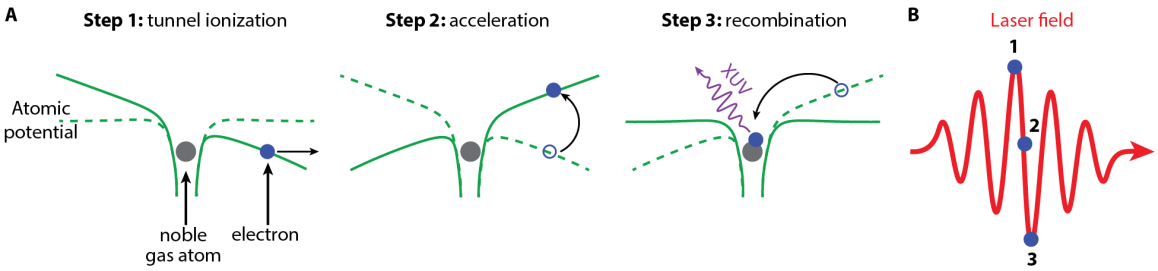

Figure 2.1 Schematic illustration of the high harmonic generation process. **(A)** The semi-classical three step model of HHG in which a noble gas atom in an intense laser field in step 1 has its atomic potential modified such that tunnel ionization of the valence electrons can occur. In step 2, the electron is accelerated in the laser field and in step 3 when the laser field switches sign, the electron recombines with its parent ion, resulting in photoemission of a harmonic multiple of the driving frequency. **(B)** Depiction of steps 1-3 of the three-step model in the laser field.

In the first step, an intense laser pulse with a power density $>10^{14}$ W/cm^2 removes an electron from the noble gas being ionized by tunnel ionization near the peak of the laser pulse's electric field.[2,3] Tunnel ionization occurs when an atom has its Coulomb potential barrier lowered by an intense enough electric field such that there is a nonzero probability of the electron being able to tunnel through the Coulomb potential barrier and away from the nucleus.[4] The tunneling is most probable when the amplitude of the electric field is at a maximum, which occurs twice during an optical cycle, exhibited by the trace **Figure 2.1B**.[5] During the second step, the electron is accelerated away from the ion in the same laser pulse and propagates classically in the electric field.[3] This is what gives the approach a semiclassical nature, as the electron is considered quantum in steps 1 and 3.[2] As the pulse switches sign there is an acceleration back towards the nucleus of the ion. In step three the

acceleration of the electron back towards the ion causes a recombination resulting in emission of coherent radiation at an energies equivalent to the sum of the kinetic energy of the electron and the ionization potential of the gas atom.[3] The energy of the coherent radiation emitted correspond to harmonic frequencies of the fundamental pulse.[6]

Based upon Corkum's model we know that the typical harmonic spectrum emitted via HHG in noble gases contains odd harmonics that have a maximum energy equal to that shown in **Equation 2.1**:

$$E_{photon} \leq 3.17\left(\frac{e^2E_0^2}{4m_e\omega^2}\right) + I_P \qquad \textbf{(2.1)}$$

where I_p is the atomic ionization potential of the noble gas and the expression $\left(\frac{e^2E_0^2}{4m_e\omega^2}\right)$ is equal to the ponderomotive potential (U_p) of a free electron in an electromagnetic field of strength E_0 and frequency ω.[1] Due to the nature of harmonic emission, **Equation 2.1** determines the maximum energy of the emitted radiation as recombination of the electron with the ion may result in a range of energies that scales nonlinearly as a harmonic spectrum. The range of emitted photon energies originates from electrons ionized at different phases of the driving field, which follow specific trajectories and recombine with the parent ion with varying kinetic energies. This maximum energy is often referred to as the cutoff energy and explains why different noble gases will produce different energy harmonics.[7]

The emission of odd harmonics by noble gases can be understood by **Equations 2.2** and **2.3**. The polarization (P) of an electric field (E) can be represented as:

$$P = \varepsilon_0\left[\chi^{(1)} * E + \chi^{(2)} * E^2 + \chi^{(3)} * E^3 + \cdots\right] \qquad \textbf{(2.2)}$$

where ε_0 is the permittivity of free space and χ is the susceptibility of the medium. Then, in the case of noble gases which are centrosymmetric, we can assume that the electron displacement is independent of the direction of the electric field.[6,8] This would result in all

even orders of χ being zero, with only odd numbered harmonics generated if the electric field follows the form of **Equation 2.3**:

$$E(t) = E_0 e^{i\omega t} \qquad (\mathbf{2.3})$$

Essentially, this demonstrates that even numbered harmonic transitions would be symmetry forbidden in the case of HHG in a centrosymmetric medium. On the other hand, even number harmonics have been observed in materials that are non-centrosymmetric, such as zincblende structured GaP bulk crystals.[9]

In addition to the presence of only odd harmonics in noble gases, the produced harmonic spectra exhibit several characteristic features. Specifically, the shape and intensity of the produced harmonic spectrum of a noble gas has low-energy harmonics that decrease in intensity until a plateau, at which point the harmonics remain at around the same relative intensity.[1] The low-energy harmonics decrease in intensity due to their classification within the perturbative regime, while harmonics after the plateau are within the nonperturbative regime.[7] This is followed by what is referred to as an "abrupt" cutoff for the highest energy harmonic, where the spectrum immediately stops at the cutoff energy, rather than slowly decreasing in harmonic intensity until the cutoff energy.[10] However, as the intensity of the laser pulse increases, the size of the plateau also increases, which affords more intense harmonics.[11] That is why the advent of powerful, few-cycle, mJ lasers has greatly improved HHG flux, bandwidth, and cutoff energies.[3]

2.2 Transient Extreme Ultraviolet Spectrometer

Figure 2.2 provides a detailed schematic of the transient XUV beamline. In brief, a Legend Elite Duo laser system (Coherent Inc.) provides 35 fs, 13 mJ, 1 kHz pulses centered at 800

nm. The output of the laser is split by a 75:25 beam splitter with ~3 mJ being used for the probe and ~10 mJ for the pump path.

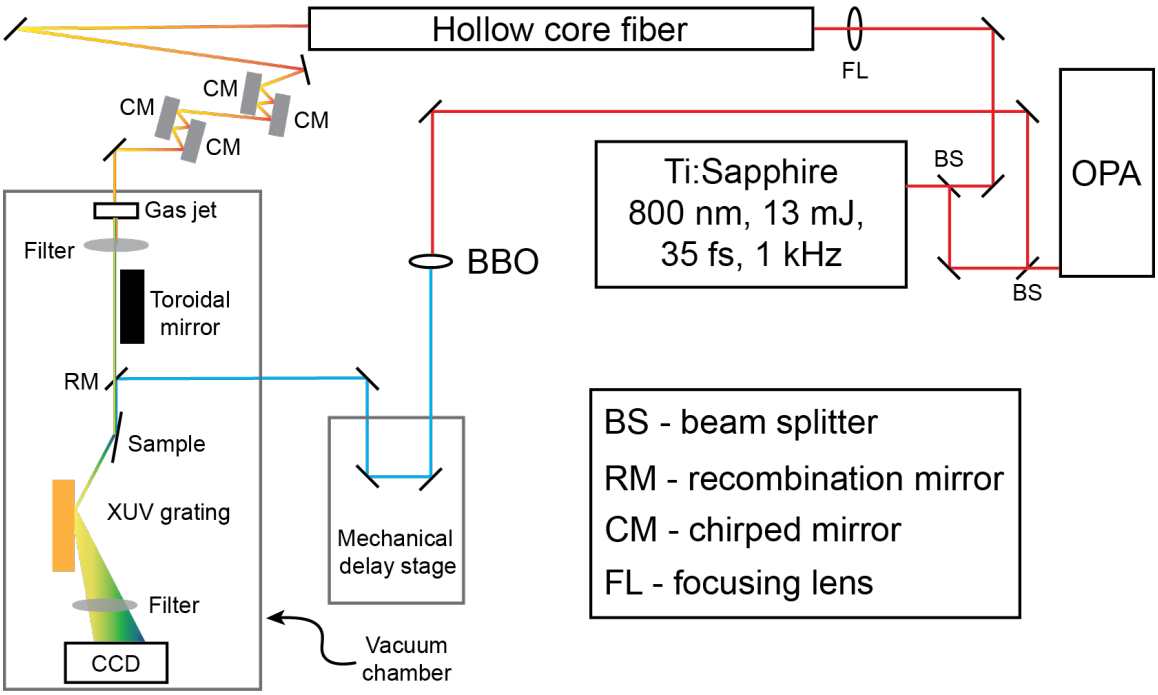

Figure 2.2 Schematic diagram of the transient XUV spectrometer.

The pump path is equipped for excitation using the p-polarized 800 nm fundamental, the 400 nm frequency doubled output of a beta-barium borate (BBO) crystal with p-polarization, or third harmonic generation (THG) of the 800 nm fundamental beam using two BBO crystals and a Michelson interferometer resulting in 266 nm excitation. The frequency doubling achieved through second harmonic generation (SHG) results in a 400 nm pump pulse energy of ~800 μJ and the tripling achieved via THG provides ~100 μJ of a 266 nm pump pulse. Pump power is modulated using a neutral density (ND) filter wheel (Thorlabs) which enables changes to pump pulse energy within ~1 μJ. Excitation wavelengths are selected based upon the type of excitation desired for the material system being studied. Typically for semiconductor samples an above band gap photoexcitation is selected, and the 266 nm and 400 nm pump wavelengths are sufficient.

The 35 fs, 800 nm probe pulses are spectrally broadened in a 500 μm diameter, 1 m hollow core fiber (HCF, Few-Cycle) filled with ~50 PSI of Ne gas. Fiber broadening results in 50%

transmission of white light with a spectrum spanning 550–950 nm. The spectrally broadened pulse is dispersion compensated on chirped mirror pairs (Ultrafast Innovation PC70) with 12 bounces. The chirped mirrors (CMs) are in pairs, with the first pair being at an incidence angle of 5° and the second pair having an angle of incidence of 19°. The chirped mirrors add -40 fs^2 per bounce by compensating group delay dispersion (GDD) oscillations.[12] This is enabled by the multilayer structure of the CMs in which a gradual change in thickness across the rectangular mirror causes a wavelength-dependent penetration depth of the incident broadband light.[13] This results in <7 fs pulses as verified by a dispersion scan shown in **Figure 2.3**. The broadband few-cycle white light probe (s-polarized) is focused into a Teflon infinite gas jet in the vacuum chamber to drive HHG. The gas jet has a ~150 μm hole at the beam focus and Ar gas flows through it during standard operation.

Following high harmonic generation, the residual white light beam is removed with a 100-200 nm thick Al filter (Luxel). A toroidal mirror focuses the XUV beam at the sample position. The XUV beam interacts with the sample at a 10° grazing incidence (80° from normal incidence) and is reflected onto a gold coated, concave X-ray grating (Hitachi) and into a UV-enhanced CCD camera (Greateyes GmbH). The pump beam enters the vacuum chamber in a recombination chamber between the toroidal mirror and the sample and is 90° with respect to the XUV probe. A d-mirror routes the pump to the sample in a near-collinear geometry with the XUV probe. An additional 100 nm Al filter between the grating and CCD filters pump scatter. Transient reflection measures the varying delay times between the pump and probe pulses by an optomechanical delay stage on the pump path.

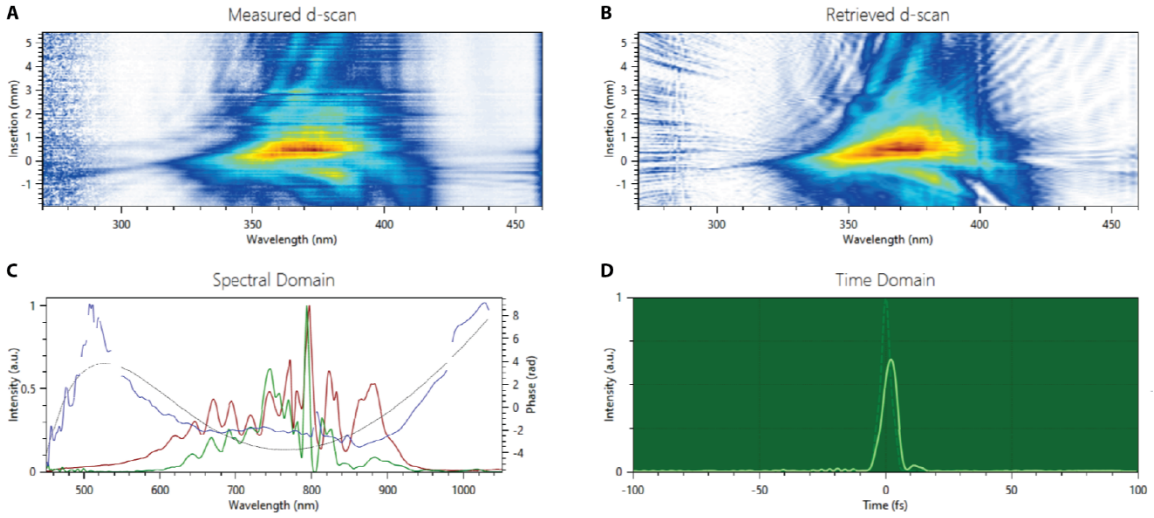

Figure 2.3 Dispersion scan of the spectrally broadened and temporally compressed output from the Ne-filled hollow-core fiber. **(A)** Shows the measured d-scan of the pulse which is retrieved in **(B)**. **(C)** The spectrum of the pulse spans ~500–950 nm. **(D)** The temporal width of the pulse is found to be 6.4 fs.

2.3 Transient Extreme Ultraviolet Spectrometer Operation

Temporal overlap, or t_0, is verified via a visible pump, visible probe measurement. Schematically, the Al filter after the gas jet is retracted so that the fundamental broadband white light beam hits the sample following the same beam path as the XUV beam. A mirror mounted on a flipping stage that can flip into the XUV beam path after the sample points the visible probe outside of the chamber where it travels an equivalent distance outside of the chamber as it would travel to reach the CCD camera. The probe beam is measured outside of the vacuum chamber using a photodiode connected to a lock-in amplifier. A MATLAB code correlates the signal from the lock-in amplifier with changes in timing based upon the position of the pump's delay stage. The pump beam is unblocked, set to a pulse energy ranging from 50–100 μJ (1.74 mJ/cm^2 at 40 μJ), and chopped at a frequency of 250 Hz with an optical chopper (Thorlabs, MC1F10). Time zero measurements are collected on Si

samples and a step function is visible when carriers have been photoexcited in the Si samples at time zero (**Fig. 2.4A**).

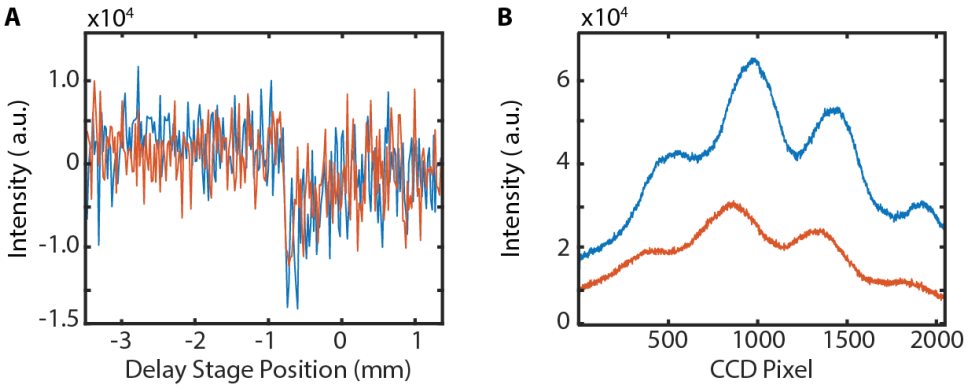

Figure 2.4 Visible pump-probe experiments and a burn test confirm temporal and spatial overlap. **(A)** Visible pump-probe experiments exhibit a step function in the visible probe beams intensity on the photodiode at time zero, plotted as a function of delay stage position. **(B)** A burn test to confirm spatial overlap of the visible pump and XUV probe beam is confirmed by damaging a Si substrate with the pump beam. The blue line denotes the harmonic spectrum prior to the burn test, while the orange line denotes the harmonic spectrum following 10 seconds of exposure to a 200 μJ 400 nm beam.

While temporal overlap can be extrapolated with the visible probe beam because the timing of the fundamental and the XUV beam should be equal if they travel the same distance, there is no simple way to confirm that the XUV mode matches spatially with the visible probe's mode. Typically, to overcome this a pinhole could be utilized for spatial filtering; however, this is challenging in a reflection geometry where both the pump and probe beams become elongated and smeared due to the grazing angle. Therefore, to confirm spatial overlap in the reflection geometry we conduct a burn test, in which we increase the intensity of the pump beam above the damage threshold of a sample to damage the sample until it no longer reflects harmonics in that spot. In practice, we again use silicon wafers. For damaging Si, we use ~200 μJ of the pump and raster the position of the pump beam while watching the harmonic profile in the CCD until the intensity of the harmonic profile decreases. **Figure 2.4B** is a before and after of the harmonic profile following ~10 seconds of burning.

With temporal and spatial overlap confirmed a transient measurement can be collected. Transient XUV spectra are collected using a MATLAB code that collects pump-on and pump-off measurements using a shutter in the pump path and a pump delay. Typical

measurements require >200 scan averages to resolve a transient signal above the noise floor, but this number of averages differs depending on the intensity of signal that a particular sample reflects and the X-ray edge of interest.

2.4 References

(1) Lewenstein, M.; Balcou, Ph.; Ivanov, M. Yu.; L'Huillier, A.; Corkum, P. B. Theory of High-Harmonic Generation by Low-Frequency Laser Fields. *Phys. Rev. A* **1994**, *49* (3), 2117–2132. https://doi.org/10.1103/PhysRevA.49.2117.

(2) Corkum, P. B. Plasma Perspective on Strong Field Multiphoton Ionization. *Phys. Rev. Lett.* **1993**, *71* (13), 1994–1997. https://doi.org/10.1103/PhysRevLett.71.1994.

(3) Jiang, C.-M. Charge Carrier Dynamics in Transition Metal Oxides Studied by Femtosecond Transient Extreme Ultraviolet Absorption Spectroscopy, UC Berkeley, 2015. https://escholarship.org/uc/item/7129618s (accessed 2026-03-23).

(4) Ammosov, M. V.; Delone, N. B.; Krainov, V. P. Tunnel Ionization of Complex Atoms and Atomic Ions in Electromagnetic Field. In *High Intensity Laser Processes*; SPIE, 1986; Vol. 0664, pp 138–141. https://doi.org/10.1117/12.938695.

(5) Kulander, K. C.; Schafer, K. J.; Krause, J. L. Dynamics of Short-Pulse Excitation, Ionization and Harmonic Conversion. In *Super-Intense Laser-Atom Physics*; Piraux, B., L'Huillier, A., Rzążewski, K., Eds.; NATO ASI Series; Springer US: Boston, MA, 1993; pp 95–110. https://doi.org/10.1007/978-1-4615-7963-2_10.

(6) Borja, L. J. Electron Dynamics in Solids Studied by Attosecond Extreme Ultraviolet Spectroscopy, UC Berkeley, 2016. https://escholarship.org/uc/item/33t5t9zr (accessed 2026-02-17).

(7) Schafer, K. J.; Yang, B.; DiMauro, L. F.; Kulander, K. C. Above Threshold Ionization beyond the High Harmonic Cutoff. *Phys. Rev. Lett.* **1993**, *70* (11), 1599–1602. https://doi.org/10.1103/PhysRevLett.70.1599.

(8) Boyd, R. *Nonlinear Optics*, 3rd ed.; Elsevier, 2008.

(9) Shcherbakov, M. R.; Zhang, H.; Tripepi, M.; Sartorello, G.; Talisa, N.; AlShafey, A.; Fan, Z.; Twardowski, J.; Krivitsky, L. A.; Kuznetsov, A. I.; Chowdhury, E.; Shvets, G. Generation of Even and Odd High Harmonics in Resonant Metasurfaces Using Single and Multiple Ultra-Intense Laser Pulses. *Nat. Commun.* **2021**, *12* (1), 4185. https://doi.org/10.1038/s41467-021-24450-9.

(10) Krause, J. L.; Schafer, K. J.; Kulander, K. C. High-Order Harmonic Generation from Atoms and Ions in the High Intensity Regime. *Phys. Rev. Lett.* **1992**, *68* (24), 3535–3538. https://doi.org/10.1103/PhysRevLett.68.3535.

(11) Ferray, M.; L'Huillier, A.; Li, X. F.; Lompre, L. A.; Mainfray, G.; Manus, C. Multiple-Harmonic Conversion of 1064 nm Radiation in Rare Gases. *J. Phys. B At. Mol. Opt. Phys.* **1988**, *21* (3), L31–L35. https://doi.org/10.1088/0953-4075/21/3/001.

(12) Pervak, V.; Ahmad, I.; Trubetskov, M. K.; Tikhonravov, A. V.; Krausz, F. Double-Angle Multilayer Mirrors with Smooth Dispersion Characteristics. *Opt. Express* **2009**, *17* (10), 7943–7951. https://doi.org/10.1364/OE.17.007943.

(13) Silva, F.; Miranda, M.; Alonso, B.; Rauschenberger, J.; Pervak, V.; Crespo, H. Simultaneous Compression, Characterization and Phase Stabilization of GW-Level 1.4 Cycle VIS-NIR Femtosecond Pulses Using a Single Dispersion-Scan Setup. *Opt. Express* **2014**, *22* (9), 10181–10191. https://doi.org/10.1364/OE.22.010181.

Chapter 3

COHERENT AND DYNAMIC SMALL POLARON DELOCALIZATION IN $CUFEO_2$

This chapter is adapted with permission from:

Mendes, J. L.*; Bhattacharyya, S.*; Huang, C.; Michelsen, J. M.; Klein, I. M.; Babbe, F.; Sayer, T.; Li, T.; Cooper, J. K.; Liu, H.; Ginsberg, N.; Montoya-Castillo, A.; Cushing, S. K. Coherent and Dynamic Small Polaron Delocalization in $CuFeO_2$. *J. Phys. Chem. Lett.* **2026**, *17* (2), 656–664. https://doi.org/10.1021/acs.jpclett.5c03430.

3.1 Abstract

Small polarons remain a bottleneck in realizing efficient transition metal oxide de-vices. Routes to engineer small polaron coupling to electronic states and lattice modes to control carrier localization remain unclear. Here, we measure small polaron formation in $CuFeO_2$ using transient extreme ultraviolet reflection spectroscopy and compare to theoretical predictions in realistically parameterized Holstein models, demonstrating that polaron localization depends on coupling to high-frequency versus low-frequency phonon bath components. We measure small polaron formation on a comparable ∼100 fs timescale to other Fe(III) compounds. Dynamic delocalization of the polaron follows formation through a coherent lattice expansion between Fe-O layers and charge-sharing with surrounding Fe(IV) states. Simulations reveal two major factors dictate polaron formation timescales: phonon density and reorganization energy distributions between acoustic and optical modes, matching experimental findings. Our work shows how electronic-structural coupling in a polaron-host material can be leveraged to suppress polaronic effects for various applications.

3.2 Introduction

Polarons play a significant role in various material physics, encompassing superconductivity, charge density waves, and electronic transport in both organic and inorganic materials.[1–6] In transition metal oxides with narrow bandwidth, the interplay between strong electron

correlations and strong electron-phonon coupling determines properties ranging from band structure to charge transport.[6] For materials with photocatalytic applications, the effect on surface chemical kinetics that benefit from charge localization and lattice reorganization must also be considered.[7,8] Iron oxide compounds, such as α-Fe_2O_3 (hematite), are prototypical photocatalysts that possess ideal charge-transfer-based band gaps in the visible spectrum and surface kinetics due to their localized d-orbitals. However, their efficiency falls short of the theoretical maximum because the same properties lead to the formation of photoexcited small polarons, which reduce carrier mobility.[9] While transition metal oxides that have an empty d-shell after bonding, such as TiO_2, tend to form photoexcited large polarons with sufficient carrier mobilities to approach near-theoretical efficiencies, the same bonding also usually leads to large UV bandgaps that limit overall solar absorption efficiency.[10]

The dynamics of small polaron formation are well studied and understood, but the mechanism for delocalizing polarons to improve carrier lifetimes remains unclear.[8,11] In α-Fe_2O_3, the photoexcited electron distorts the local lattice upon the initial electron-optical phonon scattering, forming small polarons that trap photoexcited carriers with a large carrier effective mass. One proposed approach to suppress small polaron formation is to introduce new atoms at the unit cell level, thereby decreasing the reorganization energy of the small polaron below the thermal energy.[12] Understanding the effect of atomic substitutions on small polaron formation dynamics and their correlation to photoexcited charge transport is necessary for improving photocatalysis and engineering other small-polaron-based applications.

In this work, we measure the delocalization of small polarons in $CuFeO_2$ using transient extreme ultraviolet (XUV) spectroscopy and compare the formation dynamics directly to ab-initio calculations, which consider coupling to both the optical and acoustic phonon bath. $CuFeO_2$ has a delafossite structure (**Fig. 3.1A**) with 2D Cu atomic layers substituted between Fe–O networks, and was identified by high-throughput screening techniques as a potential high-performing photocatalyst.[13–15] XUV measurements of $CuFeO_2$ have demonstrated

cathodic photocurrent not present in hematite in addition to suggestions of small polaron formation, which are further explored here.[16] The Cu atoms are expected to modulate small polaron formation in two ways: by providing increased electronic screening between photoexcited polarons in the Fe–O layers and by allowing the lattice to expand perpendicular to the Fe–O plane to reduce reorganization potentials. Our transient XUV measurements indicate that electronic screening between layers does not change the small polaron formation rate from the standard <100 fs measured for most Fe(III) oxides.[11,17,18] Quantum dynamics simulations demonstrate that this polaron formation timescale depends on electronic-structural coupling to different frequency components of the phonon bath. The ability for the lattice to expand perpendicular to the Fe–O plane, is measured to enable a polaron delocalization on a picosecond timescale through a coherent Cu–(Fe–O) *c*-axis phonon mode.[19] A corresponding nearest-neighbor Fe(III) to Fe(IV) charge compensation supports the hypothesis of an initial small-electron-polaron delocalizing beyond the initial Fe(III) site to the near-est neighbors.[20] Transient absorption microscopy reveals that the delocalized polaron leads to a longer recombination timescale when compared to α-Fe_2O_3 with similar crystallinity conditions.[17,21–23] Beyond photocatalysis, the results provide insight into a broad range of small polaron based materials and how lattice interactions and electron correlations can be leveraged to tune their properties.

3.3 Results

Figure 3.1A shows the crystal structure of $CuFeO_2$, where the Fe–O sublattices are capped by Cu layers along the *c*-axis. α-Fe_2O_3 is a prototypical example of photoexcited small polaron formation at an Fe(III) site and is shown in **Figure 3.1B** for reference.[8,17] $CuFeO_2$ is a charge transfer insulator (**Fig. 3.1C**) similar to α-Fe_2O_3, in which the valence band maximum (VBM) is dominated by Cu–O hybridization and the conduction band minimum (CBM) is dominated by Fe 3d orbitals. The additional electron density offered by the Cu atoms in the $CuFeO_2$ provides hybridization between the Cu and O atoms, which reduces the material's band gap compared to α-Fe_2O_3 and increases valence band dispersion (**Fig. 3.1D**). The conduction bands

are still relatively flat despite the delocalization offered by the Cu atoms, suggesting that localized electronic states persist in the Fe–O sublattice despite the addition of Cu.

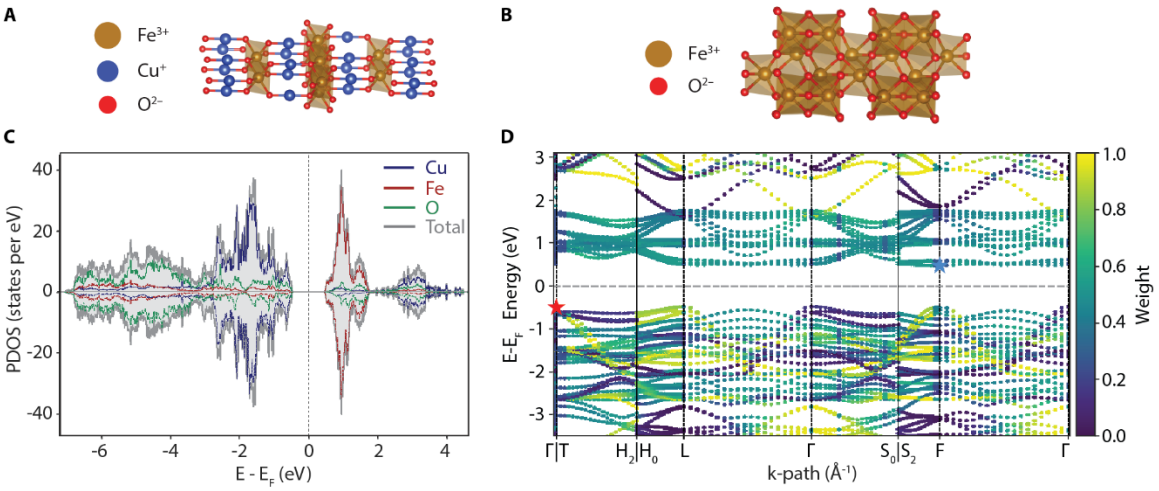

Figure 3.1 A comparison of the **(A)** delafossite crystal structure of $CuFeO_2$ where Cu atoms are inserted between Fe–O layers and **(B)** hematite (α-Fe_2O_3). **(C)** The projected density of states shows that the conduction bands are dominated by Fe orbital character while the valence bands are mixed with Cu–O orbitals. **(D)** The band structure of $CuFeO_2$ – where red (blue) stars indicate the VBM (CBM). The weights indicate the extent to which each supercell Bloch state contributes to the corresponding primitive cell state.

Transient XUV spectroscopy is used to measure small polaron formation dynamics in thin film $CuFeO_2$ following a 3.1 eV (400 nm) photoexcitation of the charge transfer transition from the Cu–O orbitals to Fe 3d orbitals. The optical excitation fluence was ~6 mJ/cm^2, which results in an initial photoexcited carrier density of ~4.4 × 10^{21} cm^{-3}.[24–26] The XUV pulse is generated from few-cycle broadband white light with energy centered around the Fe $M_{2,3}$ edge at ~54 eV. Transient XUV reflection spectroscopy is performed at a 10° grazing incidence angle, resulting in a penetration depth estimated as ~2 nm.[27] After photoexcitation, the change in the XUV spectrum is defined as $\Delta OD = -\log_{10}(I_{pump\ on}/I_{pump\ off})$. The definition is often termed reflection-absorption due to the negative sign. Under this convention, the increase in spectral intensity (red color) in **Figure 3.2A** is roughly associated with increased absorption, whereas the blue color is roughly associated with decreased absorption.

Additional experimental details, including characterization of the $CuFeO_2$ sample, can be found in the Supplementary Materials in **Appendix B**.

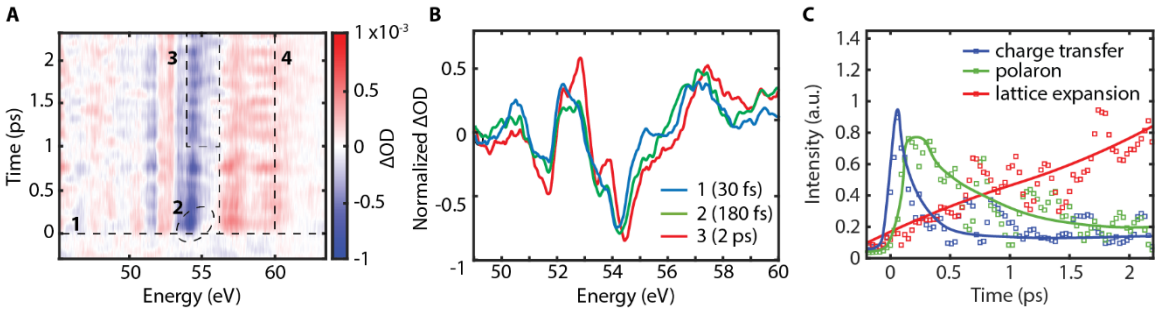

Figure 3.2 Transient XUV reflection–absorption spectrum of $CuFeO_2$ **(A)** following photoexcitation with a 400 nm pump. The red and blue colors represent increased and decreased absorption after photoexcitation, respectively. Four main spectral features are labeled in the plot. At pump–probe overlap (t_0), a series of positive and negative peaks are observed (label 1). Immediately after photoexcitation, an ultrafast spectral blue shift is observed around 55 eV (label 2), which is attributed to octahedra expansion and small polaron formation. At longer pump–probe time delays, spectral intensity and energy oscillations are observed (label 3), which is attributed to polaron induced coherent acoustic phonons. At higher XUV transition energies, increased XUV absorption is observed and attributed to photoinduced Fe(IV) states (label 4). Experimental lineouts **(B)** at 30 fs (blue), 180 fs (red), and 2.04 ps (green) which correspond to dynamics in label 1, label 2, and label 3, respectively. **(C)** Kinetics plot of the charge transfer (blue), polaron (green), and lattice expansion (red) states with "best fit" lines to visualize the kinetics of the chosen dynamics while disregarding the coherent phonon oscillations.

The measured transient XUV spectrum for the Fe $M_{2,3}$ edge is shown in **Figure 3.2**. Four distinct spectral features are identified (**Fig. 3.2A**). Immediately following photoexcitation, a series of positive and negative spectral features occur between 51 and 56 eV (**Fig. 3.2A**, label 1). This is followed by a fast spectral blue shift around 55 eV within the first ~100 fs (**Fig. 3.2A**, label 2). There are intensity oscillations in the measured spectra at longer time delays. A clear intensity oscillation is observed for the main negative peak at ~55 eV. An increased oscillation in spectral density occurs between 55.5 and 56.6 eV, which is out-of-phase compared to the oscillation of the main negative peak between 54.5 and 55.5 eV (**Fig. 3.2A**, label 3). In addition to the features between 51 and 56 eV, there are two major absorption peaks above 56 eV. These peaks emerge immediately after photoexcitation and exhibit oscillating spectral features that strongly correlate with spectral intensities below 56 eV and are out-of-phase with the oscillations between 54.5 and 55.5 eV. It should be noted that while the features in labels 1 and 2 are common among transient XUV measurements of α-Fe2O3 and other prototypical Fe(III) small polaron materials,[8,11,28,29] the features in labels

3 and 4 are not typically observed in the transient XUV spectra of photoexcited iron oxides. This suggests that the interstitial Cu layer between the Fe–O octahedra influences longer timescale dynamics.

The observed spectral changes are dominated by changes to the angular momentum coupling X-ray transition Hamiltonian at the Fe $M_{2,3}$ edge, so the measured spectra relate more to oxidation states and local bonding rather than state-filling of photoexcited carriers.[30] To understand the spectral features, we simulate the transient XUV reflection spectra of $CuFeO_2$ using a previously verified adiabatic approximation to an ab initio excited state Bethe–Salpeter equation (BSE) treatment of the XUV spectra (Supporting Information, **Appendix B**). **Figure 3.3A–C** compares experimental spectral lineouts taken from 30 fs after photoexcitation to 2 ps after photoexcitation (**Fig. 3.3A–C**) with BSE theory. The lineout immediately following photoexcitation at 30 fs matches a modeled photoexcited charge transfer state (**Fig. 3.3A**). In contrast, the lineout at 180 fs agrees with a modeled small polaron state (**Fig. 3.3B**). Kinetically, the small polaron forms in 90 ± 20 fs, consistent with previous measurements of Fe(III) oxides.[17,18] The theoretically predicted changes match for both lineouts in terms of the shift of the zero crossing and the appearance of a new multiplet peak at 54.5 eV.

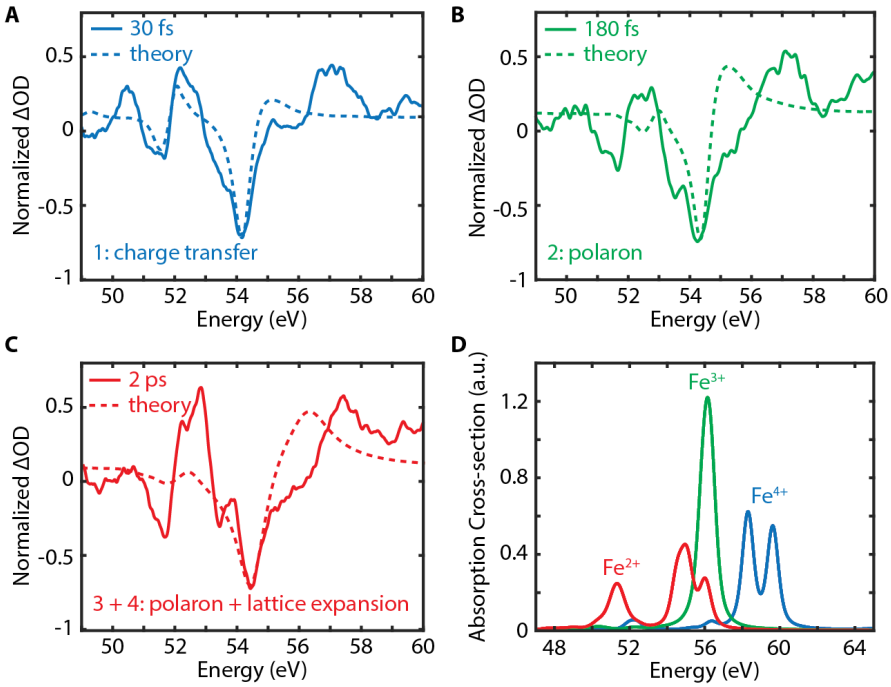

Figure 3.3 Experimental lineouts (solid lines) compared to BSE theory (dashed lines) for immediately after photoexcitation **(A)**, following polaron formation **(B)**, and the change to the polaron spectrum following lattice expansion **(C)**, which correspond the label 1, label 2, and labels 3 and 4 in **Figure 3.2A**, respectively. Ligand-field theory **(D)** for differing oxidation states of iron. The blue trace corresponding to Fe(IV) appears at the same energy as **Figure 3.2A**, label 4.

The spectral features in labels 3 and 4 in **Figure 3.2A** are where the dynamics of $CuFeO_2$ differ from previously measured iron oxide materials. The spectral splitting seen in **Figure 3.2A**, label 3 matches theory for a *c*-axis lattice expansion in the DFT unit cell starting around one picosecond after the small polaron has formed (**Fig. 3.3C**). When the small polaron is formed, the oxygen octahedra around the new Fe(II) site expand locally due to the quench of the Fe–O bond strength. This secondary lattice expansion around the polaron site expands the bond length between the oxygen and nearest neighboring Fe(IV) sites through a *c*-axis expansion, delocalizing the polaron wave function from its initial state. The lattice expansion correlates with coherent phonon oscillations measured within this region. Specifically, intensity modulation occurs between 55.4 and 56.4 eV, oscillating out of phase compared to the intensity between 54.5 and 55.2 eV (**Fig. 3.2A**, labels 3 and 4). The intensity oscillations of the differential spectra between 55.4–56.4 eV is plotted in **Figure 3.4A**. Initial oscillations are damped due to the optical phonons associated with small polaron formation, but after ~1 ps, a Fourier analysis reveals that dominant oscillations at 1.4 and 5.3 THz are

present (**Fig. 3.4B**). These frequencies correspond to mixed acoustic and optical Cu–(Fe–O plane) modes along the c-axis and along Fe–O bond lengths, respectively.[19] Due to the large anisotropy of the $CuFeO_2$ lattice, phonon modes polarized along the c-axis are much softer and anharmonic than those along the ab-plane, enabling a low-frequency c-axis lattice expansion that coherently couples to localized polaron-induced octahedra expansion.

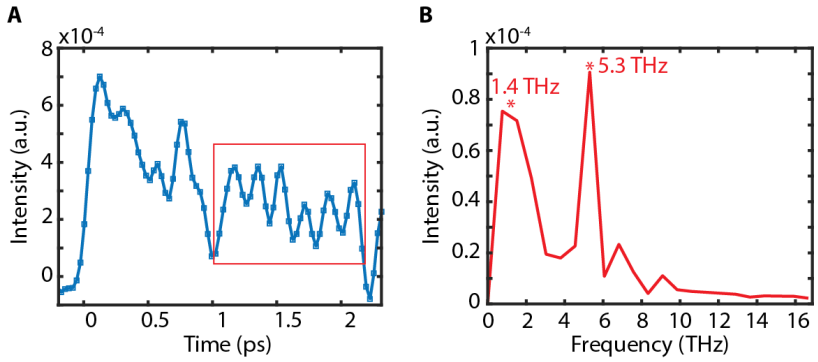

Figure 3.4 Spectral oscillations **(A)** in the main negative feature at ~55 eV in **Figure 3.2A** label 3. The oscillations in the red box were Fourier transformed **(B)** and demonstrate Cu–(Fe–O) c-axis acoustic modes at 1.4 THz and a mixture of Fe–O modes at 5.3 THz.

The spectral features at energies above 56 eV (**Fig. 3.2A**, label 4) are well represented by the formation of a local Fe(IV) state immediately after photoexcitation which would agree with a delocalization of the Fe(II) small-polaron state through lattice expansion. Modeling local oxidation states in the BSE calculations is challenging, given that carriers are filled up to the photoexcited energy in the adiabatic perturbation limit. To understand oxidation state effects, a ligand-field theory calculation using CTM4XAS is performed and reinforces that the increased XUV absorption above 56 eV is due to Fe(IV) absorption (**Fig. 3.3D**).[31] This feature also has oscillations that are out-of-phase with the Fe–O and Cu–O bond motions seen in the negative spectral features at 1.4 and 5.3 THz and plotted in **Figure 3.4A-B**. The intrinsic oxidation state in CuFeO2 in the ground state is Fe(III); our measurement suggests that there is a sudden increase in Fe(IV) states after the photoexcited charge transfer

transition. This state then oscillates out-of-phase with the Fe–O and Cu *c*-axis lattice motions, coupling to the polaronic state and dynamically delocalizing it.

The kinetics for each spectral feature are shown in **Figure 3.2C**. The Fe(IV) state in the nearest-neighbor shell forms immediately after the Fe(III) to Fe(II) charge transfer transition from photoexcitation. However, the polaron delocalization through the oscillation between the ground state bleach and Fe(IV) states does not occur until an order of magnitude longer ~1 ps timescale, compared to the ~100 fs small polaron formation measured here and in other Fe(III) oxide systems.[17,18] The transient XUV data confirm that Cu-hybridization does not alter the small polaron formation energy or kinetics through electronic screening, but rather reduces the on-site reorganization energy, which ultimately delocalizes the small polaron. The small polaron formation and delocalization process are shown schematically in **Figure 3.5** for $CuFeO_2$. Comparatively, in α-Fe_2O_3, the charge transfer initiated by photoexcitation induces a small electron polaronic state, resulting in lattice distortion and carrier trapping until recombination. In $CuFeO_2$, charge transfer also induces small polaron formation; however, the nearest neighboring atoms compensate for this charge transfer by becoming Fe(IV) in character. The lattice expansion then allows for polaron delocalization on a picosecond timescale.

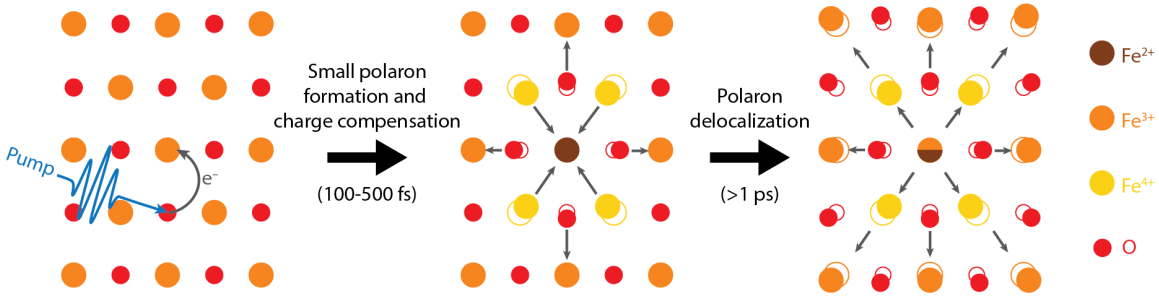

Figure 3.5 Schematic representation of the polaron formation mechanism in $CuFeO_2$. The formation of Fe^{4+} states around polaron sites and the expansion of the lattice enables delocalization of polarons on a ps timescale.

To theoretically investigate small polaron formation and its associated kinetics, we employ the dispersive Holstein Hamiltonian,[32] which encodes the coupling between electronic excitations and local phonons. We parametrize this model using experimental measurements[33] (i.e., Raman spectra) and electronic structure calculations of the materials of

interest[34–37] (see Supporting Information, **Appendix B**). We describe coupling to phonon modes via a continuous spectral density, $J(\omega)$, which we model using two Lorentzians centered on clusters of Raman-active modes around 545 and 1100 cm^{-1}. **Figure 3.6A** shows six peaks taken from the experimental Raman spectrum of $CuFeO_2$ and the resulting bimodal spectral density.[38] We further note that, consistent with spectral densities parametrized from molecular dynamics simulations in other materials, one expects the coupling distributions to low-frequency phonons to be broad and high-frequency phonon modes to be narrow.[39–42] In $CuFeO_2$, the reorganization energy (λ) that quantifies the total exciton–phonon coupling significantly exceeds the exciton hopping integral (v). This allows us to employ the perturbative Non-Interacting Blip Approximation (NIBA),[43] augmented with our recent generalized master equation framework to reach large system sizes free from finite-size effects,[44] to predict the quantum dynamics of the polaron, and enabling us to quantify the influence of phonon timescales on the speed of polaron formation.

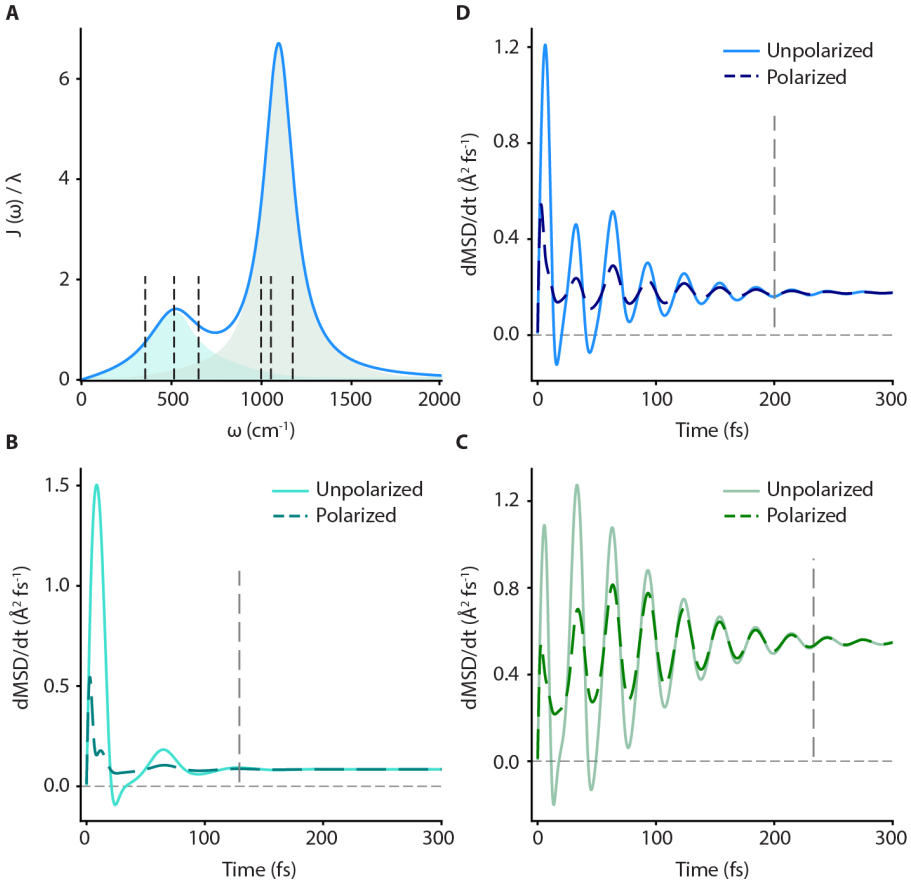

Figure 3.6 Tunability of Holstein polaron formation times via the exciton–phonon coupling distributions. **(A)** Bimodal Lorentzian spectral density based on Raman-detected phonon modes (gray dashed lines). The green and red shaded regions correspond to the low- and high-frequency regions of the full spectral density, respectively. **(B)–(D)** Polaron formation times for exciton–phonon couplings described by **(B)** the bimodal distribution in **(A)**, **(C)** the low-frequency contribution of the bimodal distribution in **(A)** with the full reorganization energy, and **(D)** the high-frequency contribution of the bimodal distribution in **(A)** with the full reorganization energy. **(B)–(D)** show the derivative of the polaron's mean squared displacement, dMSD/d*t*, for both *polarized* and *unpolarized* nonequilibrium initial conditions. Gray dashed lines indicate the polaron formation times (i.e., when both nonequilibrium simulations start to agree).

Because polaron formation timescales are not a direct observable from the quantum dynamics, we extract them indirectly.[45] Since the lattice relaxation of polaron formation is a nonequilibrium effect, the time required for the dynamics to become independent of the initial nonequilibrium preparation of the electronic excitation quantifies the polaron formation time. We employ two distinct nonequilibrium preparations of the initial excitation: one where the bare exciton arises from an impulsive Franck–Condon excitation (unpolarized) and is subsequently allowed to move and one where we allow a static exciton to fully polarize its lattice before it is allowed to move (polarized). We track the deviation between the

derivatives of their mean squared displacement (MSD), which encodes polaron mobility, and when these derivatives agree, the polarons have shed their global nonequilibrium preparation, signaling the completion of their local lattice relaxation. We identify the duration of this nonequilibrium relaxation as the polaron formation time.[45]

To understand how the form of the spectral density affects the polaron formation time, and therefore how to engineer exciton–phonon couplings to control these, we perform a detailed numerical study (see the Supporting Information section VII). In addition to our earlier insight that increased exciton-nuclear coupling decreases polaron formation times,[45] we also observe that polaron formation becomes faster when coupled to a wide and continuous distribution of phonon frequencies. Further, for a given coupling, these timescales are modulated by the distribution of reorganization energy between the optical and acoustic modes, with increasing weight in the narrow, high-frequency optical modes slowing down polaron formation. Surprisingly, the rate of formation was insensitive to the (mean) vibrational frequency.

For the spectral density appropriate to $CuFeO_2$, there is a competition of factors, with the larger, high-frequency phonon couplings also having a narrow distribution. Computationally, we unpack the spectral density to understand the relative importance of the low- and high-frequency regions. Keeping the reorganization energy fixed, when considering only the broadly distributed slow (low-frequency) phonons, the timescale of polaron formation is ∼130 fs (**Fig. 3.6C**). Contrastingly, the narrowly distributed fast (high-frequency) phonons exhibit a much longer formation timescale of ∼230 fs (**Fig. 3.6D**). Together, the full $J(\omega)$ encompassing both regions (**Fig. 3.6B**) gives a value of ∼185 fs (which is a weighted combination of the above; see **Fig. B.17**). We therefore conclude that the addition of narrowly distributed, high-frequency optical phonon modes increases the polaron formation times. Since it is a general feature of condensed phase systems for low-frequency phonon couplings to exhibit spectrally dense, quasi-continuous distributions while couplings to high-

frequency phonons are narrowly spectrally distributed, these results are likely applicable beyond transition metal oxides.

We further conclude that broadly distributed, low-frequency modes dissipate energy faster and more smoothly than narrowly distributed, high-frequency modes (see the Supporting Information section VII). The smoother response and shorter timescale for low-energy acoustic phonon coupling indicate that the multipicosecond rise of polaron delocalization in **Fig. 3.2C** likely represents the growing occupation of the acoustic phonon bath as the polaron couples to a lattice expansion.

The intersection of experimental and theoretical results also has substantial implications for the description of small polaron physics in transition metal oxides. In particular, the experiment further suggests that, after the polaron is formed, acoustic modes are populated, both in response to the polaron formation and due to the decay of high-energy optical phonons. However, the Holstein model, which offers the standard description of small polaron formation in these materials,[46–48] cannot account for such hierarchical energy flow among phonon modes. Instead, the Holstein model offers a field theoretical description of nuclear fluctuations that subsumes energy transfer-facilitating anharmonicities into an effective Gaussian phonon bath. Hence, while Holstein descriptions of small polaron physics can yield useful insights and design principles as we have shown above, precise vibrational engineering further requires the ability to explicitly probe vibrational energy flow in the presence of anharmonic phonons.

Finally, we measure the role of the delocalized polaron state on the carrier lifetime. Interconversion between the polaron and charge transfer state is also examined and confirmed by a variant of optical transient reflectance spectroscopy.[49,50] A pump beam of 540 nm center wavelength and ~0.5 ps duration is focused down to a spot with $1/e^2$ width of 270 nm on the sample to create above-bandgap excitations in the CFO. Subsequently, a wide-field 707 nm probe pulse of similar duration illuminates the sample. The probe reflection is collected by a CMOS camera, and its intensity is integrated over spatial coordinates. The

transient reflectance signal is the difference between probe reflectance with and without the pump pulse, scaled by the pump-off reflectance: $\Delta R/R = \frac{I_{\text{pump on}} - I_{\text{pump off}}}{I_{\text{pump off}}}$.

In **Figure 3.7**, signatures of both the polaron and charge transfer state have negative amplitude but with different strengths. At short timescales (~ps), a very sharp drop is observed in the transient reflectance signal (**Fig. 3.7A**), corresponding to the fast decay of the charge transfer state as it is converted to the lower amplitude polaron. This longer-lived polaron signal persists for hundreds of ps. The entire kinetic trace is fitted with an instrument response function (0.7 ps) convolved with kinetic equation $Ae^{-kt} + B\frac{k}{k_p - k}\left[e^{-kt} - e^{-k_p t}\right]$, where A and B are relative amplitudes of the charge transfer and polaron states, respectively. The extracted lifetimes of the charge transfer state ($1/k$) and polaron ($1/k_p$) are 0.52 and 770 ps. The amplitudes of the charge transfer state and polaron have a ratio of 5.6:1. A low energy acoustic mode at 8 GHz also modulates the signal. Optical transient absorption spectroscopies have observed these low-energy GHz acoustic coherent phonons in other polaron-forming iron oxides and perovskites.[51,52]

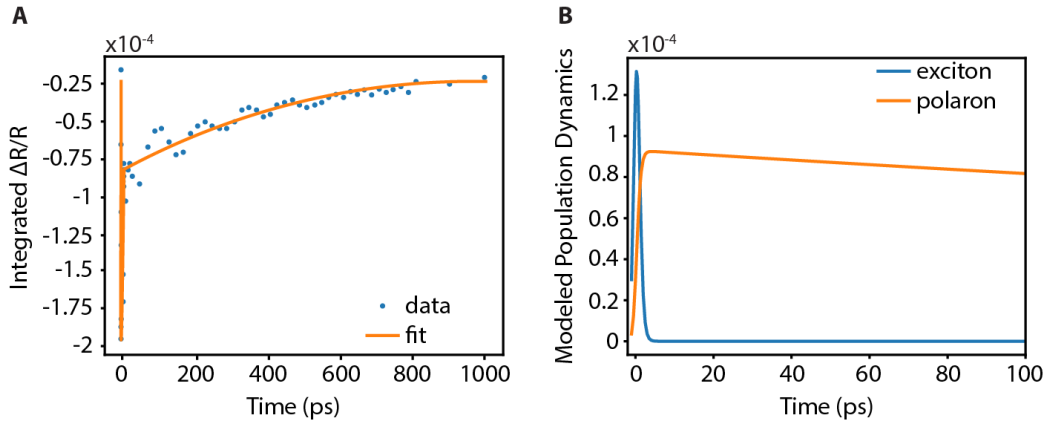

Figure 3.7 Optical reflectivity of $CuFeO_2$ **(A)** and extracted lifetimes of the charge transfer state and polaron state **(B)**. An 8 GHz acoustic phonon oscillation is observed at longer times in the spectra.

The measured kinetics using transient reflectance agree with the transient XUV findings. Given the temporal resolution of the instrument response function, an initial charge transfer state convolved with a localized polaron persists for picoseconds before transforming into the delocalized polaron state, which then persists on the order of a nanosecond. The finding

is intriguing because, although the $CuFeO_2$ is polycrystalline with grain boundaries, it has a lifetime that persists several hundred picoseconds longer than hematite with similar crystallinity conditions.[21–23] The delocalization of the polaron acts to mitigate carrier recombination and extend the lifetime of the localized carriers enabled by population of the acoustic phonon bath. This presents a parameter to tune when engineering polaron-forming semiconductors for photocatalysis, optoelectronics, and other applications.

3.4 Conclusion

The outcomes of this work provide new insight into small polaron-dominated materials and phenomena. We did not find that Cu atom hybridization changed the small polaron formation kinetics, most likely due to strong Fe–Fe electron correlations still dominating interactions. However, changing the lattice degrees of freedom was directly correlated with increasing the delocalization of the small polarons by lowering polaron reorganization energies. Leveraging simulations of lattice descriptions of small polarons in transition metal oxides, we further find that two major factors dictate polaron formation timescales: spectral phonon density and reorganization energy distributions between acoustic and optical modes. Specifically, we find that phonon bath engineering favoring strong coupling to broad acoustic phonon distributions in favor of narrowly distributed optical modes decreases polaron formation timescales. We further find that polaron delocalization is a dynamical process that occurs after the formation of small polarons, contrasting with the concept of immediate delocalized polaron formation.[28] Furthermore, the delocalization of the polaron appears to be related to longer photoexcited lifetimes in the material when compared to prototypical hematite. This work provides insights into more mobile polarons in desirable transition metal oxides, as well insights into coherent control of the lattice response to small polaron formation.

3.5 References

(1) Mott, N. F. Polaron Models of High-Temperature Superconductors. *J. Phys.: Condens. Matter* **1993,** *5,* 3487–3506.

(2) Zhang, L.; Chu, W.; Zhao, C.; Zheng, Q.; Prezhdo, O. V.; Zhao, J. Dynamics of Photoexcited Small Polarons in Transition-Metal Oxides. *J. Phys. Chem. Lett.* **2021,** *12,* 2191–2198.

(3) Ghosh, R.; Spano, F. C. Excitons and Polarons in Organic Materials. *Acc. Chem. Res.* **2020,** *53,* 2201–2211.

(4) Kudinov, E. K. Model of a Polaron Superconductor. *Phys. Solid State* **2002,** *44,* 692–703.

(5) Zhang, C.; Sous, J.; Reichman, D.; Berciu, M.; Millis, A.; Prokof'ev, N.; Svistunov, B. Bipolaronic High-Temperature Superconductivity. *Phys. Rev. X* **2023,** *13,* 011010.

(6) Nosarzewski, B.; Huang, E. W.; Dee, P. M.; Esterlis, I.; Moritz, B.; Kivelson, S. A.; Johnston, S.; Devereaux, T. P. Superconductivity, Charge Density Waves, and Bipolarons in the Holstein Model. *Phys. Rev. B* **2021,** *103,* 235156.

(7) Yim, C.; Watkins, M.; Wolf, M.; Pang, C.; Hermansson, K.; Thornton, G. Engineering Polarons at a Metal Oxide Surface. *Phys. Rev. Lett.* **2016,** *117,* 116402.

(8) Biswas, S.; Wallentine, S.; Bandaranayake, S.; Baker, L. R. Controlling Polaron Formation at Hematite Surfaces by Molecular Functionalization Probed by XUV Reflection–Absorption Spectroscopy. *J. Chem. Phys.* **2019,** *151,* 104701.

(9) Zhang, J.; Eslava, S. Understanding Charge Transfer, Defects and Surface States at Hematite Photoanodes. *Sustain. Energy Fuels.* **2019,** *3,* 1351–1364.

(10) Yan, B.; Wan, D.; Chi, X.; Li, C.; Motapothula, M. R.; Hooda, S.; Yang, P.; Huang, Z.; Zeng, S.; Ramesh, A. G.; Pennycook, S. J.; Rusydi, A.; Ariando; Martin, J.; Venkatesan, T. Anatase TiO_2: A Model System for Large Polaron Transport. *ACS Appl. Mater. Interfaces* **2018,** *10,* 38201–38208.

(11) Carneiro, L. M.; Cushing, S. K.; Liu, C.; Su, Y.; Yang, P.; Alivisatos, A.; Leone, S. R. Excitation-Wavelength-Dependent Small Polaron Trapping of Photoexcited Carriers in α-Fe2O3. *Nat. Mater.* **2017,** *16,* 819–825.

(12) Gregoire, J. M.; Zhou, L.; Haber, J. A. Combinatorial Synthesis for AI-Driven Materials Discovery. *Nat. Synth.* **2023,** *2,* 493–504.

(13) Zhao, T.; Liu, Q.-L.; Zhao, Z.-Y. High-Throughput Screening Delafossite $CuMO_2$ (M = IIIA, 3d, 4d, 5d, and RE) Optoelectronic Functional Materials Based on First-Principles Calculations. *J. Phys. Chem. C* **2019,** *123,* 14292–14302.

(14) Wolf, M.; Madsen, G. K. H.; Dimopoulos, T. Accelerated Screening of Cu-Ga-Fe Oxide Semiconductors by Combinatorial Spray Deposition and High-Throughput Analysis. *Mater. Adv.* **2023,** *4,* 2612–2624.

(15) Saadi, S.; Bouguelia, A.; Trari, M. Photocatalytic Hydrogen Evolution Over $CuCrO_2$. *Sol. Energy* **2006,** *80,* 272–280.

(16) Husek, J.; Cirri, A.; Biswas, S.; Asthagiri, A.; Baker, L. R. Hole Thermalization Dynamics Facilitate Ultrafast Spatial Charge Separation in $CuFeO_2$ Solar Photocathodes. *J. Phys. Chem. C* **2018,** *122,* 11300–11304.

(17) Husek, J.; Cirri, A.; Biswas, S.; Baker, L. R. Surface Electron Dynamics in Hematite (α-Fe_2O_3): Correlation between Ultrafast Surface Electron Trapping and Small Polaron Formation. *Chem. Sci.* **2017,** *8,* 8170–8178.

(18) Vura-Weis, J.; Jiang, C.-M.; Liu, C.; Gao, H.; Lucas, J. M.; de Groot, F. M. F.; Yang, P.; Alivisatos, A. P.; Leone, S. R. Femtosecond $M_{2,3}$-Edge Spectroscopy of Transition-Metal Oxides: Photoinduced Oxidation State Change in α-Fe_2O_3. *J. Phys. Chem. Lett.* **2013,** *4,* 3667–3671.

(19) Klobes, B.; Herlitschke, M.; Rushchanskii, K. Z.; Wille, H.-C.; Lummen, T. T. A.; van Loosdrecht, P. H. M.; Nugroho, A. A.; Hermann, R. P. Anisotropic Lattice Dynamics and Intermediate-Phase Magnetism in Delafossite $CuFeO_2$. *Phys. Rev. B* **2015,** *92,* 014304.

(20) de Mello, E. V. L.; Ranninger, J. Dynamical Properties of Small Polarons. *Phys. Rev. B* **1997,** *55,* 14872–14885.

(21) Fitzmorris, B. C.; Patete, J. M.; Smith, J.; Mascorro, X.; Adams, S.; Wong, S. S.; Zhang, J. Z. Ultrafast Transient Absorption Studies of Hematite Nanoparticles: The Effect of Particle Shape on Exciton Dynamics. *ChemSusChem* **2013,** *6,* 1907–1914.

(22) Joly, A. G.; Williams, J. R.; Chambers, S. A.; Xiong, G.; Hess, W. P.; Laman, D. M. Carrier Dynamics in α-Fe_2O_3 (0001) Thin Films and Single Crystals Probed by Femtosecond Transient Absorption and Reflectivity. *J. Appl. Phys.* **2006,** *99,* 053521.

(23) Chen, Y.-J.; Okazaki, M.; Furube, A.; Chen, L.-Y. Ultrafast Timescale Charge Carrier Dynamics in Nanocomposite Hematite Photoelectrodes. *J. Photochem. Photobiol., A* **2023,** *442,* 114820.

(24) Zürch, M.; Chang, H.-T.; Borja, L. J.; Kraus, P. M.; Cushing, S. K.; Gandman, A.; Kaplan, C. J.; Oh, M. H.; Prell, J. S.; Prendergast, D.; Pemmaraju, C. D.; Neumark, D. M.; Leone, S. R. Direct and Simultaneous Observation of Ultrafast Electron and Hole Dynamics in Germanium. *Nat. Commun.* **2017,** *8,* 15734.

(25) Cushing, S. K.; Lee, A.; Molesky, I. J. P.; Carneiro, L. M.; Chang, H.-T.; Zürch, M.; Leone, S. R. Differentiating Photoexcited Carrier and Phonon Dynamics in the Δ, L, and Γ Valleys of Si(100) with Transient Extreme Ultraviolet Spectroscopy. *J. Phys. Chem. C* **2019,** *123,* 3343–3352.

(26) de Roulet, B. R.; Drescher, L.; Sato, S. A.; Leone, S. R. Initial Electron Thermalization in Metals Measured by Attosecond Transient Absorption Spectroscopy. *Phys. Rev. B* **2024,** *110,* 174301.

(27) Liu, H.; Michelsen, J. M.; Mendes, J. L.; Klein, I. M.; Bauers, S. R.; Evans, J. M.; Zakutayev, A.; Cushing, S. K. Measuring Photoexcited Electron and Hole Dynamics in ZnTe and Modeling Excited-State Core-Valence Effects in Transient Extreme Ultraviolet Reflection Spectroscopy. *J. Phys. Chem. Lett.* **2023,** *14,* 2106–2111.

(28) Kim, Y.-J.; Mendes, J. L.; Michelsen, J. M.; Shin, H. J.; Lee, N.; Choi, Y. J.; Cushing, S. K. Coherent Charge Hopping Suppresses Photoexcited Small Polarons in $ErFeO_3$ by Antiadiabatic Formation Mechanism. *Sci. Adv.* **2024,** *10,* adk4282.

(29) Mendes, J. L.; Shin, H. J.; Seo, J. Y.; Lee, N.; Choi, Y. J.; Varley, J. B.; Cushing, S. K. Dynamic Competition between Hubbard and Superexchange Interactions Selectively Localizes Electrons and Holes through Polarons. *J. Am. Chem. Soc.* **2025,** *147,* 16018–16026.

(30) Klein, I. M.; Liu, H.; Nimlos, D.; Krotz, A.; Cushing, S. K. Ab Initio Prediction of Excited-State and Polaron Effects in Transient XUV Measurements of α-Fe_2O_3. *J. Am. Chem. Soc.* **2022,** *144,* 12834–12841.

(31) Stavitski, E.; de Groot, F. M. The CTM4XAS Program for EELS and XAS Spectral Shape Analysis of Transition Metal L Edges. *Micron* **2010,** *41,* 687–694.

(32) Holstein, T. Studies of Polaron Motion. *Ann. Phys.* **1959,** *8,* 325–342.

(33) Chen, H.-W.; Huang, C.-Y.; Shu, G.-J.; Liu, H.-L. Temperature-Dependent Optical Properties of $CuFeO_2$ through the Structural Phase Transition. *RSC Adv.* **2021,** *11,* 40173–40181.

(34) Ahart, C. S.; Rosso, K. M.; Blumberger, J. Electron and Hole Mobilities in Bulk Hematite from Spin-Constrained Density Functional Theory. *J. Am. Chem. Soc.* **2022,** *144,* 4623–4632.

(35) Ferri, M.; Elliott, J.; Farnesi Camellone, M.; Fabris, S.; Piccinin, S. Thermodynamic Stability and Native Point Defects of $CuFeO_2$ Photocathodes in Dry and Electrochemical Environments. *J. Phys. Chem. C* **2019,** *123,* 29589–29598.

(36) Ahart, C. S.; Blumberger, J.; Rosso, K. M. Polaronic Structure of Excess Electrons and Holes for a Series of Bulk Iron Oxides. *Phys. Chem. Chem. Phys.* **2020,** *22,* 10699–10709.

(37) Naveas, N.; Pulido, R.; Marini, C.; Hernández-Montelongo, J.; Silván, M. M. First-Principles Calculations of Hematite (α-Fe_2O_3) by Self-Consistent DFT+U+V. *iScience* **2023,** *26,* 106033.

(38) Li, T.; Yan, Y.; Shi, Q. A Low-Temperature Quantum Fokker-Planck Equation that Improves the Numerical Stability of the Hierarchical Equations of Motion for the Brownian Oscillator Spectral Density. *J. Chem. Phys.* **2022,** *156,* 064107.

(39) Zuehlsdorff, T. J.; Montoya-Castillo, A.; Napoli, J. A.; Markland, T. E.; Isborn, C. M. Optical Spectra in the Condensed Phase: Capturing Anharmonic and Vibronic Features Using Dynamic and Static Approaches. *J. Chem. Phys.* **2019,** *151,* 074111.

(40) Wiethorn, Z. R.; Hunter, K. E.; Zuehlsdorff, T. J.; Montoya-Castillo, A. Beyond the Condon Limit: Condensed Phase Optical Spectra from Atomistic Simulations. *J. Chem. Phys.* **2023,** *159,* 244114.

(41) Li, H.; Guo, M.; Zhou, Z.; Long, R.; Fang, W.-H. Excitation-Wavelength-Dependent Charge-Carrier Lifetime in Hematite: An Insight from Nonadiabatic Molecular Dynamics. *J. Phys. Chem. Lett.* **2023,** *14,* 2448–2454.

(42) Wiethorn, Z. R.; Hunter, K. E.; Montoya-Castillo, A.; Zuehlsdorff, T. J. Symmetry Breaking Fluctuations Split the Porphyrin Q Bands. *arXiv* **2024,** arXiv:2411.02687. https://doi.org/10.48550/arXiv.2411.02687.

(43) Dekker, H. Noninteracting-Blip Approximation for a Two-Level System Coupled to a Heat Bath. *Phys. Rev. A* **1987,** *35,* 1436–1437.

(44) Bhattacharyya, S.; Sayer, T.; Montoya-Castillo, A. Space-Local Memory in Generalized Master Rquations: Reaching the Thermodynamic Limit for the Cost of a Small Lattice Simulation. *J. Chem. Phys.* **2025,** *162,* 091102.

(45) Bhattacharyya, S.; Sayer, T.; Montoya-Castillo, A. Anomalous Transport of Small Polarons Arises from Transient Lattice Relaxation or Immovable Boundaries. *J. Phys. Chem. Lett.* **2024,** *15,* 1382–1389.

(46) Hannewald, K.; Stojanović, V. M.; Schellekens, J. M. T.; Bobbert, P. A.; Kresse, G.; Hafner, J. Theory of Polaron Bandwidth Narrowing in Organic Molecular Crystals. *Phys. Rev. B* **2004,** *69,* 075211.

(47) Ortmann, F.; Bechstedt, F.; Hannewald, K. Theory of Charge Transport in Organic Crystals: Beyond Holstein's Small-Polaron Model. *Phys. Rev. B* **2009,** *79,* 235206.

(48) Bhattacharyya, S.; Sayer, T.; Montoya-Castillo, A. Nonequilibrium Relaxation Exponentially Delays the Onset of Quantum Diffusion. *Proc. Natl. Acad. Sci. U. S. A.* **2025,** *122,* e2424582122.

(49) Delor, M.; Weaver, H. L.; Yu, Q.; Ginsberg, N. S. Imaging Material Functionality through Three-Dimensional Nanoscale Tracking of Energy Flow. *Nat. Mater.* **2020,** *19,* 56–62.

(50) Weaver, H. L.; Went, C. M.; Wong, J.; Jasrasaria, D.; Rabani, E.; Atwater, H. A.; Ginsberg, N. S. Detecting, Distinguishing, and Spatiotemporally Tracking Photogenerated Charge and Heat at the Nanoscale. *ACS Nano* **2023,** *17,* 19011–19021.

(51) Lejman, M.; Vaudel, G.; Infante, I. C.; Gemeiner, P.; Gusev, V. E.; Dkhil, B.; Ruello, P. Giant Ultrafast Photo-Induced Shear Strain in Ferroelectric $BiFeO_3$. *Nat. Commun.* **2014,** *5,* 4301.

(52) Raiser, D.; Mildner, S.; Ifland, B.; Sotoudeh, M.; Blöchl, P.; Techert, S.; Jooss, C. Evolution of Hot Polaron States with a Nanosecond Lifetime in a Manganite Perovskite. *Adv. Energy Mater.* **2017,** *7,* 1602174.

Chapter 4

COHERENT CHARGE HOPPING SUPPRESSES PHOTOEXCITED SMALL POLARONS IN $ERFEO_3$ BY ANTIADIABATIC FORMATION MECHANISM

This chapter is adapted with permission from:

Kim, Y.-J.; **Mendes, J. L.**; Michelsen, J. M.; Shin, H. J.; Lee, N.; Choi, Y. J.; Cushing, S. K. Coherent Charge Hopping Suppresses Photoexcited Small Polarons in $ErFeO_3$ by Antiadiabatic Formation Mechanism. *Sci. Adv.* **2024**, *10* (12), eadk4282. https://doi.org/10.1126/sciadv.adk4282

4.1 Abstract

Polarons are prevalent in condensed matter systems with strong electron-phonon coupling. The adiabaticity of the polaron relates to its transport properties and spatial extent. To date, only adiabatic small polaron formation has been measured following photoexcitation. The lattice reorganization energy is large enough that the first electron–optical phonon scattering event creates a small polaron without requiring substantial carrier thermalization. We measure that frustrating the iron-centered octahedra in the rare-earth orthoferrite $ErFeO_3$ leads to antiadiabatic polaron formation. Coherent charge hopping between neighboring Fe^{3+}–Fe^{2+} sites is measured with transient extreme ultraviolet spectroscopy and lasts several picoseconds before the polaron forms. The resulting small polaron formation time is an order of magnitude longer than previous measurements and indicates a shallow potential well, even in the excited state. The results emphasize the importance of considering dynamic electron-electron correlations, not just electron-phonon–induced lattice changes, for small polarons for transport, catalysis, and photoexcited applications.

4.2 Introduction

The interaction between charge carriers and a polar lattice can lead to charge localization by the local lattice deformation which is referred to as polaron formation. Polarons are of major interest for semiconducting, superconducting, and insulating materials because they

dominate transport properties.[1–4] In the strong-coupling limit, sublattice-sized small (Holstein) polarons[5, 6] reconfigure electronic states to control surface reactivity,[7, 8] ion mobility,[9, 10] and high-temperature superconductivity.[11] Understanding how the relationship between strong electron-phonon coupling and electron correlations controls polaron formation is important from both a ground-state materials and photodynamics perspective.

Optical excitation can generate electron and hole polarons by photodoping the lattice.[12-17] To date, photoexcited small polarons are measured to form within the first electron–optical phonon scattering event, even when the charge carrier has excess energy above the band edge.[16,18-23] Within the Hubbard-Holstein model for correlated electron materials, this indicates that the reorganization energy (electron-phonon coupling strength) of the small polaron is larger than the hopping integral between metal sites.[24] The hundreds of femtoseconds small polaron formation is termed adiabatic as it occurs without substantial thermalization. In this case, the photoexcited small polaron formation is almost an impulsive excitation.

In this study, we measure that the distorted FeO_6 octahedron in erbium iron oxide ($ErFeO_3$), a rare-earth orthoferrite, leads to antiadiabatic small polaron formation using transient extreme ultraviolet (XUV) spectroscopy. Photoexcitation of a ligand-to-metal charge-transfer transition creates an axially elongated FeO_6 octahedron. Multiple coherent charge hopping events are then measured between neighboring Fe^{3+}─Fe^{2+} sites. The coherent charge hopping is associated with an optical phonon mode that modulates the distance between the neighboring Fe–O–Fe bonds. The charge hopping continues until the photoexcited carriers thermalize and small polaron formation occurs on a picosecond timescale, as is characteristic of an antiadiabatic interaction.[25] The polaron formation time is an order of magnitude longer than previously measured.[16,18,20-23] The lattice reorganization energy estimated from the experiments is also smaller than the magnitude of the hopping integral, roughly estimated by the Fe *d*-orbital conduction band width, in line with time-dependent Holstein and Hubbard-

Holstein model predictions for the conditions of excited-state antiadiabatic polaron formation.

Overall, our measurements confirm that dynamical electron correlations play a critical role in controlling small polaron formation in correlated electron materials and must be considered beyond just the lattice reorganization energy.[26] This result is in contrast to a variety of previous studies in other Fe–O materials where changes to defects, dopants, spin, and symmetry always lead to a similar, adiabatic small polaron formation time, suggesting that knowledge of the reorganization energy alone was sufficient to compare the dynamics.[16,18-23] The measured interplay between optical phonons, electron correlations, and local lattice deformation provides a clear picture of how antiadiabatic excited-state polaron formation occurs. The measurement of the conditions under which antiadiabatic polaron formation occurs is also important to a broad range of small polaron-dominated applications such as polaronic superconductivity theories, charge-density wave ordering, antiferromagnetism, and charge transport in both solid-state and molecular systems.[27-29] For example, using high-frequency phonons and their instantaneous response to photoexcitation in the antiadiabatic regime is proposed for tuning electron correlations to modulate metallicity in relation to Peierls ordering.[30,31] Moreover, by confirming general Hubbard-Holstein model predictions with the experimental evidence of the excited-state behavior, the measurements increase our fundamental understanding of how strong electron-phonon coupling unfolds in correlated electron systems in nonequilibrium situations.

4.3 Results and Discussion

$ErFeO_3$ is an antiferromagnetic, charge-transfer insulator that crystallizes in an orthorhombically distorted perovskite structure with the space group *Pbnm*, as confirmed by x-ray diffraction (**Appendix C.1, Fig. C.1,** and **Table C.1**)[32] and depicted in **Figure 4.1A**. It belongs to the rare-earth orthoferrite family $RFeO_3$ (where R is a trivalent rare-earth cation) and features corner-shared FeO_6 octahedra that are orthorhombically distorted and orthorhombically rotated about the [001] axis.[33] $ErFeO_3$ exhibits rich magnetic properties arising from the magnetic transitions between the 3*d* and 4*f* electrons of Fe^{3+} and Er^{3+} ions,

respectively. These properties include a high Néel temperature,[34] large magnetoelectric coupling,[35] and ultrafast optical control of spins,[36,37] making it a potential room-temperature multiferroic candidate. Here, we use this control of the frustrated lattice versus electron correlations to explore the structural factors that determine small polaron formation.

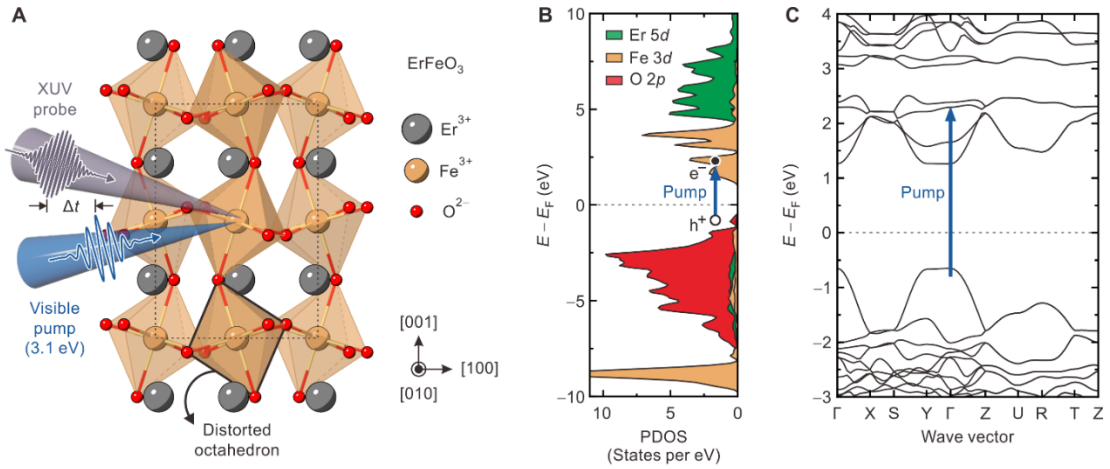

Figure 4.1 Electronic and lattice structure of $ErFeO_3$. **(A)** Crystal structure of $ErFeO_3$. The crystal has a distorted perovskite structure with an orthorhombic symmetry. Corner-sharing FeO_6 octahedra are distorted because of the presence of an Er^{3+} ion. $ErFeO_3$ is photoexcited with 50-fs, 3.1-eV pump pulses while XUV pulses probe photoinduced dynamics of the material. The unit cell of the crystal is indicated with a dotted box. **(B)** Calculated total PDOS of $ErFeO_3$. Photoexcitation generates holes (a white circle) and electrons (a black filled circle) in the O 2*p* and Fe 3*d* bands, respectively. E_F is the Fermi energy. **(C)** Calculated band structure of $ErFeO_3$ along the high-symmetry *k*-points.

Figure 4.1B and **C** presents the calculated electronic structure of $ErFeO_3$ by using density functional theory (DFT) with the Hubbard U correction (DFT + U). The calculations give a charge-transfer bandgap of approximately 1.8 eV (calculation details in **Appendix C.2.1** and **Fig. C.2**), which is consistent with the measured charge-transfer optical absorption feature at 1.8 ± 0.1 eV (**Fig. C.3**). Within the approximations of DFT + U,[38] the calculated projected density of states (PDOS) in **Figure 4.1B** has a valence band that predominantly consists of O 2*p* orbitals and a conduction band predominantly of lower-lying Fe 3*d* and higher-lying Er 5*d* orbitals.[39,40] The optical excitation used in these experiments, at 3.1 eV (400 nm), promotes electrons from the O 2*p* orbital to the unoccupied Fe 3*d* orbital through a ligand-to-metal charge-transfer transition. The calculated band structure in **Figure 4.1C** along high-symmetry k-points reveals that the valence band maximum and the conduction band

minimum are flat from the Γ- to Y-points of the Brillouin zone, indicative of strong electron correlations,[41] similar to other rare-earth orthoferrites.[42,43]

Transient XUV spectroscopy is used to measure element-specific electron and hole dynamics following a ligand-to-metal charge-transfer photoexcitation. Time-resolved differential absorption spectra are collected at the Fe $M_{2,3}$ edge around 54 eV, which corresponds to a transition from the $3p_{3/2,5/2}$ core states to the $3d$ valence state. The sample is photoexcited with a 50-fs pulse at a pump fluence of 3 mJ/cm^2 under ambient temperature (293 K). The differential absorption signal, ΔA, is calculated as $\Delta A = \log(R_{off}/R_{on})$, where R_{off} and R_{on} are the XUV reflectance spectra with the pump beam blocked and unblocked, respectively. High harmonic generation creates the XUV probe pulse (upper panel in **Fig. 4.2A**) from a few-cycle white light pulse in an argon gas medium (experimental details in **Appendix C.3** and **Fig. C.4**).[44] By using a grazing incidence angle of 10°, the XUV probe has a penetration depth of approximately 2 nm, providing a surface-sensitive geometry.[44,45] In the previous measurement of small polaron formation times in α-Fe_2O_3, bulk versus surface measurements only showed variations in the 30% range,[18] smaller than the order of magnitude change in small polaron formation time measured here.

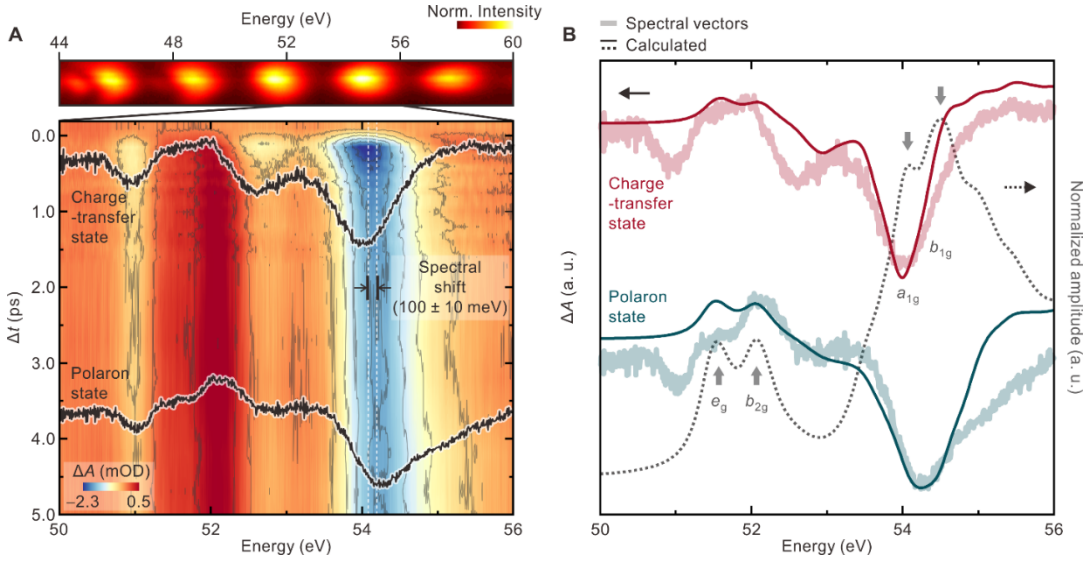

Figure 4.2 Photoinduced structural distortion and small polaron formation. (**A**) High-order harmonic profile for the XUV probe pulses (top). The color scale corresponds to the normalized harmonic intensity. Two-dimensional false color plot of time-resolved differential absorption spectra obtained at a pump fluence of 3 mJ/cm^2 (bottom). The color scale corresponds to differential absorbance (ΔA). Spectral vectors for singular

value decomposition are overlaid, representing the charge-transfer (top) and the polaron states (bottom). The spectral blue shift of the main absorption feature at ~54 eV, typically indicative of small polaron formation, is measured as 100 ± 10 meV. Dotted lines represent the fitted spectral shift (**Fig. C.5**). (**B**) Calculated differential absorption spectra compared to the primary spectral vectors. For the charge-transfer state, the FeO_6 octahedron is axially elongated because of an optical phonon within our temporal resolution, giving rise to crystal field splitting, as shown in the calculated excited-state absorption spectra of Fe^{2+} (dotted line). State-filling effects were incorporated for the photoexcited electrons and holes. For the polaron state, six Fe–O bonds in the octahedron are expanded with the overall enlargement of the unit cell.

The time-resolved differential absorption spectra are shown in **Figure 4.2A** as a pseudo-color plot (see **Fig. C.5** for the temporal lineout spectra). The first 5 ps after photoexcitation are plotted, after which the dynamics reach a steady state out to the 1-ns measurement limit of our instrument (**Fig. C.6**). The core-level transition Hamiltonian for the Fe $M_{2,3}$ edge is dominated by angular momentum components.[46] The increase and decrease in absorption in the XUV spectrum therefore do not directly relate to electron and hole energies but instead relate to the change in overall Fe site occupation (oxidation state), the presence of phonon modes, and other structural excitations such as small polarons.[46,47]

The spectral evolution exhibits two distinctive vectors and timescales within the 5-ps time frame, which can be confirmed by singular value decomposition[20,48] (see overlays in **Fig. 4.2A**). An excited-state approximation to the Bethe–Salpeter equation (BSE) is used to interpret the spectral contributions.[49,50] Briefly, the OCEAN (Obtaining Core Excitations from the Ab initio electronic structure and the NIST BSE solver) code is modified using an adiabatic approximation of the photoexcited electronic states or lattice distortions to calculate the change in the core-valence excitons that make up the XUV spectra (calculation details in **Appendix C.2.2**).[44,46,47] The initial photoexcited charge-transfer state creates four distinct bands positioned at 51.6, 52.1, 54.1, and 54.5 eV when compared to the Fe^{3+} ground state, which can be assigned to e_g, b_{2g}, a_{1g}, and b_{1g} multiplets, respectively[51] (**Fig. 4.2B**). A local elongation of the Fe–O bond in the axial direction, and a contraction of the equatorial in-plane bonds from the Jahn-Teller distortion (**Fig. C.7**), must also be included. The interatomic distance between neighboring Fe sites decreases because of this distortion.[52] Next, at a pump-probe time delay of Δt = 1 ps, the main spectral feature at 54-eV blue shifts. This spectral shift of 100 ± 10 meV (**Fig. C.5**), which also results in changes to the e_g and b_{2g} spectral amplitudes over time, corresponds to the formation of the small

polaron.[16,20,23] This is modeled as an overall expansion of the Fe–O bonds, and good agreement exists between theory and experiment in both cases.

The kinetics of the small polaron formation are determined using the assigned spectral features. A multivariate regression analysis using the spectral components is depicted in **Figure 4.3A**. A three-state sequential kinetic model is used for the best fit as outlined in **Figure 4.3B** (fitting details in **Appendix C.4** and **Fig. C.8**), including the 50-fs photoexcitation pulse. The kinetic model is consistent with past small polaron formation studies[20,21] so that relative timescales can be compared. The initial charge-transfer state thermalizes on the order of $\tau_1 = 250 \pm 80$ fs, but small polaron formation is delayed by $\tau_2 = 2.3 \pm 0.3$ ps with the incorporation of an intermediate step. This is characteristic of a balance between carrier thermalization and small polaron formation through the coherent charge hopping in the antiadiabatic regime as discussed in the next paragraph.

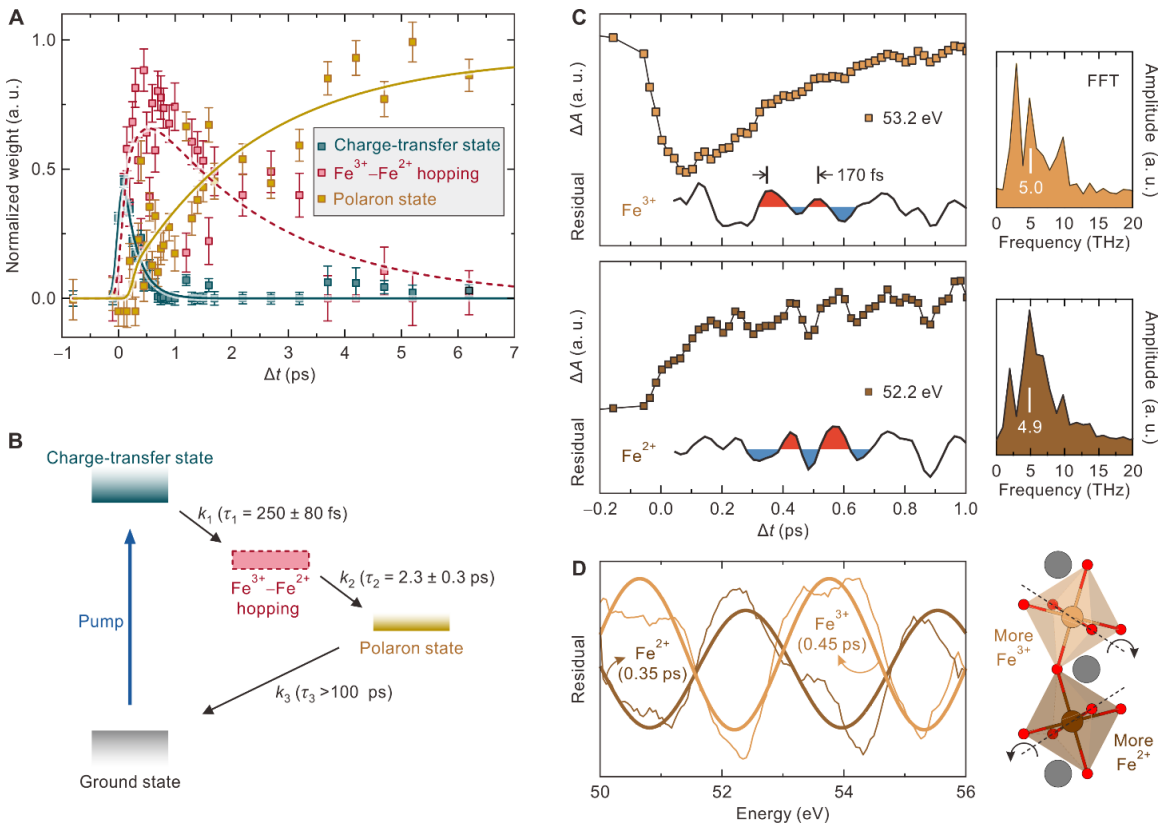

Figure 4.3 Kinetic model of the relaxation dynamics and coherent hopping motions. (**A**) The time-dependent amplitude of the charge-transfer and polaron states using a multivariate regression of the experimental data. A

three-state model was used to incorporate the intermediate step of the charge hopping events in the antiadiabatic regime. The amplitudes are fitted with a rate equation model for small polaron formation (solid and dotted lines). (**B**) Schematic of the three-state sequential kinetic model with the three time constants of τ_1, τ_2, and τ_3. (**C**) The coherent modulation of transient signals extracted at 53.2 and 52.2 eV, representing the main absorption of Fe^{3+} and Fe^{2+}, respectively. Oscillations from the initial electron–optical phonon scattering lead to coherent hopping between the photoexcited Fe^{3+} and its Fe^{2+} nearest neighbors. The fast Fourier transforms (FFT) are shown on the right. (**D**) The out-of-phase oscillations between the Fe^{3+} and Fe^{2+} spectral features at Δt between 0.3 to 0.6 ps indicative of the charge-hopping process that delays small polaron formation in the antiadiabatic regime.

Further insight into the small polaron formation process is given by the coherent oscillations in the transient XUV spectra. **Figure 4.3C** shows coherent oscillations for lineouts at 53.2 and 52.2 eV. The main decrease in absorption observed at 52.8 to 54.7 eV is indicative of the depletion of the initial Fe^{3+} state, while the main increase in absorption in the red-shifted region of 51.5 to 52.8 eV signifies the formation of the Fe^{2+} state following photoexcitation, based on the spectral assignment (see **Figs. C.7**, **C.9**, and **C.10** for the full spectrum and analysis). The coherent oscillations have a periodicity of approximately 170 fs, corresponding to a frequency of around 5.0 THz (170 cm^{-1}). The measured oscillation frequency can be correlated with a Raman-active optical phonon mode with A_g symmetry that corresponds to a rocking motion of the FeO_6 octahedra between the Er^{3+} ions;[33,53] see the schematic in **Figure 4.3D**. The optical phonon mode leads to coherent charge hopping between neighboring Fe sites by modulating the Fe–O–Fe bond length, as evidenced by the 180° out-of-phase oscillating signal between the Fe^{3+} and Fe^{2+} signals (**Fig. 4.3D**). The coherent charge hopping events in **Figure 4.3C** do not onset until carrier thermalization has occurred, matching the timescale of τ_1 from **Figure 4.3A**. Similarly, small polaron formation is not complete in **Figure 4.3A** until after the multiple coherent charge hopping events decay in **Figure 4.3C**, matching τ_2, designating the process as antiadiabatic.

Transient XUV measurements, therefore, provide a detailed picture of antiadiabatic small polaron formation (**Fig. 4.4**). The photoexcited electrons of the axially elongated FeO_6 octahedra thermalize through scattering with optical phonon modes, some of which correspond to FeO_6 octahedral rotations within the Er^{3+} sublattice. The octahedral rotations modulate Fe–O–Fe bond lengths, leading to a periodic hopping between sites. Only after multiple electron–optical phonon scattering events does the electron hopping decay,

corresponding to the creation of the small polaron. The small polaron does not lead to recombination within the hundreds-of-picoseconds timescale of the transient XUV measurement. The measured small polaron formation process is in contrast with the previously measured adiabatic mechanism, wherein the small polaron forms immediately within the first electron–optical phonon scattering event without substantial carrier thermalization.[16,18,20-23]

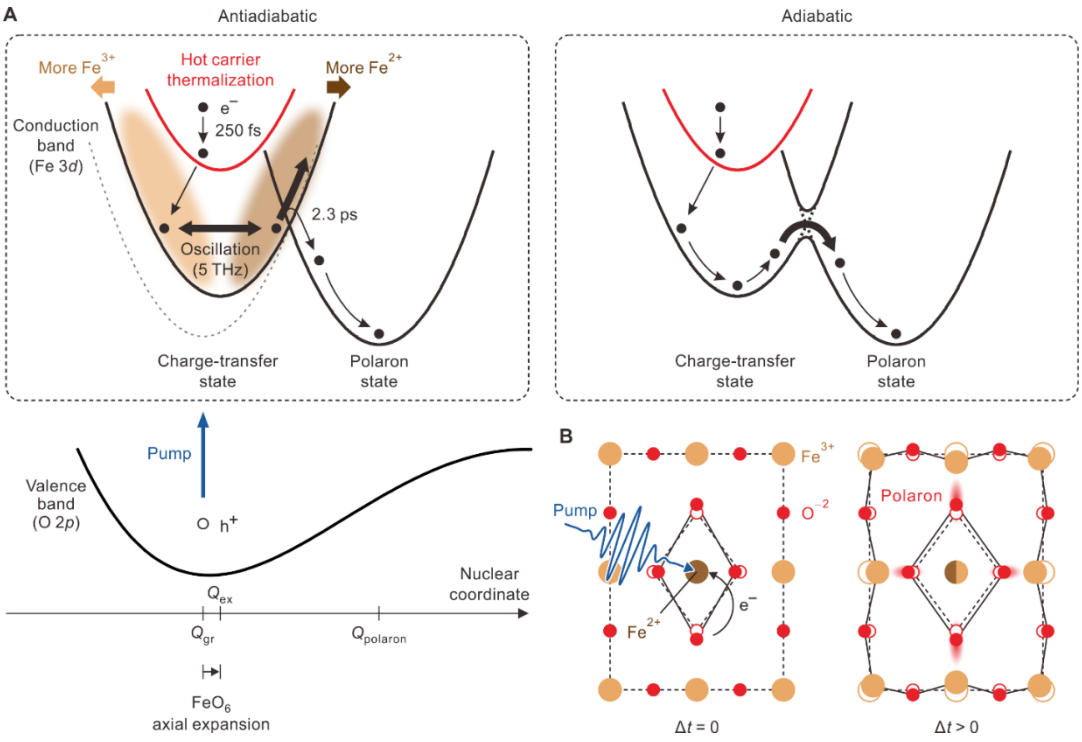

Figure 4.4 Summary of the antiadiabatic photoinduced polaron formation dynamics in $ErFeO_3$. (**A**) Potential energy curves comparing small polaron formation in the antiadiabatic (left) and adiabatic regimes (right). Upon photoexcitation, electrons instantaneously transfer from the O^{2-} to Fe^{3+} ions, generating photoexcited electrons and holes in the conduction and valence bands, respectively. In the charge-transfer state, the axial Fe─O bond is elongated, resulting in the splitting of the Fe 3*d* band at a slightly shifted nuclear coordinate from the ground- to excited-state configurations ($Q_{gr} \rightarrow Q_{ex}$). Hot carriers in the high-energy conduction band then thermalize in hundreds of femtoseconds. In the antiadiabatic polaron formation of this work, coherent charge hopping between the Fe^{3+} and Fe^{2+} lasts for a few picoseconds, delaying small polaron formation at $Q_{polaron}$, while electron tunneling is dominant in the adiabatic pictures. (**B**) Schematics of lattice deformation in $ErFeO_3$ at the charge-transfer ($\Delta t = 0$) and polaron states ($\Delta t > 0$), where the FeO_6 octahedron axially elongates upon photoexcitation and then expands equally in all axes during the small polaron formation.

The Hubbard-Holstein model predicts that the adiabaticity of small polaron formation depends on the balance of the hopping integral between Fe sites and the small polaron reorganization energy. The Hamiltonian for the Hubbard-Holstein model is shown as:[5,54]

$$H = -t\sum_{<ij>,\sigma}(c_{i\sigma}^{\dagger}c_{j\sigma} + \text{H.c.}) + U\sum_i n_{i\uparrow}n_{i\downarrow} + \omega_0\sum_i b_i^{\dagger}b_i + g\sum_{i,\sigma} n_{i\sigma}(b_i^{\dagger} + b_i) \quad \textbf{(4.1)}$$

where $c_{i\sigma}^{\dagger}$ and $c_{i\sigma}$ are the creation and annihilation operators for an electron with spin σ at site i, respectively. $b_i^{\dagger}$ and b_i are the phonon creation and annihilation operators, respectively. $n_{i\sigma}$ is the on-site electron–phonon coupling density of $c_{i\sigma}^{\dagger}c_{i\sigma}$ with strength g, which reflects the electron-phonon coupling and therefore polaron reorganization energy. The hopping amplitude is denoted by t and ω_0 is a dispersionless phonon frequency. The reorganization energy is typically parameterized by the phonon frequency and deformation potential, balanced with the on-site interaction.

Previous studies on α-Fe_2O_3 demonstrated that the blue shift of the main XUV spectral feature can be related to the small polaron reorganization energy.[16,18-23] In these studies, a spectral shift of ~1 eV corresponded to a formation energy of 0.4 to 0.6 eV, consistent with the theoretical predictions. Here, the measured spectral shift is 100 ± 10 meV, which is $^1/_{10}$ of the reported value for α-Fe_2O_3. This would bound the small polaron formation energy of $ErFeO_3$ as <100 meV, or <50 meV if the same XUV relation holds. In support of this estimate, the polaron formation rate is roughly $^1/_{10}$ of that reported for α-Fe_2O_3. t_h can be bounded as <300 meV by the half-bandwidth of the relevant Fe 3*d* conduction band (~0.6 eV; **Fig. 4.1B**), and ω_0 corresponds to the measured phonon energy at approximately 20 meV (**Fig. 4.3C**).

A time-dependent solution of the Hubbard-Holstein model is needed to parameterize the antiadiabatic excited-state small polaron formation.[25] In ground-state solutions to the Hubbard-Holstein or Holstein model, the "adiabaticity ratio" parameterization of ω_0/t_h would here denote an adiabatic regime for polaron hopping.[26,55,56] In the ground state, adiabatic refers to whether the lattice changes instantaneously upon polaron motion and should not be

confused with the excited-state or nonequilibrium definition of adiabaticity used in this paper, which refers to the formation time after photoexcitation. The measured coherent electron hopping and decreased polaron formation energy is consistent, however, with ground-state definitions of a "large" polaron regime but transport measurements are needed before further comment can be made.

4.4 Conclusion

Our measurements therefore indicate that a complete picture of photoexcited polaron formation in correlated electron systems must include the balance of the charge hopping integral versus the lattice-based reorganization energy. Usually, a Holstein-like model is considered sufficient, focusing mainly on the reorganization energy, but our results suggest that a full Hubbard-Holstein-like model needs to be used when the polaron formation energy approaches the electron bandwidth. The coherent charge hopping between Fe–Fe sites suggests small polaron transport in $ErFeO_3$ requires a coordination of phonons, electron correlations, and lattice deformations at adjacent sites. This behavior is opposite to previous measurements of adiabatic excited-state dynamics where polaron hopping occurs only through a phonon-mediated lattice deformation.[16,18,20-23]

4.5 References

(1) Alexandrov, A. S.; Devreese, J. T. *Advances in Polaron Physics*; Springer: Berlin, **2010**.

(2) Rettie, A. J. E.; Chemelewski, W. D.; Emin, D.; Mullins, C. B. Unravelling Small-Polaron Transport in Metal Oxide Photoelectrodes. *J. Phys. Chem. Lett.* **2016**, *7*, 471–479.

(3) Coropceanu, V.; Cornil, J.; da Silva Filho, D. A.; Olivier, Y.; Silbey, R.; Brédas, J.-L. Charge Transport in Organic Semiconductors. *Chem. Rev.* **2007**, *107*, 926–952.

(4) Franchini, C.; Reticcioli, M.; Setvin, M.; Diebold, U. Polarons in Materials. *Nat. Rev. Mater.* **2021**, *6*, 560–586.

(5) Holstein, T. Studies of Polaron Motion: Part I. The Molecular-Crystal Model. *Ann. Phys.* **1959**, *8*, 325–342.

(6) Emin, D. Optical Properties of Large and Small Polarons and Bipolarons. *Phys. Rev. B* **1993**, *48*, 13691–13702.

(7) Pastor, E.; Sachs, M.; Selim, S.; Durrant, J. R.; Bakulin, A. A.; Walsh, A. Electronic Defects in Metal Oxide Photocatalysts. *Nat. Rev. Mater.* **2022**, *7*, 503–521.

(8) Ziwritsch, M.; Müller, S.; Hempel, H.; Unold, T.; Abdi, F. F.; van de Krol, R.; Friedrich, D.; Eichberger, R. Direct Time-Resolved Observation of Carrier Trapping and Polaron Conductivity in $BiVO_4$. *ACS Energy Lett.* **2016**, *1*, 888–894.

(9) Ellis, B.; Perry, L. K.; Ryan, D. H.; Nazar, L. F. Small Polaron Hopping in Li_xFePO_4 Solid Solutions: Coupled Lithium-Ion and Electron Mobility. *J. Am. Chem. Soc.* **2006**, *128*, 11416–11422.

(10) Delmas, C.; Maccario, M.; Croguennec, L.; Le Cras, F.; Weill, F. Lithium Deintercalation in $LiFePO_4$ Nanoparticles via a Domino-Cascade Model. *Nat. Mater.* **2008**, *7*, 665–671.

(11) Alexandrov, A. S.; Mott, N. F. Bipolarons. *Rep. Prog. Phys.* **1994**, *57*, 1197–1288.

(12) Arvind, M.; Tait, C. E.; Guerrini, M.; Krumland, J.; Valencia, A. M.; Cocchi, C.; Mansour, A. E.; Koch, N.; Barlow, S.; Marder, S. R.; Behrends, J.; Neher, D. Quantitative Analysis of Doping-Induced Polarons and Charge-Transfer Complexes of Poly(3-hexylthiophene) in Solution. *J. Phys. Chem. B* **2020**, *124*, 7694–7708.

(13) Jacobs, I. E.; Moulé, A. J. Controlling Molecular Doping in Organic Semiconductors. *Adv. Mater.* **2017**, *29*, 1703063.

(14) Tailor, N. K.; Saini, S. K.; Kumar, M.; Satapathi, S. Polaron-Mediated Photoconduction in Lead-Free Single-Crystalline Perovskite Thin-Film Devices. *J. Phys. Chem. C* **2022**, *126*, 11165–11173.

(15) René de Cotret, L. P.; Otto, M. R.; Pöhls, J.-H.; Luo, Z.; Kanatzidis, M. G.; Siwick, B. J. Direct Visualization of Polaron Formation in the Thermoelectric SnSe. *Proc. Natl. Acad. Sci. U.S.A.* **2022**, *119*, e2113967119.

(16) Carneiro, L. M.; Cushing, S. K.; Liu, C.; Su, Y.; Yang, P.; Alivisatos, A. P.; Leone, S. R. Excitation-Wavelength-Dependent Small Polaron Trapping of Photoexcited Carriers in α-Fe_2O_3. *Nat. Mater.* **2017**, *16*, 819–825.

(17) Wu, B.; Ning, W.; Xu, Q.; Manjappa, M.; Feng, M.; Ye, S.; Fu, J.; Lie, S.; Yin, T.; Wang, F.; Goh, T. W.; Harikesh, P. C.; Tay, Y. K. E.; Shen, Z. X.; Huang, F.; Singh, R.; Zhou, G.; Gao, F.; Sum, T. C. Strong Self-Trapping by Deformation Potential Limits Photovoltaic Performance in Bismuth Double Perovskite. *Sci. Adv.* **2021**, *7*, eabd3160.

(18) Biswas, S.; Wallentine, S.; Bandaranayake, S.; Baker, L. R. Controlling Polaron Formation at Hematite Surfaces by Molecular Functionalization Probed by XUV Reflection-Absorption Spectroscopy. *J. Chem. Phys.* **2019**, *151*, 104701.

(19) Zhang, L.; Chu, W.; Zhao, C.; Zheng, Q.; Prezhdo, O. V.; Zhao, J. Dynamics of Photoexcited Small Polarons in Transition-Metal Oxides. *J. Phys. Chem. Lett.* **2021**, *12*, 2191–2198.

(20) Husek, J.; Cirri, A.; Biswas, S.; Baker, L. R. Surface Electron Dynamics in Hematite (α-Fe_2O_3): Correlation Between Ultrafast Surface Electron Trapping and Small Polaron Formation. *Chem. Sci.* **2017**, *8*, 8170–8178.

(21) Vura-Weis, J.; Jiang, C.-M.; Liu, C.; Gao, H.; Lucas, J. M.; de Groot, F. M. F.; Yang, P.; Alivisatos, A. P.; Leone, S. R. Femtosecond $M_{2,3}$-Edge Spectroscopy of Transition-Metal Oxides: Photoinduced Oxidation State Change in α-Fe_2O_3. *J. Phys. Chem. Lett.* **2013**, *4*, 3667–3671.

(22) Londo, S.; Biswas, S.; Pinchuk, I. V.; Boyadzhiev, A.; Kawakami, R. K.; Baker, L. R. Ultrafast Optical Spin Switching in Ferrimagnetic Nickel Ferrite ($NiFe_2O_4$) Studied by XUV Reflection-Absorption Spectroscopy. *J. Phys. Chem. C* **2022**, *126*, 2669–2678.

(23) Porter, I. J.; Cushing, S. K.; Carneiro, L. M.; Lee, A.; Ondry, J. C.; Dahl, J. C.; Chang, H.-T.; Alivisatos, A. P.; Leone, S. R. Photoexcited Small Polaron Formation in Goethite (α-FeOOH) Nanorods Probed by Transient Extreme Ultraviolet Spectroscopy. *J. Phys. Chem. Lett.* **2018**, *9*, 4120–4124.

(24) Capone, M.; Grilli, M.; Stephan, W. Small Polaron Formation in Many-Particle States of the Hubbard-Holstein Model: The One-Dimensional Case. *Eur. Phys. J.* **1999**, *11*, 551–557.

(25) Novelli, F.; de Filippis, G.; Cataudella, V.; Esposito, M.; Vergara, I.; Cilento, F.; Sindici, E.; Amaricci, A.; Giannetti, C.; Prabhakaran, D.; Wall, S.; Perucchi, A.; Dal Conte, S.; Cerullo, G.; Capone, M.; Mishchenko, A.; Grüninger, M.; Nagaosa, N.; Parmigiani, F.; Fausti, D. Witnessing the Formation and Relaxation of Dressed Quasi-Particles in a Strongly Correlated Electron System. *Nat. Commun.* **2014**, *5*, 5112.

(26) Costa, N. C.; Seki, K.; Yunoki, S.; Sorella, S. Phase Diagram of the Two-Dimensional Hubbard-Holstein Model. *Commun. Phys.* **2020**, *3*, 80.

(27) Xiao, B.; Costa, N. C.; Khatami, E.; Batrouni, G. G.; Scalettar, R. T. Charge Density Wave and Superconductivity in the Disordered Holstein Model. *Phys. Rev. B* **2021**, *103*, L060501.

(28) Karakuzu, S.; Tocchio, L. F.; Sorella, S.; Becca, F. Superconductivity, Charge-Density Waves, Antiferromagnetism, and Phase Separation in the Hubbard-Holstein Model. *Phys. Rev. B* **2017**, *96*, 205145.

(29) Ramakumar, R.; Das, A. N. Polaron Cross-Overs and d-Wave Superconductivity in Hubbard-Holstein Model. *Eur. Phys. J.* **2004**, *41*, 197–200.

(30) Fehske, H.; Hager, G.; Jeckelmann, E. Metallicity in the Half-Filled Holstein-Hubbard Model. *Europhys. Lett.* **2008**, *84*, 57001.

(31) Takada, Y.; Chatterjee, A. Possibility of a Metallic Phase in the Charge-Density-Wave–Spin-Density-Wave Crossover Region in the One-Dimensional Hubbard-Holstein Model at Half Filling. *Phys. Rev. B* **2003**, *67*, 081102.

(32) Oh, D. G.; Kim, J. H.; Shin, H. J.; Choi, Y. J.; Lee, N. Anisotropic and Nonlinear Magnetodielectric Effects in Orthoferrite $ErFeO_3$ Single Crystals. *Sci. Rep.* **2020**, *10*, 11825.

(33) Weber, M. C.; Guennou, M.; Zhao, H. J.; Íñiguez, J.; Vilarinho, R.; Almeida, A.; Moreira, J. A.; Kreisel, J. Raman Spectroscopy of Rare-Earth Orthoferrites $RFeO_3$ (R = La, Sm, Eu, Gd, Tb, Dy). *Phys. Rev. B* **2016**, *94*, 214103.

(34) Zhou, Z.; Guo, L.; Yang, H.; Liu, Q.; Ye, F. Hydrothermal Synthesis and Magnetic Properties of Multiferroic Rare-Earth Orthoferrites. *J. Alloys Compd.* **2014**, *583*, 21–31.

(35) Zhang, X. X.; Xia, Z. C.; Ke, Y. J.; Zhang, X. Q.; Cheng, Z. H.; Ouyang, Z. W.; Wang, J. F.; Huang, S.; Yang, F.; Song, Y. J.; Xiao, G. L.; Deng, H.; Jiang, D. Q. Magnetic Behavior and Complete High-Field Magnetic Phase Diagram of the Orthoferrite $ErFeO_3$. *Phys. Rev. B* **2019**, *100*, 054418.

(36) Nova, T. F.; Cartella, A.; Cantaluppi, A.; Först, M.; Bossini, D.; Mikhaylovskiy, R. V.; Kimel, A. V.; Merlin, R.; Cavalleri, A. An Effective Magnetic Field from Optically Driven Phonons. *Nat. Phys.* **2017**, *13*, 132–136.

(37) de Jong, J. A.; Kimel, A. V.; Pisarev, R. V.; Kirilyuk, A.; Rasing, T. Laser-Induced Ultrafast Spin Dynamics in $ErFeO_3$. *Phys. Rev. B* **2011**, *84*, 104421.

(38) Gomes, E. O.; Fabris, G. S. L.; Ferrer, M. M.; Motta, F. V.; Bomio, M. R. D.; Andres, J.; Longo, E.; Sambrano, J. R. Computational Procedure to an Accurate DFT Simulation to Solid State Systems. *Comput. Mater. Sci.* **2019**, *170*, 109176.

(39) Panneerselvam, I. R.; Baldo, C., III; Sahasranaman, M.; Murugesan, S.; Rangaswamy, N.; Pai, S. D. K. R.; Selvarathinam, Y. Large Power Factors in Wide Band Gap Semiconducting $RFeO_3$ Materials for High-Temperature Thermoelectric Applications. *ACS Appl. Energy Mater.* **2020**, *3*, 11193–11205.

(40) Wang, Z.-Q.; Ian, Y.-S.; Zeng, Z.-Y.; Chen, X.-R.; Chen, Q.-F. Magnetic Structures and Optical Properties of Rare-Earth Orthoferrites $RFeO_3$ (R = Ho, Er, Tm, and Lu). *Solid State Commun.* **2019**, *288*, 10–17.

(41) Tanaka, A.; Ueda, H. Stability of Ferromagnetism in the Hubbard Model on the Kagome Lattice. *Phys. Rev. Lett.* **2003**, *90*, 067204.

(42) Hollinsworth, B. S.; Mazumdar, D.; Brooks, C. M.; Mundy, J. A.; Das, H.; Cherian, J. G.; McGill, S. A.; Fennie, C. J.; Schlom, D. G.; Musfeldt, J. L. Direct Band Gaps in Multiferroic *h*-$LuFeO_3$. *Appl. Phys. Lett.* **2015**, *106*, 082902.

(43) Han, H.; Kim, D.; Chae, S.; Park, J.; Nam, S. Y.; Choi, M.; Yong, K.; Kim, H. J.; Son, J.; Jang, H. M. Switchable Ferroelectric Photovoltaic Effects in Epitaxial *h*-$RFeO_3$ Thin Films. *Nanoscale* **2018**, *10*, 13261–13269.

(44) Liu, H.; Michelsen, J. M.; Mendes, J. L.; Klein, I. M.; Bauers, S. R.; Evans, J. M.; Zakutayev, A.; Cushing, S. K. Measuring Photoexcited Electron and Hole Dynamics in ZnTe and Modeling Excited-State Core-Valence Effects in Transient Extreme Ultraviolet Reflection Spectroscopy. *J. Phys. Chem. Lett.* **2023**, *14*, 2106–2111.

(45) Kaplan, C. J.; Kraus, P. M.; Ross, A. D.; Zürch, M.; Cushing, S. K.; Jager, M. F.; Chang, H.-T.; Gullikson, E. M.; Neumark, D. M.; Leone, S. R. Femtosecond Tracking of Carrier Relaxation in Germanium with Extreme Ultraviolet Transient Reflectivity. *Phys. Rev. B* **2018**, *97*, 205202.

(46) Klein, I. M.; Liu, H.; Nimlos, D.; Krotz, A.; Cushing, S. K. Ab Initio Prediction of Excited-State and Polaron Effects in Transient XUV Measurements of α-Fe_2O_3. *J. Am. Chem. Soc.* **2022**, *144*, 12834–12841.

(47) Klein, I. M.; Krotz, A.; Lee, W.; Michelsen, J. M.; Cushing, S. K. Ab Initio Calculations of XUV Ground and Excited States for First-Row Transition Metal Oxides. *J. Phys. Chem. C* **2023**, *127*, 1077–1086.

(48) Hruska, E.; Husek, J.; Bandaranayake, S.; Baker, L. R. Visible Light Absorption and Hot Carrier Trapping in Anatase TiO_2: The Role of Surface Oxygen Vacancies. *J. Phys. Chem. C* **2022**, *126*, 10752–10761.

(49) Vinson, J.; Rehr, J. J.; Kas, J. J.; Shirley, E. L. Bethe–Salpeter Equation Calculations of Core Excitation Spectra. *Phys. Rev. B* **2011**, *83*, 115106.

(50) Gilmore, K.; Vinson, J.; Shirley, E. L.; Prendergast, D.; Pemmaraju, C. D.; Kas, J. J.; Vila, F. D.; Rehr, J. J. Efficient Implementation of Core-Excitation Bethe–Salpeter Equation Calculations. *Comput. Phys. Commun.* **2015**, *197*, 109–117.

(51) Pavlov, V. V.; Akbashev, A. R.; Kalashnikova, A. M.; Rusakov, V. A.; Kaul, A. R.; Bayer, M.; Pisarev, R. V. Optical Properties and Electronic Structure of Multiferroic Hexagonal Orthoferrites $RFeO_3$ (R = Ho, Er, Lu). *J. Appl. Phys.* **2012**, *111*.

(52) Hafiz, H.; Suzuki, K.; Barbiellini, B.; Orikasa, Y.; Callewaert, V.; Kaprzyk, S.; Itou, M.; Yamamoto, K.; Yamada, R.; Uchimoto, Y.; Sakurai, Y.; Sakurai, H.; Bansil, A. Visualizing Redox Orbitals and Their Potentials in Advanced Lithium-Ion Battery Materials Using High-Resolution X-Ray Compton Scattering. *Sci. Adv.* **2017**, *3*, e1700971.

(53) Schober, A.; Fowlie, J.; Guennou, M.; Weber, M. C.; Zhao, H.; Íñiguez, J.; Gibert, M.; Triscone, J.-M.; Kreisel, J. Vibrational Properties of $LaNiO_3$ Films in the Ultrathin Regime. *APL Mater.* **2020**, *8*, 061102.

(54) Hubbard, J.; Flowers, B. H. Electron Correlations in Narrow Energy Bands III. An Improved Solution. *Proc. R. Soc. Lond. A* **1964**, *281*, 401–419.

(55) Tezuka, M.; Arita, R.; Aoki, H. Phase Diagram for the One-Dimensional Hubbard-Holstein Model: A Density-Matrix Renormalization Group Study. *Phys. Rev. B* **2007**, *76*, 155114.

(56) Mitrić, P.; Janković, V.; Vukmirović, N.; Tanasković, D. Spectral Functions of the Holstein Polaron: Exact and Approximate Solutions. *Phys. Rev. Lett.* **2022**, *129*, 096401.

(57) Géneaux, R.; Chang, H.-T.; Schwartzberg, A. M.; Marroux, H. J. B. Source Noise Suppression in Attosecond Transient Absorption Spectroscopy by Edge-Pixel Referencing. *Opt. Express* **2021**, *29*, 951–960.

Chapter 5

DYNAMIC COMPETITION BETWEEN HUBBARD AND SUPEREXCHANGE INTERACTIONS SELECTIVELY LOCALIZES ELECTRONS AND HOLES THROUGH POLARONS

This chapter is adapted with permission from:

Mendes, J. L.; Shin, H. J.; Seo, J. Y.; Lee, N.; Choi, Y. J.; Varley, J. B.; Cushing, S. K. Dynamic Competition Between Hubbard and Superexchange Interactions Selectively Localizes Electrons and Holes Through Polarons. *J. Am. Chem. Soc.* **2025**, *147* (19), 16018–16026. https://doi.org/10.1021/jacs.4c16837

5.1 Abstract

Controlling the effects of photoexcited polarons in transition metal oxides can enable the long time-scale charge separation necessary for renewable energy applications and controlling new quantum phases through dynamically tunable electron–phonon coupling. In previously studied transition metal oxides, polaron formation is facilitated by a photoexcited ligand-to-metal charge transfer (LMCT). When the polaron is formed, oxygen atoms move away from iron centers, which increases carrier localization at the metal center and decreases charge hopping. Studies of yttrium iron garnet and erbium iron oxide have suggested that strong electron and spin correlations can modulate photoexcited polaron formation. To understand the interplay between strong spin and electronic correlations in highly polar materials, we studied gadolinium iron oxide ($GdFeO_3$), which selectively forms photoexcited polarons through an Fe–O–Fe superexchange interaction. Excitation-wavelength-dependent transient extreme ultraviolet (XUV) spectroscopy selectively excites LMCT and metal-to-metal charge transfer (MMCT) transitions. The LMCT transition suppresses photoexcited polaron formation due to the balance between superexchange and Hubbard interactions, while MMCT transitions result in photoexcited polaron formation within 250 ± 40 fs. Ab initio theory demonstrates that electron and hole polarons localize on iron centers following MMCT. In addition to understanding how strong electronic and spin correlations can control

strong electron–phonon coupling, these experiments separately measure electron and hole polaron interactions on neighboring metal centers for the first time, providing insight into a large range of charge-transfer and Mott–Hubbard insulators.

5.2 Introduction

Polaron formation in transition metal oxide materials has been widely explored for its effects on ground-state transport in correlated materials and solar energy processes like photocatalysis.[1–5] In highly polar materials, the coupling of photoexcited charge carriers to phonons in the lattice localizes carriers in the form of polarons.[6] Parameters to dynamically control laser-driven strong electron–phonon coupling is an ongoing search. Understanding and controlling the underlying physics that determines the formation of polarons in materials could provide meaningful improvements to a wide range of material classes, from organic electronics to solar energy systems and exotic quantum phases.[7,8]

Hematite (α-Fe_2O_3) and other iron oxides have been extensively explored for their photoexcited polaron formation dynamics.[9–12] Most of these materials are charge-transfer insulators, where the valence band maximum (VBM) is dominated by O 2p orbitals, and the conduction band minimum (CBM) is dominated by metal 3d orbitals. An above-band gap photoexcitation induces a ligand-to-metal charge transfer (LMCT) transition from oxygen to the metal center. The electronic structures of metal oxides also span intermediate and Mott–Hubbard insulators, where the VBM is dominated by either mixed oxygen/metal orbitals or entirely metal orbitals, respectively. These differing electronic structures pose a unique route for the modulation of carrier localization by polaron formation following photoexcitation.

Almost uniformly across iron oxides, photoexcited small polaron formation occurs within a few hundred femtoseconds of the charge transfer transition.[10,13,14] A subsequent expansion of Fe–O bond lengths and localization of electron density on polaronic iron sites has been measured using a variety of X-ray spectroscopies. Recent work exploring the tunability of polaronic properties has been demonstrated using structural distortions and strong electron and spin correlations. For example, rare-earth orthoferrite $ErFeO_3$ was found to have weaker

polaronic binding energies because the polaron formation rate was slowed by strong electronic correlations.[12] Additional work comparing hematite and $Y_3Fe_5O_{12}$ (YIG) finds that strong spin-selective dynamics reduce polaron formation in YIG and increase its photocatalytic efficiency by an order of magnitude with respect to hematite.[15] Transient XUV and X-ray spectroscopies, however, have yet to be applied to the simultaneous measurement of electron and hole polarons in intermediate and Mott–Hubbard insulating iron oxides.

Here, we employ excitation-wavelength-dependent transient extreme ultraviolet (XUV) reflection spectroscopy to explore the relation between superexchange and Hubbard interactions in influencing strong carrier localization through polarons in single-crystal rare-earth orthoferrite $GdFeO_3$. This intermediate insulator (mixed O 2p/Fe 3d VBM) is a model material system for many perovskite Mott–Hubbard insulators due to its crystal structure.[16,17] $GdFeO_3$ and other rare-earth orthoferrites have been explored as candidates for photoelectrochemical oxygen reduction and evolution, as well as magneto-optical and spintronic applications due to their demonstrated multiferroicity.[18,19] Through transient XUV spectroscopy, we find that LMCT from O 2p to Fe 3d orbitals results in the suppression of photoexcited polaron formation, while a metal-to-metal charge transfer (MMCT) induces photoexcited polaron formation. The MMCT enables polarons by superexchange across an Fe–O–Fe bond, resulting in hole and electron polarons localized on neighboring iron centers, and a reduced radiative lifetime (<100 ps for MMCT versus 1.2 ± 0.4 ns for LMCT). Polaron formation is suppressed following a higher energy LMCT due to the balance of on-site Coulomb repulsion (U) from oxygen-dominated valence orbitals and superexchange in the final spin state. While thermalization of these carriers occurs in ∼350 fs, the final spin state from the LMCT prevents the polaron formation. Ab initio density functional theory (DFT) and the Bethe–Salpeter equation (BSE) simulate the photoexcited XUV dynamics. Polaron-induced lattice distortions and charge localization within a defect supercell approach were assessed with different levels of electronic structure theory, ranging from DFT incorporating on-site Hubbard *U* parameters with variational polaron self-interaction-corrected (pSIC) total-energy functional models to hybrid functionals with different fractions of exact

exchange. The results provide new insight into tuning polaronic properties via strong electronic and spin correlations for transition metal oxide materials, particularly identifying superexchange interactions as a new dynamical carrier localization and polaron design parameter.

5.3 Experimental Section

5.3.1 Synthesis of Single-Crystalline $GdFeO_3$

Single crystals of $GdFeO_3$ were synthesized using the flux method, employing PbO, PbF_2, PbO_2, and B_2O_3 as fluxes in a high-temperature furnace. A stoichiometric mixture of Gd_2O_3 and Fe_2O_3 powders was thoroughly combined with the flux compounds and placed in a platinum crucible. The mixture was heated to 1250 °C for 16 h to ensure complete dissolution. Then, it was cooled slowly to 850 °C at a rate of 2 °C/h, and further cooled to room temperature at a rate of 100 °C/h. This process yielded large cuboid shaped $GdFeO_3$ crystals, with individual crystals obtaining lengths of up to 1 cm on a side. Characterization of the $GdFeO_3$ single crystals can be found in the Supporting Information, **Appendix D**.

5.3.2 Transient Extreme Ultraviolet (XUV) Spectroscopy

For both photoexcitation wavelengths, the pump pulses are ~50 fs with a fluence of ~11 mJ/cm^2 and are time-delayed with respect to the probe pulse. In the case of 800 nm photoexcitation, this results in a photoexcited carrier density of $\sim 7.3 \times 10^{20}$ cm^{-3}, and for 400 nm excitation a carrier density of $\sim 3.7 \times 10^{20}$ cm^{-3}, details of the carrier density calculation can be found in the Supporting Information, **Appendix D**. The DFT-calculated unit cell of $GdFeO_3$ has a volume of $\sim 2.4 \times 10^{-22}$ cm^3 and given that each unit cell contains 4 iron atoms, there are approximately $\sim 1.6 \times 10^{22}$ Fe atoms/cm^3. This would result in ~4.5% and ~2.3% of iron atoms excited following 800 and 400 nm photoexcitation, respectively. The XUV probe pulse is generated by high harmonic generation in Ar gas from a few-cycle white light pulse. The transient extreme ultraviolet reflection experiment employs a 10° grazing incidence geometry, which results in a ~2 nm penetration depth.[20] The Fe $M_{2,3}$ edge

at ~54 eV corresponds to transitions from the $3p_{3/2,5/2}$ core levels into 3d core levels. The change in transient reflection following photoexcitation is defined by $\Delta OD = -\log10(I_{pump\ on}/I_{pump\ off})$. Additional details about the transient extreme ultraviolet spectrometer can be found in the Supporting Information, **Appendix D**.

5.3.3 Ab initio Polaron and Core-Level Spectra Modeling

The theoretical framework we employ to fully analyze the transient core-level spectra has been described in detail previously.[21] We compute both the ground-state X-ray absorption at the Fe $M_{2,3}$ edge in $GdFeO_3$ and differential effects to the core-level $GdFeO_3$ spectra following excitation-wavelength-dependent photoexcitation and polaron formation. These effects are calculated with an ab initio theoretical approach which employs density functional theory and the Bethe–Salpeter equation (DFT+BSE). The DFT+BSE approach employs DFT using the Quantum ESPRESSO package[22,23] and the existing OCEAN code[24–26] (Obtaining Core-level Excitations using Ab-initio calculations and the NIST BSE solver). We have modified the BSE to use excited state distributions to determine transient changes in the XUV spectra. We first calculate the band structure of $GdFeO_3$ using DFT. Then, the BSE is solved to obtain the core–valence exciton wave functions and transient XUV spectra can be plotted from the complex dielectric function calculated by OCEAN. A modification to the OCEAN code, discussed previously,[21,27] is employed to model the initial 800 nm MMCT and 400 nm LMCT states.

Polaronic distortions are modeled using a DFT+BSE approach where we apply a semiempirical distortion to an FeO_6 octahedra and calculate its resulting Fe $M_{2,3}$ edge spectra. Polaronic distortions calculated using this technique are termed DFT+BSE. The polaronic distortions are modeled independently of the different charge transfer transitions, but it is implied that only MMCT could induce hole polarons on iron centers. We further model polaronic lattice distortions using a defect supercell approach with hybrid and polaron self-interaction corrected exchange-correlation functionals (HSE06 and pSIC) as implemented in the VASP code.[28–32] These functionals either incorporate a fraction of Hartree–Fock (HF) exact exchange to improve self-interaction errors and a description of

charge localization (e.g., hybrid functionals) that depends on an empirical parameter (α, the HF mixing parameter), or employ a variational approach from a closed-shell system for a parameter-free ab initio methodology for calculating polaron properties that removes the sensitivity to empirical parameters like α or Hubbard U parameters.[29] These methods were used to identify structural distortions and relative energetics associated with electron and hole polaron formation at different sites in $GdFeO_3$ and to assess their sensitivity to empirical parameters in the calculations. We generally refer to the polaron-containing structures and subsequent X-ray spectra obtained via these approaches (hybrid functionals and/or with the pSIC approach) as pSIC+DFT+BSE. Additional details about ab initio modeling of photoexcited XUV dynamics can be found in the Supporting Information section, **Appendix D**.

5.4 Results and Discussion

5.4.1 Defect Supercell Calculations of Polarons

$GdFeO_3$ has an orthorhombic symmetry in the Pbnm space group, as shown in **Figure 5.1A**.[17] The FeO_6 octahedra are strained due to the large rare-earth atom in the crystal structure, resulting in a 154° Fe–O–Fe bond angle.[33] Strong electron correlations introduced by both the Fe d and Gd f orbitals enable a mixed Fe d/O p band at the VBM and a metal d band at the CBM, as shown in **Figure 5.1B**. This contrasts with previously measured iron oxides whose density of states follow a charge-transfer insulating structure where the VBM is dominated by O 2p orbitals.[10,21] DFT+U is used to accurately describe the extent of carrier localization and on-site repulsion in $GdFeO_3$.[17] Magnetization studies of $GdFeO_3$ have demonstrated that it is a canted, G-type antiferromagnet (AFM) below its Néel temperature (TN) of ∼650 K, resulting in a weak ferromagnetism due to the Dzyaloshinskii–Moriya (DM) interaction.[34–36] The Fe^{3+} ions in the $GdFeO_3$ take a high-spin (HS) electronic configuration in their ground state, and the octahedral tilts of adjacent FeO_6 octahedra are measured to have strong antisymmetric exchange interactions (superexchange).[37,38]

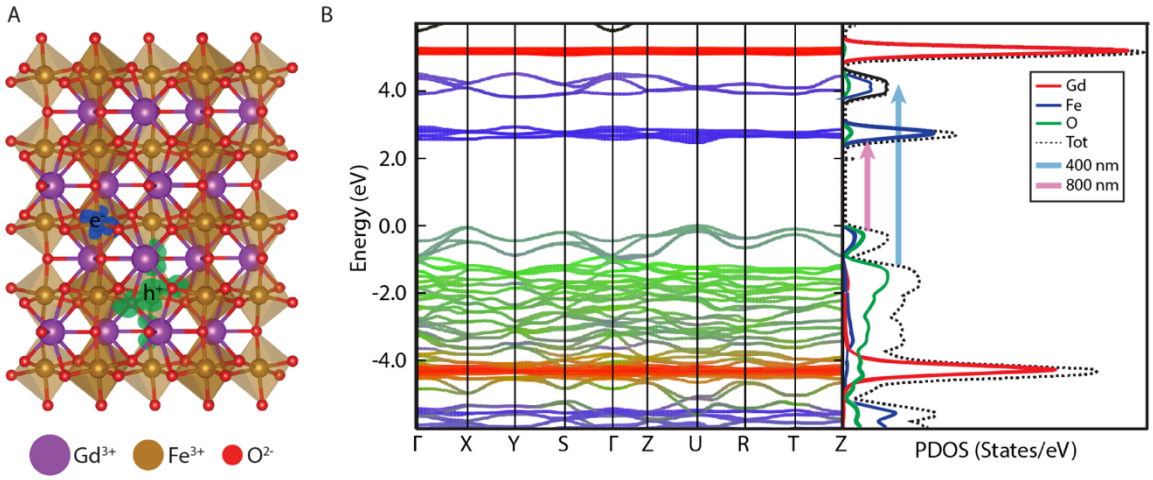

Figure 5.1 GdFeO3 crystal structure, calculated electronic band structure, and projected density of states. **(A)** $GdFeO_3$ crystal structure with electron (blue) and hole (green) polaron charge densities as calculated with exchange correlation functionals that correct for self-interaction errors, referred to as defect supercell calculations. The electron and hole polarons are both predicted to be centered on iron atoms. **(B)** Calculated electronic band structure and the projected density of states (PDOS) with the HSE06 hybrid functional with 15% exact exchange for the studied AFM ground state, including tentative assignments of band transitions associated with the 800 nm (pink arrow) and 400 nm (blue arrow) excitations that lead to the polaron formation. The bandgap is overestimated due to deficiencies associated with the DFT of transition metals, but the band structure and contributions of relative orbitals are preserved. The excitation arrows are adjusted accordingly to showcase the transition densities expected based upon the experimentally measured band gap.

Figure 5.1B shows the two photoexcitation pathways used in the excitation-wavelength-dependent XUV measurements. In the case of the 400 nm (3.1 eV) photoexcitation, carriers are excited from lower-lying valence bands that are dominated by O 2p orbitals into higher-energy Fe 3d and Gd 6f orbital-dominated conduction bands. Photoexcitation with 400 nm light follows a LMCT mechanism. The lower-energy 800 nm (1.55 eV) photoexcitation induces transitions from the VBM, which are mixed in O 2p and Fe 3d orbital character, into lower-energy conduction bands dominated by Fe 3d orbitals. The mixed nature of the VBM in $GdFeO_3$ poses an opportunity for both MMCT and LMCT to occur.[39] These excitation energies provide different possible pathways for polaron formation.

We employ a defect supercell approach with hybrid and polaron self-interaction corrected exchange-correlation functionals (HSE06 and pSIC) to calculate ab initio polaronic distortions in GdFeO3. Further details of the calculations can be found in the Experimental section and the Supporting Information, **Appendix D**. These methods identify structural distortions and relative energetics associated with electron and hole polaron formation at

different sites in $GdFeO_3$ and assess their sensitivity to empirical parameters in the calculations. The charge localization of both electron and hole polarons from defect supercell calculations (**Fig. 5.1A**) predicts that the electron polaron localizes on one single iron site. The hole polaron is less localized than the electron polaron; however, its charge density is predicted to be centered over an iron site as well. A polaron formed following MMCT would induce both electron and hole polaron formation on iron centers. We hypothesize that the lack of an oxygen-centered polaron from the mixed orbital VB means that the LMCT may not lead to polaron formation.

5.4.2 Hubbard–Holstein Model of Polaron Formation

To understand the defect supercell-predicted localization of electron and hole polarons on iron centers in $GdFeO_3$, we must understand the conditions that make polaron formation favorable in a material system. The model Hamiltonian that follows the two-site Hubbard–Holstein model in eq 1 presents the relevant properties that dictate polaron formation:

$$H = -t_{ij}\sum_{\langle ij\rangle\sigma}(c_{i\sigma}^{\dagger}c_{j\sigma} + H.C.) + U\sum_{i} n_{i\uparrow}n_{i\downarrow} + J\sum_{ij}\overrightarrow{S_i}\cdot\overrightarrow{S_j} + \omega_0\sum_{i} b_i^{\dagger}b_i + g\sum_{i,\sigma} n_{i\sigma}\left(b_i + b_i^{\dagger}\right) \quad (\mathbf{5.1})$$

where t_{ij} is the hopping integral, $c_{i\sigma}^{\dagger}$ and $c_{j\sigma}$ are the creation and annihilation operators, respectively, with spin, σ, for an electron at site *i* and *j*.[40–45] *U* is the on-site Coulombic repulsion, n_i is the number operator, *g* corresponds to the electron–phonon coupling strength, and ω_0 refers to the phonon frequency. $b_i^{\dagger}$ and b_i are the creation and annihilation operators, respectively, for phonons at site *i*. *J* denotes the superexchange interaction between neighboring metal sites.[46] The Hubbard–Holstein Hamiltonian is commonly downfolded to a t–J model.[47,48] Here we consider the Hubbard–Holstein model for simplicity, but a t-J Hamiltonian could be applied under certain coupling regimes.

Polarons exist in a strongly electron–phonon coupled regime, as carriers are localized by strong interactions with the lattice. Alternatively, when electron–phonon coupling is sufficiently weak, carriers may conduct freely in materials and polaron formation is

suppressed. This indicates that for polaron formation to be favorable $t \ll g$, while polaron formation would be weak or suppressed when $t \gg g$. In a $U \gg t$ regime at half-filling, $J \approx 4t^2/U$, and for an antiferromagnet $t_{eff} \propto J$ and $t_{eff} \propto 1/U$.[46,49,50] We note that this is an oversimplification, as U and J are changing many body wave functions. DMFT work to study the interplay of electron–phonon coupling and the superexchange interaction find that as g increases, J decreases, meaning that superexchange is suppressed in a strongly electron–phonon coupled regime.[41] On-site Coulombic repulsions are inversely related to J, and thus, J is also expected to be suppressed in a regime where U is sufficiently large.[46]

The defect supercell calculations of $GdFeO_3$ predict that both electron and hole polarons will form on metal sites (**Fig. 5.1A**). This contradicts previous measurements of polaron formation, in which the hole polaron would be localized on a ligand site and the electron polaron would be localized on a metal site. We hypothesize that this is primarily due to the different accessible excitation manifolds within this intermediate insulator. $GdFeO_3$ is expected to have strong J in its ground state due to the AFM configuration of adjacent Fe sites and the tilted FeO_6 octahedra.[38] However, the strong U associated with an MMCT will decrease charge hopping and increase the likelihood of polaron formation. On the other hand, LMCT would originate from a ligand with weak U, which would be associated with weakened electron–phonon coupling. In this case, charge hopping would be expected to be strong, and polaron formation will be suppressed.

5.4.3 Suppressed Polaron Formation Following LMCT

XUV spectroscopy has been employed extensively for the measurement of photoexcited polaron formation dynamics because it can evaluate ultrafast, element-specific electronic-structural dynamics.[9,10,14] Spectrally, polaron formation in iron oxide materials has been characterized in the XUV as a shift to higher energies at the Fe $M_{2,3}$ edge. As carriers localize on the iron center, more energy is required to induce the core-to-valence 3p to 3d transition at the iron site. This has held for charge-transfer polarons across Fe–O materials with dynamics that agree well with transient X-ray diffraction and ultrafast optical techniques.[51,52]

Transient XUV reflectivity at the Fe $M_{2,3}$ edge of $GdFeO_3$ pumped with 400 nm (3.1 eV) light is shown in **Figure 5.2A**. The Fe $M_{2,3}$ edge is characterized immediately after photoexcitation by a negative absorption feature (blue) centered around 54 eV. This spectral feature can be described by a reduction in the population of the Fe^{3+} ground state (**Fig. D.4**) as electrons are excited into Fe d orbitals in the $GdFeO_3$ conduction bands.[10] Transient increases in absorption are present in the 400 nm pumped spectra (**Fig. 5.2A**) from ~52.6–52.9 and ~55.6–58.0 eV. Despite no spectral shift to higher energies being observed at the Fe $M_{2,3}$ edge following 400 nm photoexcitation, there is a decrease in intensity over time (**Fig. 5.2A**). **Figure 5.2C** provides an exponential fit of this decrease in intensity, resulting in a rate constant of $\tau_{400\text{ nm hot carriers}} = 360 \pm 70$ fs, which we attribute to the cooling rate of the hot carriers, in line with XUV studies of photoexcited carrier cooling.[20,53–55]

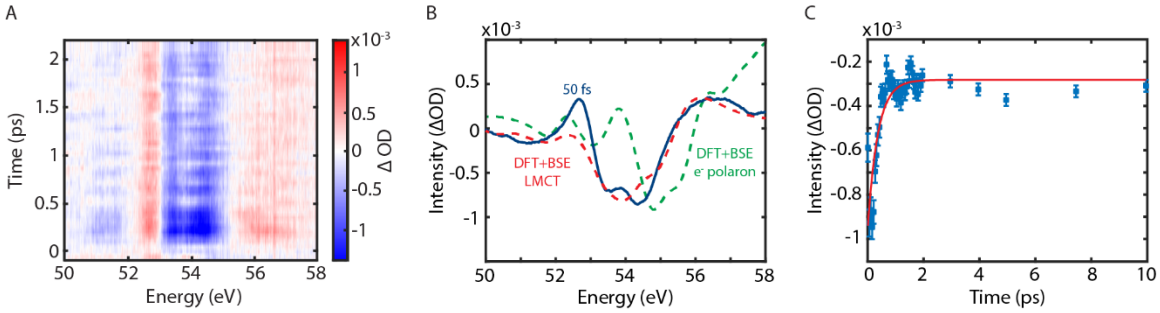

Figure 5.2 Transient XUV spectra following 400 nm photoexcitation and DFT+BSE theory lineouts. **(A)** Transient XUV spectra following 400 nm photoexcitation. **(B)** Experimental lineout from 50 fs after 400 nm photoexcitation (blue) compared to DFT+BSE theory lineouts that model the 400 nm LMCT state (red) and an electron polaron state on an iron atom (green) show agreement with a LMCT state following 400 nm photoexcitation. **(C)** Fitting of the thermalization at the Fe $M_{2,3}$ edge following 400 nm photoexcitation, averaged over the Fe $M_{2,3}$ edge feature.

Due to the strong contribution of angular momentum to the core-level transition Hamiltonian at the Fe $M_{2,3}$ edge, increases (red) and decreases (blue) in absorption in the XUV spectrum do not directly relate to electron and hole energies following photoexcitation, but instead relate to changes in oxidation state, phonon modes, and other structural distortions such as small polarons.[10,12] To understand the origin of the spectral features at the Fe $M_{2,3}$ edge of $GdFeO_3$, we use a density functional theory and Bethe–Salpeter equation (DFT+BSE) approach to model the excited state X-ray edge dynamics. The method uses the Quantum ESPRESSO[22,23] and the OCEAN[24–26] (Obtaining Core Excitations from the Ab initio

electronic structure and the NIST BSE solver) codes. Our defect supercell approach with hybrid and polaron self-interaction corrected exchange-correlation functionals (HSE06 and pSIC) calculates ab initio polaronic distortions in $GdFeO_3$ which are applied to our DFT+BSE framework (pSIC+DFT+BSE). We also model charge transfer and semiempirical polaronic states using this DFT+BSE approach. The theoretical methods applied here are discussed in more detail in the Experimental section and Supporting Information, **Appendix D**.

Figure 5.2B compares an experimental lineout following 400 nm photoexcitation with DFT+BSE theory modeled 400 nm LMCT and electron polaron states. There is good agreement between experimental lineouts at varying time delays following the 400 nm pump and the modeled 400 nm LMCT state. There is poor agreement between the 400 nm experimental lineouts and the DFT+BSE-modeled polaron state that shifts to higher energy. Furthermore, the increases in absorption following 400 nm photoexcitation (**Fig. 5.2A**) from ~52.6–52.9 and ~55.6–58.0 eV are described by high-spin Fe^{2+} states forming as LMCT from the oxygen to iron atoms occurs (**Fig. 5.3A**) using ligand-field multiplet theory.[56] A low-spin (LS) Fe^{2+} state does not agree with the experimentally measured spectrum (**Fig. 5.3A**).

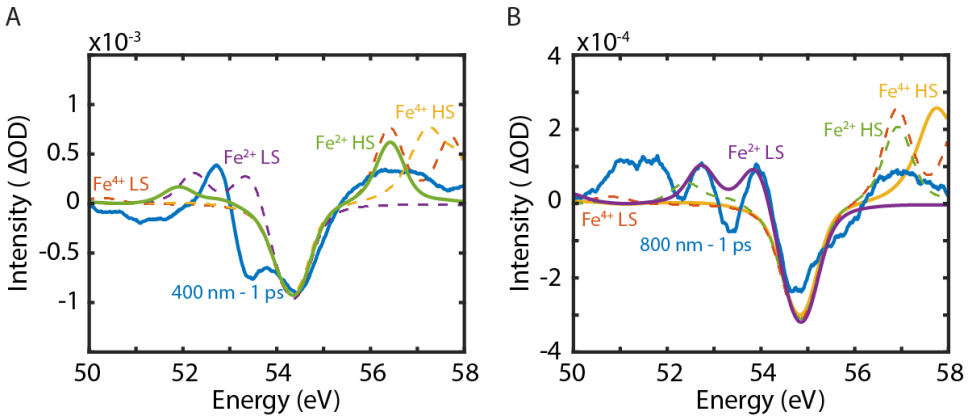

Figure 5.3 Experimental (blue) 400 nm LMCT state **(A)** and 800 nm polaron and trapped Fe^{2+} low-spin state **(B)**. CTM4XAS calculated Fe^{4+} high-spin state (yellow), Fe^{4+} low-spin state (red), Fe^{2+} high-spin state (green), and Fe^{2+} low-spin state (purple). Each oxidation and spin state are plotted for comparison, but the solid lines refer to the assigned CTM4XAS calculated spin states for both experimental spectra.

The photoexcited LMCT state occurs on the same time scale as the pulse width and is present up to our temporal detection limit of 1 ns (**Fig. D.5B**). The nonradiative recombination is, therefore, longer than our instrument's 1 ns temporal limit. An exponential fit of the radiative lifetime of $GdFeO_3$ gives a time constant of $\tau_{400\ nm\ radiative} = 1.2 \pm 0.4$ ns (**Fig. D.3**), but we cannot confirm if the radiative lifetime is from defects or polarons based on our measurement limits. Further details of fluorescence lifetime measurements can be found in the Supporting Information, **Appendix D**.

If we consider the hot carrier thermalization from **Figure 5.2C**, with a time constant of $\tau_{400\ nm\ hot\ carriers} = 360 \pm 70$ fs and compare it to the DFT-calculated phonon band dispersion for $GdFeO_3$, we can approximate the energetic extent of carrier cooling to the CBM. $GdFeO_3$ has its highest frequency phonon mode occurring around ~17 THz, which corresponds to ~70.3 meV.[57] At a first-order approximation, we can apply **Equation 5.2** to calculate the amount of energy the hot carriers cool by

$$\Delta E_{hot\ carriers} = \frac{\tau_{400\ nm\ hot\ carriers}}{\tau_{e-ph}/2} * E_{ph} \quad (\mathbf{5.2})$$

where E_{ph} is the highest frequency phonon mode and $\tau_{e\text{-}ph}$ is the electron–phonon scattering rate, which can also be approximated by the highest frequency phonon mode in the phonon band dispersion. The factor of 2 corresponds to the half phonon period frequency on which electron–phonon scattering occurs, a common approximation in literature.[58,59] This results in ~750 meV of thermalization. The experimentally measured direct band gap of single crystal $GdFeO_3$ is ~1.4 eV (**Fig. D.1**), so electrons excited by the 400 nm pump would be ~2.2 eV above the VBM. This would indicate that excitations occur from ~1 eV below the VBM and the PDOS demonstrates that oxygen orbitals dominate those valence bands (**Fig. 5.1B**), which supports that a LMCT occurs following 400 nm photoexcitation.

Our DFT+BSE, ligand-field multiplet theory, and fluorescence lifetime measurements, therefore, support that LMCT following 400 nm photoexcitation forms a high-spin Fe^{2+} excited state, but strong coupling to phonons that would induce a polaronic lattice distortion is not present. The lack of a spectral shift to higher energies following 400 nm

photoexcitation suggests that polaron formation is suppressed or so weak that it does not influence the transient spectra, and does not compete with the free carriers and their thermalization during the LMCT step (**Fig. 5.2B**).[10,12]

5.4.4 Polaron Formation Following MMCT

Transient XUV reflectivity at the Fe $M_{2,3}$ edge of $GdFeO_3$ following 800 nm (1.55 eV) photoexcitation is shown in **Figure 5.4**. Like 400 nm pumped transient XUV reflectivity spectra, the Fe $M_{2,3}$ edge following an 800 nm pump is characterized immediately after photoexcitation by a negative absorption feature (blue) centered around 54 eV. Unlike in the 400 nm spectra, the negative absorption feature pumped with 800 nm excitation has a spectral blueshift at the Fe $M_{2,3}$ edge from ~52.8–55.8 eV (blue) that begins shortly after photoexcitation. This spectral shift is most prominent from ~54.4–56.0 eV and has a time constant of 250 ± 40 fs (**Fig. D.6**) with an energy shift of 420 ± 150 meV. Following this spectral shift, a peak splitting results in a positive absorption feature (red, ~53.5–54.3 eV) within the Fe $M_{2,3}$ edge in the 800 nm pumped spectra. Additionally, following 800 nm photoexcitation, an increase in absorption (**Fig. 5.4**) that appears from ~50.0–52.8 eV and ~56.3–58.0 eV is measured.

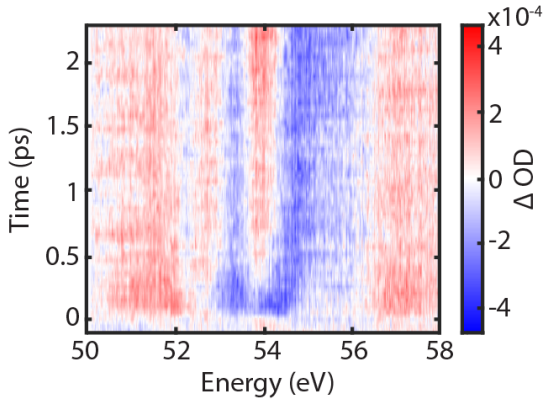

Figure 5.4 Transient XUV reflection–absorption spectrum following 800 nm photoexcitation.

The spectral lineout 50 fs after 800 nm photoexcitation in **Figure 5.5A** (blue) agrees well with DFT+BSE theory (red) for a modeled 800 nm MMCT state. The DFT-calculated PDOS (**Fig. 5.1B**) demonstrates that this excitation originates from mixed O 2p/Fe 3d valence bands

and, therefore, could be either LMCT or MMCT in character. We find that the positive absorption features (**Fig. 5.4**) at lower energies (~50.0–52.8 eV) and higher energies (~56.3–58.0 eV) in the 800 nm pumped spectra are associated with the creation of low-spin Fe^{2+} and high-spin Fe^{4+} states, respectively (**Fig. 5.3B**). The formation of high-spin Fe^{4+} states and low-spin Fe^{2+} states suggests that MMCT transitions are occurring between iron atoms following photoexcitation.[39] Section D.5, in the Supporting Information, **Appendix D**, further discusses ligand-field multiplet theory to model these spin states.

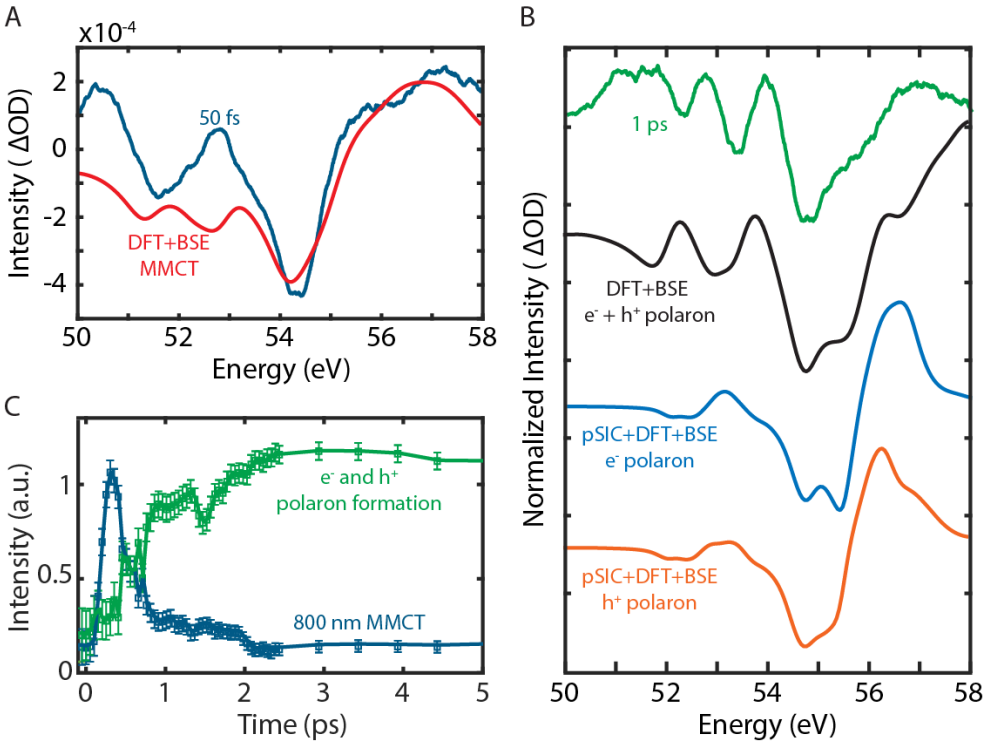

Figure 5.5 Experimental lineouts after 800 nm photoexcitation and DFT+BSE theory. **(A)** Experimental lineout (blue) 50 fs after 800 nm photoexcitation and DFT+BSE theory calculated 800 nm MMCT state (red). **(B)** The polaron state that forms within a few hundred femtoseconds of 800 nm photoexcitation is modeled using DFT+BSE theory (black) for an electron and hole polaron and using the defect supercell pSIC+DFT+BSE theory for electron (blue) and hole (orange) polarons and is shown experimentally (green, 1 ps after 800 nm photoexcitation). Singular value decomposition **(C)** of the experimental 800 nm pumped transient spectra reveals the kinetics of photoexcited electron and hole polaron formation in $GdFeO_3$.

Figure 5.5B shows agreement between the experiment after the blueshift (green), DFT+BSE theory for a convolved electron and hole polaron (black), and pSIC+DFT+BSE theory for both electron (blue) and hole (orange) polarons at neighboring iron sites. The pSIC+DFT+BSE-calculated electron and hole polarons occur at similar energies, suggesting

that the electron and hole polarons are convolved spectrally. This confirms agreement between semiempirical DFT+BSE and ab initio pSIC+DFT+BSE theory, suggesting that different levels of theory can similarly describe the spectral shifts and features associated with convolved electron and hole polaron formation at the Fe $M_{2,3}$ edge. Singular value decomposition (SVD) in **Figure 5.5C** illustrates the transition of the MMCT state to the convolved electron and hole polaron state in the spectra. **Figure D.7** provides further details of the SVD analysis. The SVD plot demonstrates that the MMCT state transitions to the convolved electron and hole polaron state within the first picosecond following 800 nm photoexcitation. Long time-scale 800 nm XUV spectra (**Fig. D.5A**) reveal that the spectral shift lasts out to our instrument's temporal detection limit, and a fit of the exponential non-radiative decay reveals a time constant of 150 ± 30 ps.

5.4.5 Polaron Formation and Fe–O–Fe Superexchange

In addition to forming photoexcited electron and hole polarons on iron centers following 800 nm photoexcitation, a strong spectral splitting of the Fe $M_{2,3}$ edge feature occurs following polaron formation. The spectral splitting in the 800 nm spectra (**Fig. 5.4**) results in an increase in absorption at ~53.5–54.3 eV that arises 330 ± 50 fs following photoexcitation. In the transient XUV spectra following 400 nm photoexcitation (**Fig. 5.2A**), there is spectral splitting that occurs at the Fe $M_{2,3}$ edge (53.8 eV), but it is weaker in intensity than the 800 nm photoexcitation, does not result in a positive signal, and does not change in intensity over time.

The spectral splitting can be attributed to t_{2g} and e_g crystal field splitting expected from the $GdFeO_3$ Fe^{3+} high-spin ground state (**Fig. D.4**).[37,60] This high-spin electronic configuration is preserved following 400 nm LMCT (**Fig. 5.3A**), as demonstrated by the lack of change in spectral splitting between the ground state spectra and excited state 400 nm pumped spectra (**Figs. 5.2A** and **D.4**). Additionally, the increases in absorption following 400 nm photoexcitation (**Fig. 5.2A**) result in the formation of an Fe^{2+} high-spin state, that appears as increases in absorption at ~52.6–52.9 and ~55.6–58 eV (**Fig. 5.3A**). This indicates that the suppression of polaron formation following 400 nm photoexcitation is related to the

preservation of the spin state of the iron atoms following LMCT. Furthermore, the LMCT state does not induce polaron formation because the electron density added to the iron atom originates from an oxygen atom. The ground state DFT predicted bond angle between Fe–O–Fe octahedra (~147.1°) is highly conducive to superexchange. The Hubbard interaction is also weak on the oxygen atom. In this regime, the effective charge hopping integral, t_{eff}, remains large, suppressing polaron formation in the final, thermalized high spin state.

In the case of 800 nm photoexcitation, the strong electron–phonon coupling induced by photoexcited electron and hole polarons influences the dynamics of spectral splitting at the Fe $M_{2,3}$ edge. This is evidenced by the t_{2g} and e_g crystal field splitting in the 800 nm pumped spectra (**Fig. 5.4**) experiencing a transient increase in absorption at ~53.5–54.3 eV.[61] As demonstrated in the DFT+BSE and pSIC+DFT+BSE modeled spectra (**Fig. 5.5B**), the Fe^{2+} and Fe^{4+} centers created following MMCT begin forming electron and hole polarons, respectively. The hole polaron charge density is distributed across the oxygen and Fe^{4+} iron atom, while the electron polaron charge density is localized on the Fe^{2+} site (**Fig. 5.1A**). This is supported by ligand-field multiplet theory modeling of both high-spin and low-spin configurations of Fe^{2+} and Fe^{4+} (**Fig. 5.3B**), that agrees well with a low-spin Fe^{2+} configuration following photoexcitation. The Fe^{4+} feature at higher energies does not experience this spectral splitting, which suggests that the iron that forms the hole polaron does not experience this spin crossover and remains in a high-spin configuration. This agrees with reports of delocalization, or "sharing", of holes across a metal and ligand participating in superexchange.[62,63]

The distortion induced by the polarons is anisotropic (**Fig. D.10**) and results in a Jahn–Teller distortion of the axial Fe–O ligands between the Fe–O–Fe bond length that is participating in polaron formation (**Fig. 5.6A**). The Jahn–Teller effect has been demonstrated to induce changes to Fe–O–Fe bond angles that affect the superexchange interaction.[64–67] This oxygen-ligand-mediated superexchange enables spins that would have otherwise been misaligned in a high-spin state on the neighboring iron atoms to be transferred to a low-spin Fe^{2+} orbital configuration.[68] However, the bond angle is reduced by ~1.2° according to the DFT

calculations, decreasing the superexchange and the effective charge hopping integral.[69–71] The Hubbard interaction is large for the MMCT between Fe centers and electron–phonon coupling can therefore dominate, resulting in polaron formation.

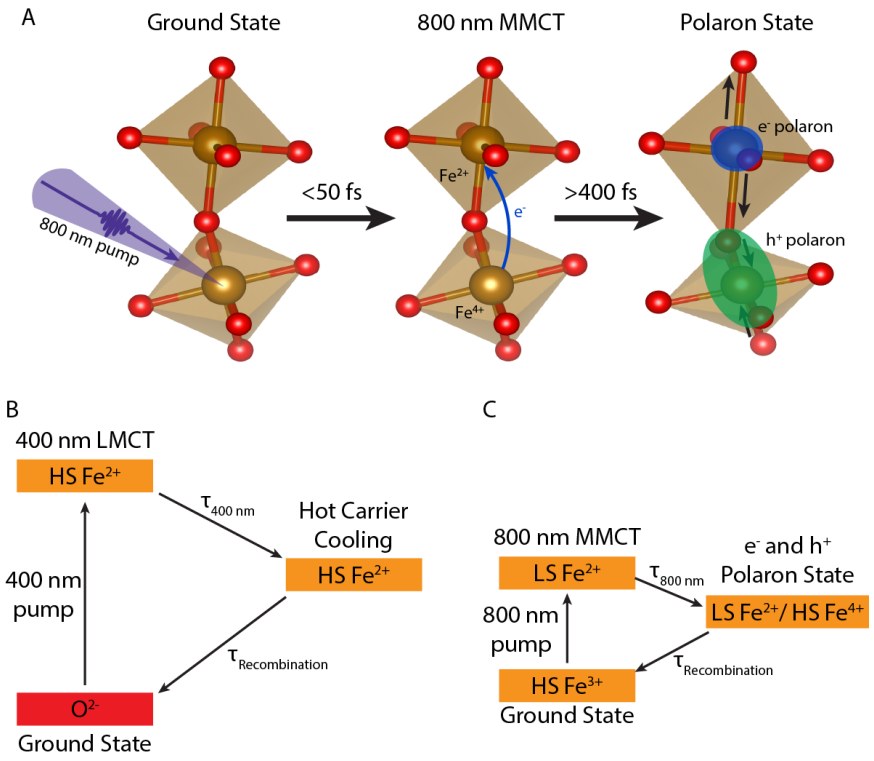

Figure 5.6 Schematic of superexchange across the Fe–O–Fe bond that gives rise to spin crossover on Fe^{2+} centers during photoexcited electron and hole polaron formation. **(A)** Within the first 50 fs, the 800 nm MMCT state results in a charge transfer from one iron center to another. After >400 fs, electron and hole polaron formation results in an expansion and contraction along the Fe–O–Fe bond length, which modulates its bond angle, inducing Jahn–Teller distortions and trapping the high-spin Fe^{2+} state. Diagram of the excitation pathways and spin manifolds present following both 400 nm **(B)** and 800 nm excitation **(C)**. The fitting for the time constants for both hot carrier cooling following 400 nm LMCT ($\tau_{400\ nm}$ = 360 ± 70 fs) and polaron formation and superexchange following 800 nm MMCT ($\tau_{800\ nm}$ = 250 ± 40 fs) are discussed further in the Supporting Information, **Appendix D**.

Iron oxides specifically have been reported to experience optical modification of the exchange interaction on sub-picosecond time scales, supporting this conclusion.[68] Particularly in the case of Mott insulators, whose VBM and CBM are dominated by metal orbitals, exchange interactions are calculated to be reversibly modulated by electric fields on ultrafast time scales.[42] The octahedral site distortion in rare-earth orthoferrites is responsible for orbital and spin ordering, the modulation of that distortion

through polaron formation enables the trapping of a low-spin Fe^{2+} state induced by Fe–O–Fe superexchange following 800 nm MMCT.[71−73]

5.5 Conclusion

Excitation-wavelength-dependent small polaron formation is measured in the intermediate insulator $GdFeO_3$ using transient XUV reflection spectroscopy. Photoexcitation with an 800 nm pump results in both electron and hole polaron formation at neighboring iron sites and strong spectral splitting at the Fe $M_{2,3}$ edge, a spin crossover occurring on the iron atoms. A higher-energy 400 nm pump results in the suppression of polarons. This suggests a metal-metal polaron formation mechanism in which nearest-neighbor iron sites form a hole and electron polaron. The ability to modulate polaron formation by varying excitation wavelength has been studied previously in hematite.[10] However, this mostly results in changes to the polaron's mobility, lifetime, and recombination properties as carriers populate different energy levels of the conduction bands. In the case of $GdFeO_3$, we have suppressed photoexcited polaron formation with weak on-site repulsions following a higher-energy 400 nm photoexcitation, while inducing polaron formation when electron–phonon coupling is dominated by MMCT following 800 nm photoexcitation. The excitation-wavelength-dependent modulation of polaron formation is of interest for applications that employ polarons for charge separation and those that would benefit from carrier mobility offered by the suppression of polaron formation. Tuning spin properties and the exchange integral of these materials presents additional variables for controlling polaron formation in this class of highly polar materials. From a materials engineering perspective, polaronic tunability merits further study in intermediate and Mott–Hubbard insulating transition metal oxide materials.

5.6 References

(1) Franchini, C.; Reticcioli, M.; Setvin, M.; Diebold, U. Polarons in Materials. *Nat. Rev. Mater.* **2021,** *6,* 560–586.

(2) Cheng, C.; Zhou, Z.; Long, R. Time-Domain View of Polaron Dynamics in Metal Oxide Photocatalysts. *J. Phys. Chem. Lett.* **2023,** *14,* 10988–10998.

(3) Suntivich, J.; Hautier, G.; Dabo, I.; Crumlin, E. J.; Kumar, D.; Cuk, T. Probing Intermediate Configurations of Oxygen Evolution Catalysis across the Light Spectrum. *Nat. Energy* **2024,** *9,* 1191–1198.

(4) Rettie, A. J. E.; Chemelewski, W. D.; Emin, D.; Mullins, C. B. Unravelling Small-Polaron Transport in Metal Oxide Photoelectrodes. *J. Phys. Chem. Lett.* **2016,** *7,* 471–479.

(5) Pastor, E.; Sachs, M.; Selim, S.; Durrant, J. R.; Bakulin, A. A.; Walsh, A. Electronic Defects in Metal Oxide Photocatalysts. *Nat. Rev. Mater.* **2022,** *7,* 503–521.

(6) Emin, D. *Polarons*; Cambridge University Press, **2012**.

(7) Yazdani, N.; Bodnarchuk, M. I.; Bertolotti, F.; Masciocchi, N.; Fureraj, I.; Guzelturk, B.; Cotts, B. L.; Zajac, M.; Rainò, G.; Jansen, M.; Boehme, S. C.; Yarema, M.; Lin, M.-F.; Kozina, M.; Reid, A.; Shen, X.; Weathersby, S.; Wang, X.; Vauthey, E.; Guagliardi, A.; Kovalenko, M. V.; Wood, V.; Lindenberg, A. M. Coupling to Octahedral Tilts in Halide Perovskite Nanocrystals Induces Phonon-Mediated Attractive Interactions between Excitons. *Nat. Phys.* **2024,** *20,* 47–53.

(8) Ghosh, R.; Spano, F. C. Excitons and Polarons in Organic Materials. *Acc. Chem. Res.* **2020,** *53,* 2201–2211.

(9) Biswas, S.; Wallentine, S.; Bandaranayake, S.; Baker, L. R. Controlling Polaron Formation at Hematite Surfaces by Molecular Functionalization Probed by XUV Reflection-Absorption Spectroscopy. *J. Chem. Phys.* **2019,** *151,* 104701.

(10) Carneiro, L. M.; Cushing, S. K.; Liu, C.; Su, Y.; Yang, P.; Alivisatos, A. P.; Leone, S. R. Excitation-Wavelength-Dependent Small Polaron Trapping of Photoexcited Carriers in α-Fe_2O_3. *Nat. Mater.* **2017,** *16,* 819–825.

(11) Vura-Weis, J.; Jiang, C.-M.; Liu, C.; Gao, H.; Lucas, J. M.; de Groot, F. M. F.; Yang, P.; Alivisatos, A. P.; Leone, S. R. Femtosecond M2,3-Edge Spectroscopy of Transition-Metal Oxides: Photoinduced Oxidation State Change in α-Fe_2O_3. *J. Phys. Chem. Lett.* **2013,** *4,* 3667–3671.

(12) Kim, Y.-J.; Mendes, J. L.; Michelsen, J. M.; Shin, H. J.; Lee, N.; Choi, Y. J.; Cushing, S. K. Coherent Charge Hopping Suppresses Photoexcited Small Polarons in $ErFeO_3$ by Antiadiabatic Formation Mechanism. *Sci. Adv.* **2024,** *10,* eadk4282.

(13) Bandaranayake, S.; Hruska, E.; Londo, S.; Biswas, S.; Baker, L. R. Small Polarons and Surface Defects in Metal Oxide Photocatalysts Studied Using XUV Reflection-Absorption Spectroscopy. *J. Phys. Chem. C* **2020,** *124,* 22853–22870.

(14) Husek, J.; Cirri, A.; Biswas, S.; Baker, L. R. Surface Electron Dynamics in Hematite (α-Fe_2O_3): Correlation Between Ultrafast Surface Electron Trapping and Small Polaron Formation. *Chem. Sci.* **2017,** *8,* 8170–8178.

(15) Gajapathy, H.; Bandaranayake, S.; Hruska, E.; Vadakkayil, A.; Bloom, B. P.; Londo, S.; McClellan, J.; Guo, J.; Russell, D.; de Groot, F. M. F.; Yang, F.; Waldeck, D. H.; Schultze, M.; Baker, L. R. Spin Polarized Electron Dynamics Enhance Water Splitting Efficiency by Yttrium Iron Garnet Photoanodes: A New Platform for Spin Selective Photocatalysis. *Chem. Sci.* **2024,** *15,* 3300–3310.

(16) Bu, X.; Li, Y. Optical Signature for Distinguishing between Mott-Hubbard, Intermediate, and Charge-Transfer Insulators. *Phys. Rev. B* **2022,** *106,* L241101.

(17) Zhu, X.-H.; Xiao, X.-B.; Chen, X.-R.; Liu, B.-G. Electronic Structure, Magnetism and Optical Properties of Orthorhombic $GdFeO_3$ from First Principles. *RSC Adv.* **2017,** *7,* 4054–4061.

(18) Khan, H.; Ahmad, T. Perspectives and Scope of ABO_3 Type Multiferroic Rare-Earth Perovskites. *Chin. J. Phys.* **2024,** *91,* 199–219.

(19) Podlesnyak, A.; Nikitin, S. E.; Ehlers, G. Low-Energy Spin Dynamics in Rare-Earth Perovskite Oxides. *J. Phys.: Condens. Matter* **2021,** *33,* 403001.

(20) Liu, H.; Michelsen, J. M.; Mendes, J. L.; Klein, I. M.; Bauers, S. R.; Evans, J. M.; Zakutayev, A.; Cushing, S. K. Measuring Photoexcited Electron and Hole Dynamics in ZnTe and Modeling Excited State Core-Valence Effects in Transient Extreme Ultraviolet Reflection Spectroscopy. *J. Phys. Chem. Lett.* **2023,** *14,* 2106–2111.

(21) Klein, I. M.; Liu, H.; Nimlos, D.; Krotz, A.; Cushing, S. K. Ab Initio Prediction of Excited-State and Polaron Effects in Transient XUV Measurements of α-Fe_2O_3. *J. Am. Chem. Soc.* **2022,** *144,* 12834–12841.

(22) Giannozzi, P.; Baroni, S.; Bonini, N.; Calandra, M.; Car, R.; Cavazzoni, C.; Ceresoli, D.; Chiarotti, G. L.; Cococcioni, M.; Dabo, I.; et al. QUANTUM ESPRESSO: A Modular and Open-Source Software Project for Quantum Simulations of Materials. *J. Phys.: Condens. Matter* **2009,** *21,* 395502.

(23) Giannozzi, P.; Andreussi, O.; Brumme, T.; Bunau, O.; Buongiorno Nardelli, M.; Calandra, M.; Car, R.; Cavazzoni, C.; Ceresoli, D.; Cococcioni, M.; Colonna, N.; Carnimeo, I.; Dal Corso, A.; de Gironcoli, S.; Delugas, P.; DiStasio, R. A.; Ferretti, A.; Floris, A.; Fratesi, G.; Fugallo, G.; Gebauer, R.; Gerstmann, U.; Giustino, F.; Gorni, T.; Jia, J.; Kawamura, M.; Ko, H.-Y.; Kokalj, A.; Küçükbenli, E.; Lazzeri, M.; Marsili, M.; Marzari, N.; Mauri, F.; Nguyen, N. L.; Nguyen, H.-V.; Otero-de-la-Roza, A.; Paulatto, L.; Poncé, S.; Rocca, D.; Sabatini, R.; Santra, B.; Schlipf, M.; Seitsonen, A. P.; Smogunov, A.; Timrov, I.; Thonhauser, T.; Umari, P.; Vast, N.; Wu, X.; Baroni, S. Advanced Capabilities for Materials Modelling with Quantum ESPRESSO. *J. Phys.: Condens. Matter* **2017,** *29,* 465901.

(24) Vinson, J. Advances in the OCEAN-3 Spectroscopy Package. *Phys. Chem. Chem. Phys.* **2022,** *24,* 12787–12803.

(25) Vinson, J.; Rehr, J. J.; Kas, J. J.; Shirley, E. L. Bethe-Salpeter Equation Calculations of Core Excitation Spectra. *Phys. Rev. B* **2011,** *83,* 115106.

(26) Gilmore, K.; Vinson, J.; Shirley, E. L.; Prendergast, D.; Pemmaraju, C. D.; Kas, J. J.; Vila, F. D.; Rehr, J. J. Efficient Implementation of Core-Excitation Bethe-Salpeter Equation Calculations. *Comput. Phys. Commun.* **2015,** *197,* 109–117.

(27) Klein, I. M.; Krotz, A.; Lee, W.; Michelsen, J. M.; Cushing, S. K. Ab Initio Calculations of XUV Ground and Excited States for First-Row Transition Metal Oxides. *J. Phys. Chem. C* **2023,** *127,* 1077–1086.

(28) Sadigh, B.; Erhart, P.; Åberg, D. Variational Polaron Self-Interaction-Corrected Total-Energy Functional for Charge Excitations in Insulators. *Phys. Rev. B* **2015,** *92,* 075202.

(29) Heyd, J.; Scuseria, G. E.; Ernzerhof, M. Hybrid Functionals Based on a Screened Coulomb Potential. *J. Chem. Phys.* **2003,** *118,* 8207–8215.

(30) Zhou, F.; Sadigh, B.; Erhart, P.; Åberg, D. Ab Initio Prediction of Fast Non-Equilibrium Transport of Nascent Polarons in SrI_2: A Key to High-Performance Scintillation. *npj Comput. Mater.* **2016,** *2,* 1–7.

(31) Paier, J.; Marsman, M.; Hummer, K.; Kresse, G.; Gerber, I. C.; Angyan, J. G. Screened Hybrid Density Functionals Applied to Solids. *J. Chem. Phys.* **2006,** *124,* 154709.

(32) Varley, J. B.; Janotti, A.; Franchini, C.; Van de Walle, C. G. Role of Self-Trapping in Luminescence and p-Type Conductivity of Wide-Band-Gap Oxides. *Phys. Rev. B* **2012,** *85,* 081109.

(33) Li, H.; Chen, Y.; Xi, S.; Wang, J.; Sun, S.; Sun, Y.; Du, Y.; Xu, Z. J. Degree of Geometric Tilting Determines the Activity of FeO_6 Octahedra for Water Oxidation. *Chem. Mater.* **2018,** *30,* 4313–4320.

(34) Cashion, J. D.; Cooke, A. H.; Martin, D. M.; Wells, M. R. Magnetic Interactions in Gadolinium Orthoferrite. *J. Phys. C: Solid State Phys.* **1970,** *3,* 1612.

(35) Das, M.; Roy, S.; Mandal, P. Giant Reversible Magnetocaloric Effect in a Multiferroic $GdFeO_3$ Single Crystal. *Phys. Rev. B* **2017,** *96,* 174405.

(36) Paul, P.; Ghosh, P. S.; Rajarajan, A. K.; Babu, P. D.; Rao, T. V. C. Ground State Spin Structure of $GdFeO_3$: A Computational and Experimental Study. *J. Magn. Magn. Mater.* **2021,** *518,* 167407.

(37) Yuan, X.; Sun, Y.; Xu, M. Effect of Gd Substitution on the Structure and Magnetic Properties of $YFeO_3$ Ceramics. *J. Solid State Chem.* **2012,** *196,* 362–366.

(38) Shah, J.; Kotnala, R. K. Room Temperature Magnetoelectric Coupling Enhancement in Mg-Substituted Polycrystalline $GdFeO_3$. *Scr. Mater.* **2012,** *67,* 316–319.

(39) Mikhaylovskiy, R. V.; Huisman, T. J.; Gavrichkov, V. A.; Polukeev, S. I.; Ovchinnikov, S. G.; Afanasiev, D.; Pisarev, R. V.; Rasing, T.; Kimel, A. V. Resonant Pumping of d–d Crystal Field Electronic Transitions as a

Mechanism of Ultrafast Optical Control of the Exchange Interactions in Iron Oxides. *Phys. Rev. Lett.* **2020,** *125,* 157201.

(40) Chatterjee, J.; Das, A. N. Role of the Superexchange Interaction in Magnetic Transition and Polaron Crossover. *Physica B: Condens. Matter* **2004,** *384,* 89–94.

(41) Li, S.; Johnston, S. Suppressed Superexchange Interactions in the Cuprates by Bond-Stretching Oxygen Phonons. *Phys. Rev. B* **2023,** *108,* L201113.

(42) Mentink, J. H.; Balzer, K.; Eckstein, M. Ultrafast and Reversible Control of the Exchange Interaction in Mott Insulators. *Nat. Commun.* **2015,** *6,* 6708.

(43) Berger, E.; Valášek, P.; Von Der Linden, W. Two-Dimensional Hubbard-Holstein Model. *Phys. Rev. B* **1995,** *52,* 4806–4814.

(44) Hubbard, J. Electron Correlations in Narrow Energy Bands. *Proc. R. Soc. London, Ser. A* **1963,** *276,* 238–257.

(45) Holstein, T. Studies of Polaron Motion: Part I. The Molecular-Crystal Model. *Ann. Phys.* **1959,** *8,* 325–342.

(46) Anderson, P. W. New Approach to the Theory of Superexchange Interactions. *Phys. Rev.* **1959,** *115,* 2–13.

(47) Cappelluti, E.; Ciuchi, S.; Fratini, S. Polaronic Features in the Optical Properties of the Holstein t-J Model. *Phys. Rev. B* **2007,** *76,* 125111.

(48) Fehske, H.; Roder, H.; Mistriotis, A.; Buttner, H. The Phase Diagram of the 2D Holstein-t-J Model Near Half Filling. *J. Phys.: Condens. Matter* **1993,** *5,* 3565.

(49) Pavarini, E.; Koch, E. Origin of Jahn-Teller Distortion and Orbital Order in $LaMnO_3$. *Phys. Rev. Lett.* **2010,** *104,* 086402.

(50) Endres, H.; Noack, R. M.; Hanke, W.; Poilblanc, D.; Scalapino, D. J. Dynamical Properties of Two Coupled Hubbard Chains at Half-Filling. *Phys. Rev. B* **1996,** *53,* 5530–5540.

(51) Panuganti, S.; Cuthriell, S. A.; Leonard, A. A.; Quintero, M. A.; Laing, C. C.; Guzelturk, B.; Zhang, X.; Chen, L. X.; Kanatzidis, M. G.; Schaller, R. D. Transient X-Ray Diffraction Reveals Nonequilibrium Phase Transition in Thin Films of $CH_3NH_3PbI_3$ Perovskite. *ACS Energy Lett.* **2023,** *8,* 691–698.

(52) Zhang, J.; Shi, J.; Chen, Y.; Zhang, K. H. L.; Yang, Y. Bimolecular Self-Trapped Exciton Formation in Bismuth Vanadate. *J. Phys. Chem. Lett.* **2022,** *13,* 9815–9821.

(53) Jiang, C.-M.; Baker, L. R.; Lucas, J. M.; Vura-Weis, J.; Alivisatos, A. P.; Leone, S. R. Characterization of Photo-Induced Charge Transfer and Hot Carrier Relaxation Pathways in Spinel Cobalt Oxide (Co_3O_4). *J. Phys. Chem. C* **2014,** *118,* 22774–22784.

(54) Molesky, I. J. P.; Lee, A.; Cushing, S. K.; Chang, H.-T.; Ondry, J. C.; Alivisatos, A. P.; Leone, S. R. Characterization of Carrier Cooling Bottleneck in Silicon Nanoparticles by Extreme Ultraviolet (XUV) Transient Absorption Spectroscopy. *J. Phys. Chem. C* **2021,** *125,* 9319–9329.

(55) Verkamp, M.; Leveillee, J.; Sharma, A.; Lin, M.-F.; Schleife, A.; Vura-Weis, J. Carrier-Specific Hot Phonon Bottleneck in $CH_3NH_3PbI_3$ Revealed by Femtosecond XUV Absorption. *J. Am. Chem. Soc.* **2021,** *143,* 20176–20182.

(56) Stavitski, E.; de Groot, F. M. F. The CTM4XAS Program for EELS and XAS Spectral Shape Analysis of Transition Metal L Edges. *Micron* **2010,** *41,* 687–694.

(57) Panneerselvam, I. R.; Baldo, C., III; Sahasranaman, M.; Murugesan, S.; Rangaswamy, N.; Pai, S. D. K. R.; Selvarathinam, Y. Large Power Factors in Wide Band Gap Semiconducting $RFeO_3$ Materials for High-Temperature Thermoelectric Applications. *ACS Appl. Energy Mater.* **2020,** *3,* 11193–11205.

(58) Gu, X.; Fan, Z.; Bao, H.; Zhao, C. Y. Revisiting Phonon-Phonon Scattering in Single-Layer Graphene. *Phys. Rev. B* **2019,** *100,* 064306.

(59) Endo, M.; Kimura, S.; Tani, S.; Kobayashi, Y. Coherent Control of Acoustic Phonons in a Silica Fiber Using a Multi-GHz Optical Frequency Comb. *Commun. Phys.* **2021,** *4,* 1–8.

(60) Khalil, M.; Marcus, M. A.; Smeigh, A. L.; McCusker, J. K.; Chong, H. H. W.; Schoenlein, R. W. Picosecond X-Ray Absorption Spectroscopy of a Photoinduced Iron(II) Spin Crossover Reaction in Solution. *J. Phys. Chem. A* **2006,** *110,* 38–44.

(61) Zhang, K.; Ash, R.; Girolami, G. S.; Vura-Weis, J. Tracking the Metal-Centered Triplet in Photoinduced Spin Crossover of $Fe(Phen)_3^{2+}$ with Tabletop Femtosecond M-Edge X-Ray Absorption Near-Edge Structure Spectroscopy. *J. Am. Chem. Soc.* **2019,** *141,* 17180–17188.

(62) Occhialini, C. A.; Tseng, Y.; Elnaggar, H.; Song, Q.; Blei, M.; Tongay, S. A.; Bisogni, V.; de Groot, F. M. F.; Pelliciari, J.; Comin, R. Nature of Excitons and Their Ligand-Mediated Delocalization in Nickel Dihalide Charge-Transfer Insulators. *Phys. Rev. X* **2024,** *14,* 031007.

(63) Takubo, K.; Mizokawa, T.; Son, J.-Y.; Nambu, Y.; Nakatsuji, S.; Maeno, Y. Unusual Superexchange Pathways in an NiS_2 Triangular Lattice with Negative Charge-Transfer Energy. *Phys. Rev. Lett.* **2007,** *99,* 037203.

(64) Takada, Y.; Masaki, M. Polarons in Jahn-Teller Crystals: Intrinsic Difference between e_g and t_{2g} Electrons. *J. Supercond. Nov. Magn.* **2007,** *20,* 629–633.

(65) Titus Samuel Sudandararaj, A.; Sathish Kumar, G.; Dhivya, M.; Eithiraj, R. D.; Banu, I. B. S. Band Structure Calculation and Rietveld Refinement of Nanoscale $GdFeO_3$ with Affirmation of Jahn Teller's Distortion on Electric and Magnetic Properties. *J. Alloys Compd.* **2019,** *783,* 393–398.

(66) Panchwanee, A.; Reddy, V. R.; Gupta, A.; Bharathi, A.; Phase, D. M. Study of Local Distortion and Spin Reorientation in Polycrystalline Mn Doped $GdFeO_3$. *J. Alloys Compd.* **2018,** *745,* 810–816.

(67) Kim, B. H.; Min, B. I. Nearest and Next-Nearest Superexchange Interactions in Orthorhombic Perovskite Manganites $RMnO_3$ (R = Rare Earth). *Phys. Rev. B* **2009,** *80,* 064416.

(68) Mikhaylovskiy, R. V.; Hendry, E.; Secchi, A.; Mentink, J. H.; Eckstein, M.; Wu, A.; Pisarev, R. V.; Kruglyak, V. V.; Katsnelson, M. I.; Rasing, T.; Kimel, A. V. Ultrafast Optical Modification of Exchange Interactions in Iron Oxides. *Nat. Commun.* **2015,** *6,* 8190.

(69) Feinberg, D.; Germain, P.; Grilli, M.; Seibold, G. Joint Superexchange-Jahn-Teller Mechanism for Layered Antiferromagnetism in $LaMnO_3$. *Phys. Rev. B* **1998,** *57,* R5583–R5586.

(70) Anderson, P. W. Antiferromagnetism. Theory of Superexchange Interaction. *Phys. Rev.* **1950,** *79,* 350–356.

(71) Zhou, J.-S.; Alonso, J. A.; Pomjakushin, V.; Goodenough, J. B.; Ren, Y.; Yan, J.-Q.; Cheng, J.-G. Intrinsic Structural Distortion and Superexchange Interaction in the Orthorhombic Rare-Earth Perovskites $RCrO_3$. *Phys. Rev. B* **2010,** *81,* 214115.

(72) Zhou, J.-S.; Goodenough, J. B. Intrinsic Structural Distortion in Orthorhombic Perovskite Oxides. *Phys. Rev. B* **2008,** *77,* 132104.

(73) Eibschütz, M.; Shtrikman, S.; Treves, D. Mössbauer Studies of Fe^{57} in Orthoferrites. *Phys. Rev.* **1967,** *156,* 562–577.

Chapter 6

METAL-TO-METAL CHARGE TRANSFER POLARON DYNAMICS IN MOTT-HUBBARD INSULATOR FAYALITE

6.1 Abstract

Photoexcited carrier localization through the formation of polarons remains a bottleneck in realizing efficient, earth-abundant photocatalyst devices. Understanding the fundamental properties that dictate polaron dynamics in transition metal oxide photocatalysts is necessary to tune and control polarons. While many studies of polaronic characteristics in charge-transfer insulators have been undertaken, few exist of Mott insulators. Here, we measure photoexcited polaron formation in Mott insulator fayalite (Fe_2SiO_4) using element-specific transient extreme ultraviolet (XUV) spectroscopy. We find that this Fe(II) oxide exhibits the characteristic spectral blueshift at the Fe $M_{2,3}$ associated with small polaron formation. The polaron forms with a 130 ± 40 fs time constant and a magnitude of 460 ± 90 meV. Electronic structure calculations support a Mott-Hubbard picture in which Fe 3d states dominate the band edges for metal-to-metal charge transfer transitions, distinguishing fayalite from more widely studied charge-transfer iron oxides with ligand-to-metal charge transfer transitions. Our results show that strong electronic correlations in Fe_2SiO_4 drive ultrafast carrier localization on ultrafast timescales and establish transient XUV spectroscopy as a sensitive probe of polaron formation in Mott insulating iron oxides.

6.2 Introduction

Mott insulators, while not metallic in character, have large carrier densities that compete with on-site Coulomb repulsions that could become conductive in the excited state, but ultimately localize carriers in the ground state.[1] When on-site Coulomb repulsions are smaller than the charge transfer energy, a lower Hubbard band containing metal d orbitals arises at the valence band maximum. This electronic structure gives rise to a wide range of strongly correlated properties in the form of strong magnetic interactions,[2] superconductivity,[3] and metal-insulator transitions (MIT).[4,5] These strong on-site Coulombic repulsions also serve to

strongly localize the carriers in the metal orbitals of Mott insulators. This strong carrier localization can result in the formation of polarons and has been demonstrated across a range of Mott insulators through both theory[6–9] and experiments.[10,11]

Photoexcited polarons form when excess charge carriers couple strongly to lattice vibrations and localize. In Fe(III) oxide systems small polaron formation, dynamics, and transport have been well characterized in many charge transfer insulators,[12–15] however Mott insulators have yet to be explored as widely in these systems. Recent transient extreme ultraviolet (XUV) spectroscopy of intermediate iron oxide insulators has suggested that photoexcitation can induce both metal-to-metal charge transfer (MMCT) and ligand-to-metal charge transfer (MMCT) transitions to modify polaronic dynamics.[16] In charge transfer insulators, photoexcited small polarons are generally formed following charge transfer from O 2p orbitals to Fe 3d orbitals, or a LMCT.[17,18] This differs in intermediate insulators where polarons may also form following MMCT.[16] The dynamics of photoexcited small polaron formation in Mott insulators would therefore be expected to follow a charge transfer pathway that more closely resembles that of intermediate insulators, rather than charge transfer insulators. Mott insulating Fe_2SiO_4 therefore presents an interesting route through which strong electronic correlations and MMCT-accessible charge transfer pathways dictate photoexcited small polaron formation in Fe(II) oxides.

Fe_2SiO_4 is a particularly useful model Mott insulator to compare to polaron formation in charge-transfer and intermediate insulating iron oxides. Its band gap energy is reported to be in the visible spectrum, and thus accessible via optical excitation, and occurs naturally as a mineral.[19,20] As a result, Fe_2SiO_4 provides an opportunity to examine if photoexcited carrier localization and polaron formation in a Mott insulator follows the same mechanism as charge-transfer insulators, or whether the correlated Fe 3d orbitals and resulting Hubbard d bands in the electronic structure modulate polaron formation, much like intermediate insulators. Transient extreme ultraviolet (XUV) spectroscopy at the Fe $M_{2,3}$ edge is

particularly valuable because it has been widely employed to directly measure the electron-structural effects of polaron formation across a myriad of iron oxides.[15–18,21]

Here we investigate photoexcited polaron formation in the Mott Insulator fayalite (Fe_2SiO_4) measured with transient XUV reflection-absorption spectroscopy at the Fe $M_{2,3}$ X-ray edge. This probe is particularly sensitive to changes in local Fe electronic structure and oxidation state that follows polaron-induced carrier localization and has been demonstrated across a range of charge-transfer and intermediate insulating Fe(III) oxides. We observe a spectral shift to higher energy characteristic of photoexcited small polaron formation with a rate constant of 130 ± 40 fs and a magnitude of 460 ± 90 meV. We use density functional theory and Bethe–Salpeter equation (DFT+BSE) theory to disentangle the resulting dynamics in this Fe(II) Mott insulator. Together, these results provide insight into the nature of photoexcited carrier localization through polarons in strongly correlated iron oxide systems.

6.3 Methods

6.3.1 Transient Extreme Ultraviolet Spectrometer

Here we describe the experimental methods used to measure the Fe_2SiO_4 samples. The transient extreme ultraviolet (XUV) reflectivity spectrometer is described previously.[15,22] A Legend Elite Duo laser system (Coherent Inc.) with 35 fs, 13 mJ, 1 kHz pulses centered at 800 nm is split by a 75:25 beam splitter with ~10 mJ used for the pump path and ~3 mJ being used to generate a few-cycle white light beam (<6 fs, 550-950 nm) for high harmonic generation (HHG). The pump path uses the 400 nm frequency doubled output of a BBO crystal with p-polarization, pumped with the 800 nm output of the Ti:Sapphire laser. The optical excitation fluence used in the Fe_2SiO_4 measurements was ~14 mJ/cm^2. Transient reflection is measured at a 10° grazing incidence (80° from normal incidence) geometry and measures the varying delay times between the pump and probe pulses by an optomechanical delay stage. The photoexcited dynamics were probed with an XUV pulse produced with an s-polarized few-cycle white light pulse by HHG in argon. The residual white light beam is removed with a 100 nm thick Al filter (Luxel). The generated XUV continuum is used to

probe the Fe $M_{2,3}$ absorption edges at ~54 eV. An edge-pixel referencing scheme was used to denoise the spectra due to intensity fluctuations and used signal-free spectral regions.[23]

The static XUV reflectivity of Fe_2SiO_4 is obtained by normalizing the static XUV reflectivity spectrum of the sample by the static reflectivity of a Si wafer, which should not absorb the XUV beam below the Si K edge at ~100 nm. The spectrometer was calibrated using the photoionization continuum of neon gas.[24]

6.3.2 Core-Level Spectral Modeling

Geometry optimization and density functional theory (DFT) calculations were conducted using the Quantum ESPRESSO package with norm-conserving general gradient approximation (GGA), Perdew– Burke–Ernzerhof (PBE) pseudopotentials.[25–27] Geometry optimizations employed an input Fe_2SiO_4 unit cell containing 28 atoms and were based upon the lattice constants for the unit cell of a = 10.4710 Å, b = 6.1414 Å, and c = 4.7979 Å. A 200 Rydberg kinetic energy cutoff and a 4 × 6 × 8 Monkhorst– Pack k-mesh sampling of the first Brillouin zone sampled 100 bands. The starting magnetization was set to a sum of zero for Fe^{2+} ions to represent the antiferromagnetic orientation of neighboring spins at 293 K. The structures employed in the DFT and DFT+BSE calculations described below were fully relaxed and calculations were performed to a convergence of 10^{-8} eV/atom with the forces on ions under 10^{-3} eV/Å.

The theoretical framework we employ to model the ground-state core-level Fe_2SiO_4 spectra at the Fe $M_{2,3}$ has been described previously.[14] Briefly, the ground-state spectrum is calculated with an ab initio theoretical approach which employs density functional theory and the Bethe–Salpeter equation (DFT+BSE). The DFT+BSE approach employs DFT using the Quantum ESPRESSO package[26,27] and the existing OCEAN code (Obtaining Core-level Excitations using Ab-initio calculations and the NIST BSE solver).[28–30]

In practice, we first calculate the band structure of Fe_2SiO_4 using DFT. Then, the BSE is solved to obtain the core–valence exciton wave functions and the XUV spectra can be plotted from the complex dielectric function calculated by OCEAN. For Fe_2SiO_4 the BSE was solved

using a 4 × 6 × 8 k-point mesh and a dielectric constant of 11.0. A 1.0 scaling factor for the Slater G parameter was employed with a 100 Rydberg energy cutoff. A 4.0 Bohr screening radius and a 2 ×2 ×2 screening mesh were applied. Finally, a 0.1 eV broadening was implemented to replicate the linewidth broadening observed in the experiment.

6.4 Results and Discussion

Fayalite belongs to the olivine mineral group, being the end member in a series where x = 2 in the stoichiometry $Mg_{2-x}Fe_xSiO_4$.[31] These olivine minerals are abundant in the earth's crust and have been shown to participate in the silicate-carbonate cycle to sequester CO_2 on geologically-relevant, millennia timescales.[32,33] It has an orthorhombic symmetry, belonging to the *Pnma* space group, as depicted in **Figure 6.1A.** Its UV-Visible reflection spectrum, shown in **Figure 6.1B**, is characterized by a lower energy peak, attributed to dipole forbidden d-d transitions, or MMCT. These d-d transitions are expected to be present in Mott insulators and are not typically observed in charge-transfer insulators. This characterization confirms some of the Mott insulating properties of fayalite. An increase in reflectivity at higher photon energies in the UV-Visible reflection spectrum of Fe_2SiO_4 is characteristic of dipole allowed p-d transitions, denoting LMCT transitions. This UV-Visible reflection spectrum agrees with the DFT predicted band structure and atom-projected density of states shown in **Figure 6.1C** and **D**. The Mott insulating nature of the material results in a VBM and CMB dominated by Fe 3d orbital character (**Fig. 6.1D**).

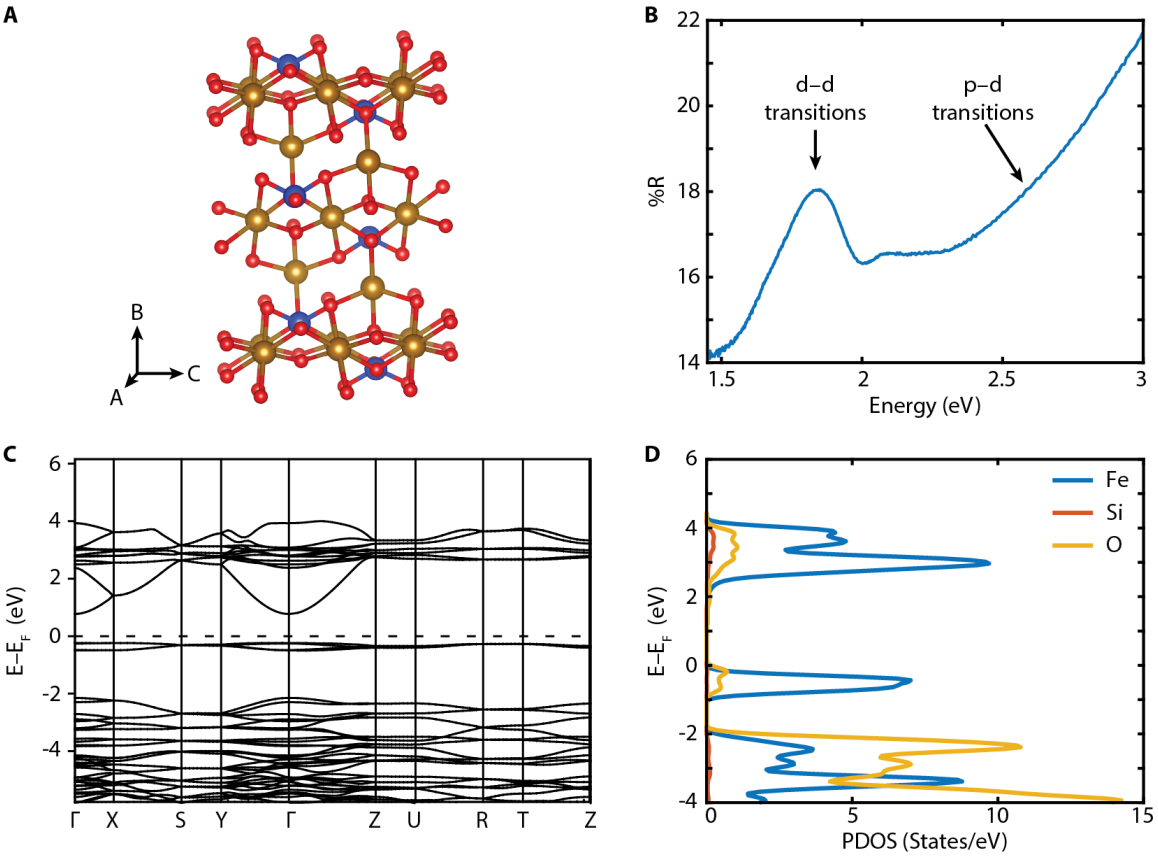

Figure 6.1 Fayalite crystal structure, UV-Visible reflection spectrum, DFT calculated band structure for fayalite, and atom-projected density of states. **(A)** The olivine phase of fayalite crystallizes in an orthorhombic crystal structure. **(B)** UV-Visible reflection spectrum of fayalite where the initial increase in reflectivity is attributed to dipole forbidden d-d transitions, appearing at ~1.75 eV, and is followed by dipole allowed p-d transitions more characteristic of an insulator. **(C)** DFT calculated band structure for fayalite, no Hubbard U value was applied in this calculation. **(D)** Atom-projected density of states, where the lower and upper Hubbard bands from Fe 3d orbitals can be seen centered around the fermi level, and lower energy valence bands have O 2p character.

Transient XUV reflection-absorption spectroscopy measures the photoexcited polaron formation dynamics of Fe_2SiO_4 following photoexcitation with a 3.1 eV (400 nm) pump beam. Measurements result in surface sensitive spectra, with a probe penetration depth of ~2 nm. The differential reflection-absorption following photoexcitation is defined as $\Delta OD = -\log_{10}(I_{pump\ on}/I_{pump\ off})$.

Figure 6.2A shows a representative transient spectrum of Fe_2SiO_4 measured at the Fe $M_{2,3}$ X-ray edge at ~54 eV, probing 3p to 3d transitions. Immediately following photoexcitation, there is an increase in absorption at ~53.0 – 54.0 eV (**Fig. 6.2A**, red feature) and a

neighboring decrease in absorption from ~54.0 – 55.8 eV (**Fig. 6.2A**, blue feature). The transient features experience a blue shift that begins immediately after photoexcitation, and this spectral shift is complete after ~200 fs. **Figure 6.2B** demonstrates lineouts from the transient spectra immediately following photoexcitation (blue) and 1 ps after photoexcitation (green) when the spectral shift is complete. We attribute the blue lineout in **Figure 6.2B** to the charge transfer state immediately following photoexcitation, as a range of XUV experiments at the Fe $M_{2,3}$ edge support this assignment.[15–18,34,35] However, excited-state DFT+BSE theory is necessary to confirm these states. We assign the green lineout in **Figure 6.2B** to the photoexcited polaron state, as is indicated in literature. A fitting of the spectral blueshift associated with the polaron formation (**Fig. 6.2C**) results in a shift with a magnitude of 460 ± 90 meV and a time constant of 130 ± 40 fs.

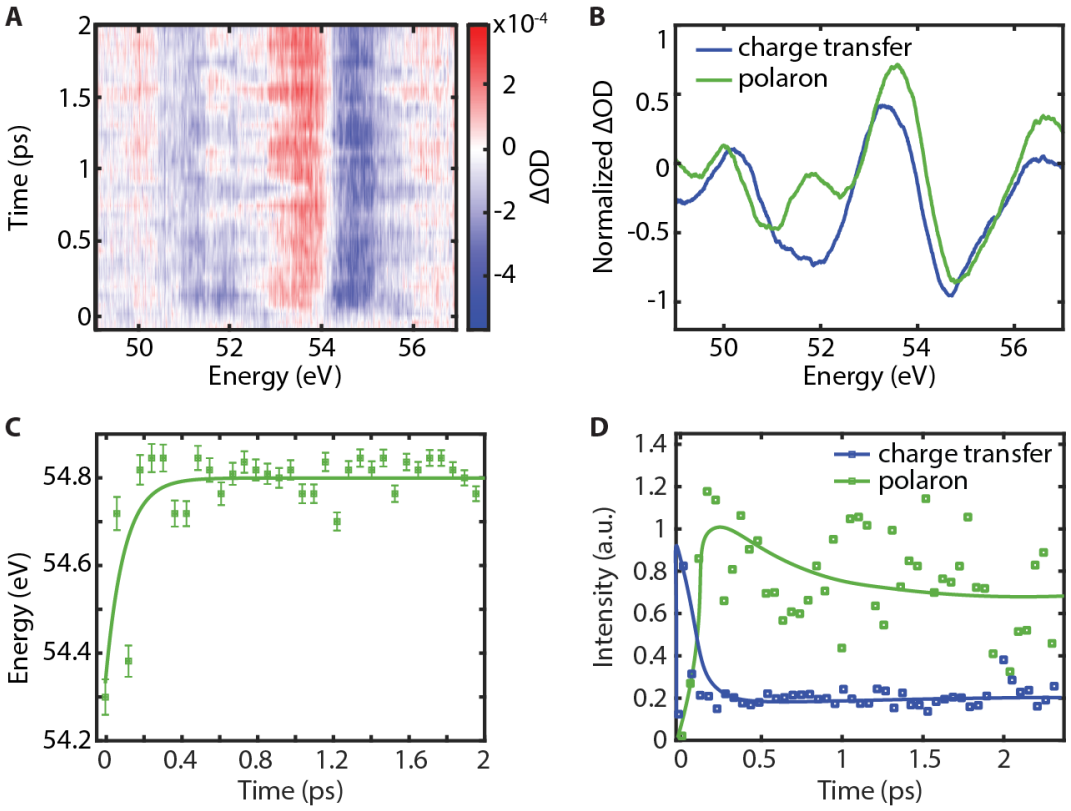

Figure 6.2 Representative transient XUV spectrum at the Fe M2,3 edge centered at ~54 eV **(A)**. Spectral lineouts 30 fs (blue) and 1 ps (green) after photoexcitation with a 400 nm pump **(B)**, where the lineout at 30 fs is attributed to the charge transfer state and the lineout at 1 ps is attributed to the polaron state. A fitting of the spectra blueshift at the Fe $M_{2,3}$ edge **(C)**, taken by averaging the signal at the blue feature in **(A)** from ~54.0 – 55.0 eV, reveals that polaron formation occurs with a time constant of 130 ± 40 fs. Singular value decomposition

(D) of the charge transfer (blue) and polaron (green) states from **(B)** where the charge transfer state begins to transition to the polaron state within 10s of fs.

We further conduct singular value decomposition (SVD) to extract the contributions of the charge transfer and polaronic states to the spectrum at different timepoints. **Figure 6.2D** shows the SVD of the Fe_2SiO_4 spectrum and demonstrates a transition from the charge transfer state to the polaron state that occurs in 10s of fs.

Figure 6.3 shows preliminary DFT+BSE theory of the ground-state Fe $M_{2,3}$ edge spectrum of Fe_2SiO_4 (blue line), in moderate agreement with the experimentally measured ground state XUV absorption. The higher energy feature above the edge is not as well described by theory, and further development, through tuning of on-site repulsions and the Hubbard U parameter may be necessary to fully describe the ground state spectrum.

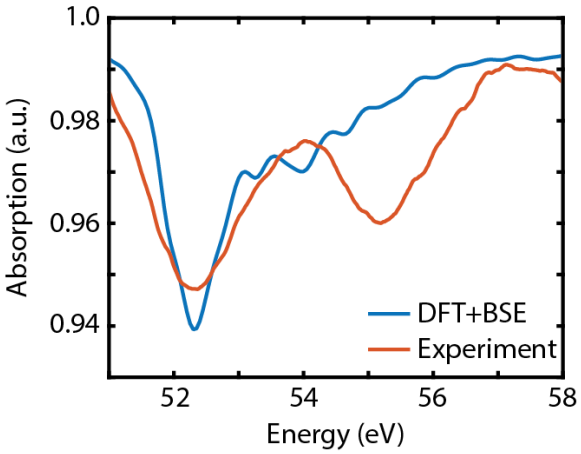

Figure 6.3 Preliminary DFT+BSE theory of the ground state reflectivity of Fe_2SiO_4 at the Fe $M_{2,3}$ edge.

Additionally, excited-state DFT+BSE theory is merited in the case of Fe_2SiO_4 to model not only state-filling dynamics associated with an above band gap excitation, but also the character of the spectral shift. While much XUV literature that suggests the spectral shift to higher energy is associated with a polaron, the exact character of the polaron remains unclear.[12,14,15] As discussed in **Chapter 5** of this thesis, in the case of MMCT, hole polarons may also form on Fe centers, and may not necessarily be spectrally distinct from electron polarons on iron centers.[16] DFT+BSE modeling of both hole and electron polarons in fayalite

following photoexcited polaron formation is merited here to deconvolve the excited state dynamics observed in these experiments.

6.5 Conclusion

In this work, we measured the photoexcited dynamics of Mott insulator fayalite using transient XUV spectroscopy at the Fe $M_{2,3}$ edge. Following 400 nm above band gap photoexcitation, we observe a spectral shift to higher energy, characteristic of photoexcited polaron formation in other iron oxide systems. Having MMCT and LMCT excitation manifolds accessible suggests that electron and hole polarons may form at Fe sites. While these measurements, in the context of the other studies in this thesis, support assignment of the spectral blueshift to photoexcited polaron formation, additional excited-state DFT+BSE calculations are required to fully assign the physical phenomena occurring. Overall, this study demonstrates that fayalite is an important comparison between charge-transfer, intermediate, and Mott insulating iron oxides and provides new insight into how strong electronic correlations govern carrier localization.

6.6 References

(1) Milloch, A.; Fabrizio, M.; Giannetti, C. Mott Materials: Unsuccessful Metals with a Bright Future. *Npj Spintron.* **2024**, *2* (1), 49. https://doi.org/10.1038/s44306-024-00047-y.

(2) Lu, L.; Song, M.; Liu, W.; Reyes, A. P.; Kuhns, P.; Lee, H. O.; Fisher, I. R.; Mitrović, V. F. Magnetism and Local Symmetry Breaking in a Mott Insulator with Strong Spin Orbit Interactions. *Nat. Commun.* **2017**, *8* (1), 14407. https://doi.org/10.1038/ncomms14407.

(3) Phillips, P. W.; Yeo, L.; Huang, E. W. Exact Theory for Superconductivity in a Doped Mott Insulator. *Nat. Phys.* **2020**, *16* (12), 1175–1180. https://doi.org/10.1038/s41567-020-0988-4.

(4) Mott, N. F. Metal-Insulator Transition. *Rev. Mod. Phys.* **1968**, *40* (4), 677–683. https://doi.org/10.1103/RevModPhys.40.677.

(5) Laad, M. S.; Craco, L. Mott Transitions: A Brief Review. *Adv. Quantum Technol.* **2024**, *7* (12), 2200186. https://doi.org/10.1002/qute.202200186.

(6) Colussi, V. E.; Caleffi, F.; Menotti, C.; Recati, A. Lattice Polarons across the Superfluid to Mott Insulator Transition. *Phys. Rev. Lett.* **2023**, *130* (17), 173002. https://doi.org/10.1103/PhysRevLett.130.173002.

(7) Wohlfeld, K.; Daghofer, M.; Oleś, A. M.; Horsch, P. Spectral Properties of Orbital Polarons in Mott Insulators. *Phys. Rev. B* **2008**, *78* (21), 214423. https://doi.org/10.1103/PhysRevB.78.214423.

(8) Koepsell, J.; Bourgund, D.; Sompet, P.; Hirthe, S.; Bohrdt, A.; Wang, Y.; Grusdt, F.; Demler, E.; Salomon, G.; Gross, C.; Bloch, I. Microscopic Evolution of Doped Mott Insulators from Polaronic Metal to Fermi Liquid. *Science* **2021**, *374* (6563), 82–86. https://doi.org/10.1126/science.abe7165.

(9) Seifert, U. F. P.; Balents, L. Spin Polarons and Ferromagnetism in Doped Dilute Moiré-Mott Insulators. *Phys. Rev. Lett.* **2024**, *132* (4), 046501. https://doi.org/10.1103/PhysRevLett.132.046501.

(10) Kim, J. H.; Schönhoff, G.; Lorke, M.; et al. Ultrafast reversible phase engineering in $MoTe_2$ thin film via polaron formation. *J. Korean Phys. Soc.* **2024**, *84*, 907–913. https://doi.org/10.1007/s40042-024-01077-9.

(11) Miyamoto, T.; Matsui, Y.; Terashige, T.; Morimoto, T.; Sono, N.; Yada, H.; Ishihara, S.; Watanabe, Y.; Adachi, S.; Ito, T.; Oka, K.; Sawa, A.; Okamoto, H. Probing Ultrafast Spin-Relaxation and Precession Dynamics in a Cuprate Mott Insulator with Seven-Femtosecond Optical Pulses. *Nat. Commun.* **2018**, *9* (1), 3948. https://doi.org/10.1038/s41467-018-06312-z.

(12) Bandaranayake, S.; Hruska, E.; Londo, S.; Biswas, S.; Baker, L. R. Small Polarons and Surface Defects in Metal Oxide Photocatalysts Studied Using XUV Reflection–Absorption Spectroscopy. *J. Phys. Chem. C* **2020**, *124* (42), 22853–22870. https://doi.org/10.1021/acs.jpcc.0c07047.

(13) Biswas, S.; Wallentine, S.; Bandaranayake, S.; Baker, L. R. Controlling Polaron Formation at Hematite Surfaces by Molecular Functionalization Probed by XUV Reflection-Absorption Spectroscopy. *J. Chem. Phys.* **2019**, *151* (10), 104701. https://doi.org/10.1063/1.5115163.

(14) Klein, I. M.; Liu, H.; Nimlos, D.; Krotz, A.; Cushing, S. K. Ab Initio Prediction of Excited-State and Polaron Effects in Transient XUV Measurements of α-Fe_2O_3. *J. Am. Chem. Soc.* **2022**, *144* (28), 12834–12841. https://doi.org/10.1021/jacs.2c03994.

(15) Kim, Y.-J.; Mendes, J. L.; Michelsen, J. M.; Shin, H. J.; Lee, N.; Choi, Y. J.; Cushing, S. K. Coherent Charge Hopping Suppresses Photoexcited Small Polarons in $ErFeO_3$ by Antiadiabatic Formation Mechanism. *Sci. Adv.* **2024**, *10* (12), eadk4282. https://doi.org/10.1126/sciadv.adk4282.

(16) Mendes, J. L.; Shin, H. J.; Seo, J. Y.; Lee, N.; Choi, Y. J.; Varley, J. B.; Cushing, S. K. Dynamic Competition between Hubbard and Superexchange Interactions Selectively Localizes Electrons and Holes through Polarons. *J. Am. Chem. Soc.* **2025**. https://doi.org/10.1021/jacs.4c16837.

(17)Carneiro, L. M.; Cushing, S. K.; Liu, C.; Su, Y.; Yang, P.; Alivisatos, A. P.; Leone, S. R. Excitation-Wavelength-Dependent Small Polaron Trapping of Photoexcited Carriers in α-Fe_2O_3. *Nat. Mater.* **2017**, *16* (8), 819–825. https://doi.org/10.1038/nmat4936.

(18) Mendes, J. L.; Bhattacharyya, S.; Huang, C.; Michelsen, J. M.; Klein, I. M.; Babbe, F.; Sayer, T.; Li, T.; Cooper, J. K.; Liu, H.; Ginsberg, N. S.; Montoya-Castillo, A.; Cushing, S. K. Coherent and Dynamic Small Polaron Delocalization in $CuFeO_2$. *J. Phys. Chem. Lett.* **2026**, *17* (2), 656–664. https://doi.org/10.1021/acs.jpclett.5c03430.

(19) Jiang, X.; Guo, G. Y. Electronic Structure, Magnetism, and Optical Properties of Fe_2SiO_4 Fayalite at Ambient and High Pressures: A GGA + U Study. *Phys. Rev. B* **2004**, *69* (15), 155108. https://doi.org/10.1103/PhysRevB.69.155108.

(20) Xiong, W.; Giammar, D. Forsterite Carbonation in Zones with Transport Limited by Diffusion. *Environ. Sci. Technol. Lett.* **2014**, *1* (8), 333–338. https://doi.org/10.1021/ez500182s.

(21) Husek, J.; Cirri, A.; Biswas, S.; Baker, L. R. Surface Electron Dynamics in Hematite (α-Fe_2O_3): Correlation between Ultrafast Surface Electron Trapping and Small Polaron Formation. *Chem. Sci.* **2017**, *8* (12), 8170–8178. https://doi.org/10.1039/C7SC02826A.

(22) Liu, H.; Michelsen, J. M.; Mendes, J. L.; Klein, I. M.; Bauers, S. R.; Evans, J. M.; Zakutayev, A.; Cushing, S. K. Measuring Photoexcited Electron and Hole Dynamics in ZnTe and Modeling Excited State Core-Valence Effects in Transient Extreme Ultraviolet Reflection Spectroscopy. *J. Phys. Chem. Lett.* **2023**, 2106–2111. https://doi.org/10.1021/acs.jpclett.2c03894.

(23) Géneaux, R.; Chang, H.-T.; Schwartzberg, A. M.; Marroux, H. J. B. Source Noise Suppression in Attosecond Transient Absorption Spectroscopy by Edge-Pixel Referencing. *Opt. Express* **2021**, *29* (2), 951. https://doi.org/10.1364/OE.412117.

(24) Codling, K.; Madden, R. P.; Ederer, D. L. Resonances in the Photo-Ionization Continuum of Ne I (20-150 eV). *Phys. Rev.* **1967**, *155* (1), 26–37. https://doi.org/10.1103/PhysRev.155.26.

(25) Perdew, J. P.; Burke, K.; Ernzerhof, M. Generalized Gradient Approximation Made Simple. *Phys. Rev. Lett.* **1996**, *77* (18), 3865–3868. https://doi.org/10.1103/PhysRevLett.77.3865.

(26) Giannozzi, P.; Baroni, S.; Bonini, N.; Calandra, M.; Car, R.; Cavazzoni, C.; Ceresoli, D.; Chiarotti, G. L.; Cococcioni, M.; Dabo, I.; Corso, A. D.; Gironcoli, S. de; Fabris, S.; Fratesi, G.; Gebauer, R.; Gerstmann, U.; Gougoussis, C.; Kokalj, A.; Lazzeri, M.; Martin-Samos, L.; Marzari, N.; Mauri, F.; Mazzarello, R.; Paolini, S.; Pasquarello, A.; Paulatto, L.; Sbraccia, C.; Scandolo, S.; Sclauzero, G.; Seitsonen, A. P.; Smogunov, A.; Umari, P.; Wentzcovitch, R. M. QUANTUM ESPRESSO: A Modular and Open-Source Software Project for Quantum Simulations of Materials. *J. Phys. Condens. Matter* **2009**, *21* (39), 395502. https://doi.org/10.1088/0953-8984/21/39/395502.

(27) Giannozzi, P.; Andreussi, O.; Brumme, T.; Bunau, O.; Buongiorno Nardelli, M.; Calandra, M.; Car, R.; Cavazzoni, C.; Ceresoli, D.; Cococcioni, M.; Colonna, N.; Carnimeo, I.; Dal Corso, A.; de Gironcoli, S.; Delugas, P.; DiStasio, R. A.; Ferretti, A.; Floris, A.; Fratesi, G.; Fugallo, G.; Gebauer, R.; Gerstmann, U.; Giustino, F.; Gorni, T.; Jia, J.; Kawamura, M.; Ko, H.-Y.; Kokalj, A.; Küçükbenli, E.; Lazzeri, M.; Marsili, M.; Marzari, N.; Mauri, F.; Nguyen, N. L.; Nguyen, H.-V.; Otero-de-la-Roza, A.; Paulatto, L.; Poncé, S.; Rocca, D.; Sabatini, R.; Santra, B.; Schlipf, M.; Seitsonen, A. P.; Smogunov, A.; Timrov, I.; Thonhauser, T.; Umari, P.; Vast, N.; Wu, X.; Baroni, S. Advanced Capabilities for Materials Modelling with Quantum ESPRESSO. *J. Phys. Condens. Matter* **2017**, *29* (46), 465901. https://doi.org/10.1088/1361-648X/aa8f79.

(28) Vinson, J. Advances in the OCEAN-3 Spectroscopy Package. *Phys. Chem. Chem. Phys.* **2022**, *24* (21), 12787–12803. https://doi.org/10.1039/D2CP01030E.

(29) Vinson, J.; Rehr, J. J.; Kas, J. J.; Shirley, E. L. Bethe-Salpeter Equation Calculations of Core Excitation Spectra. *Phys. Rev. B* **2011**, *83* (11), 115106. https://doi.org/10.1103/PhysRevB.83.115106.

(30) Gilmore, K.; Vinson, J.; Shirley, E. L.; Prendergast, D.; Pemmaraju, C. D.; Kas, J. J.; Vila, F. D.; Rehr, J. J. Efficient Implementation of Core-Excitation Bethe–Salpeter Equation Calculations. *Comput. Phys. Commun.* **2015**, *197*, 109–117. https://doi.org/10.1016/j.cpc.2015.08.014.

(31) Akimoto, S.-I.; Fujisawa, H. Demonstration of the Electrical Conductivity Jump Produced by the Olivine-Spinel Transition. *J. Geophys. Res. 1896-1977* **1965**, *70* (2), 443–449. https://doi.org/10.1029/JZ070i002p00443.

(32) Bremen, A. M.; Ploch, T.; Mhamdi, A.; Mitsos, A. A Mechanistic Model of Direct Forsterite Carbonation. *Chem. Eng. J.* **2021**, *404*, 126480. https://doi.org/10.1016/j.cej.2020.126480.

(33) Grayevsky, R.; Reiss, A. G.; Emmanuel, S. Carbon Storage through Rapid Conversion of Forsterite into Solid Oxalate Phases. *Energy Fuels* **2023**, *37* (1), 509–517. https://doi.org/10.1021/acs.energyfuels.2c03245.

(34) Bandaranayake, S.; Hruska, E.; Londo, S.; Biswas, S.; Baker, L. R. Small Polarons and Surface Defects in Metal Oxide Photocatalysts Studied Using XUV Reflection–Absorption Spectroscopy. *J. Phys. Chem. C* **2020**, *124* (42), 22853–22870. https://doi.org/10.1021/acs.jpcc.0c07047.

(35) Biswas, S.; Wallentine, S.; Bandaranayake, S.; Baker, L. R. Controlling Polaron Formation at Hematite Surfaces by Molecular Functionalization Probed by XUV Reflection-Absorption Spectroscopy. *J. Chem. Phys.* **2019**, *151* (10), 104701. https://doi.org/10.1063/1.5115163.

Chapter 7

EXPERIMENTALLY MAPPING THE PHASE DIAGRAMS OF PHOTOEXCITED SMALL POLARONS

7.1 Abstract

Understanding the fundamental properties that dictate photoexcited polarons in materials is critical to tuning their properties. Theoretical models of polarons have only recently been extended to the excited state. Experimental measurements of polaron formation and transport have been widely undertaken across a range of materials, from photocatalysts and superconductors to soft conducting polymers. Here, we map quasi-equilibrated excited state experimental measurements of quantities such as polaron strength onto phase diagrams of the Holstein, Hubbard–Holstein, and t-J–Holstein models. This work demonstrates that tuning electron–phonon coupling strength, electron localization, and spin exchange can be leveraged to suppress or control polarons in transition metal oxides. We find that the t-J–Holstein model best describes the measured iron oxides and could be generally applied to a wide range of systems that exhibit polaron formation in the excited state. This work combines experimental data with ground state models to provide a robust parameter space for informing photoexcited polaron design.

7.2 Introduction

Polarons dominate material physics, ranging from solar energy materials,[1] O-LEDs,[2] organic semiconductors,[3] conducting polymers,[4] and even superconductors.[5] A polaron is the localization of a charge carrier due to coupling with local lattice deformations. The extent of the charge carrier's localization results in a distinction between small and large polarons, but this definition is often ambiguous.[6] It is generally accepted that a small polaron is localized to a unit cell or less in a strong coupling perturbation limit, while large polarons span multiple unit cells; however, the crossover between small and large polarons is an active area of study.[6,7] Extensive work has been undertaken both experimentally and computationally to understand and model polaronic behavior in emergent materials, ranging from scanning

probe microscopy and core-level spectroscopies to numerical solutions of the Holstein model, which describes polaronic mobility.[8–12] Small polarons have been measured and theoretically described in the ground state for decades.[13–16] Here, we focus on understanding the fundamental properties of *photoexcited* polarons in solid-state materials, an area that remains less understood, despite a range of measurements of individual systems.

Photoexcited polarons form when a charge transfer transition redistributes the charge density between two local orbitals and the carriers couple to lattice vibrations. For example, in a transition metal oxide that is a charge transfer insulator, photoexcitation transfers an electron from a dispersive O 2p orbital to a localized transition metal d-orbital. Usually, during the photoexcited carrier thermalization time, the polarizable lattice of the transition-metal oxide locally distorts, trapping the charge carrier. This has been widely studied in the candidate photoelectrode hematite (α-Fe_2O_3), showing that small-polaron formation occurs within <100 fs during the first electron–optical-phonon scattering event.[10,17,18] It has been further demonstrated that though these polarons form within the first electron–optical-phonon scattering event, the resulting localized polaronic state dominates carrier transport and persists up to carrier recombination and relaxation.[17] Polaron localization reduces carrier mobility and photoconversion efficiency, limiting the solar energy and fuel applications of hematite despite its otherwise favorable energetic properties.

Since initial measurements on α-Fe_2O_3, a wide range of transition metal oxides have been measured to modify, understand, and suppress small polaron formation in strongly polar semiconductors.[17–21] Altering the nature of the local lattice, the metal center, surface functionalization, and spin correlations has reduced the strength and even suppressed small polarons in this class of materials. However, succinct design rules that can be used to predict new materials or extend ground state small polaron properties to the excited state have yet to be realized.

Here, we map a range of experimental photoexcited small polaron measurements in transition metal oxides onto three ground-state models: the Holstein, Hubbard–Holstein, and t-J–Holstein Hamiltonians. The resulting phase diagrams are constructed using ultrafast X-ray

spectroscopy techniques that measure polaron and phonon energies which can be used to approximate the polaron binding energy and electron–phonon coupling strength, supplemented by experimentally derived exchange energies per spin in literature. We focus particularly on iron oxide systems to standardize metal centers for comparison of the results. Additionally, we consider only measurements of electron polarons on metal centers within these transition metal oxides, due largely to the fact that more X-ray spectroscopy-based measurements of electron polarons exist in literature. While hole polarons are likely also forming on ligand sites during the photoexcited polaron formation process in these materials, it is challenging to measure both simultaneously. We demonstrate that commonly employed scaling factors for polaron mobility and strength remain valid in the quasi-equilibrated excited state employed here and can be derived from ground state parameters. The Holstein model effectively maps long-lived excited state dynamics onto the small-to-large polaron transition but provides limited insight beyond the role of the electron–phonon coupling strength. The Hubbard–Holstein model accounts for on-site repulsion (U) and well describes the small-to-large polaron transition, but it predicts bipolaron regimes that are rarely observed experimentally in the systems considered here. The t-J–Holstein model, related to the Hubbard–Holstein model in the strong coupling limit, provides the most insight by accurately describing when superexchange competes with electron–phonon coupling to reduce polaron localization in the excited state. These findings highlight that on-site electron-spin correlations are critical design parameters for controlling polarons in the photoexcited state. The resulting phase diagram parameterizations provide an applicable quasi-equilibrium excited-state descriptor not only for solid-state systems but also molecular semiconductors,[22] and therefore we expect it to find wide use across solar energy materials,[23] soft conducting polymers,[24] and even insight into correlated quantum phases like superconductors.[25,26]

7.3 Theory

In the ground state, polarons at their simplest can be described by the Holstein Hamiltonian:[7,27]

$$H = -t\sum_{\langle ij\rangle\sigma}(c_{i\sigma}^{\dagger}c_{j\sigma} + c_{j\sigma}^{\dagger}c_{i\sigma}) + \omega_0\sum_i b_i^{\dagger}b_i + g\sum_{i,\sigma} n_{i\sigma}(b_i + b_i^{\dagger}) \quad \textbf{(7.1)}$$

where t is the hopping integral, $c_{i\sigma}^{\dagger}$and $c_{j\sigma}$ are the creation and annihilation operators, respectively, with spin, σ, for an electron at sites *i* and *j*. *U* is the on-site Coulombic repulsion, n_i is the number operator for electron spin, g corresponds to the electron–phonon coupling strength, and ω_0 refers to the phonon frequency. $b_i^{\dagger}$ and b_i are the creation and annihilation operators, respectively, for phonons at site *i*.

The Holstein Hamiltonian, while insightful regarding the balance of electron–phonon coupling strengths, phonon frequency, and hopping integral, does not sufficiently capture the physics of complex transition-metal oxides. A Hubbard *U* term can be added to the Holstein model to accurately describe strong on-site repulsions of the d orbitals, particularly at half-filling, as is the case for most of the Fe(III) oxides considered in this work.[28,29] The ratio of the charge hopping integral, *t,* to *U* influences the orbital mixing within the band structure. It determines whether the material is a charge transfer insulator or a Mott insulator.[30] In a charge transfer insulator, the upper valence bands (VBs) are dominated by ligand orbitals, and metal d orbitals dominate the lower conduction bands (CBs). In a Mott insulator, the upper VBs and lower CBs are dominated by metal d orbitals due to the emergence of the Hubbard *d* band. *U* contributes to carrier localization and thus modulates polaron formation. A representative Hubbard–Holstein Hamiltonian can be written as:

$$H = -t\sum_{\langle ij\rangle\sigma}(c_{i\sigma}^{\dagger}c_{j\sigma} + c_{j\sigma}^{\dagger}c_{i\sigma}) + U\sum_i n_{i\uparrow}n_{i\downarrow} + \omega_0\sum_i b_i^{\dagger}b_i + g\sum_{i,\sigma} n_{i\sigma}(b_i + b_i^{\dagger}) \quad \textbf{(7.2)}$$

This Hamiltonian can be further downfolded into a t-J–Holstein model in the limit $U >> t$, which holds for the measured transition metal oxides in this work.[31,32] This downfold

includes the spin-exchange integral (J) and, for antiferromagnetic (AFM) materials, describes superexchange in which a spin can undergo indirect exchange mediated by a ligand between two metal sites. AFM superexchange is favored when metal-ligand-metal bond angles are close to 180° and scales with the bond distance and bond angles, as described by Goodenough-Kanamori rules.[33–35] At half-filling, $J = 4t^2/U$. If $t + J >> g$, then no polaron forms, and photoexcited carriers thermalize to the band edge. If $t + J << g$, a polaron forms – often without significant thermalization following photoexcitation. As J, t, and U are all interrelated, modifying one through materials design will modify the others, and thus a balance must be struck between the parameters when considering materials design that aims to tune polarons. The downfolded t-J–Holstein Hamiltonian can be written as:

$$H = -t\sum_{\langle ij\rangle\sigma}(c_{i\sigma}^{\dagger}c_{j\sigma} + c_{j\sigma}^{\dagger}c_{i\sigma}) + J\sum_{ij}\vec{S_i}\cdot\vec{S_j} + \omega_0\sum_i b_i^{\dagger}b_i + g\sum_{i,\sigma} n_{i\sigma}\left(b_i + b_i^{\dagger}\right) \quad \textbf{(7.3)}$$

Each Hamiltonian outlined above describes different polaronic coupling regimes and models polaronic properties accordingly. The consideration of on-site repulsions and spin exchange in the Hubbard–Holstein and t-J–Holstein models, respectively, increases the complexity of each model Hamiltonian, but also acts to more accurately predict the polaronic properties of strongly electron- and spin-correlated materials.

7.4 Polaron Parameterization from Experimental Measurements

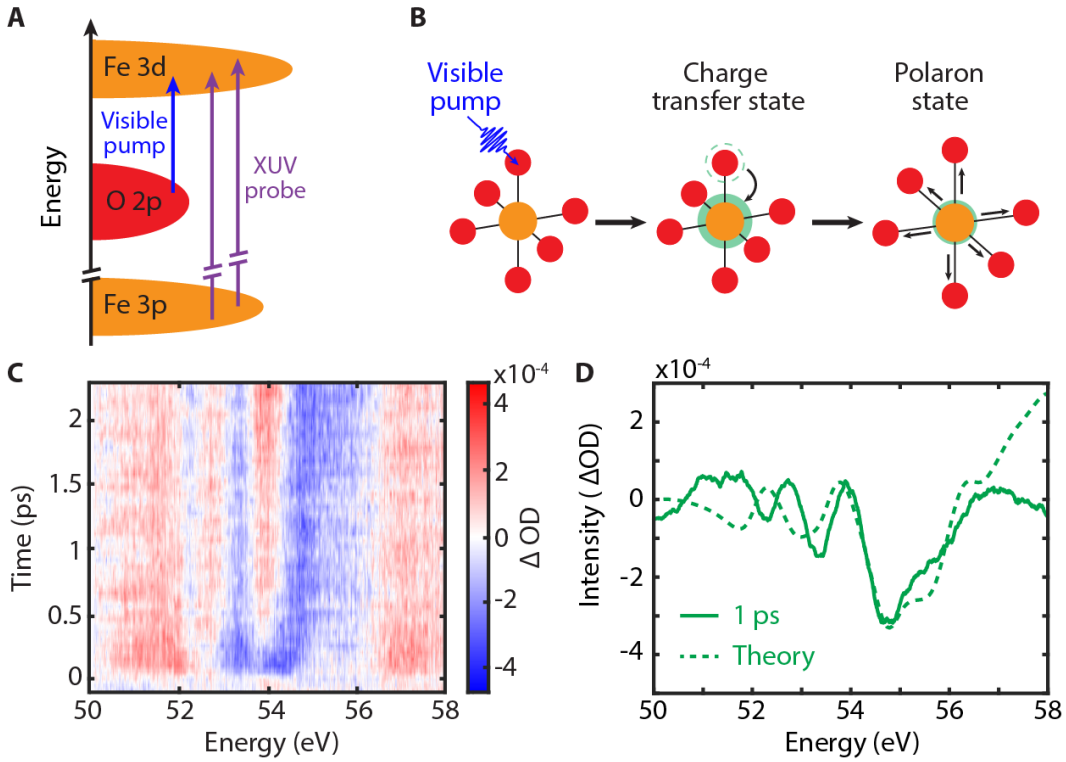

Figure 7.1 Transient XUV spectroscopy probes Fe $M_{2,3}$ edge to measure polaron formation. **(A)** Schematic representation of the 3p to 3d core-valence transition being probed during a transient XUV experiment following an above band gap photoexcitation. **(B)** Diagram of the carrier localization and structural distortion caused by photoexcited small electron polaron formation where photoexcitation typically induces ligand-to-metal charge transfer (LMCT). The excited electron density (green) on the metal sites couples to a lattice mode that locally expands the FeO_6 octahedron and further localizes the carriers. **(C)** Representative transient XUV reflectivity spectra at the Fe $M_{2,3}$ edge in $GdFeO_3$ centered at ~54 eV. At pump-probe overlap (t_0), a series of positive and negative peaks are observed. Immediately after photoexcitation with an 800 nm pump, an ultrafast spectral blueshift is observed around ~55 eV, which is attributed to octahedra expansion and small polaron formation. **(D)** Representative experimental lineout after polaron formation is complete (1 ps) compared with DFT+BSE calculated polaronic spectra.

While these models, especially the Holstein model, have been widely applied to ground state polaronic properties, they are rarely compared to excited state polaron dynamics. Extensive nonequilibrium modeling of photoexcited polaron formation and trapping suggest that these equilibrium models are insufficient when considering the ultrafast dynamics within the first electron–phonon scattering event as photoexcited charge transfer and polaron formation occurs.[1,36–39] Here, we consider the parameterization of excited-state experiments within the framework of these ground-state model Hamiltonians using thermalized, quasi-equilibrated localized polaronic states. In this regime, the parameterization considers polaron binding

energies following formation. The spectral shifts associated with these binding energies persist for tens to hundreds of picoseconds and do not recover to their ground states within the temporal window of the experiments considered. Therefore, we consider these long-lived spectral shifts to be quasi-equilibrated when considering their role in the photoexcited polaronic dynamics and applicable to the ground-state Hamiltonian framework considered herein.

We employ transient extreme ultraviolet (XUV) reflection-absorption spectroscopy to measure the photoexcited polaron energy and phonon frequency. Transient XUV employs an above band gap pump to photoexcite samples and a core-valence probe that is sensitive to changes in electronic structure, local coordination, and oxidation state. An example of the experimental characterization is shown in **Figure 7.1**.

In the iron oxide systems considered here, a 3p to 3d core-to-valence transition is probed at the Fe $M_{2,3}$ edge. **Figure 7.1A** schematically represents the core-valence transition being probed following above band gap excitation. The resulting transient XUV spectrum is directly sensitive to the changes of the angular momentum coupling, electronic screening, and structural distortions following photoexcitation at the Fe $M_{2,3}$ edge. Upon photoexcitation, electron polarons are formed and localize carriers onto Fe sites and induce anisotropic lattice distortions, expanding Fe–O bond lengths (**Fig. 7.1B**). This reduces the overlap between Fe 3d and O 2p orbitals, further localizing the electron polaron at the Fe site. As a result, a higher energy XUV photon is necessary to induce the Fe 3p to 3d core-valence transition following photoexcitation, which is why a transient blueshift is observed. The magnitude and kinetics of this shift report on the extent and speed of the photoexcited polaron localization (**Fig. 7.1C**).

These spectral shifts dominate the transient spectra out to hundreds of picoseconds to nanoseconds, suggesting that the localized polaronic state dominates these spectra well after initial formation and hot carrier thermalization. The spectral shifts associated with photoexcited polaron formation dominate the spectra such that we can ascribe them to be quasi-equilibrated out to long timescales, as has been demonstrated in perovskite

systems.[40,41]Further, pump-fluence-dependent studies of photoexcited polarons using transient XUV spectroscopy finds that the transient dynamics are independent of fluence, though high excitation densities are typically required in these experiments to resolve signal.[42]

This spectral shift to higher energies has been verified through a range of theoretical predictions of X-ray edges, extending from semi-empirical charge transfer multiplet theory to first-principles density functional theory (DFT) and Bethe-Salpeter equation (BSE) theory.[43–49] In our work, we validate the differential spectrum of the polaron feature using a DFT+BSE calculated X-ray spectrum that accounts for photoexcited carriers and polaronic lattice distortions (**Fig. 7.1D**).[20,48] The spectrum is then decomposed into the appropriate excited states to extract the related kinetics using singular value decomposition (**Fig. 7.2**). Heating effects are deconvolved from the spectra by modeling isotropic lattice expansions associated with lattice heating models and are not found to meaningfully contribute to the measured dynamics out to nanosecond timescales.[20]

We particularly expect electron polaron formation in charge transfer insulating iron oxides, which have conduction bands dominated by iron *d* orbitals. An above band gap excitation would thus induce a ligand-to-metal charge transfer (LMCT) from ligand dominated valence bands to metal dominated conduction bands, forming electron polarons on metal sites and hole polarons on ligand sites. Here, we cannot experimentally resolve the O K edge and therefore consider only electron polarons. This polaron formation may differ for intermediate and Mott insulators, which have different accessible excitation manifolds. These intermediate and Mott insulators may have metal-to-metal charge transfer (MMCT) transitions induced by photoexcitation, where electron and hole polarons can both be formed on metal sites.

As shown in **Figure 7.2**, a variety of polaron formation kinetics have been measured using transient XUV spectroscopy. In hematite, polaron formation occurs within the first electron–optical-phonon scattering time of ~100 fs.[50] In $CuFeO_2$, a polaron forms on the same timescale as hematite, but a *c*-axis lattice expansion on a picosecond timescale enables a

delocalization of the initial polaron state.[51] In $ErFeO_3$, coherent charge hopping occurs before dephasing, and polarons are formed on a 2.3 ± 0.3 ps timescale, indicating large-polaron or mixed polaron/free electron conduction behavior.[52] $GdFeO_3$ does not form a polaron under 400 nm photoexcitation of a ligand-to-metal charge transfer (LMCT) that preserves the high-spin ground state. In contrast, 800 nm photoexcitation of a metal-to-metal charge transfer (MMCT) forms polarons in 250 ± 40 fs.[20]

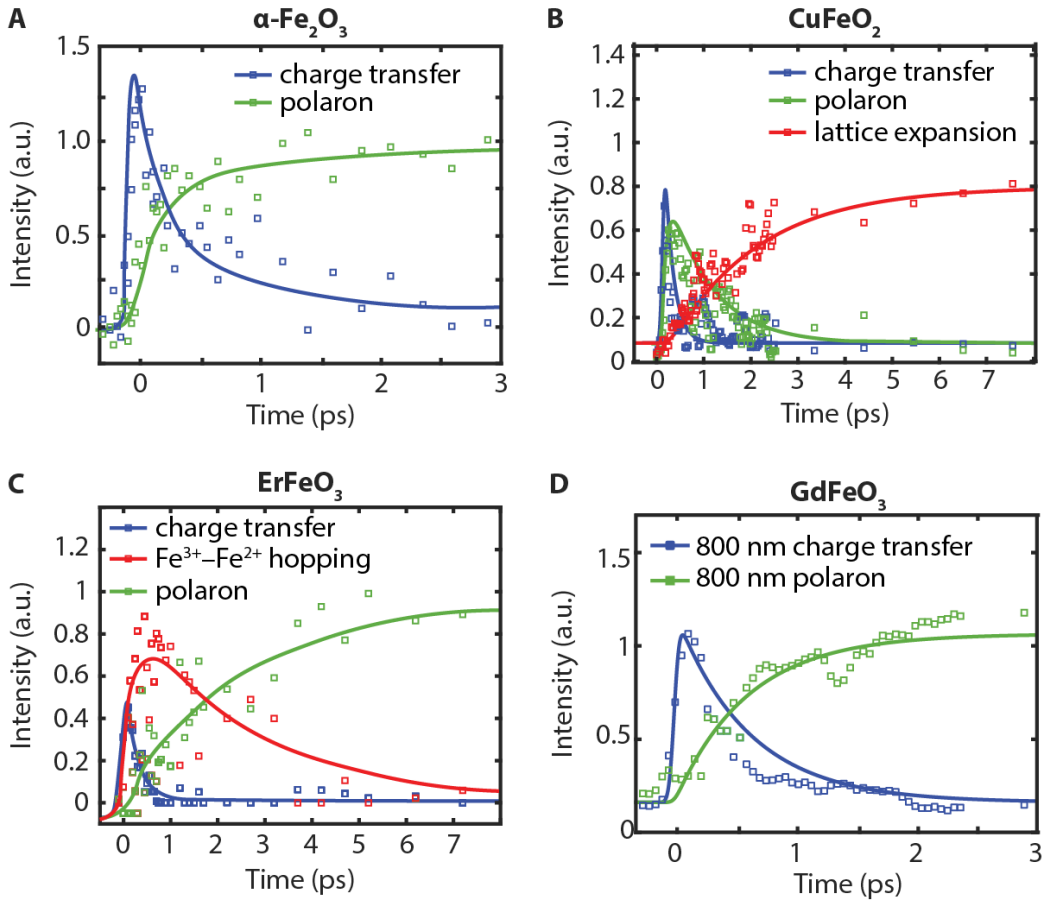

Figure 7.2 Formation timescales and dynamics for polaron-forming Fe-O-based materials. **(A)** Hematite forms a polaron within ~100 fs, leaving few free carriers. **(B)** $CuFeO_2$ forms a polaron within ~100 fs, which relaxes on a picosecond timescale through a *c*-axis expansion and subsequent delocalization. **(C)** $ErFeO_3$ forms a polaron only after a period of Fe^{2+}–Fe^{3+} charge hopping associated with superexchange. **(D)** $GdFeO_3$ only forms a polaron following an 800 nm metal-to-metal charge transfer (MMCT) whereas no polarons form following a 400 nm ligand-to-metal charge transfer due to superexchange mechanisms under different spin configurations.

We have found, consistent with optical reflectivity experiments,[53] that the spectral blueshift of the XUV signal corresponding to polaron formation is approximately twice the polaron binding energy ($E_{polaron}$), to a first order approximation. $E_{polaron}$ is calculated from the

magnitude of the spectral shift at the Fe $M_{2,3}$ edge, and the timescale of this shift measures the phonon energy associated with the polaron formation (ω_0). For most materials, ω_0 is on the order of the highest optical phonon frequency, which is fairly consistent for iron oxide-based materials at 80–100 meV.[54] The polaron energy can be described by **Equation 7.4**:

$$E_{polaron} = -\frac{g^2}{w_0} + t \exp\left(-\frac{g^2}{\omega_0^2}\right) cos(k) + \cdots \qquad (\mathbf{7.4})$$

where *k* is momentum. For the materials measured here, except $ErFeO_3$ which exhibits large-polaron-like behavior, we can truncate the sum of the polaron energy in the first term due to the small electronic bandwidths of the measured iron oxides. Using the parameterization of experimental XUV spectra and the truncation of **Equation 7.4**, we can estimate the electron–phonon coupling parameter, *g*. DFT+U calculations are used to approximate the electronic hopping integral *t*.[55,56] Note that the expression for electronic bandwidth goes as 2*dt* where *d* is the dimensionality, here *d* is taken as three. We employ a ground-state approximation of *t* however we note that during photoexcitation there can be subtle changes that modify *t*, where intuitively it is found that the electron hopping decreases as polaron formation and renormalization occur, due to localization effects.[57] Direct experimental measurements of the renormalization of the electronic hopping integral remain scarce in literature, and excited-state calculations require computationally demanding, method-dependent quantum dynamics methods.[58–60] A Lang-Firsov approach can be used to estimate the effective electronic hopping integral (t_{eff}) following photoexcited polaron formation, however, because we approximate the electronic hopping integral (*t*) from ground-state theory, we consider the undressed hopping integral, rather than direct approximations of the polaronic excited state.[7,61,62]

The measured and calculated parameterization of the scalar quantities of the Holstein, Hubbard–Holstein, and t-J–Holstein models for a range of polaron forming transition metal oxides are given in **Table 7.1**, following the above outlined parameterization.

Table 7.1 Parameters of the Holstein, Hubbard–Holstein, and t-J–Holstein Hamiltonians. All values are in units of eV. *J* is approximated as exchange energy per spin. A detailed discussion of the errors associated with these

parameters can be found in the Supporting Information. "–" denotes no known literature value for one of the necessary parameters.

	$E_{polaron}$	ω_0	$2dt$	J	$g = \sqrt{E_{polaron} * w_0}$	$\lambda = \frac{g^2}{2dt\omega_0}$	$\gamma = \frac{\omega_0}{2dt}$	$g/2dt$	$4/\left(\frac{J}{t}\right) = U/t$
α-Fe_2O_3	0.50 ± 0.05 [50]	0.08 [63]	0.19 [48]	0.0097 ± 0.0031 [64,65]	0.20 ± 0.01	2.63 ± 0.26	1.26	1.05 ± 0.05	13.07 ± 4.18
$CuFeO_2$	0.35 ± 0.05 [51]	0.09 [66]	0.34 [51]	0.025 ± 0.018 [67]	0.18 ± 0.013	1.03 ± 0.15	0.79	0.52 ± 0.04	9.21 ± 6.63
$ErFeO_3$	0.05 ± 0.005 [52]	0.02 [52]	0.91 [52]	0.38 ± 0.16 [68]	0.03 ± 0.002	0.05 ± 0.005	0.07	0.03 ± 0.0015	1.59 ± 0.067
$BiFeO_3$	0.65 ± – [69]	0.07 [69–71]	0.33 [69]	0.176 ± 0.05 [72]	0.21 ± –	1.97 ± –	0.64	0.65 ± –	1.32 ± 0.38
α-FeOOH	0.55 ± – [73]	0.08 [73–75]	0.22 [76]	0.19 ± –[77]	0.21 ± –	2.50 ± –	1.09	0.84 ± –	0.79 ± –
$GdFeO_3$	0.20 ± 0.08 [20]	0.07 [54]	0.13 [20]	0.136 ± 0.04 [78]	0.12 ± 0.02	1.54 ± 0.62	1.62	0.91 ± 0.18	0.68 ± 0.20
a-TiO_2	0.10 ± – [79]	0.11 [80,81]	1.51 [82]	–	0.10 ± –	0.07 ± –	0.21	0.07 ± –	–
$BiVO_4$	0.44 ± – [83]	0.10 [84]	0.79 [85]	–	0.21 ± –	1.86 ± –	0.39	0.27 ± –	–

For some of the systems described in **Table 7.1**, it is important to consider superexchange and the Hubbard interaction. Of the above materials, $GdFeO_3$ is the only material that is not a charge transfer insulator. A charge transfer insulator has a valence band (VB) dominated by O 2p orbitals and a conduction band (CB) primarily composed of Fe 3d orbitals. $GdFeO_3$ is an intermediate insulator, meaning that the VB is composed of mixed Fe and O orbital character, the CB is dominated by Fe d orbitals much like charge transfer insulators. This enables above band gap excitation of both LMCT and MMCT transitions. To determine the magnitude of the exchange integral, J is taken as the exchange energy per spin, which is equivalent to zJ_1S^2 where z is the connectivity, J_1 corresponds to values derived from inelastic neutron scattering (INS) and Raman scattering experiments in literature, and S corresponds

to the spin of the system.[86,87] Further details on the experimentally derived exchange energies and their associated uncertainties can be found in the **Supporting Information**. Superexchange at half-filling goes as $J = 4t^2/U$, so changes to either J or U will modulate polaron formation. U/t is thus $4/(J/t)$ in the strong coupling limit of small polarons.

7.5 Mapping to Phase Diagrams

Here we consider the experimentally derived parameters in terms of the phase diagrams of the Holstein, Hubbard–Holstein, and t-J–Holstein Hamiltonians. These phase diagrams serve to visualize the influence of different parameters on properties such as polaron strength, carrier localization, on-site repulsions, and spin exchange. We map the measured iron oxide materials to identify different material properties that modulate polaronic parameters, thereby informing design rules. We note that these phase diagrams serve as schematic frameworks to visualize the effects of changes to the parameters from the previous section, rather than quantitative predictions of polaronic behavior.

For the Holstein phase diagram, we use two scalar ratios. The first relates to the polaron's strength, $g^2/2dt\omega_0$. The second is $\omega_0/2dt$, which describes the mobility of the polaron via phonons versus free-carrier conduction. Based on **Table 7.1** and the scalar ratios, we construct a phase diagram mapping the measured and derived parameters within the stated approximations in **Figure 7.3**. We consider the atomic limit to be the upper right corner of **Figure 7.3**, where carriers are completely localized. In the bottom left of **Figure 7.3**, photoexcited carriers approach a free carrier limit. We can make a general yet representative cutoff between large and small polarons based on when **Equation 7.4** approaches zero. This is a blurred, approximate transition that is widely debated in the literature, but it is depicted here for simplicity and as a guide to the eye so that the polaron strength can be contextualized in terms of extent of carrier localization.[6,88,89]

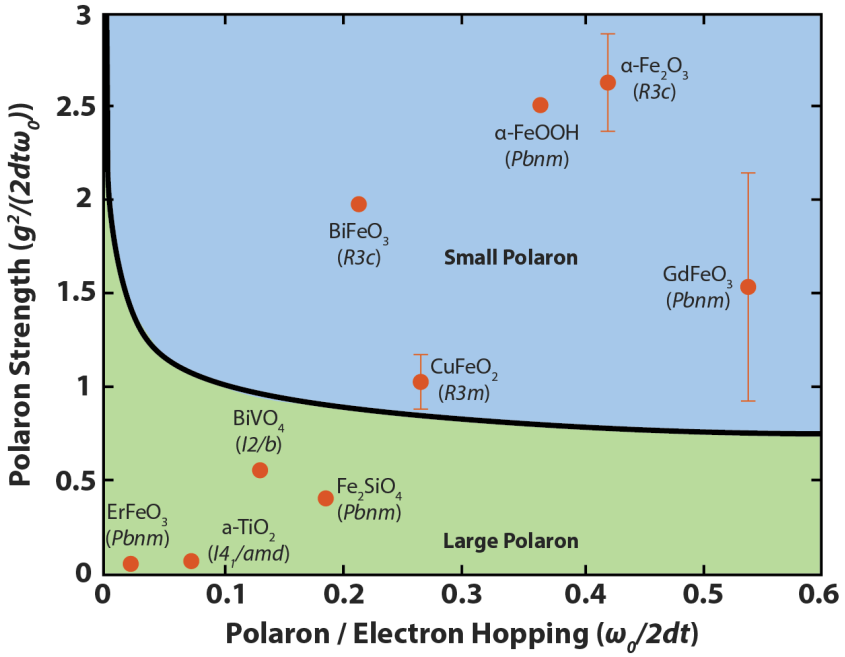

Figure 7.3 Mapping measured polarons onto a Holstein Hamiltonian's phase diagram. Materials and their symmetry group are shown next to the orange dots. The transition between small (blue) and large (green) polarons is schematically denoted by color shading and the solid black line. The upper right corner that we attribute to the atomic limit where carriers are strongly localized depicts a regime where $t << g$, while the lower left corner denotes a free conduction regime in which $t >> g$.

The circles in **Figure 7.3** represent transient XUV data from References [20,50–52,69,73,90] and optical transient absorption spectra for $BiVO_4$.[83] The agreement between measured polaron properties, where the material falls on the phase diagram with respect to the scaling factors, and the small-to-large polaron crossover is found to be qualitatively predictive. For example, α-Fe_2O_3 and α-FeOOH are found to be in the upper right corner near the limit of strong polarons and low mobility, which has been widely experimentally demonstrated.[36,91,92] $CuFeO_2$, which has been found to have a polaron with a weaker binding energy than hematite and goethite due to a coherent c-axis lattice expansion that delocalizes the polaron, falls into the middle of the diagram. $BiVO_4$, which is often debated as having an intermediate-sized polaron, falls on the left boundary close to the crossover between small and large polarons.[93,94] $ErFeO_3$ can be found in the lower left corner because $t >> g$ due to strong superexchange interactions, which result in a strong electron hopping integral (t) and weakened electron–phonon coupling strength (g).[95] Anatase TiO_2, a large polaron material, is also shown for comparison and agrees with the small-to-large polaron crossover depicted

in the phase diagram. It is notable that the Holstein model does not well describe materials in the free-carrier limit as $E_{polaron} \sim 2dt$.[7,12]

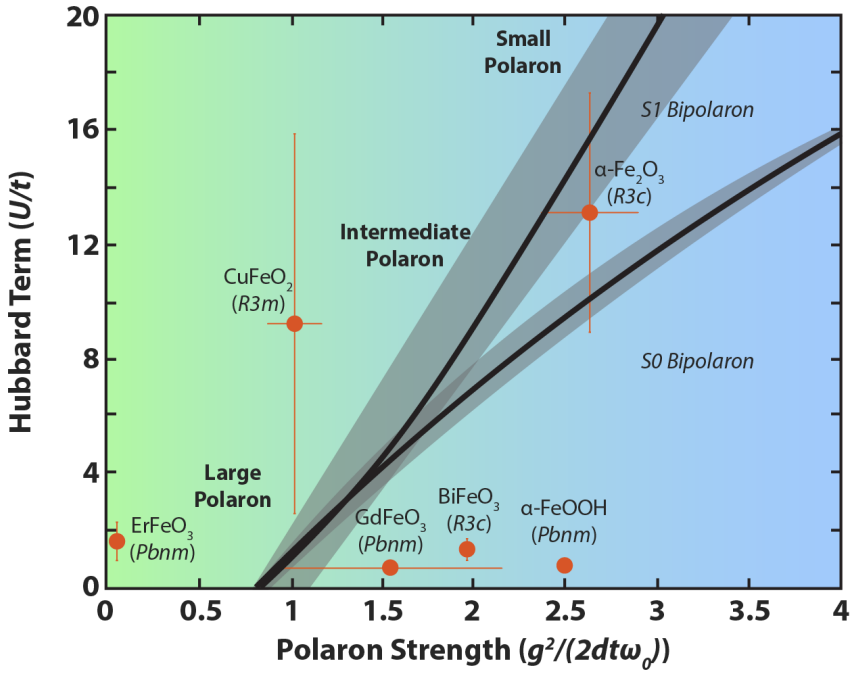

Figure 7.4 Mapping experimentally measured polarons to the diagram of the Hubbard–Holstein model. Small (blue) to large (green) polaron behavior is depicted by the color shading. The black dotted line depicts the boundary between individual polarons and bipolarons. Orange dots depict each measured iron oxide. We do not include the measured materials for which there are no reported *J* values. The S1/S0 regions indicate where the model predicts bipolaron behavior. The lack of measured bipolarons suggests over-localization is predicted within the Hubbard–Holstein model. Adapted from reference [96].

We next increase the complexity of our phase diagram by considering a two-particle Hubbard–Holstein model in **Figure 7.4**. Only materials with a reported *J* value, as given in **Table 7.1**, are shown. We do not consider literature reported *U* values as they vary widely depending on the level of theory and functionals applied. The Hubbard parameter acts in multiple regimes. On the phase diagram, it is plotted on the left-hand side by using the relation $J = 4t^2/U$ where *J* is the exchange energy per spin. We consider the experimentally derived *J* values to be more reliable reporters of exchange and on-site repulsions, as selecting accurate *U* parameters in DFT remains a challenge. We note that this is only a first-order approximation, since the relation between *U* and *J* depend on many-body wave functions. On the x-axis the polaron strength is parameterized the same as the y-axis of the Holstein model. Depending on the ratio of *U* to polaron strength, the Hubbard-Holstein model predicts

a range of large to small polarons in both extended and bipolaron states. For a relatively small electron–phonon coupling strength, the polarons exist independently of each other. Under the strong electron–phonon coupling limit, the U term is overcome, and bipolarons are predicted either on the same site (S0) or neighboring bound sites (S1).

In the weak-coupling region, where U dominates the electron–phonon coupling strength, we find that the model accurately maps the small-to-intermediate-to-large polaron regime for the single-polaron case, providing more detail than the Holstein model alone. On the other hand, in the strong-coupling region, bipolarons are predicted but are not observed experimentally, resulting in an inaccurate mapping. For example, spatially resolved measurements of hematite down to the quasiparticle limit do not support the presence of S1 bipolarons on neighboring bound sites,[97] which suggests that as polaron strength increases with respect to *U*, an overestimation of the carrier effective mass suggests bipolarons when they are not observed experimentally. Notably, when the Hubbard model is applied to models of superconductivity and two-dimensional materials, it is found that this model also overestimates the carrier's effective mass in a strong electron–phonon coupled limit, due to over-localization.[98–100] This supports that the Hubbard–Holstein model overestimates bipolarons, and while a sufficient framework for systems with weaker electron–phonon coupling strength, may not be sufficient for describing those at the strong electron–phonon coupling limit.[101–103] However, including the Hubbard term for these transition-metal oxides yields a more accurate delineation of the single-polaron species on the left side of **Figure 7.4** and their classification.

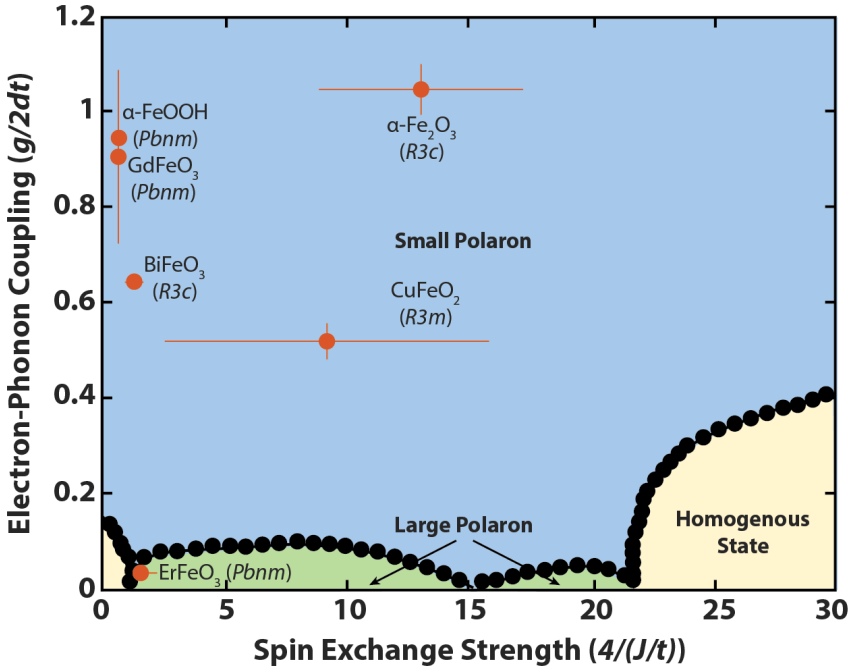

Figure 7.5 Experimentally derived polaronic parameters mapped to a phase diagram of the t-J–Holstein model. Regions corresponding to small polaron (blue), large polaron (green), and near-free carrier (yellow – homogenous state) behavior are shown by shading. Materials are represented by an orange dot and labelled to include their symmetry group. Adapted from reference [104].

We then map the measured iron oxides onto the phase diagram of the t-J–Holstein Hamiltonian for the materials where measured J values exist in literature (**Table 7.1**). **Figure 7.5** shows the phase diagram for the ratios of $g/2dt$ and $4/(J/t)$. The parameters g and J must be scaled by that material's t for comparison to the phase diagram of Reference [104]. **Figure 7.5** compares how polaron formation varies as J is modulated for the measured materials. Areas corresponding to small polaron, large polaron, and near-free carrier conduction (homogenous state) are mapped.

The materials that form small polarons mostly agree with the small polaron designation on the phase diagram, while $ErFeO_3$, with its balance of charge hopping and spin exchange, falls into the large polaron regime of the phase diagram. While measurements of $ErFeO_3$ have suggested small polaron behavior, spatially resolved measurements or ab initio theory determining the polaron size must be undertaken to confirm its size.[52] Given that $ErFeO_3$ has polaron binding energies an order of magnitude weaker than hematite and on par with a-

TiO_2, which is known to form large polarons, further studies are merited to understand the size of polarons within this material.

The diagram depicts that tuning the spin exchange interaction is an effective, though not necessarily straightforward, way to control the small polaron. It must be balanced against the strength of the electron–phonon coupling parameter. Considering these two parameters together reveals that tuning the spin exchange can lead to a rich range of polaron sizes, dynamics, and strengths, extending beyond the electron–phonon parameter of the Holstein model. Superexchange depends on both the Fe-O bond length and the Fe-O-Fe bond angle, as well as spin interactions, providing general guidelines for polaron-based material design. This schematic depiction achieved by mapping experimentally derived parameters to ground-state-theory-based phase diagrams suggests that exchange is a promising route by which polaronic properties may be modulated.

7.6 Conclusions

We find that the Holstein, Hubbard–Holstein, and t-J–Holstein models provide useful qualitative frameworks to classify excited state polaronic dynamics across a range of transition metal oxides. We find that experimental transient XUV experiments can be parameterized within each Hamiltonian's framework and schematically applied to phase-space diagrams previously limited to theory, yielding agreement between experiment and theory. In particular, the t-J–Holstein Hamiltonian yields the clearest set of design parameters by incorporating spin degrees of freedom and providing the most accurate qualitative distinctions between the measured iron oxides. Although this is of particular interest for iron oxides with half-filled d orbitals, the design parameter can be generalized to other transition-metal oxides for which measured superexchange interactions are available.[105,106] We demonstrate that tuning electron–phonon coupling strength (g), electron localization (t), and spin exchange (J) can be leveraged to suppress or control polaron formation in transition metal oxides. Because these values are interrelated, one must balance them to optimize control over polarons. This work combines experimental data with ground-state theoretical models to provide qualitative phase diagrams that inform polaron design and extract specific

material parameters that can be tuned for polaron modulation, while also highlighting a need for future nonequilibrium theory and ultrafast experiments to fully connect ultrafast dynamics to ground-state polaronic predictions.

7.7 References

(1) Cheng, C.; Zhou, Z.; Long, R. Time-Domain View of Polaron Dynamics in Metal Oxide Photocatalysts. *J. Phys. Chem. Lett.* **2023**, *14* (49), 10988–10998. https://doi.org/10.1021/acs.jpclett.3c02869.

(2) Yang, K.; Kwon, D.; Nam, S.; Kim, J.; Chung, Y. S.; Yoo, H.; Park, I.; Park, Y.; Kim, J. W.; Lee, J. Interfacial Exciton-Polaron Quenching in Organic Light-Emitting Diodes. *Phys. Rev. X* **2024**, *14* (4), 041009. https://doi.org/10.1103/PhysRevX.14.041009.

(3) Ghosh, R.; Spano, F. C. Excitons and Polarons in Organic Materials. *Acc. Chem. Res.* **2020**, *53* (10), 2201–2211. https://doi.org/10.1021/acs.accounts.0c00349.

(4) Liu, X.; Gao, K.; Li, Y.; Fu, J.; Wei, J.; Xie, S. Polaron Formation Dynamics in Conducting Polymers. *Synth. Met.* **2007**, *157* (8), 380–385. https://doi.org/10.1016/j.synthmet.2007.04.008.

(5) Naamneh, M.; O'Quinn, E. C.; Paris, E.; McNally, D.; Tseng, Y.; Pudełko, W. R.; Gawryluk, D. J.; Shamblin, J.; Cohen-Stead, B.; Shi, M.; Radovic, M.; Lang, M. K.; Schmitt, T.; Johnston, S.; Plumb, N. C. Persistence of Small Polarons into the Superconducting Doping Range of $Ba_{1-x}K_xBiO_3$. *Phys. Rev. Res.* **2025**, *7* (4), 043082. https://doi.org/10.1103/s3p1-cy1s.

(6) Franchini, C.; Reticcioli, M.; Setvin, M.; Diebold, U. Polarons in Materials. *Nat. Rev. Mater.* **2021**, *6* (7), 560–586. https://doi.org/10.1038/s41578-021-00289-w.

(7) *Polarons in Advanced Materials*; Alexandrov, A. S., Ed.; Hull, R., Osgood, R. M., Parisi, J., Warlimont, H., Series Eds.; Springer Series in Materials Science; Springer Netherlands: Dordrecht, 2007; Vol. 103. https://doi.org/10.1007/978-1-4020-6348-0.

(8) Yim, C.-M.; Allan, M.; Pang, C. L.; Thornton, G. Scanning Tunneling Microscopy Visualization of Polaron Charge Trapping by Hydroxyls on TiO_2(110). *J. Phys. Chem. C* **2024**, *128* (33), 14100–14106. https://doi.org/10.1021/acs.jpcc.4c03751.

(9) Fehske, H.; Trugman, S. A. Numerical Solution of the Holstein Polaron Problem. In *Polarons in Advanced Materials*; Alexandrov, A. S., Ed.; Springer Netherlands: Dordrecht, 2007; pp 393–461. https://doi.org/10.1007/978-1-4020-6348-0_10.

(10) Johnston, C. R.; Speelman, R.; Arcidiacono, A.; Bridgewater, C.; Rassouli, L.; Ma, X.; Vargas-Hurlston, I.; Kupferberg, J.; Martin, L.; Martinson, A. B. F.; Dupuis, M.; Geiger, F. M.; King, S. B. Watching Polarons Dance: Coherent Carrier–Phonon Coupling in Hematite Revealed by Transient Absorption Spectroscopy. *J. Am. Chem. Soc.* **2025**, *147* (44), 40338–40346. https://doi.org/10.1021/jacs.5c11324.

(11) Bhattacharyya, S.; Sayer, T.; Montoya-Castillo, A. Nonequilibrium relaxation exponentially delays the onset of quantum diffusion. *Proc. Natl. Acad. Sci. U.S.A.* **2025**, *122* (19), e2424582122. https://doi.org/10.1073/pnas.2424582122

(12) Kloss, B.; Reichman, D. R.; Tempelaar, R. Multiset Matrix Product State Calculations Reveal Mobile Franck-Condon Excitations Under Strong Holstein-Type Coupling. *Phys. Rev. Lett.* **2019**, *123* (12), 126601. https://doi.org/10.1103/PhysRevLett.123.126601.

(13) Emin, D. Transport Properties of Small Polarons. *J. Solid State Chem.* **1975**, *12* (3), 246–252. https://doi.org/10.1016/0022-4596(75)90314-X.

(14) Fratini, S.; Ciuchi, S. Dynamical Mean-Field Theory of Transport of Small Polarons. *Phys. Rev. Lett.* **2003**, *91* (25), 256403. https://doi.org/10.1103/PhysRevLett.91.256403.

(15) Holstein, T. Studies of Polaron Motion: Part II. The "Small" Polaron. *Ann. Phys.* **2000**, *281* (1), 725–773. https://doi.org/10.1006/aphy.2000.6021.

(16) Zhao, G.; Smolyaninova, V.; Prellier, W.; Keller, H. Electrical Transport in the Ferromagnetic State of Manganites: Small-Polaron Metallic Conduction at Low Temperatures. *Phys. Rev. Lett.* **2000**, *84* (26), 6086–6089. https://doi.org/10.1103/PhysRevLett.84.6086.

(17) Carneiro, L. M.; Cushing, S. K.; Liu, C.; Su, Y.; Yang, P.; Alivisatos, A. P.; Leone, S. R. Excitation-Wavelength-Dependent Small Polaron Trapping of Photoexcited Carriers in α-Fe_2O_3. *Nat. Mater.* **2017**, *16* (8), 819–825. https://doi.org/10.1038/nmat4936.

(18) Biswas, S.; Wallentine, S.; Bandaranayake, S.; Baker, L. R. Controlling Polaron Formation at Hematite Surfaces by Molecular Functionalization Probed by XUV Reflection-Absorption Spectroscopy. *J. Chem. Phys.* **2019**, *151* (10), 104701. https://doi.org/10.1063/1.5115163.

(19) Gao, C.; Zhang, L.; Zheng, Q.; Zhao, J. Tuning the Lifetime of Photoexcited Small Polarons on Rutile TiO_2 Surface via Molecular Adsorption. *J. Phys. Chem. C* **2021**, *125* (49), 27275–27282. https://doi.org/10.1021/acs.jpcc.1c07697.

(20) Mendes, J. L.; Shin, H. J.; Seo, J. Y.; Lee, N.; Choi, Y. J.; Varley, J. B.; Cushing, S. K. Dynamic Competition between Hubbard and Superexchange Interactions Selectively Localizes Electrons and Holes through Polarons. *J. Am. Chem. Soc.* **2025**. https://doi.org/10.1021/jacs.4c16837.

(21) Batzill, M. Fundamental Aspects of Surface Engineering of Transition Metal Oxide Photocatalysts. *Energy Environ. Sci.* **2011**, *4* (9), 3275–3286. https://doi.org/10.1039/C1EE01577J.

(22) Emin, D. Formation and Hopping Motion of Molecular Polarons. *Phys. Rev. B* **2000**, *61* (21), 14543–14553. https://doi.org/10.1103/PhysRevB.61.14543.

(23) Rettie, A. J. E.; Chemelewski, W. D.; Emin, D.; Mullins, C. B. Unravelling Small-Polaron Transport in Metal Oxide Photoelectrodes. *J. Phys. Chem. Lett.* **2016**, *7* (3), 471–479. https://doi.org/10.1021/acs.jpclett.5b02143.

(24) Liu, X.; Gao, K.; Li, Y.; Fu, J.; Wei, J.; Xie, S. Polaron Formation Dynamics in Conducting Polymers. *Synth. Met.* **2007**, *157* (8), 380–385. https://doi.org/10.1016/j.synthmet.2007.04.008.

(25) Kudinov, E. K. Model of a Polaron Superconductor. *Phys. Solid State* **2002**, *44* (4), 692–703. https://doi.org/10.1134/1.1470561.

(26) Mott, N. F. Polaron Models of High-Temperature Superconductors. *J. Phys. Condens. Matter* **1993**, *5* (22), 3487. https://doi.org/10.1088/0953-8984/5/22/003.

(27) Holstein, T. Studies of Polaron Motion: Part I. The Molecular-Crystal Model. *Ann. Phys.* **1959**, *8* (3), 325–342. https://doi.org/10.1016/0003-4916(59)90002-8.

(28) Berger, E.; Valášek, P.; Von Der Linden, W. Two-Dimensional Hubbard-Holstein Model. *Phys. Rev. B* **1995**, *52* (7), 4806–4814. https://doi.org/10.1103/PhysRevB.52.4806.

(29) Chatterjee, J.; Das, A. N. Role of the Superexchange Interaction in Magnetic Transition and Polaron Crossover. *Phys. B Condens. Matter* **2004**, *348* (1), 89–94. https://doi.org/10.1016/j.physb.2003.11.075.

(30) Bu, X.; Li, Y. Optical Signature for Distinguishing between Mott-Hubbard, Intermediate, and Charge-Transfer Insulators. *Phys. Rev. B* **2022**, *106* (24), L241101. https://doi.org/10.1103/PhysRevB.106.L241101.

(31) Dobry, A.; Greco, A.; Koval, S.; Riera, J. Exact Diagonalization Study of the Two-Dimensional t-J-Holstein Model. *Phys. Rev. B* **1995**, *52* (19), 13722–13725. https://doi.org/10.1103/PhysRevB.52.13722.

(32) Vidmar, L.; Bonča, J.; Maekawa, S. Optical Conductivity in the t-J–Holstein Model. *Phys. Rev. B* **2009**, *79* (12), 125120. https://doi.org/10.1103/PhysRevB.79.125120.

(33) Whangbo, M.-H.; Koo, H.-J.; Dai, D.; Jung, D. Effect of Metal−Ligand Bond Lengths on Superexchange Interactions in Jahn−Teller D^4 Ion Systems: Spin Dimer Analysis of the Magnetic Structure of Marokite $CaMn_2O_4$. *Inorg. Chem.* **2002**, *41* (21), 5575–5581. https://doi.org/10.1021/ic0202458.

(34) Feinberg, D.; Germain, P.; Grilli, M.; Seibold, G. Joint Superexchange–Jahn-Teller Mechanism for Layered Antiferromagnetism in $LaMnO_3$. *Phys. Rev. B* **1998**, *57* (10), R5583–R5586. https://doi.org/10.1103/PhysRevB.57.R5583.

(35) Takada, Y.; Masaki, M. Polarons in Jahn–Teller Crystals: Intrinsic Difference between e_g and t_{2g} Electrons. *J. Supercond. Nov. Magn.* **2007**, *20* (7), 629–633. https://doi.org/10.1007/s10948-007-0280-1.

(36) Li, H.; Zhou, Z.; Vasenko, A. S.; Chulkov, E. V.; Fang, Q.; Long, R. Formation and Recombination Dynamics of Polarons in Goethite: A Time-Domain Ab Initio Study. *J. Phys. Chem. Lett.* **2024**, *15* (39), 10018–10025. https://doi.org/10.1021/acs.jpclett.4c02493.

(37) Bhattacharyya, S.; Sayer, T.; Montoya-Castillo, A. Nonequilibrium Relaxation Exponentially Delays the Onset of Quantum Diffusion. *Proc. Natl. Acad. Sci. U.S.A.* **2025**, *122* (19), e2424582122. https://doi.org/10.1073/pnas.2424582122

(38) Cheng, C.; Zhu, Y.; Zhou, Z.; Long, R.; Fang, W.-H. Photoinduced Small Electron Polarons Generation and Recombination in Hematite. *Npj Comput. Mater.* **2022**, *8* (1), 148. https://doi.org/10.1038/s41524-022-00814-7.

(39) Zhang, L.; Chu, W.; Zhao, C.; Zheng, Q.; Prezhdo, O. V.; Zhao, J. Dynamics of Photoexcited Small Polarons in Transition-Metal Oxides. *J. Phys. Chem. Lett.* **2021**, *12* (9), 2191–2198. https://doi.org/10.1021/acs.jpclett.1c00003.

(40) Simbula, A.; Pau, R.; Wang, Q.; Liu, F.; Sarritzu, V.; Lai, S.; Lodde, M.; Mattana, F.; Mula, G.; Geddo Lehmann, A.; Spanopoulos, I. D.; Kanatzidis, M. G.; Marongiu, D.; Quochi, F.; Saba, M.; Mura, A.; Bongiovanni, G. Polaron Plasma in Equilibrium with Bright Excitons in 2D and 3D Hybrid Perovskites. *Adv. Opt. Mater.* **2021**, *9* (16), 2100295. https://doi.org/10.1002/adom.202100295.

(41) Meng, J.; Lan, Z.; Lin, W.; Liang, M.; Zou, X.; Zhao, Q.; Geng, H.; E. Castelli, I.; E. Canton, S.; Pullerits, T.; Zheng, K. Optimizing the Quasi-Equilibrium State of Hot Carriers in All-Inorganic Lead Halide Perovskite Nanocrystals through Mn Doping: Fundamental Dynamics and Device Perspectives. *Chem. Sci.* **2022**, *13* (6), 1734–1745. https://doi.org/10.1039/D1SC05799E.

(42) Biswas, S.; Husek, J.; Londo, S.; Baker, L. R. Highly Localized Charge Transfer Excitons in Metal Oxide Semiconductors. *Nano Lett.* **2018**, *18* (2), 1228–1233. https://doi.org/10.1021/acs.nanolett.7b04818.

(43) Groot, F. de. Multiplet Effects in X-Ray Spectroscopy. *Coord. Chem. Rev.* **2005**, *249* (1), 31–63. https://doi.org/10.1016/j.ccr.2004.03.018.

(44) Stavitski, E.; de Groot, F. M. F. The CTM4XAS Program for EELS and XAS Spectral Shape Analysis of Transition Metal L Edges. *Micron* **2010**, *41* (7), 687–694. https://doi.org/10.1016/j.micron.2010.06.005.

(45) Vinson, J. Advances in the OCEAN-3 Spectroscopy Package. *Phys. Chem. Chem. Phys.* **2022**, *24* (21), 12787–12803. https://doi.org/10.1039/D2CP01030E.

(46) Vinson, J.; Rehr, J. J.; Kas, J. J.; Shirley, E. L. Bethe-Salpeter Equation Calculations of Core Excitation Spectra. *Phys. Rev. B* **2011**, *83* (11), 115106. https://doi.org/10.1103/PhysRevB.83.115106.

(47) Gilmore, K.; Vinson, J.; Shirley, E. L.; Prendergast, D.; Pemmaraju, C. D.; Kas, J. J.; Vila, F. D.; Rehr, J. J. Efficient Implementation of Core-Excitation Bethe–Salpeter Equation Calculations. *Comput. Phys. Commun.* **2015**, *197*, 109–117. https://doi.org/10.1016/j.cpc.2015.08.014.

(48) Klein, I. M.; Liu, H.; Nimlos, D.; Krotz, A.; Cushing, S. K. Ab Initio Prediction of Excited-State and Polaron Effects in Transient XUV Measurements of α-Fe_2O_3. *J. Am. Chem. Soc.* **2022**, *144* (28), 12834–12841. https://doi.org/10.1021/jacs.2c03994.

(49) Zhou, F.; Sadigh, B.; Erhart, P.; Åberg, D. Ab Initio Prediction of Fast Non-Equilibrium Transport of Nascent Polarons in SrI_2: A Key to High-Performance Scintillation. *Npj Comput. Mater.* **2016**, *2* (1), 1–7. https://doi.org/10.1038/npjcompumats.2016.22.

(50) Carneiro, L. M.; Cushing, S. K.; Liu, C.; Su, Y.; Yang, P.; Alivisatos, A. P.; Leone, S. R. Excitation-Wavelength-Dependent Small Polaron Trapping of Photoexcited Carriers in α-Fe_2O_3. *Nat. Mater.* **2017**, *16* (8), 819–825. https://doi.org/10.1038/nmat4936.

(51) Mendes, J. L.; Bhattacharyya, S.; Huang, C.; Michelsen, J. M.; Klein, I. M.; Babbe, F.; Sayer, T.; Li, T.; Cooper, J. K.; Liu, H.; Ginsberg, N. S.; Montoya-Castillo, A.; Cushing, S. K. Coherent and Dynamic Small Polaron Delocalization in $CuFeO_2$. *J. Phys. Chem. Lett.* **2026**, *17* (2), 656–664. https://doi.org/10.1021/acs.jpclett.5c03430.

(52) Kim, Y.-J.; Mendes, J. L.; Michelsen, J. M.; Shin, H. J.; Lee, N.; Choi, Y. J.; Cushing, S. K. Coherent Charge Hopping Suppresses Photoexcited Small Polarons in $ErFeO_3$ by Antiadiabatic Formation Mechanism. *Sci. Adv.* **2024**, *10* (12), eadk4282. https://doi.org/10.1126/sciadv.adk4282.

(53) Ahmad, J.; Uwe, H. Small-Polaron Excitations in $Ba_{1-X}K_XBiO_3$ Studied by Optical Reflectivity Measurements. *Phys. Rev. B* **2005**, *72* (12), 125103. https://doi.org/10.1103/PhysRevB.72.125103.

(54) Panneerselvam, I. R.; Baldo, C.; Sahasranaman, M.; Murugesan, S.; Rangaswamy, N.; Pai, S. D. K. R.; Selvarathinam, Y. Large Power Factors in Wide Band Gap Semiconducting $RFeO_3$ Materials for High-Temperature Thermoelectric Applications. *ACS Appl. Energy Mater.* ***2020****, 3* (11), 11193–11205. https://doi.org/10.1021/acsaem.0c02128.

(55) Chandler, C. J.; Prosko, C.; Marsiglio, F. The Effect of Next-Nearest Neighbour Hopping in the One, Two, and Three Dimensional Holstein Model. *Sci. Rep.* **2016**, *6* (1), 32591. https://doi.org/10.1038/srep32591.

(56) Souza, T. X. R.; Marsiglio, F. Systematic Study of the Superconducting Critical Temperature in Two- and Three-Dimensional Tight-Binding Models: A Possible Scenario for Superconducting H_3S. *Phys. Rev. B* **2016**, *94* (18), 184509. https://doi.org/10.1103/PhysRevB.94.184509.

(57) Majidi, M. A. Electron Hopping Integral Renormalization Due to Anharmonic Phonons. *J. Phys. Conf. Ser.* **2018**, *1011* (1), 012080. https://doi.org/10.1088/1742-6596/1011/1/012080.

(58) Bhattacharyya, S.; Sayer, T.; Montoya-Castillo, A. Mori Generalized Master Equations Offer an Efficient Route to Predict and Interpret Polaron Transport. *Chem. Sci.* **2024**, *15* (40), 16715–16723. https://doi.org/10.1039/D4SC03144J.

(59) Zhang, C.; Zhong, Y.; Tao, Z.-G.; Qin, X.; Shang, H.; Lan, Z.; Prezhdo, O. V.; Gong, X.-G.; Chu, W.; Xiang, H. Advancing Nonadiabatic Molecular Dynamics Simulations in Solids with E(3) Equivariant Deep Neural Hamiltonians. *Nat. Commun.* **2025**, *16* (1), 2033. https://doi.org/10.1038/s41467-025-57328-1.

(60) Tian, L.; Sachs, M.; Verga, L. G.; Kunzelmann, V. F.; Kafizas, A.; Sharp, I. D.; Cushing, S. K.; Walsh, A.; Durrant, J. R. Optical Spectroscopic Determination of Photoexcited Small-Polaron Hopping in Transition Metal Oxide Photocatalysts. *Chem. Sci.* **2026**, *17* (8), 4203–4212. https://doi.org/10.1039/D5SC08101G.

(61) Stephan, W.; Capone, M.; Grilli, M.; Castellani, C. Influence of Electron-Phonon Interaction on Superexchange. *Phys. Lett. A* **1997**, *227* (1–2), 120–126. https://doi.org/10.1016/S0375-9601(96)00950-

(62) Hohenadler, M.; von der Linden, W. Lang-Firsov Approaches to Polaron Physics: From Variational Methods to Unbiased Quantum Monte Carlo Simulations. In *Polarons in Advanced Materials*; Alexandrov, A. S., Ed.; Springer Netherlands: Dordrecht, 2007; pp 463–502. https://doi.org/10.1007/978-1-4020-6348-0_11.

(63) Shelton, J. L.; Knowles, K. E. Polaronic Optical Transitions in Hematite (α-Fe_2O_3) Revealed by First-Principles Electron–Phonon Coupling. *J. Chem. Phys.* **2022**, *157* (17), 174703. https://doi.org/10.1063/5.0116233.

(64) Hill, A. H.; Jacobsen, H.; Stewart, J. R.; Jiao, F.; Jensen, N. P.; Holm, S. L.; Mutka, H.; Seydel, T.; Harrison, A.; Lefmann, K. Magnetic Properties of Nano-Scale Hematite, α-Fe_2O_3, Studied by Time-of-Flight Inelastic Neutron Spectroscopy. *J. Chem. Phys.* **2014**, *140* (4), 044709. https://doi.org/10.1063/1.4862235.

(65) Samuelsen, E. J.; Shirane, G. Inelastic Neutron Scattering Investigation of Spin Waves and Magnetic Interactions in α-Fe_2O_3. *Phys. Status Solidi B* **1970**, *42* (1), 241–256. https://doi.org/10.1002/pssb.19700420125.

(66) Klobes, B.; Herlitschke, M.; Rushchanskii, K. Z.; Wille, H.-C.; Lummen, T. T. A.; Van Loosdrecht, P. H. M.; Nugroho, A. A.; Hermann, R. P. Anisotropic Lattice Dynamics and Intermediate-Phase Magnetism in Delafossite $CuFeO_2$. *Phys. Rev. B* **2015**, *92* (1), 014304. https://doi.org/10.1103/PhysRevB.92.014304.

(67) Ye, F.; Fernandez-Baca, J. A.; Fishman, R. S.; Ren, Y.; Kang, H. J.; Qiu, Y.; Kimura, T. Magnetic Interactions in the Geometrically Frustrated Triangular Lattice Antiferromagnet $CuFeO_2$. *Phys. Rev. Lett.* **2007**, *99* (15), 157201. https://doi.org/10.1103/PhysRevLett.99.157201.

(68) Koshizuka, N.; Ushioda, S. Inelastic-Light-Scattering Study of Magnon Softening in $ErFeO_3$. *Phys. Rev. B* **1980**, *22* (11), 5394–5399. https://doi.org/10.1103/PhysRevB.22.5394.

(69) Chen, W.; Wang, T.; Yu, C.-C.; Jing, Y.; Li, X.; Xiong, W. Small Polaron-Induced Ultrafast Ferroelectric Restoration in $BiFeO_3$. *Phys. Rev. X* **2025**, *15* (2), 021046. https://doi.org/10.1103/PhysRevX.15.021046.

(70) Fukumura, H.; Matsui, S.; Harima, H.; Takahashi, T.; Itoh, T.; Kisoda, K.; Tamada, M.; Noguchi, Y.; Miyayama, M. Observation of Phonons in Multiferroic $BiFeO_3$ Single Crystals by Raman Scattering. J. *Phys. Condens. Matter* **2007**, *19* (36), 365224. https://doi.org/10.1088/0953-8984/19/36/365224

(71) Wang, Y.; Saal, J. E.; Wu, P.; Wang, J.; Shang, S.; Liu, Z.-K.; Chen, L.-Q. First-Principles Lattice Dynamics and Heat Capacity of $BiFeO_3$. *Acta Mater.* **2011**, *59* (10), 4229–4234. https://doi.org/10.1016/j.actamat.2011.03.047.

(72) Jeong, J.; Goremychkin, E. A.; Guidi, T.; Nakajima, K.; Jeon, G. S.; Kim, S.-A.; Furukawa, S.; Kim, Y. B.; Lee, S.; Kiryukhin, V.; Cheong, S.-W.; Park, J.-G. Spin Wave Measurements over the Full Brillouin Zone of Multiferroic $BiFeO_3$. *Phys. Rev. Lett.* **2012**, *108* (7), 077202. https://doi.org/10.1103/PhysRevLett.108.077202.

(73)Molesky, I. J. P.; Cushing, S. K.; Carneiro, L. M.; Lee, A.; Ondry, J. C.; Dahl, J. C.; Chang, H.-T.; Alivisatos, A. P.; Leone, S. R. Photoexcited Small Polaron Formation in Goethite (α-FeOOH) Nanorods Probed by Transient Extreme Ultraviolet Spectroscopy. *J. Phys. Chem. Lett.* **2018**, *9* (14), 4120–4124. https://doi.org/10.1021/acs.jpclett.8b01525.

(74)Hu, Q.; Kim, D. Y.; Yang, W.; Yang, L.; Meng, Y.; Zhang, L.; Mao, H.-K. FeO_2 and FeOOH under Deep Lower-Mantle Conditions and Earth's Oxygen–Hydrogen Cycles. *Nature* **2016**, *534* (7606), 241–244. https://doi.org/10.1038/nature18018.

(75)Khan, I.; Hashmi, A.; Farooq, M. U.; Hong, J. Two-Dimensional Magnetic Semiconductor in Feroxyhyte. *ACS Appl. Mater. Interfaces* **2017**, *9* (40), 35368–35375. https://doi.org/10.1021/acsami.7b08499.

(76) Liu, X.; Liu, H.; Zong, M.; Chen, M.; He, H.; Wang, R.; Lu, X. Mn Substitution and Distribution in Goethite and Influences on Its Photocatalytic Properties: A Combined Study Using First-Principles Calculations and Photocatalytic Experiments. *Am. Mineral.* **2023**, *108* (5), 968–977. https://doi.org/10.2138/am-2022-8182.

(77) Abrashev, M. V.; Ivanov, V. G.; Stefanov, B. S.; Todorov, N. D.; Rosell, J.; Skumryev, V. Raman Spectroscopy of alpha-FeOOH (Goethite) Near Antiferromagnetic to Paramagnetic Phase Transition. *J. Appl. Phys.* **2020**, *127* (20), 205108. https://doi.org/10.1063/5.0006352

(78) Zhu, X.-H.; Xiao, X.-B.; Chen, X.-R.; Liu, B.-G. Electronic Structure, Magnetism and Optical Properties of Orthorhombic $GdFeO_3$ from First Principles. *RSC Adv.* **2017**, *7* (7), 4054–4061. https://doi.org/10.1039/C6RA25259A.

(79) De Lile, J. R.; Kang, S. G.; Son, Y.-A.; Lee, S. G. Investigating Polaron Formation in Anatase and Brookite TiO_2 by Density Functional Theory with Hybrid-Functional and DFT+U Methods. *ACS Omega* **2019**, *4* (5), 8056–8064. https://doi.org/10.1021/acsomega.9b00443

(80) Kang, Y.; Peelaers, H.; Van de Walle, C. G. First-Principles Study of Electron-Phonon Interactions and Transport in Anatase TiO_2. *Phys. Rev. B* **2019**, *100* (12), 121113. https://doi.org/10.1103/PhysRevB.100.121113.

(81) Moser, S.; Moreschini, L.; Jaćimović, J.; Barišić, O. S.; Berger, H.; Magrez, A.; Chang, Y. J.; Kim, K. S.; Bostwick, A.; Rotenberg, E.; Forró, L.; Grioni, M. Tunable Polaronic Conduction in Anatase TiO_2. *Phys. Rev. Lett.* **2013**, *110* (19), 196403. https://doi.org/10.1103/PhysRevLett.110.196403.

(82) Labat, F.; Baranek, P.; Adamo, C. Structural and Electronic Properties of Selected Rutile and Anatase TiO_2 Surfaces: An Ab Initio Investigation. *J. Chem. Theory Comput.* **2008**, *4* (2), 341–352. https://doi.org/10.1021/ct700221w.

(83) Zhang, J.; Shi, J.; Chen, Y.; Zhang, K. H. L.; Yang, Y. Bimolecular Self-Trapped Exciton Formation in Bismuth Vanadate. *J. Phys. Chem. Lett.* **2022**, *13* (42), 9815–9821. https://doi.org/10.1021/acs.jpclett.2c02596.

(84) Liu, T.; Zhang, X.; Guan, J.; Catlow, C. R. A.; Walsh, A.; Sokol, A. A.; Buckeridge, J. Insight into the Fergusonite–Scheelite Phase Transition of ABO_4-Type Oxides by Density Functional Theory: A Case Study of the Subtleties of the Ground State of $BiVO_4$. *Chem. Mater.* **2022**, *34* (12), 5334–5343. https://doi.org/10.1021/acs.chemmater.1c04417.

(85) Yin, W.-J.; Wei, S.-H.; Al-Jassim, M. M.; Turner, J.; Yan, Y. Doping Properties of Monoclinic $BiVO_4$ Studied by First-Principles Density-Functional Theory. *Phys. Rev. B* **2011**, *83* (15), 155102. https://doi.org/10.1103/PhysRevB.83.155102.

(86) Radcliffe, J. M. Approximate Free Energies for Heisenberg Ferromagnets. *Phys. Rev.* **1968**, *165* (2), 635–641. https://doi.org/10.1103/PhysRev.165.635.

(87) Anderson, P. W. Antiferromagnetism. Theory of Superexchange Interaction. *Phys. Rev.* **1950**, *79* (2), 350–356. https://doi.org/10.1103/PhysRev.79.350.

(88) Zhang, C. Light Polarons with Electron-Phonon Coupling. *Phys. Rev. B* **2024**, *109* (16), 165119. https://doi.org/10.1103/PhysRevB.109.165119.

(89) Zhang, K.; Fu, C.; Kelly, S.; Liang, L.; Kang, S.-H.; Jiang, J.; Zhang, R.; Wang, Y.; Wan, G.; Siriviboon, P.; Yoon, M.; Ye, P. D.; Wu, W.; Li, M.; Huang, S. Thickness-Dependent Polaron Crossover in Tellurene. Sci. Adv. 2025, 11 (2), eads4763. https://doi.org/10.1126/sciadv.ads4763

(90) Hruska, E.; Husek, J.; Bandaranayake, S.; Baker, L. R. Visible Light Absorption and Hot Carrier Trapping in Anatase TiO_2: The Role of Surface Oxygen Vacancies. *J. Phys. Chem. C* **2022**, *126* (26), 10752–10761. https://doi.org/10.1021/acs.jpcc.2c02978.

(91) Redondo, J.; Reticcioli, M.; Gabriel, V.; Wrana, D.; Ellinger, F.; Riva, M.; Franceschi, G.; Rheinfrank, E.; Sokolović, I.; Jakub, Z.; Kraushofer, F.; Alexander, A.; Belas, E.; Patera, L. L.; Repp, J.; Schmid, M.; Diebold, U.; Parkinson, G. S.; Franchini, C.; Kocan, P.; Setvin, M. Real-Space Investigation of Polarons in Hematite Fe_2O_3. *Sci. Adv.* **2024**, *10* (44), eadp7833. https://doi.org/10.1126/sciadv.adp7833.

(92) Alexandrov, V.; Rosso, K. M. Electron Transport in Pure and Substituted Iron Oxyhydroxides by Small-Polaron Migration. *J. Chem. Phys.* **2014**, *140* (23), 234701. https://doi.org/10.1063/1.4882065.

(93) Wu, H.; Zhang, L.; Qu, S.; Du, A.; Tang, J.; Ng, Y. H. Polaron-Mediated Transport in $BiVO_4$ Photoanodes for Solar Water Oxidation. *ACS Energy Lett.* **2023**, *8* (5), 2177–2184. https://doi.org/10.1021/acsenergylett.3c00465.

(94) Kweon, K. E.; Hwang, G. S. Structural Phase-Dependent Hole Localization and Transport in Bismuth Vanadate. *Phys. Rev. B* **2013**, *87* (20), 205202. https://doi.org/10.1103/PhysRevB.87.205202

(95) Alam, M.; Mandal, K. Origin of Ferroelectricity in Multiferroic $ErFeO_3$. *Phys. B Condens. Matter* **2021**, *612*, 412935. https://doi.org/10.1016/j.physb.2021.412935.

(96) Macridin, A.; Sawatzky, G. A.; Jarrell, M. Two-Dimensional Hubbard-Holstein Bipolaron. *Phys. Rev. B* **2004**, *69* (24), 245111. https://doi.org/10.1103/PhysRevB.69.245111.

(97) Redondo, J.; Reticcioli, M.; Gabriel, V.; Wrana, D.; Ellinger, F.; Riva, M.; Franceschi, G.; Rheinfrank, E.; Sokolović, I.; Jakub, Z.; Kraushofer, F.; Alexander, A.; Belas, E.; Patera, L. L.; Repp, J.; Schmid, M.; Diebold,

U.; Parkinson, G. S.; Franchini, C.; Kocan, P.; Setvin, M. Real-Space Investigation of Polarons in Hematite Fe_2O_3. *Sci. Adv.* **2024**, *10* (44), eadp7833. https://doi.org/10.1126/sciadv.adp7833.

(98) Dimashko, Y. A. Pairing of Two Holes by a Single String. *Zh. Eksp. Teor. Fiz.***1993**, *103*, 526-546.

(99) Huang, L.; Ayral, T.; Biermann, S.; Werner, P. Extended Dynamical Mean-Field Study of the Hubbard Model with Long-Range Interactions. *Phys. Rev. B* **2014**, *90* (19), 195114. https://doi.org/10.1103/PhysRevB.90.195114.

(100) Pakdel, S.; Olsen, T.; Thygesen, K. S. Effect of Hubbard U-Corrections on the Electronic and Magnetic Properties of 2D Materials: A High-Throughput Study. *Npj Comput. Mater.* **2025**, *11* (1), 18. https://doi.org/10.1038/s41524-024-01503-3.

(101) Nosarzewski, B.; Huang, E. W.; Dee, P. M.; Esterlis, I.; Moritz, B.; Kivelson, S. A.; Johnston, S.; Devereaux, T. P. Superconductivity, Charge Density Waves, and Bipolarons in the Holstein Model. *Phys. Rev. B* **2021**, *103* (23), 235156. https://doi.org/10.1103/PhysRevB.103.235156.

(102) Bonča, J.; Trugman, S. A. Bipolarons in the Extended Holstein Hubbard Model. *Phys. Rev. B* **2001**, *64* (9), 094507. https://doi.org/10.1103/PhysRevB.64.094507.

(103) De Filippis, G.; Cataudella, V.; Iadonisi, G.; Marigliano Ramaglia, V.; Perroni, C. A.; Ventriglia, F. Polaron and Bipolaron Formation in the Hubbard-Holstein Model: Role of next-Nearest-Neighbor Electron Hopping. *Phys. Rev. B* **2001**, *64* (15), 155105. https://doi.org/10.1103/PhysRevB.64.155105.

(104) Fehske, H.; Roder, H.; Mistriotis, A.; Buttner, H. The Phase Diagram of the 2D Holstein-t-J Model near Half Filling. *J. Phys. Condens. Matter* **1993**, *5* (22), 3565. https://doi.org/10.1088/0953-8984/5/22/008.

(105) Ji, G.; Xu, M.; Kendrick, L. H.; Chiu, C. S.; Brüggenjürgen, J. C.; Greif, D.; Bohrdt, A.; Grusdt, F.; Demler, E.; Lebrat, M.; Greiner, M. Coupling a Mobile Hole to an Antiferromagnetic Spin Background: Transient Dynamics of a Magnetic Polaron. *Phys. Rev. X* **2021**, *11* (2), 021022. https://doi.org/10.1103/PhysRevX.11.021022.

(106) Davydova, M.; Zhang, Y.; Fu, L. Itinerant Spin Polaron and Metallic Ferromagnetism in Semiconductor Moiré Superlattices. *Phys. Rev. B* **2023**, *107* (22), 224420. https://doi.org/10.1103/PhysRevB.107.224420.

Appendix A

ULTRAFAST HOLE TRANSPORT AND ELECTRON LOCALIZATION IN SUPERATOMIC $RE_6SE_8CL_2$

A.1 Abstract

Cluster-assembled van der Waals superatomic crystals represent an intriguing class of materials, exhibiting unique ultrafast electronic and structural responses arising from their hierarchical crystal structure. These materials bridge the properties of semiconductors, molecular solids, and nanocrystal arrays, hosting a range of many-body interactions that can be controlled with atomically precise structures. To establish the structure-function correlation, it is necessary to understand element-specific electronic states arising from complex superatomic unit cells. Here, we use transient XUV spectroscopy to individually probe the dynamics of photoexcited electrons and holes in $Re_6Se_8Cl_2$ superatomic crystals. We simultaneously measure photodynamics at the Re O_2 and Se $M_{4,5}$ edges, enabling decomposition of excited-state dynamics into the contributions of electron, hole, band gap, and phonon dynamics occurring around Re and Se atoms. By correlating spectral features at the Re and Se edges, we infer the existence of flat conduction bands and identify hot hole transfer from Re to Se atoms. The system exhibits phonon oscillations driven by hole-mediated displacive excitations. The measurements highlight that carrier transport is dominated by charge transfer between metallic sites and drives phonon coupling in the nonequilibrium state. This work provides insights into the optoelectronic applications of superatomic crystals for future tuning of emergent material properties.

A.2 Introduction

The material properties and functions in hierarchical structures are an emerging field in materials science.[1–3] While structure-function relationships are well understood in many cases, they are challenging for hierarchical materials with complex chemical compositions and structures due to the correlated behavior of electrons and phonons.[4] Two-dimensional van der Waals (vdW) superatomic crystals are emerging materials that have this challenge.

Unlike conventional crystals, superatomic crystals use atomically precise clusters as building blocks that form long-range crystalline order. The materials are composed of discrete, modular clusters that mirror traditional atomic solids.[1,2,5,6] The macroscopic properties of superatomic crystals can be widely tuned by modifications of the chemical composition[7–9] or atomic coordination,[10] leading to complex many-body interactions and rich dynamics.

Meanwhile, superatomic crystals have shown promising applications in optoelectronics,[11] thermoelectricity,[12–14] and catalysis.[15] For example, superatomic materials have demonstrated significant thermoelectric performance without systematic material optimization.[16] Recent optical studies reveal efficient quasi-ballistic exciton transport in superatomic crystals up to room temperature, with exciton mobility exceeding Si, making them promising candidates for efficient optoelectronic devices.[17] Other optical studies have provided insight into charge density waves, coherent exciton transport, carrier, and phonon dynamics in $Re_6Se_8Cl_2$.[6,17–19] Further, tuning of electron and phonon bandwidths1 and superconductivity[9,20,21] have been demonstrated.

The observed material properties are largely due to the intrinsically strong electron-phonon interactions in superatomic cyrstals.[22,23] Superatomic crystals have a complex unit cell and hierarchical lattice structure, enabling these unique phonon dynamics. Typical phonon spectra consist of both localized molecular vibrations and long-range coherent phonons expected for crystals.[24,25] Meanwhile, electronic excitations create molecular-like excitons that exhibit large binding energies. Despite its fundamental importance, understanding excited-state carrier-phonon dynamics in superatomic crystals is challenging due to the interplay between the complex unit-cell structure, electronic band structures, and various vibrational modes.

In this work, we measure the carrier- and element-resolved ultrafast electronic dynamics in the vdW superatomic semiconductor, $Re_6Se_8Cl_2$ (**Figure A.1A**), using transient extreme ultraviolet (XUV) reflection-absorption spectroscopy. In our measurements, carrier- and element-specific relaxation processes following photoexcitation are separately resolved. We

measure the thermalization and intervalley charge redistribution of holes from Re to Se sites and confirm the existence of flat conduction bands (CBs) through minimal electron thermalization dynamics. Hole-mediated coherent cluster-tilt displacive phonon motions are observed in the transient spectra, supporting carrier-phonon coupling within the two-dimensional layers of $Re_6Se_8Cl_2$. The element-specific observation of flat CBs and the displacive excitation of coherent phonon motions provides insights into the nature of enhanced thermal transport properties within this class of superatomic crystals.[17,25,26] Our observations provide a guide for designing chemical structures and atomic-precise spatial layouts in these hierarchical superatomic crystals, which can potentially enhance energy transport from the nanoscale to mesoscopic levels.

A.3 Results and Discussion

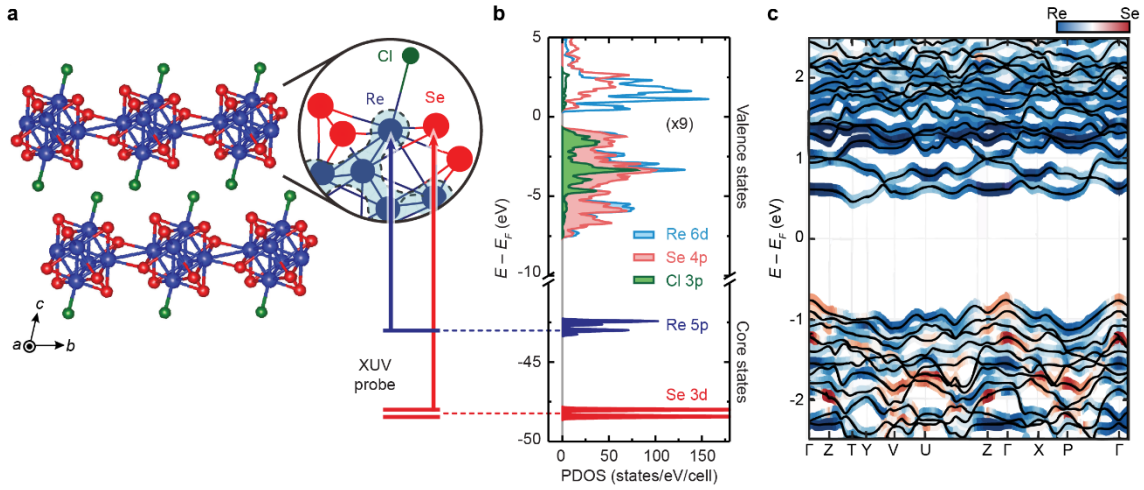

Figure A.1 $Re_6Se_8Cl_2$ crystal and electronic structure. **(A)** Crystal structure of the $Re_6Se_8Cl_2$ single crystal projected along the *a*-axis. The broadband XUV probe can selectively measure the transient dynamics of charge carriers at both the Re O_2 and Se $M_{4,5}$ edges following photoexcitation. **(B)** Calculated projected electronic density of states (PDOS). The valence states are composed of Re 6d, Se 4p, and Cl 3p orbitals. Core electrons in Re 5p and Se 3d orbitals are excited to these states by the XUV probe pulses. The calculation includes the spin-orbit splitting of the core orbitals. E_F is Fermi energy and valence states are scaled by a factor of 9 for better visibility. **(C)** Calculated atom-projected band structure of $Re_6Se_8Cl_2$ along the high-symmetry k-path. The atomic contributions to the electronic structure indicated by a color gradient from red to blue, representing Se to Re, respectively. The CBs are predominantly composed of Re 6d orbitals, while the VBs are hybridized with Re 6d and Se 4p orbitals.

The layered structure of $Re_6Se_8Cl_2$ is shown in **Figure A.1A**. Each layer in this superatomic semiconductor is composed of covalently bonded $Re_6Se_8Cl_2$ clusters arranged in a pseudo-

square lattice within the *a–b* plane. These two-dimensional layers are stacked along the *c*-axis through vdW interactions, giving rise to a hierarchical crystal structure.[5] This hierarchical structure leads to unusual electron-phonon coupling,[17,18] primarily due to the interplay between bound excitons, localized molecular dynamics, and the long-range collective response. The calculated projected density of states (PDOS) using density functional theory (DFT) predicts an indirect band gap (Eg) of 1.2 eV as shown in **Figure A.1B**, similar to measured and reported values (see the **Supporting Information Section** for details of DFT calculations).[5] The upper valence bands (VBs) have strong hybridization between the Re 6d and Se 4p orbitals, with minor contributions from Cl 3p orbitals. The atomic orbital-resolved electronic band structure, shown in **Figure A.1C**, shows that $Re_6Se_8Cl_2$ has an indirect band gap between the valence band maximum (VBM) at the Γ point and the conduction band minimum (CBM) at the T point.[24]

Transient XUV reflection-absorption spectroscopy measures element-specific core-to-valence transitions and can separate electron and hole dynamics at individual elemental X-ray edges.[27] In our experiment, a 3.1 eV (400 nm) excitation pulse generates electron-hole pairs across the band gap of single crystalline $Re_6Se_8Cl_2$. The excitation fluence used in transient XUV experiments was ~9 mJ/cm^2, resulting in an excited carrier density of ~4.1 x 10^{21} cm^{-3}. The resulting carrier dynamics are probed by a broadband XUV pulse in a 10° grazing incidence reflection geometry. The XUV pulse simultaneously measures the Re O_2 and Se $M_{4,5}$ edges, revealing the local chemical environment around Re and Se sites, as shown in **Figures A.2** and **A.3**, respectively. More details of the experimental configuration can be found in the **Supporting Information Section**.

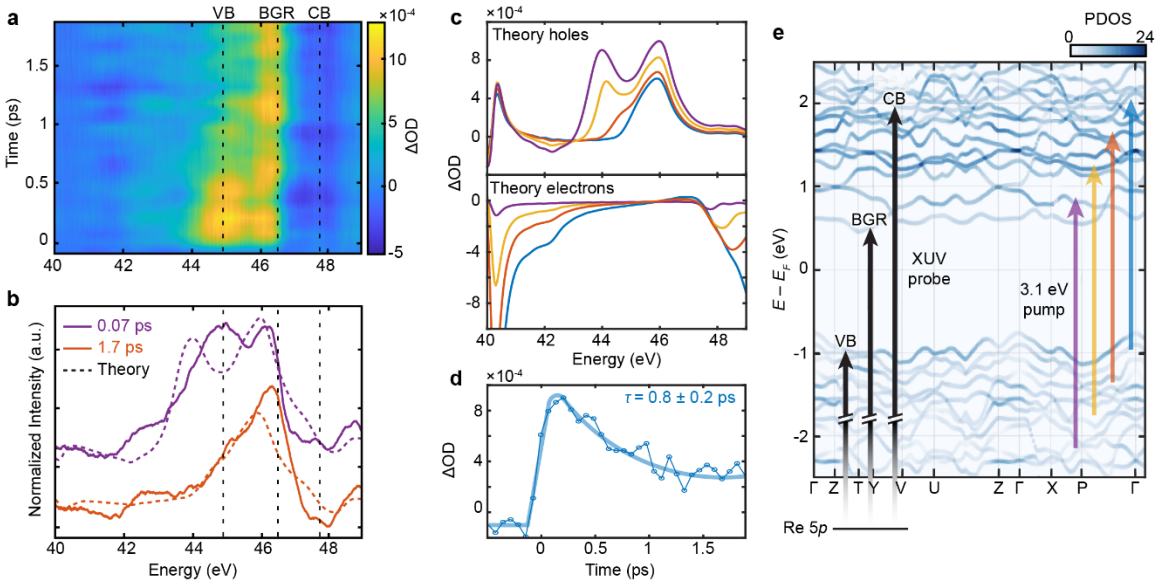

Figure A.2 Carrier relaxation dynamics at the Re O2 edge. **(A)** Transient XUV reflection-absorption spectra at the Re O_2 edge. Three main spectral features for the valence bands (VB), band gap renormalization (BGR), and conduction bands (CB) are denoted as dotted lines. **(B)** Experimental and BSE theory calculated transient differential absorption spectra, shown as solid and dotted lines, respectively, at two time delays (0.07 and 1.7 ps) following photoexcitation. The BSE calculated spectra model an initial charge transfer state with electrons filled to the same energy (2.0 eV) above the VBM in both time points. In comparison, holes are filled up to 3.1 eV below the CBM (0.07 ps, purple dashed line) and 1.5 eV below the CBM (1.7 ps, orange dashed line), suggesting strong hole thermalization in the VBs with very minimal electron thermalization. **(C)** BSE theory calculated Re O_2 edge spectra for holes only (top) and electrons only (bottom). The BSE modeling of holes and electrons uses a state-filling model in which holes are modeled from the VBM down to energies as low as 3.1 eV below the CBM, to consider the possible allowed transitions following the 3.1 eV pump. Similarly, electrons are modeled starting at the CBM and up to 3.1 eV above the VBM. The modeled hole energies in c correspond to hole cutoff energies of 3.1 eV (purple), 2.5 eV (yellow), 2.0 eV (orange), and 1.5 eV (blue). The modeled electron energies correspond to electron cutoff energies of 3.1 eV (blue), 2.5 eV (orange), 2.0 eV (yellow), and 1.5 eV (purple). **(D)** Kinetic trace of hot hole thermalization at the Re O_2 edge averaged across ~44–45 eV. The solid line indicates a fitted curve. **(E)** Re projected band structure of $Re_6Se_8Cl_2$. The colored arrows (right) depict the corresponding state-filling electron and hole energies that are modeled in **C** and are color coded accordingly.

We first focus on understanding the photodynamics occurring at the Re sites. **Figure A.2A** shows the transient XUV reflection-absorption at the Re O_2 edge. The reflection-absorption is defined as $\Delta OD = -\log_{10}(\frac{I_{\text{pump on}}}{I_{\text{pump off}}})$. In this definition, a positive signal (**Fig. A.2A**, yellow) represents a transient decrease in XUV reflectivity, which corresponds to an increase in XUV absorption. The two transient spectral lineouts at $\Delta t = 0.07$ and 1.7 ps show a clear difference between the initial and final excited states (**Fig. A.2B**). The positive signal at ~45 eV shifts to higher energies (blueshift) with concomitant decreases in amplitude. The increase in absorption around ~46.5 eV also blueshifts but with a lesser magnitude than the peak at ~45

eV. There is a decrease in absorption (**Fig. A.2A**, blue) that is centered around ~47.8 eV and does not shift spectrally or experience a decrease in amplitude.

To understand the origin of the spectral features at the Re O_2 and Se $M_{4,5}$ edges of $Re_6Se_8Cl_2$, we use a density functional theory (DFT) and Bethe–Salpeter equation (BSE) approach to model the excited state X-ray edge dynamics. The method uses Quantum ESPRESSO[28,29] and an excited state modification to the OCEAN (Obtaining Core Excitations from the electronic structure and the NIST BSE solver) code.[30–33] The theoretical methods applied here are discussed in more detail in **A.S4**. Briefly, to model carrier thermalization, we define two state-filling cutoff energies, E_h and E_e. Where E_h is the maximum hole depth in the VBs referenced from the CMB to encompass all possible transitions in momentum space by the pump and E_e is the maximum electron height in the CBs referenced from the VBM. In the case of our 3.1 eV excitation employed in the transient XUV experiments, this means that E_e, $E_h \leq 3.1$ eV, and smaller values correspond to carrier thermalization toward the respective band edges of the carriers. E_h and E_e are phenomenological state-filling cutoff energies that parameterize the modeled spectral sensitivity to hole and electron occupations. While these cutoffs describe the bounds of the pump-accessible excitations, they do not imply that a single photoexcited electron–hole pair simultaneously occupies both cutoffs. Additionally, the BSE state-filling model considers dynamically blocking (electrons) and allowing (holes) core-level transitions and does not consider carrier density. More details on these cutoff energies can be found in **A.S4.B**.

Figure A.2B shows experimental and BSE modeled lineouts for two different time delays in the transient spectra. We model the state immediately following photoexcitation (**Fig. A.2B**, purple dashed line) based upon an electron cutoff energy of 2.0 eV and a hole cutoff energy of 3.1 eV. This suggests that the increased absorption between ~44–46.5 eV is primarily due to the photoexcited hole population in the VBs. The increased absorption is due to this state-filling effect, where photoinjected holes increase the available density of states in the VBs, leading to enhanced XUV absorption.[34] Similarly, the decrease in absorption from ~46.5–49 eV is well described by photoexcited electrons occupying CBs and blocking XUV

transitions, leading to decreased XUV absorption. This theoretical assignment agrees well with experimental spectra immediately following photoexcitation, suggesting that transitions are being probed from deep VBs into CBs near the CBM.

The orange dashed line in **Figure A.2B** well describes the transient spectra at later times (1.7 ps). This lineout was modeled with a state-blocking E_e and E_h of 2.0 eV. This suggests that there is significant thermalization of holes at the Re O_2 edge following photoexcitation, but minimal thermalization of electrons. Further, the blueshift observed experimentally at ~45 eV in **Figure A.2A** is well described by BSE theory modeling hole thermalization at the Re O_2 edge, with no electron thermalization modeled. The spectral shift associated with hole thermalization in the VBs occurs on a timescale of 0.8 ± 0.2 ps, with an energy shift of ~0.4 eV (**Fig. A.2D**).

The photoinduced changes at the Re O_2 edge can be understood as a mixed contribution from photoexcited electrons, holes, and band gap dynamics. To quantify their relative contribution, we apply a singular value decomposition (SVD), described in more detail in **A.S3**. The first component is best described by hole thermalization in the VBs, as demonstrated by our BSE theory in **Figure A.2C (top)**. The second and third components are well described by band gap renormalization (BGR) and absorption by electrons in the CBs. In addition to photoexcited electron and hole dynamics, SVD reveals that BGR is observed around ~46.5 eV. Microscopically, photoexcitation modifies the Coulomb screening, reducing the band gap.[35] The reduction of the minimum band gap enables XUV transition into the otherwise forbidden gap region, causing a red shift of the XUV transition to the CB immediately following photoexcitation.

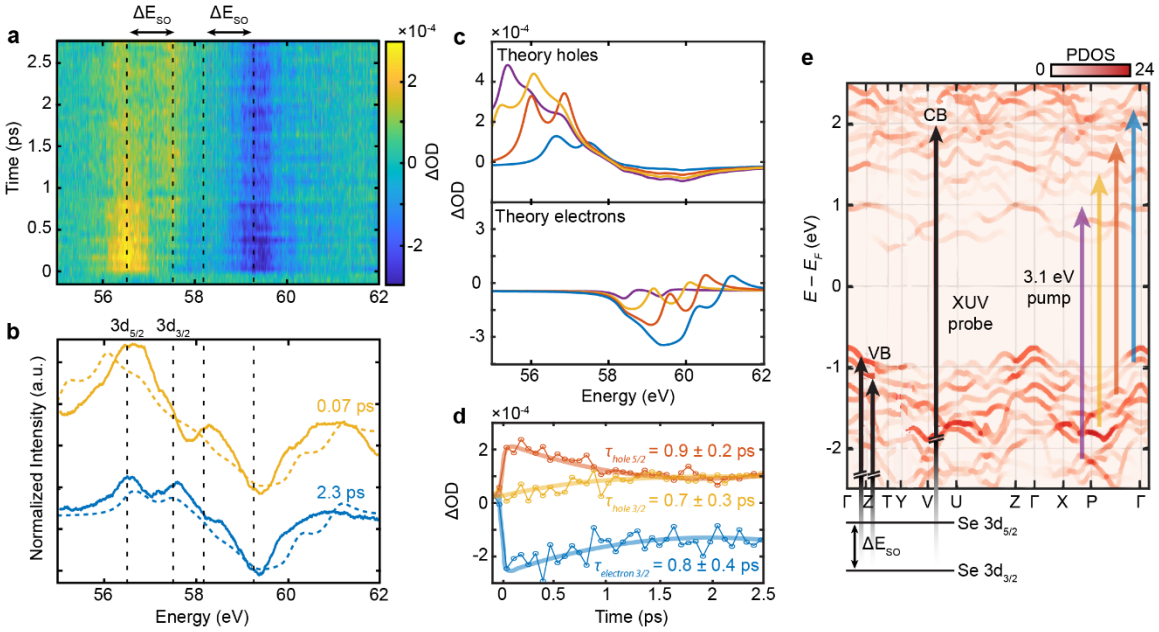

Figure A.3 Carrier relaxation dynamics in Se. (A) Transient XUV reflection-absorption spectra at the Se $M_{4,5}$ edge. **(B)** Experimental and BSE calculated transient differential absorption spectra, shown as solid and dashed lines, respectively, at two time delays ($\Delta t = 0.07$ and 2.3 ps) following photoexcitation. The Se $3d_{5/2}$ and $3d_{3/2}$ transitions are depicted as vertical dashed black lines, with one pair denoting transitions to the VBs and the other pair denoting CB transitions. **(C)** As in **Figure A.2C**, BSE theory calculated spectra for holes **(top)** and electrons **(bottom)** uses a state-filling model in which $E_h \leq 3.1$ eV, and $E_e \leq 3.1$ eV. The modeled holes correspond to holes filling 3.1 eV (purple), 2.5 eV (yellow), 2.0 eV (orange), and 1.5 eV (blue) below the CBM. The modeled electrons correspond to electrons filling to 3.1 eV (blue), 2.5 eV (orange), 2.0 eV (yellow), and 1.5 eV (purple) above the VBM. **(D)** Kinetic profiles for thermalization of holes and electrons at Se sites. The feature at ~56.5 eV attributed to a Se $3d_{5/2}$ transition to the VB has a time constant of 0.9 ± 0.2 ps (red). The feature at ~57.5 eV associated with a Se $3d_{3/2}$ transition to the VB increases in intensity with a time constant of 0.7 ± 0.3 ps (yellow). The electrons in the CB at ~59.3 eV have a thermalization time constant of 0.8 ± 0.4. **(E)** Atom-projected band structure for Se atoms where the color scale of the band structure indicates the PDOS of Se and the colored arrows (right) depict the corresponding state-filling electron and hole energies that are modeled in **(C)**.

We performed similar transient XUV reflectance measurements at the Se $M_{4,5}$ edges around ~57 eV (**Fig. A.3A**) and find that the spectral response at the Se $M_{4,5}$ edge is qualitatively different from the Re O_2 edge. Immediately after photoexcitation, there is a transient increase in XUV absorption around ~56.5 eV, and two transient decreases in absorption are present at ~58.1 eV and ~59.3 eV, respectively (**Fig. A.3B**, yellow solid line). At longer pump-probe time delays, the reduced absorption at ~58.1 eV disappears, and an increased absorption feature appears at ~57.5 eV (**Fig. A.3B**, blue solid line).

The transient XUV spectra at the Se $M_{4,5}$ edges reflect local carrier densities around Se atoms and can be understood through photoexcited state-filling effects.[33,34] The Se $M_{4,5}$ edge consists of core-to-valence transitions from two spin-orbit separated Se 3 core levels, $3d_{3/2}$ and $3d_{5/2}$, with ~ 1 eV energy spacing.[36] We assign the transient reflectance changes at ~57.5 eV and ~59.3 eV to an XUV transition from the Se $3d_{3/2}$ core-level to the VBs and CBs, respectively. Similarly, spectral changes at ~56.5 eV and ~58.1 eV are assigned to XUV transitions from the Se $3d_{5/2}$ core level. The ~1 eV spacing of the spin-orbit transitions is consistent with our measured and BSE calculated ground-state core-level absorption spectra shown in **Figure A.S3** in the **Supporting Information**.

We further deconvolve the transient dynamics of $Re_6Se_8Cl_2$ at the Se $M_{4,5}$ edges through BSE modeling of photoexcited thermalization dynamics. **Figure A.3B** compares BSE modeled transient dynamics and experimental lineouts immediately after photoexcitation (0.07 ps) and following thermalization (2.3 ps). The modeled lineout immediately following photoexcitation is based upon state-filling of electrons up to 3.1 eV above the VBM. In comparison, a hole cutoff energy of 2.5 eV best agrees with the experimental lineout at 0.07 ps (**Fig. A.3B**, yellow dashed line). For lineouts following carrier thermalization (**Fig. A.3B**, blue dashed line), BSE state-filling of an electron cutoff energy of 3.1 eV and a hole cutoff energy of 1.5 eV best agree with experiment. This suggests that, like carriers at the Re O_2 edge, there is little to no electron thermalization, while the holes do thermalize.

The lack of a clear Se $M_{4,5}$ edge thermalization signal is consistent with our BSE modeling indicating that the photoexcited electrons remain well above the CBM over the temporal duration sampled. This suggests limited electron thermalization toward the band edge, or electron redistribution within relatively flat CBs of similar Se character that can only be weakly distinguished at the Se edge. Further, this suggests the Se $M_{4,5}$ edge's sensitivity to higher energy CBs than the Re edge, as BSE state-filling of electrons at the Re edge agree better with spectra at lower electron cutoff energies (**Fig. A.3C**). We fit the thermalization

of holes at the Se M_5 edge, an increase in hole signal at the Se M_4 edge, and a decrease in electron signal at the M_4 edge in Figure A.3D.

The element-specific dynamics at Re and Se atoms can be further used to infer the distribution of photoexcited carriers in the excited state. As shown in **Figures A.2** and **A.3**, photoexcited electrons are distributed on both Re and Se atoms. Meanwhile, based on the atomic projected band structure (**Fig. A.1C**), transient spectra (**Figs. A.2A** and **A.3A**), and BSE calculations (**Figs. A.2B** and **A.3B**), we observe that the initial hole states have strong Re orbital contributions. This observation is consistent with our experimental findings that hot holes occur predominantly at the Re sites after photoexcitation and our BSE theory that requires 0.6 eV higher hole cutoff energies on Re sites than Se sites to agree with experiment. As hot holes thermalize at the Re edge, a spectral crossing appears at the Se edge from ~57–58 eV (**Fig. A.3A**), where the initial electron spectral weight (blue) after photoexcitation is transferred to holes (yellow) at later times.

This spectral crossing at Se edge could be intuitively understood as a transient increase in hole concentration around the Se atoms during carrier diffusion. Schematically, during the hole thermalization, hot holes migrate from the initial photoexcited states towards the Γ point at the top of the VB, which has increasing contributions from Se atoms (**Fig. A.1C**). The net effect of hot hole thermalization is equivalent to hot hole transfer from Re to Se atoms in the unit cell. Given that the spectral crossing timescale at Se sites is comparable to the hole thermalization time at the Re edge (**Figs. A.2D** and **A.3D**), this suggests that the hole transfer from Re to Se atoms slows down overall hole diffusion at Se sites, which leads to the observed spectral crossing at the Se edge.

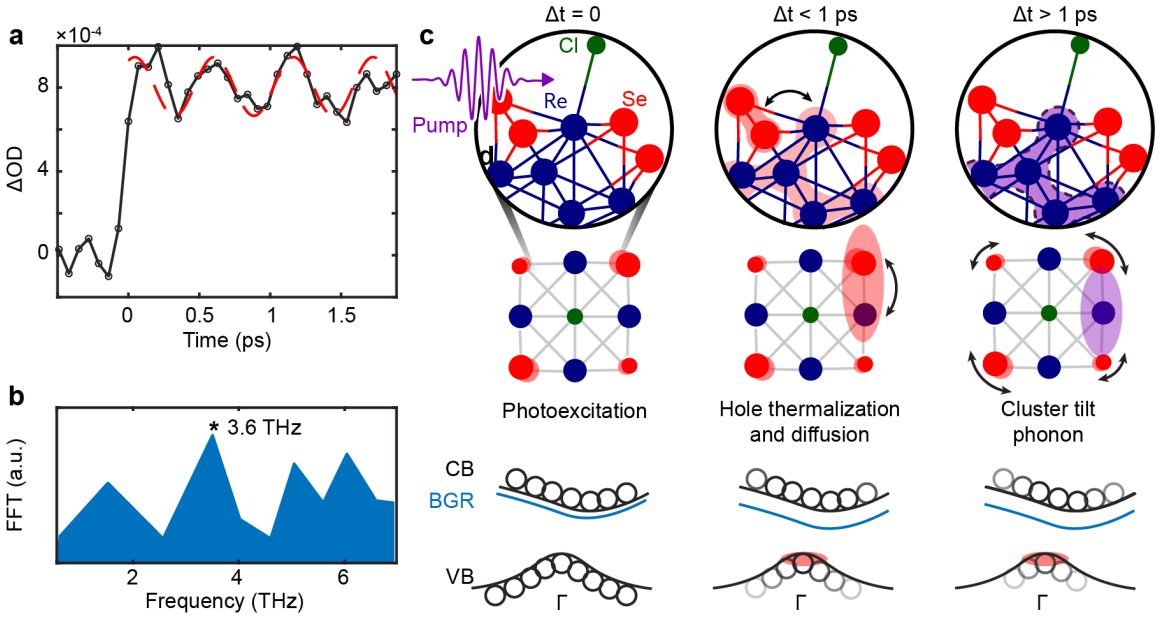

Figure A.4 Ultrafast hole thermalization, diffusion, and phonon oscillations in $Re_6Se_8Cl_2$. **(A)** Kinetic profile of intensity oscillation averaged across ~45.9 – 46.3 eV, fitted with a sine function (dashed red line). The oscillation period is measured to be 270 fs, which corresponds to 3.6 THz as shown in panel **B**. **(B)** Fast Fourier transform (FFT) of the kinetic profile in panel **A**. The highest amplitude oscillation frequency is indicated with an asterisk. **(C)** Overall schematics for the photoinduced electronic dynamics in $Re_6Se_8Cl_2$. The atomic view of the time-evolution of the photoexcited states **(top)**, two-dimensional view of the clusters **(middle)**, and charge carrier dynamics depicted onto a simplified band structure **(bottom)**. The element- and carrier-sensitive XUV probe enables elucidation of the initial charge carrier distribution in the VB and CB, and their relaxation dynamics with coupling to displacive phonons. The cluster tilt phonon mode accompanies vibrations of the Se atoms at the corner, leading to the in-plane distortion of a cluster.

We measure phonon oscillations in our transient XUV absorption spectra at the Re O_2 edge (**Fig. A.2A**). The kinetic profile and a fit curve display a time-dependent modulation of intensity with a periodicity of 270 fs (3.6 THz) (**Fig. A.4A**). The periodicity aligns with a coherent phonon motion associated with the twisting of superatomic clusters in an $Re_6Se_8Cl_2$ layer, primarily driven by the displacement of the corner Se atoms (**Figs. A.4B** and **A.4C**).[18] These two-dimensional phonon modes, fall within the frequency range of 1.69–5.25 THz and can be linked to the electronic modulation of free charge carriers. The oscillation has a cosine character at t_0 that suggests the mechanism of this oscillation is due to displacive excitation of coherent phonons (DECP) rather than impulsive stimulated Raman scattering (ISRS).[18,37,38] Specifically, this coherent oscillation is only present in the positive absorption signal at the Re O_2 edge, suggesting that DECP is hole-mediated.[39] Mechanistically, this can be understood as photoexcited holes transporting through metallic sites from Re to Se atoms

in $Re_6Se_8Cl_2$ single crystals and the thermalization and the associated intravalley charge redistribution dynamics across different momenta mediate coherent phonon oscillations, facilitating energy dissipation.

Although the coupling between clusters in $Re_6Se_8Cl_2$is generally less favorable compared to others in its family,[5,40] the coupling between photoexcited electrons and long-range two-dimensional phonons, such as twisting modes, and acoustic polarons from the Holstein–Peierls model,[41] can lead to further flattening of the CB. Consequently, this results in the exceptionally low-loss quasi-ballistic transport behavior in $Re_6Se_8Cl_2$, as has been reported in other studies.[17,24] Notably, hole thermalization is observed at both the Re O_2 and Se $M_{4,5}$ edges in the more dispersive VBs, while electron thermalization is minimal in the flat CBs. Our consensus is that the electrons experience very little relative thermalization in energy compared to holes in the $Re_6Se_8Cl_2$ superatomic crystal, suggesting that the VBs are much more curved and delocalized than the CBs. We further find that hole transport from Re to Se atoms displacively excites coherent cluster twisting phonons, which facilitate energy transfer towards adjacent interclusters within 2D metal layers.

A.4 Conclusion

In summary, we report transient XUV reflection-absorption spectroscopy on the photoexcited dynamics in $Re_6Se_8Cl_2$ superatomic crystals. Photoinduced electron, hole, phonon, and band gap dynamics are observed and separated at both Re and Se sites. By correlating the ultrafast dynamics at Re and Se atoms, we infer the existence of flat conduction bands and identify an ultrafast hole transfer from Re to Se atoms. Our results provide a detailed picture of element- and carrier-specific dynamics in superatomic crystals, as well as new insights into the real-space charge transfer processes in $Re_6Se_8Cl_2$, paving the way for a deeper understanding of more complex many-body interactions in superatomic crystals. These observations underscore the impact of nonequilibrium many-body effects and enhance the understanding of photoexcited electron and hole dynamics across different elements in superatomic crystals. These insights are vital for advancing the application of

novel photophysics and for driving the development of exotic phases, such as doping-induced superconductivity,[9] in superatomic crystals.

A.5 References

(1) Pinkard, A.; Champsaur, A. M.; Roy, X. Molecular Clusters: Nanoscale Building Blocks for Solid-State Materials. *Acc. Chem. Res.* **2018**, *51* (4), 919–929. https://doi.org/10.1021/acs.accounts.8b00016.

(2) Doud, E. A.; Voevodin, A.; Hochuli, T. J.; Champsaur, A. M.; Nuckolls, C.; Roy, X. Superatoms in Materials Science. *Nat. Rev. Mater.* **2020**, *5* (5), 371–387. https://doi.org/10.1038/s41578-019-0175-3.

(3) Fang, H.; Sun, Q.; Jena, P. Cluster-Based Materials: Design and Applications. *Chem. Soc. Rev.* **2026.** https://doi.org/10.1039/D5CS00663E.

(4) Li, Z.; Xu, Z.; Ao, L.; Chen, P.; Sun, Q.; Ding, H.; Wang, Z.; Duan, S.; Bi, X.; Zhou, L.; Li, Q.; Ong, C.-S.; Tang, P.; Yuan, H. Hierarchical Structure Control And Unconventional Thermal Response of Excitonic Emission in a Superatomic Semiconductor. *Adv. Funct. Mater.* **2025.** https://doi.org/10.1002/adfm.202523687.

(5) Zhong, X.; Lee, K.; Choi, B.; Meggiolaro, D.; Liu, F.; Nuckolls, C.; Pasupathy, A.; De Angelis, F.; Batail, P.; Roy, X.; Zhu, X. Superatomic Two-Dimensional Semiconductor. *Nano Lett.* **2018**, *18* (2), 1483–1488. https://doi.org/10.1021/acs.nanolett.7b05278.

(6) Kim, H.; Lee, K.; Dismukes, A. H.; Choi, B.; Roy, X.; Zhu, X.; Bonn, M. Charge Carrier Scattering and Ultrafast Auger Dynamics in Two-Dimensional Superatomic Semiconductors. *Appl. Phys. Lett*. **2020**, *116* (20), 201109. https://doi.org/10.1063/5.0001839.

(7) Ogura, K. S.; Cordova, D. L. M.; Aoki, T.; Milligan, G. M.; Yao, Z.-F.; Arguilla, M. Q. Functionalization and Structural Evolution of Conducting Quasi-One-Dimensional Chevrel-Type Telluride Nanocrystals. *Chem. Mater.* **2024**, *36* (9), 4714–4725. https://doi.org/10.1021/acs.chemmater.4c00468.

(8) He, S.; Evans, A. M.; Meirzadeh, E.; Han, S. Y.; Russell, J. C.; Wiscons, R. A.; Bartholomew, A. K.; Reed, D. A.; Zangiabadi, A.; Steigerwald, M. L.; Nuckolls, C.; Roy, X. Site-Selective Surface Modification of 2D Superatomic Re_6Se_8. *J. Am. Chem. Soc.* **2022**, *144* (1), 74–79. https://doi.org/10.1021/jacs.1c10833.

(9) Telford, E. J.; Russell, J. C.; Swann, J. R.; Fowler, B.; Wang, X.; Lee, K.; Zangiabadi, A.; Watanabe, K.; Taniguchi, T.; Nuckolls, C.; Batail, P.; Zhu, X.; Malen, J. A.; Dean, C. R.; Roy, X. Doping-Induced Superconductivity in the Van Der Waals Superatomic Crystal $Re_6Se_8Cl_2$. *Nano Lett.* **2020**, *20* (3), 1718–1724. https://doi.org/10.1021/acs.nanolett.9b04891.

(10) Reber, A. C.; Khanna, S. N. Superatoms: Electronic and Geometric Effects on Reactivity. *Acc. Chem. Res.* **2017**, *50* (2), 255–263. https://doi.org/10.1021/acs.accounts.6b00464.

(11) Xie, S.; Ni, K.; Zhu, Y. Electronic Properties of Carbon-Based Superatomic Structures. *Adv. Funct. Mater.* **2025.** https://doi.org/10.1002/adfm.202508106.

(12) Yang, M.; Wang, Y.; Deng, J.; Ying, T.; Zhang, Q.; Liang, N.; Liu, X.; Song, B.; Guo, J.; Chen, X. Intrinsically Ultralow Thermal Conductivity in All-Inorganic Superatomic Bulk Crystals. *Appl. Phys. Rev.* **2026**, *13* (1), 011433. https://doi.org/10.1063/5.0309916.

(13) Ong, W.-L.; O'Brien, E. S.; Dougherty, P. S. M.; Paley, D. W.; Higgs, C. F., III; McGaughey, A. J. H.; Malen, J. A.; Roy, X. Orientational Order Controls Crystalline and Amorphous Thermal Transport in Superatomic Crystals. *Nat. Mater*. **2017**, *16* (1), 83–88. https://doi.org/10.1038/nmat4739.

(14) Yu, F.; Yang, X.; Li, R.; Liu, R.; Wan, C.; Dai, Y.; Wang, Z. Super-Defects in Superatomic Crystals. *Acta Mater*. **2024**, 275, 120047. https://doi.org/10.1016/j.actamat.2024.120047.

(15) Luo, Z.; Castleman, A. W. Special and General Superatoms. *Acc. Chem. Res.* **2014**, *47* (10), 2931–2940. https://doi.org/10.1021/ar5001583.

(16) Li, T.; Du, P.-H.; Bai, L.; Sun, Q.; Jena, P. Thermoelectric Figure of Merit of a Superatomic Crystal $Re_6Se_8I_2$ Monolayer. *Phys. Rev. Appl.* **2022**, *18* (6), 064067. https://doi.org/10.1103/PhysRevApplied.18.064067.

(17) Tulyagankhodjaev, J. A.; Shih, P.; Yu, J.; Russell, J. C.; Chica, D. G.; Reynoso, M. E.; Su, H.; Stenor, A. C.; Roy, X.; Berkelbach, T. C.; Delor, M. Room-Temperature Wavelike Exciton Transport in a Van Der Waals Superatomic Semiconductor. *Science* **2023**, *382* (6669), 438–442. https://doi.org/10.1126/science.adf2698.

(18) Lee, K.; Maehrlein, S. F.; Zhong, X.; Meggiolaro, D.; Russell, J. C.; Reed, D. A.; Choi, B.; De Angelis, F.; Roy, X.; Zhu, X. Hierarchical Coherent Phonons in a Superatomic Semiconductor. *Adv. Mater.* **2019**, *31* (36), 1903209. https://doi.org/10.1002/adma.201903209.

(19) Xing, S.; Wu, L.; Wang, Z.; Chen, X.; Liu, H.; Han, S.; Lei, L.; Zhou, L.; Zheng, Q.; Huang, L.; Lin, X.; Chen, S.; Xie, L.; Chen, X.; Gao, H.-J.; Cheng, Z.; Guo, J.; Wang, S.; Ji, W. Interweaving Polar Charge Orders in a Layered Metallic Superatomic Crystal. *Phys. Rev. X* **2022**, *12* (4), 041034. https://doi.org/10.1103/PhysRevX.12.041034.

(20) Chen, X.; Fei, G.; Song, Y.; Ying, T.; Huang, D.; Pan, B.; Yang, D.; Yang, X.; Chen, K.; Zhan, X.; Wang, J.; Zhang, Q.; Li, Y.; Gu, L.; Gou, H.; Chen, X.; Li, S.; Cheng, J.; Liu, X.; Hosono, H.; Guo, J.; Chen, X. Superatomic Charge-Density-Wave in Cluster-Assembled $Au_6Te_{12}Se_8$ Superconductors. *J. Am. Chem. Soc.* **2022**, *144* (45), 20915–20922. https://doi.org/10.1021/jacs.2c09499.

(21) Ikeda, M.; Zhang, Z.; Goto, H.; Eguchi, R.; Liao, Y.-F.; Ishii, H.; Kubozono, Y. Pressure Dependence of Superconductivity in a Charge-Density-Wave Superconductor $Bi_2Rh_3Se_2$. *Inorg. Chem.* **2023**, *62* (19), 7453–7460. https://doi.org/10.1021/acs.inorgchem.3c00744.

(22) Liu, Z.; Li, Y.; Kahng, E.; Xue, S.; Du, X.; Li, S.; Jin, R. Tailoring the Electron–Phonon Interaction In $Au_{25}(SR)_{18}$ Nanoclusters Via Ligand Engineering and Insight into Luminescence. *ACS Nano* **2022**, *16* (11), 18448–18458. https://doi.org/10.1021/acsnano.2c06586.

(23) Du, P.-H.; Zhang, C.; Sun, J.; Li, T.; Sun, Q. Phase Stability, Strong Four-Phonon Scattering, And Low Lattice Thermal Conductivity in Superatom-Based Superionic Conductor Na_3OBH_4. *ACS Appl. Mater. Interfaces* **2022**, *14* (42), 47882–47891. https://doi.org/10.1021/acsami.2c14435.

(24) Shih, P.; Berkelbach, T. C. Theory of Acoustic Polarons in the Two-Dimensional SSH Model Applied To the Layered Superatomic Semiconductor $Re_6Se_8Cl_2$. *J. Chem. Phys.* **2024**, *160* (20), 204705. https://doi.org/10.1063/5.0205066.

(25) Zeng, X.; Niu, G.; Wang, X.; Jiang, J.; Sui, L.; Zhang, Y.; Chen, A.; Jin, M.; Yuan, K. Strain-Engineered Thermoelectric Performance in Superatomic Semiconductor $Re_6Se_8Cl_2$: The Role of Four-Phonon Scattering and Coherent Phonons. *J. Phys. Chem. Lett.* **2025**, *16* (12), 3122–3132. https://doi.org/10.1021/acs.jpclett.5c00404.

(26) Xiong, W.; Huang, H.; Wu, Y.; Xu, X.; Li, G.; Gu, Z.; Zeng, S. Decoupling Ultralow Coherent and Particle-Like Phonon Transport via Bonding Hierarchy in Soft Superionic Crystals. *Adv. Sci.* **2025**, *12* (31), e06807. https://doi.org/10.1002/advs.202506807.

(27) Zong, A.; Nebgen, B. R.; Lin, S.-C.; Spies, J. A.; Zuerch, M. Emerging Ultrafast Techniques for Studying Quantum Materials. *Nat. Rev. Mater.* **2023**, *8* (4), 224–240. https://doi.org/10.1038/s41578-022-00530-0.

(28) Giannozzi, P.; Baroni, S.; Bonini, N.; Calandra, M.; Car, R.; Cavazzoni, C.; Ceresoli, D.; Chiarotti, G. L.; Cococcioni, M.; Dabo, I.; Corso, A. D.; de Gironcoli, S.; Fabris, S.; Fratesi, G.; Gebauer, R.; Gerstmann, U.; Gougoussis, C.; Kokalj, A.; Lazzeri, M.; Martin-Samos, L.; Marzari, N.; Mauri, F.; Mazzarello, R.; Paolini, S.; Pasquarello, A.; Paulatto, L.; Sbraccia, C.; Scandolo, S.; Sclauzero, G.; Seitsonen, A. P.; Smogunov, A.; Umari, P.; Wentzcovitch, R. M. QUANTUM ESPRESSO: A Modular and Open-source Software Project for Quantum Simulations of Materials. *J. Phys. Condens. Matter* **2009**, *21* (39), 395502. https://doi.org/10.1088/0953-8984/21/39/395502.

(29) Giannozzi, P.; Andreussi, O.; Brumme, T.; Bunau, O.; Buongiorno Nardelli, M.; Calandra, M.; Car, R.; Cavazzoni, C.; Ceresoli, D.; Cococcioni, M.; Colonna, N.; Carnimeo, I.; Dal Corso, A.; de Gironcoli, S.;

Delugas, P.; DiStasio, R. A.; Ferretti, A.; Floris, A.; Fratesi, G.; Fugallo, G.; Gebauer, R.; Gerstmann, U.; Giustino, F.; Gorni, T.; Jia, J.; Kawamura, M.; Ko, H.-Y.; Kokalj, A.; Küçükbenli, E.; Lazzeri, M.; Marsili, M.; Marzari, N.; Mauri, F.; Nguyen, N. L.; Nguyen, H.-V.; Otero-de-la-Roza, A.; Paulatto, L.; Poncé, S.; Rocca, D.; Sabatini, R.; Santra, B.; Schlipf, M.; Seitsonen, A. P.; Smogunov, A.; Timrov, I.; Thonhauser, T.; Umari, P.; Vast, N.; Wu, X.; Baroni, S. Advanced Capabilities for Materials Modelling with Quantum ESPRESSO. *J. Phys. Condens. Matter* **2017**, *29* (46), 465901. https://doi.org/10.1088/1361-648X/aa8f79.

(30) Gilmore, K.; Vinson, J.; Shirley, E. L.; Prendergast, D.; Pemmaraju, C. D.; Kas, J. J.; Vila, F. D.; Rehr, J. J. Efficient Implementation of Core-Excitation Bethe–Salpeter Equation Calculations. *Comput. Phys. Commun.* **2015**, *197*, 109–117. https://doi.org/10.1016/j.cpc.2015.08.014.

(31) Vinson, J. Advances in the OCEAN-3 Spectroscopy Package. *Phys. Chem. Chem. Phys.* **2022**, *24* (21), 12787–12803. https://doi.org/10.1039/D2CP01030E.

(32) Vinson, J.; Rehr, J. J.; Kas, J. J.; Shirley, E. L. Bethe-Salpeter Equation Calculations of Core Excitation Spectra. *Phys. Rev. B* **2011**, *83* (11), 115106. https://doi.org/10.1103/PhysRevB.83.115106.

(33) Klein, I. M.; Krotz, A.; Lee, W.; Michelsen, J. M.; Cushing, S. K. Ab Initio Calculations of XUV Ground and Excited States for First-Row Transition Metal Oxides. *J. Phys. Chem. C* **2023**, *127* (2), 1077–1086. https://doi.org/10.1021/acs.jpcc.2c06548.

(34) Molesky, I. J. P.; Lee, A.; Cushing, S. K.; Chang, H.-T.; Ondry, J. C.; Alivisatos, A. P.; Leone, S. R. Characterization of Carrier Cooling Bottleneck in Silicon Nanoparticles by Extreme Ultraviolet (XUV) Transient Absorption Spectroscopy. *J. Phys. Chem. C* **2021**, *125* (17), 9319–9329. https://doi.org/10.1021/acs.jpcc.1c02101.

(35) Rossi, T. C.; Qiao, L.; Dykstra, C. P.; Rodrigues Pela, R.; Gnewkow, R.; Wallick, R. F.; Burke, J. H.; Nicholas, E.; March, A. M.; Doumy, G.; Buchholz, D. B.; Deparis, C.; Zúñiga-Pérez, J.; Weise, M.; Ellmer, K.; Fondell, M.; Draxl, C.; van der Veen, R. M. Dynamic Control of X-Ray Core-Exciton Resonances by Coulomb Screening in Photoexcited Semiconductors. *Commun. Mater.* **2025**, *6* (1), 191. https://doi.org/10.1038/s43246-025-00909-w.

(36) Clancy, J. P.; Chen, N.; Kim, C. Y.; Chen, W. F.; Plumb, K. W.; Jeon, B. C.; Noh, T. W.; Kim, Y.-J. Spin-Orbit Coupling in Iridium-Based 5d Compounds Probed by X-Ray Absorption Spectroscopy. *Phys. Rev. B* **2012**, *86* (19), 195131. https://doi.org/10.1103/PhysRevB.86.195131.

(37) Zeiger, H. J.; Vidal, J.; Cheng, T. K.; Ippen, E. P.; Dresselhaus, G.; Dresselhaus, M. S. Theory for Displacive Excitation of Coherent Phonons. *Phys. Rev. B* **1992**, *45* (2), 768–778. https://doi.org/10.1103/PhysRevB.45.768.

(38) Stevens, T. E.; Kuhl, J.; Merlin, R. Coherent Phonon Generation and the Two Stimulated Raman Tensors. *Phys. Rev. B* **2002**, *65* (14), 144304. https://doi.org/10.1103/PhysRevB.65.144304.

(39) Adelman, J. R.; Laurell, H.; Drescher, L. B.; Le, H. K. D.; Yang, P.; Leone, S. R. Coherently Coupled Carrier and Phonon Dynamics in Elemental Tellurium Probed by Extreme Ultraviolet Transient Absorption. *Phys. Rev. B* **2025**, *111* (18), 184315. https://doi.org/10.1103/PhysRevB.111.184315.

(40) Li, Q.; Liu, F.; Russell, J. C.; Roy, X.; Zhu, X. Strong Polaronic Effect in a Superatomic Two-Dimensional Semiconductor. *J. Chem. Phys.* **2020**, *152* (17), 171101. https://doi.org/10.1063/5.0006455.

(41) Mozafari, E.; Stafström, S. Polaron Dynamics in a Two-Dimensional Holstein-Peierls System. *J. Chem. Phys.* **2013**, *138* (18), 184104. https://doi.org/10.1063/1.4803691.

A.S1 $Re_6Se_8Cl_2$ Sample Preparation

$Re_6Se_8Cl_2$ crystals were synthesized via chemical vapor transport adapted from previous reports.[42,43] Re (330 mg, 1.77 mmol), Se (190 mg, 2.41 mmol) and $ReCl_5$ (200 mg, 0.55 mmol) were ground and mixed using an agate mortar inside the glove box, and subsequently pressed into a pellet. The pellet was sealed in a 20 cm quartz tube under vacuum and heated in a tube furnace at a rate of 1 °C/min to 1100 °C for 3 days. To achieve large single crystals, the tube was then cooled over six hours to a temperature gradient of 1100–1030 °C and held for 270 hours. The tube was further cooled to room temperature over 12 hours, and the furnace was then shut off. To extract pristine $Re_6Se_8Cl_2$ single crystals, a gradient of 300–25 °C was used to separate any excess volatile components, yielding ~1–3 mm single crystals at the top section of the tube. Typical bulk samples have a few millimeters in lateral dimensions. **Figure A.S1** shows a picture of a typical sample piece used in the transient XUV experiments.

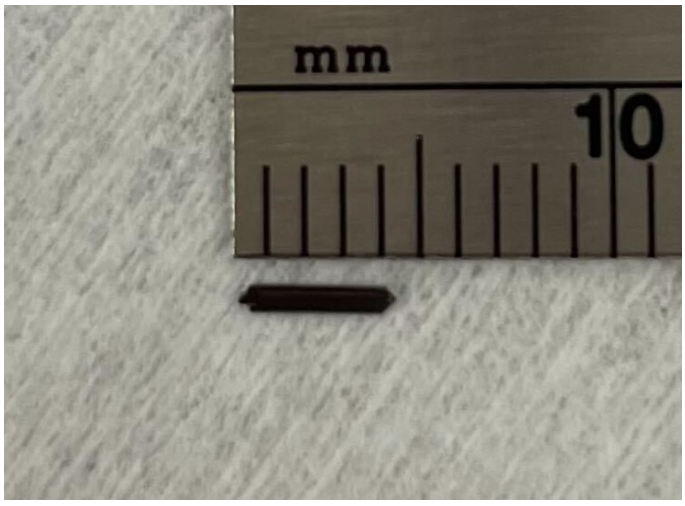

Figure A.S1 A typical mm-size single crystalline bulk $Re_6Se_8Cl_2$ sample used in our transient XUV measurements.

A.S2 Transient Extreme Ultraviolet Spectrometer

The transient extreme ultraviolet (XUV) reflection-absorption spectrometer is described previously.[44–46] Briefly, a Legend Elite Duo Ti:Sapphire system (Coherent Inc.) with 1 kHz, 35 fs, 13 mJ pulses centered around 800 nm is split by a 75:25 beam splitter. ~3 mJ generates

a few-cycle white light beam (<6 fs, 550–950) for high harmonic generation (HHG) and ~10 mJ is used for the pump path. The pump path employs the 400 nm frequency doubled output of a BBO crystal with p-polarization, pumped with the 800 nm output from the Ti:Sapphire laser for an above band gap photoexcitation of the Re6Se8Cl2 single crystals. The optical excitation fluence used in these experiments was ~9 mJ/cm^2, resulting in an excited carrier density of ~4.1 x 10^{21} cm^{-3}.[47]

Transient reflection is measured at a 10° grazing incidence (80° from normal incidence) geometry and measures the varying delay times between the pump and probe pulses using an optomechanical delay stage. The photoexcited dynamics were probed with an XUV pulse produced through HHG in argon with an s-polarized few-cycle white light pulse driving HHG. The fundamental white light beam is removed with a 100 nm thick Al filter (Luxel). The generated XUV continuum is used to probe the Re O_2 and Se $M_{4,5}$ absorption edges between 40–60 eV. An edge-pixel referencing scheme uses signal free spectral regions to denoise intensity fluctuations in the spectra.[48]

A.S3 Spectral Analysis

The transient XUV spectra at the Re O_2 edge consists of contributions from electrons, holes, and band shifts. We apply singular value decomposition (SVD) to all pump-probe delays within the transient spectrum to extract the weights of relevant dynamics and reconstruct the transient spectrum at the Re O_2 edge using the fewest number of singular values. The SVD analysis factorizes the two-dimensional matrix of the transient spectrum by rotating (U), scaling (S), and then again rotating (V) the matrix. The scaling matrix contains the singular values along its diagonal, which we refer to as the number of components. The number of singular values or components in the scaling matrix is selected to minimize the total number of singular values, where at the Re O_2 edge three singular values are needed.

Following SVD, we ascribe component 1 to holes, component 2 to electrons, and component 3 to band gap renormalization (BGR). **Figure A.S2** shows the components of the SVD analysis. Component 1 well describes excited state hole effects, attributed to an increase in

absorption at the edge. Due to the minimal band gap renormalization shift, and minimal thermalization in the electron component with respect to time, components 2 and 3 are combined in a weighted average to visualize not only the spectral shift associated with BGR but also minimal electron thermalization. It is worth noting that the lineouts in component 1 are an order of magnitude more intense than those in the weighted average of components 2 and 3. The reconstructed spectra in **Figure A.S2C** is well described by three components, where the band gap renormalization shift is not observed with less than three components.

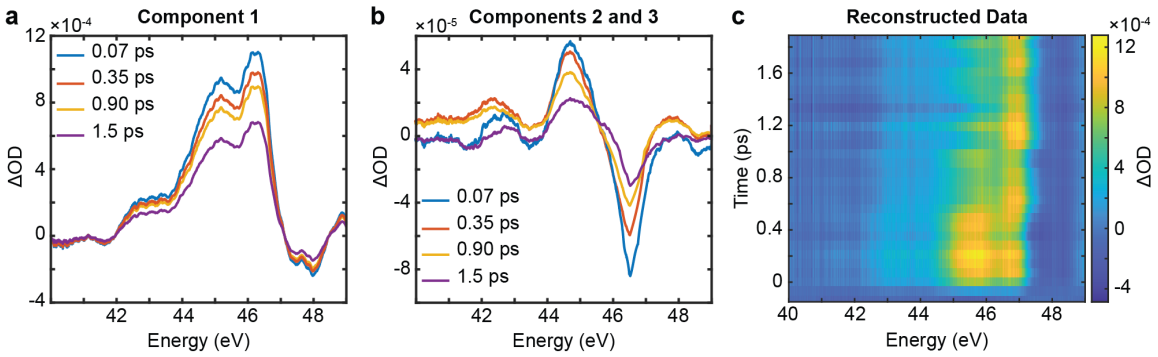

Figure A.S2 Component 1 **(A)** of the SVD analysis at the Re O_2 edge. Components 2 and 3 **(B)** are plotted as a weighted average as they are an order of magnitude weaker than component 1. The SVD reconstruction **(C)** agrees with transient XUV spectra of the Re O_2 edge shown in **Figure A.2A** in the main text.

A.S4 Ab Initio Modeling

A.S4.A Density Functional Theory

Geometry optimization and density functional theory (DFT) calculations were conducted using the Quantum ESPRESSO package with norm-conserving general gradient approximation (GGA), Perdew– Burke–Ernzerhof (PBE) pseudopotentials.[28,29,49] Geometry optimizations employed an input Re6Se8Cl2 unit cell containing 16 atoms and were based upon the lattice parameters $a = b = c = 6.67$ Å. A 300 Rydberg kinetic energy cutoff and an 8 × 8 × 8 Monkhorst– Pack k-mesh sampling of the first Brillouin zone was used to sample 250 bands. The structures employed in the DFT and BSE calculations described below were fully relaxed and calculations were performed to a convergence of 10^{-8} eV/atom with the forces on ions under 10^{-3} eV/Å.

A.S4.B Bethe–Salpeter Equation Theory of Core-Level Spectra

The fully relaxed parameters used in the DFT calculations discussed in **A.S4.A** were applied to the BSE calculations of the $Re_6Se_8Cl_2$ ground state reflectivity at the Re O_2 and Se $M_{4,5}$ edges. The method uses Quantum ESPRESSO[28,29] and an excited state modification to the OCEAN (Obtaining Core Excitations from the Ab initio electronic structure and the NIST BSE solver) code.[30–32] The BSE calculation employed a screening mesh of 2 × 2 × 2, a dielectric constant of 21.8 at 293 K, a 4.0 Bohr screening radius, and a 0.7 scaling factor for the Slater G parameter. A spectral broadening of 0.25 eV was applied for all calculated spectra.

The calculated ground state reflectivity of $Re_6Se_8Cl_2$ is plotted in **Figure A.S3** and is compared to experimentally measured XUV ground states at either edge. As shown in **Figure A.S3**, the BSE calculated ground state agrees well with the measured ground state reflectivity of the sample.

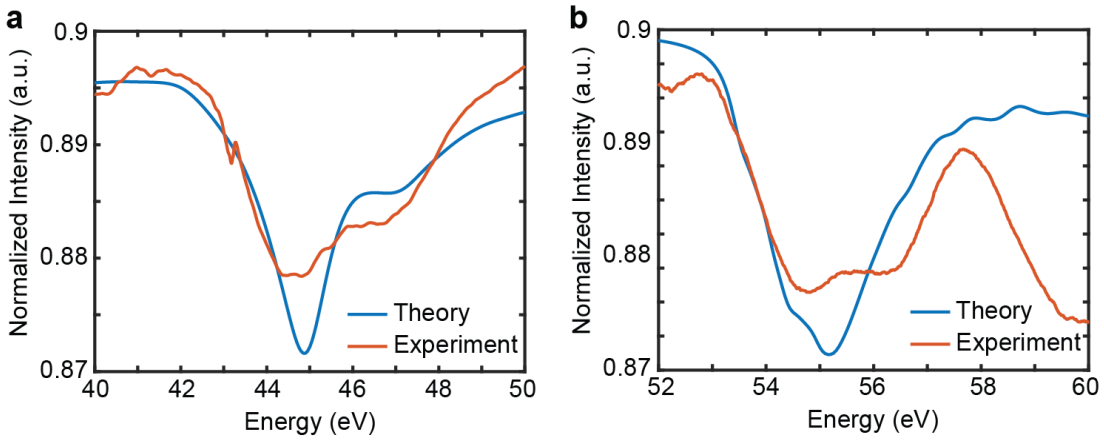

Figure A.S3 Ground state reflectivity at the **(A)** Re O_2 and **(B)** the Se $M_{4,5}$ edges. BSE theory of the edges (blue) is compared to experimental static XUV reflectivity (orange) for good agreement.

Following ground state calculations of the XUV reflectivity as the Re O_2 and Se $M_{4,5}$ edges, excited state calculations were performed using a modification to the OCEAN code discussed previously.[33] The modification to the OCEAN code enables selective excitation to valence and conduction bands at different points in momentum space, to simulate state-filling of electrons and holes following photoexcitation. To model above band gap photoexcitation,

we populate the conduction band with electrons and similarly populate the valence band with holes to model the state-filling of carriers following photoexcitation. This population of electrons and holes effectively forbids or allows XUV transitions to specific points in k-space but does not account for carrier density, therefore, the modeled peak position and relative intensity is used to compare experiment to theory. We model our transient XUV spectra by calculating the differential absorption between the calculated ground state and the calculated excited state spectra. **Figures A.2** and **A.3** in the main text demonstrate agreement between BSE modeled excited states at the Re O_2 and Se $M_{4,5}$ edges, respectively.

Specifically, to model carrier thermalization and excited-state state filling of electrons and holes, we employ two "cutoff" energies: E_h and E_e. Where E_h is the maximum hole depth possible following 3.1 eV excitation the valence bands and Ee is the maximum electron energy accessible following 3.1 eV excitation in the conduction bands. Here, E_h is defined as the energy separation between the CBM and the deepest depopulated valence state, while E_e is defined as the energy separation between the VBM and the highest populated conduction state. state. **Equations A.S1** and **A.S2** depict this relation:

$$E_h = E_{CBM} - E_{occ}^{h} \quad \textbf{(A.S1)}$$

$$E_e = E_{occ}^{e} - E_{VBM} \quad \textbf{(A.S2)}$$

Here, E_{occ}^{h} and E_{occ}^{e} are the energetic positions within the band structure of the electrons and holes that are being applied through the excited-state BSE modeling. Thus, E_h and E_e are employed to parameterize the pump-accessible excited carrier manifold rather than directly visualize carrier energies referenced to their own band edges. For the 3.1 eV pump employed in our XUV experiments, the largest allowed values are E_e, $E_h \leq 3.1$ eV, and smaller values correspond to carrier thermalization toward the respective band edges of the carriers.

This parameterization allows us to separably map the thermalization of electrons and holes. **Figures A.S4** and **A.S5** show different energy holes **(A)** and electrons **(B)** to model thermalization effects immediately following excitation, all the way to thermalization at the

band edge at the Re O_2 and Se $M_{4,5}$ edges, respectively. **Figure A.S4C** presents the combination of spectra calculated in **A.S4A** and **A.S4B** where a fixed electron cutoff energy of 2.0 eV is applied to mimic little-to-no electron thermalization at the Re O_2 edge, and a varied hole cutoff energy is employed to model ultrafast hole cooling to the valence band edge. This scenario agrees best with experimental XUV spectra at the Re O_2 edge. Similarly, **Figure A.S5C** presents the combination of spectra calculated in **A.S5A** and **A.S5B** at the Se $M_{4,5}$ edge, however, a fixed electron cutoff energy of 3.1 eV is applied to mimic little-to-no electron thermalization, and a varied hole cutoff energy is employed to model ultrafast hole cooling to the valence band edge. This scenario agrees best with experimental spectra at the Se $M_{4,5}$ edge and suggests that higher energy electrons are being probed at the Se $M_{4,5}$ edge due to the element-specific nature of the core-level probe. Different projected densities of states are probed by different core-valence transitions. However, in both the case of Re and Se atoms, very minimal electron thermalization is observed spectrally, as supported by BSE theory.

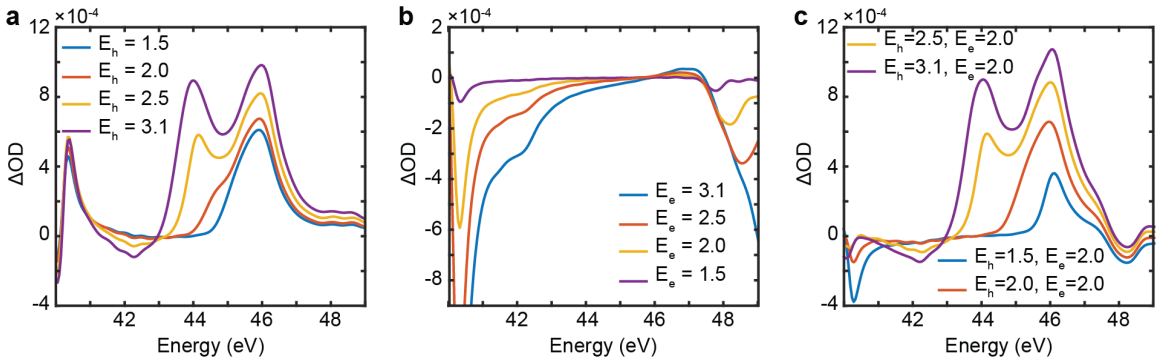

Figure A.S4 BSE modeled excited-state carrier dynamics for holes **(A)**, electrons **(B)**, and holes and electrons together **(C)** at the Re O_2 edge. The electron and hole cutoff energies correspond to the VBM and CBM of the $Re_6Se_8Cl_2$ electronic structure respectively.

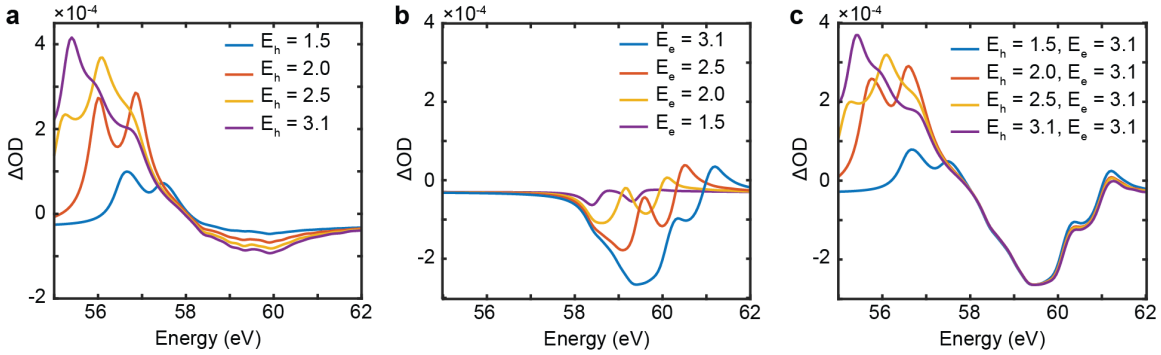

Figure A.S5 BSE modeled excited-state carrier dynamics for holes **(A)**, electrons **(B)**, and holes and electrons together **(C)** at the Se $M_{4,5}$ edge. A higher electron energy is needed in **(C)** to agree with experiment compared to the Re O_2 edge, suggesting higher energy electrons are selectively probed at the Se $M_{4,5}$ edge due to the element-sensitivity of the transient XUV technique.

A.S5 References

(42) Choi, B.; Lee, K.; Voevodin, A.; Wang, J.; Steigerwald, M. L.; Batail, P.; Zhu, X.; Roy, X. Two-Dimensional Hierarchical Semiconductor with Addressable Surfaces. *J. Am. Chem. Soc.* **2018**, *140* (30), 9369–9373. https://doi.org/10.1021/jacs.8b05010.

(43) Leduc, L.; Perrin, A.; Sergent, M. Structure du dichlorure et octaséléniure d'hexarhénium, $Re_6Se_8Cl_2$: composé bidimensionnel à clusters octaédriques Re_6. *Acta Cryst C* **1983**, *39* (11), 1503–1506. https://doi.org/10.1107/S010827018300904X.

(44)Liu, H.; Michelsen, J. M.; Mendes, J. L.; Klein, I. M.; Bauers, S. R.; Evans, J. M.; Zakutayev, A.; Cushing, S. K. Measuring Photoexcited Electron and Hole Dynamics in ZnTe and Modeling Excited State Core-Valence Effects in Transient Extreme Ultraviolet Reflection Spectroscopy. *J. Phys. Chem. Lett.* **2023**, 2106–2111. https://doi.org/10.1021/acs.jpclett.2c03894.

(45)Kim, Y.-J.; Mendes, J. L.; Michelsen, J. M.; Shin, H. J.; Lee, N.; Choi, Y. J.; Cushing, S. K. Coherent Charge Hopping Suppresses Photoexcited Small Polarons in $ErFeO_3$ by Antiadiabatic Formation Mechanism. *Science Advances* **2024**, *10* (12), eadk4282. https://doi.org/10.1126/sciadv.adk4282.

(46)Mendes, J. L.; Shin, H. J.; Seo, J. Y.; Lee, N.; Choi, Y. J.; Varley, J. B.; Cushing, S. K. Dynamic Competition between Hubbard and Superexchange Interactions Selectively Localizes Electrons and Holes through Polarons. *J. Am. Chem. Soc.* **2025,** *147* (19), 16018–16026. https://doi.org/10.1021/jacs.4c16837.

(47)Zhong, X.; Lee, K.; Choi, B.; Meggiolaro, D.; Liu, F.; Nuckolls, C.; Pasupathy, A.; De Angelis, F.; Batail, P.; Roy, X.; Zhu, X. Superatomic Two-Dimensional Semiconductor. *Nano Lett.* **2018**, *18* (2), 1483–1488. https://doi.org/10.1021/acs.nanolett.7b05278.

(48)Géneaux, R.; Chang, H.-T.; Schwartzberg, A. M.; Marroux, H. J. B. Source Noise Suppression in Attosecond Transient Absorption Spectroscopy by Edge-Pixel Referencing. *Opt. Express* **2021**, *29* (2), 951. https://doi.org/10.1364/OE.412117.

(49)Perdew, J. P.; Burke, K.; Ernzerhof, M. Generalized Gradient Approximation Made Simple. *Phys. Rev. Lett*. **1996**, *77* (18), 3865–3868. https://doi.org/10.1103/PhysRevLett.77.3865.

Appendix B

SUPPORTING INFORMATION FOR CHAPTER 3: COHERENT AND DYNAMIC SMALL POLARON DELOCALIZATION IN $CUFEO_2$

This appendix contains supporting information for **Chapter 3** and is adapted with permission from:

Mendes, J. L.*; Bhattacharyya, S.*; Huang, C.; Michelsen, J. M.; Klein, I. M.; Babbe, F.; Sayer, T.; Li, T.; Cooper, J. K.; Liu, H.; Ginsberg, N.; Montoya-Castillo, A.; Cushing, S. K. Coherent and Dynamic Small Polaron Delocalization in $CuFeO_2$. *J. Phys. Chem. Lett.* **2026**, *17* (2), 656–664. https://doi.org/10.1021/acs.jpclett.5c03430

B.1 Material Synthesis and Characterization

B.1.1 Preparation of the $CuFeO_2$ Thin Films

Thin-film samples of rhombohedral $CuFeO_2$ were prepared using magnetron co-sputtering in a Lesker LAB Line sputtering system. The samples were deposited on quartz substrates (25 × 75 mm^2, CGQ-0640-01, Chemglass) that were cleaned beforehand. The sputtering process used 2″ Cu and Fe targets with RF powers of 34 W and 136 W, respectively. A reactive atmosphere of 10% oxygen in argon at a pressure of 10 mTorr was used. During the 30-minute deposition step, samples are heated to 200° C to aid the crystallization process. Following deposition, the samples underwent a 6-hour post-annealing process at 600° C in a quartz glass tube furnace under a flowing argon atmosphere (100 sccm).

The metal composition ratio is determined using inductively coupled plasma mass spectroscopy (Agilent 7900 ICP-MS). For this samples are digested in nitric acid and diluted before injection. The overall Cu/Fe ratio is determined to be close to stoichiometric, with 1.03. The sample thickness is determined to be 200.4 ± 0.1 nm via spectroscopic ellipsometry.

B.1.2 Ground State Optical Characterization

The optical band gap of thin film $CuFeO_2$ was measured using UV-Visible reflectance spectroscopy (Cary 5000, Agilent Technologies). **Figure B.1** presents an $(\alpha hv)^{1/r}$ vs energy plot where r =1/2 for direct allowed (**Fig. B.1A**) and r = 2 for indirect allowed (**Fig. B.1B**) energy transitions. For a Tauc plot analysis, the reflectance spectra were transformed using the Kubelka-Munk function using **Equation B.1**:

$$F(R_\infty) = \frac{(1-R_\infty)^2}{2R_\infty} \quad \textbf{(B.1)}$$

where $R_\infty = R_{sample}/R_{standard}$.[1] The direct band gap is estimated to be ~1.63 eV and the indirect band gap is estimated to be ~ 1.48 eV.

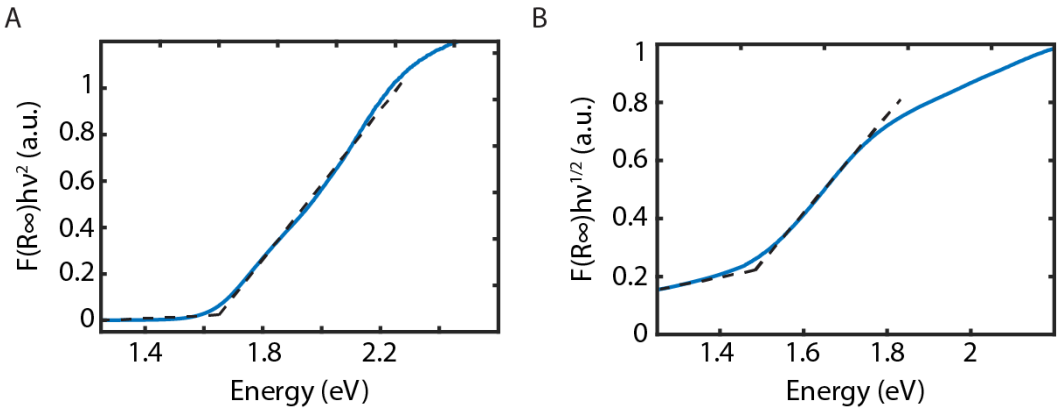

Figure B.1 Tauc plot of the ground state reflectivity of the polycrystalline $CuFeO_2$ thin film for direct allowed **(A)** and indirect allowed **(B)** electronic transitions.

B.1.3 Structural Characterization

The crystal structure of the $CuFeO_2$ thin film was characterized via X-ray diffraction (XRD). **Figure B.2** details the experimental XRD trace (blue) and calculated XRD features (black) from the ICDD database (ICSD #01-075-2146). When comparing the experimentally measured diffraction pattern against a simulated pattern we find that the peak positions agree and the $CuFeO_2$ film adopts the expected rhombohedral crystal structure.

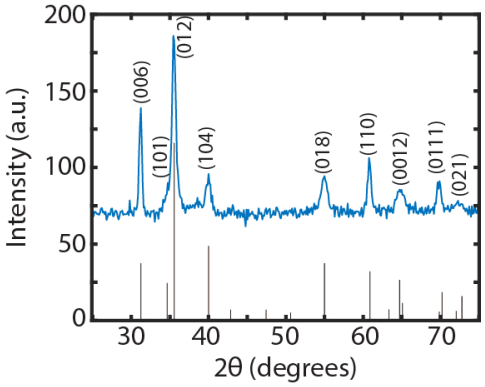

Figure B.2 Experimental (blue) and calculated (black) XRD spectrum of thin film $CuFeO_2$.

Further structural characterization was achieved by collecting Raman spectra of the $CuFeO_2$ thin films. The E_g and A_{1g} modes previously reported for $CuFeO_2$ are observed at 348 and 688 cm-1, respectively (**Fig. B.3**).[2]

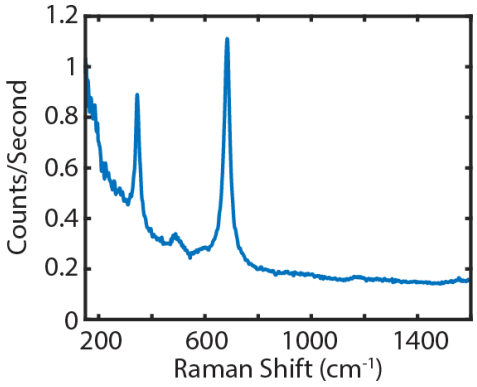

Figure B.3 Raman shift of $CuFeO_2$.

B.2 Experimental Setup: Transient Extreme Ultraviolet Reflectivity Spectrometer

The transient extreme ultraviolet (XUV) reflectivity spectrometer has been described previously.[3,4] Briefly, the reported thin film $CuFeO_2$ measurements were obtained using photoexcitation from a ~35 fs, 400 nm frequency-doubled output of a BBO crystal with p-polarization, pumped by an 800 nm, 1 kHz regeneratively amplified Ti:Sapphire laser (Coherent Legend Elite Duo). The optical excitation fluence was approximately 6 mJ/cm^2, resulting in an initial photoexcited carrier density of ~4.4×10^{21} cm^{-3}.[5–7] Transient reflection was measured by varying the delay times between the pump and probe pulses using an

optomechanical delay stage on the pump line. The XUV probe pulse was generated by high-harmonic generation in argon gas using an s-polarized few-cycle white light beam (<6 fs, 550–950 nm), characterized previously.[3] A 200 nm thick Al filter (Luxel) was used to remove the fundamental white light beam. The resulting XUV continuum probed the Fe $M_{2,3}$ absorption edge around 54 eV. A 10° grazing incidence reflection geometry (80° from normal incidence) was employed. Edge-pixel referencing based on signal-free spectral regions was used to reduce noise due to intensity fluctuations.[8]

B.3 Experimental Setup: Transient Optical Reflectance Spectroscopy

A 540 nm pump pulse was generated by a Light Conversion non-collinear optical para-metric amplifier (model PN13F1) using the third harmonic of the fundamental 1080 nm seed pulse from a Light Conversion Pharos laser (model 10-200-PP). A 707 nm probe pulse was generated by a Light Conversion non-collinear optical parametric amplifier (model PN15F2) using the second harmonic of the fundamental seed pulse. The laser repetition rate was 200 kHz; the pump was modulated at 660 Hz, and the pump–probe delay times were con-trolled by a mechanical stage.

The pump and probe beams were spatially filtered through 25 μm and 50 μm pinholes, respectively. The pump beam was telescoped to a diameter of ∼12 mm, while the probe beam was telescoped to 1 mm and focused into the back focal plane of the objective of a home-built microscope using an f = 300 mm lens. The two beams were combined using a dichroic mirror (DMLP505, Thorlabs), and a 50/50 beamsplitter reflected both beams into a high numerical aperture (1.4 NA) oil-immersion objective (Leica HC PL APO 63×/1.40 NA) and onto the sample, resulting in overlapped confocal pump and wide-field probe illumination. Probe light reflected from the sample–substrate interface, as well as scattered from the sample, was collected through the same objective. The probe light was isolated with a long-pass filter (FEL605, Thorlabs) and focused onto a charged metal oxide semiconductor (CMOS) detector with 5.86 μm square pixels, triggered at 660 Hz (PixeLINK PL-D752, equipped with a Sony IMX174 global shutter sensor), using an f = 500 mm lens placed one tube length (200 mm) away from the back focal plane of the objective. The total

magnification is calculated as 63 × 500/200 = 157.5, giving a spatial resolution of 37.2 nm/pixel. Data were cropped to maintain a field of view of 4 μm × 4 μm. The transient reflectance signal was generated by taking the difference in integrated signal between pump-on and pump-off frames, normalized to the integrated pump-off intensities, yielding ΔR/R. Setup automation and data acquisition were implemented in LabVIEW 2014 (64-bit). Data analysis and plotting were performed using a combination of ImageJ (Fiji) and Python. The pump fluence (0.42 mJ/cm^2) was chosen to remain within a regime where the spatially integrated signal decay was independent of pump power, corresponding to a carrier density of ∼10^{19} cm^{-3}.

In fitting the population dynamics, the entire trace was modeled by convolving the decay dynamics with the instrument response function. The fitting parameters are summarized below in **Table B.1**.

TABLE B.1 Fitting parameters of the $CuFeO_2$ population dynamics.

Parameter	Value
A	-5.2 x 10^{-4}
B	-9.3 x 10^{-5}
k	1.9 ps^{-1}
k_p	1.3 x 10^{-3} ps^{-1}

B.4 Electronic Structure Calculation

To investigate the electronic structure of $CuFeO_2$, we adopted a primitive cell crystal structure from the Materials Project database (Materials Project ID: mp-510281). We computed the total density of states (DOS), projected density of states (PDOS), and band structure calculations using density functional theory (DFT) with the Perdew–Burke–Ernzerhof (PBE) generalized gradient approximation (GGA) for the exchange-correlation functional,[9] along with projector augmented-wave (PAW) pseudopotentials.[10] The primitive

cell is hexagonal, with lattice parameters: a = b = 3.0709 Å, c = 17.2513 Å, and angles α = β = 90°, γ = 120°. This unit cell contains 12 atoms in total, comprising three distinct Fe atoms, three Cu atoms, and six O atoms.

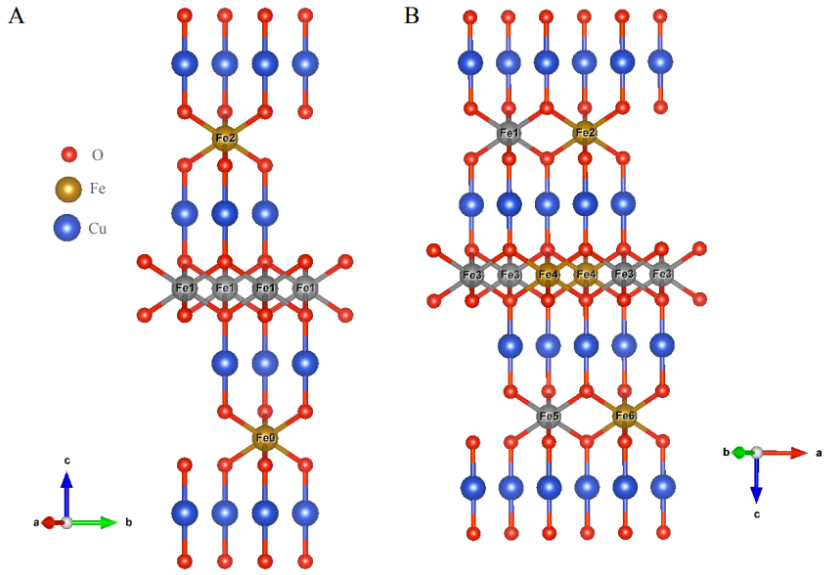

Figure B.4 Crystal structure of $CuFeO_2$ in the primitive cell **(A)** and supercell **(B)**. Gold and grey spheres represent Fe atoms, but with different spin polarization. Cu and O atoms are represented in blue and red, respectively.

Before discussing the electronic properties of $CuFeO_2$, one must first establish the correct magnetic ordering. In the primitive cell, three crystallographically distinct Fe atoms are present. Given that $CuFeO_2$ is known to exhibit antiferromagnetic (AFM) behavior, one may anticipate pursuing an A-type AFM configuration, where the Fe^{3+} spins are aligned parallel within the same crystallographic layer but antiparallel between adjacent layers, corresponding to a layered AFM structure. This magnetic arrangement is illustrated in **Figure B.4A**. However, self-consistent field (SCF) calculations for this configuration yielded a nonzero total magnetization (**Fig. B.5A**), indicating that the A-type AFM ordering does not correctly capture the true ground-state magnetic structure of $CuFeO_2$. Instead, following the approach described in Ref. [11], we adopted a G-type antiferromagnetic

configuration, where the Fe spins alternate in all nearest-neighbor directions, resulting in complete cancellation of spin moments even within each layer.

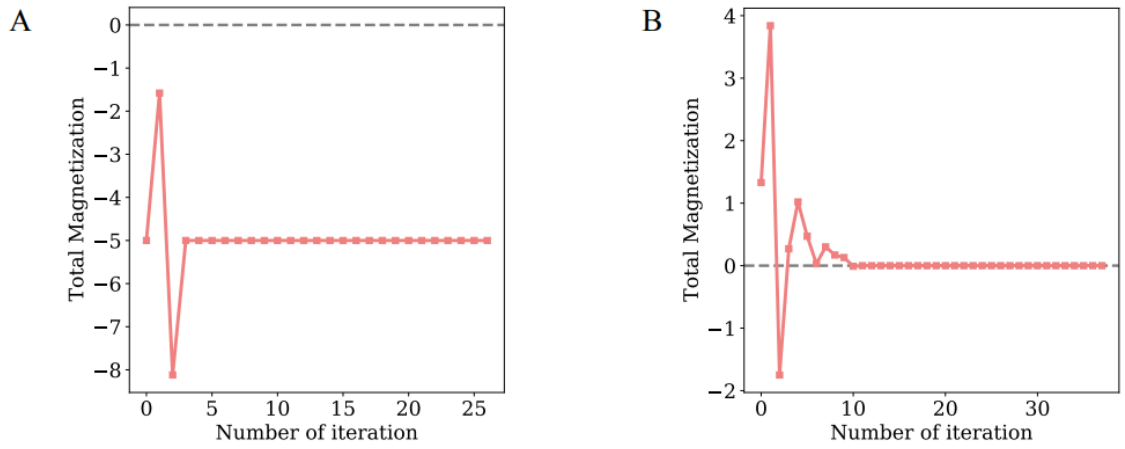

Figure B.5 Total magnetization of the $CuFeO_2$ as a function of number of SCF iterations in the primitive cell **(A)** and the 2 × 1 × 1 supercell **(B)**.

To accommodate this spin arrangement, we constructed a 2 × 1 × 1 supercell, containing 24 atoms in total: 6 Fe, 6 Cu, and 12 O atoms. The spin configuration for each Fe atom in this G-type AFM structure is shown in **Figure B.4B**. The SCF results for this configuration, shown in **Figure B.5B**, confirm that the total magnetization converges to zero – an essential criterion for correctly modeling an antiferromagnetic material. **Figure B.6** also confirms the G-type AFM behavior of $CuFeO_2$ as we can see the magnetization cancels within each layer. Having thus satisfied the antiferromagnetic nature of $CuFeO_2$, we performed all subsequent electronic structure calculations using the 2 × 1 × 1 supercell. To accurately describe the localized nature of the Fe 3d electrons, we applied a Hubbard U correction, following widely adopted practices in transition metal oxide studies.[12] We computed the Hubbard U parameter using a recently developed linear-response approach within the framework of density functional perturbation theory (DFPT).[13] Specifically, we obtained U values for all magnetically distinct Fe atoms from a single-shot DFPT iteration, and consistently used these values for both the DOS and band structure calculations. **Table B.2** summarizes these U values, which we calculated using both atomic projection and orthogonalized atomic projection schemes.[14] We performed all the DFT calculations using the QUANTUM

ESPRESSO package.[15–17] We use a 90 Rydberg kinetic energy cutoff for the wavefunction, and an 1150 Rydberg kinetic energy cutoff for the charge density. For the SCF calculations, we sampled the Brillouin zone with a Monkhorst–Pack 6 × 12 × 2 k-point grid, followed by a denser 12 × 24 × 4 grid for non-self-consistent (NSCF) runs. We evaluated the electronic band structure along high-symmetry paths using 133 k-points.

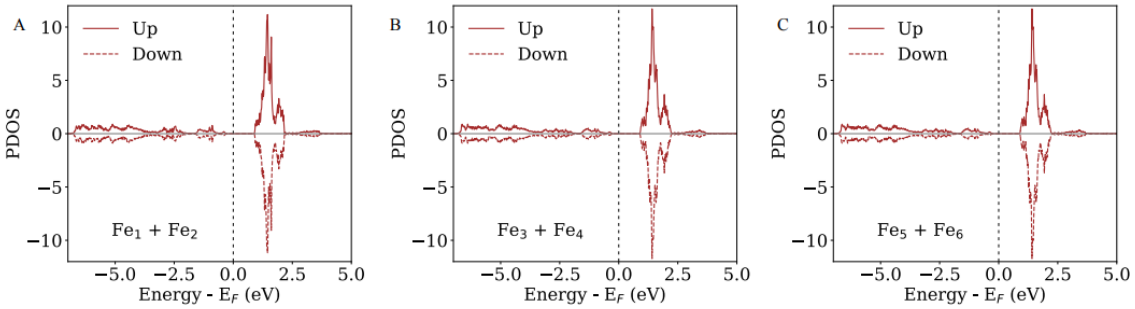

Figure B.6 Fe-projected magnetization of each layer in $CuFeO_2$ supercell. **(A)**: magnetization of the top layer, **(B)**: magnetization of the middle layer, and **(C)**: magnetization of the bottom layer.

Since we performed the band structure calculations using a supercell, we applied the following band unfolding procedure to recover the band structure for the primitive cell:

- Generated the high-symmetry k-path for the primitive cell using the VASPKIT tool.[18]
- Constructed the corresponding k-path in the supercell using the open-source Python package BandUPpy.[19–21]
- Performed the SCF and NSCF (band structure) calculations in the supercell using the generated k-points.
- Unfolded the resulting band structure using BandUPpy to obtain the band structure in the Brillouin zone of the primitive cell. The unfolded bands come with weights that indicate the extent to which each supercell Bloch state contributes to the corresponding primitive cell state.

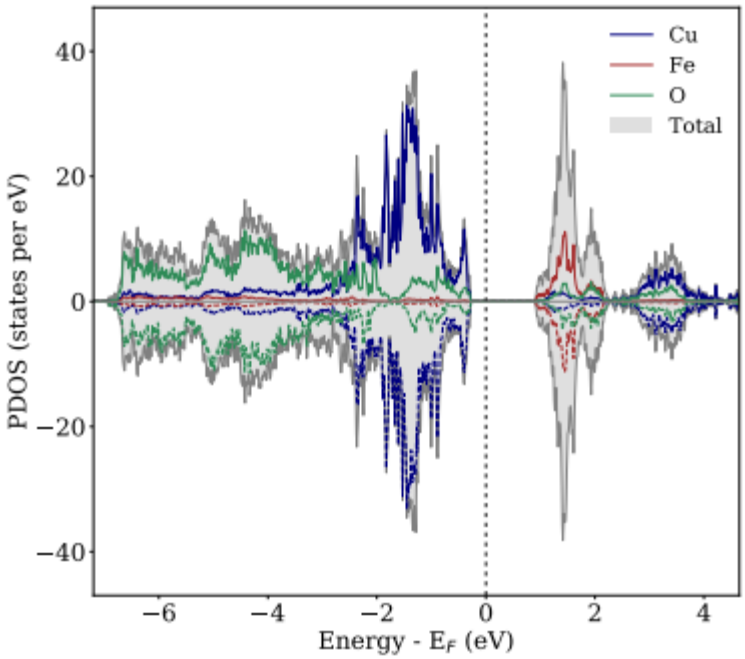

Figure B.7. Projected and total density of states in $CuFeO_2$ using orthogonalized atomic projection for Hubbard U parameter.

Table B.2 Computed Hubbard U parameters for 6 Fe centers using atomic and ortho-atomic projection type.

Fe	atomic	ortho-atomic
Fe_1	4.3960	5.4638
Fe_2	4.3960	5.4638
Fe_3	4.4022	5.4680
Fe_4	4.4022	5.4680
Fe_5	4.4022	5.4680
Fe_6	4.4022	5.4680

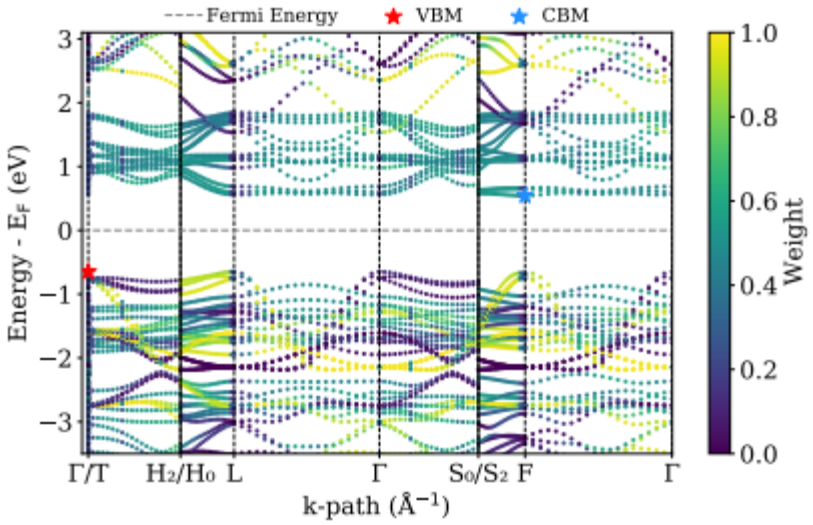

Figure B.8 Band structure of $CuFeO_2$ using orthogonalized atomic projection for Hubbard U parameter.

In the main text, we show the projected DOS and unfolded band structure using Hubbard U parameters obtained via atomic projection. Here, we also report the projected DOS and unfolded band structure with U parameters using the orthogonalized atomic projection scheme. **Figures B.7** and **B.8** show the DOS and band structure obtained when using orthogonalized atomic projection for the determination of the Hubbard U. We find that the bandgap in $CuFeO_2$ is approximately 0.95 eV when using atomic projection and 1.19 eV with the orthogonalized atomic projection scheme. These values are consistent with previous literature values that estimate the bandgap between 0.8-1.5 eV.[22–24]

B.5 Theoretical Calculations of Ground and Excited State Core-Level Spectra

The theoretical framework for interpreting the experimental transient core-level spectra has been described previously.[25] In brief, we employ an ab initio combined theoretical approach based on density functional theory (DFT) and the Bethe–Salpeter equation (BSE). This approach is implemented using the Quantum ESPRESSO package[15–17] along with modifications to the existing OCEAN code (Obtaining Core-level Excitations using Ab Initio Calculations and the NIST BSE solver).[26–29] These modifications enable the inclusion of

excited-state distributions, allowing us to determine how the ground-state band structure relates to the observed transient changes in the XUV spectra.

B.5.1 Fe $M_{2,3}$ Edge Ground State Calculations

The OCEAN package does not support projector-augmented wave (PAW) pseudopotentials, so the DFT portion of our BSE calculations was conducted using Troullier–Martins norm-conserving pseudopotentials within the generalized gradient approximation (GGA) and the Perdew–Burke–Ernzerhof (PBE) functional.[9,30] Prior to the OCEAN calculations, a 2 × 2 × 1 supercell of antiferromagnetic (AFM) ordered $CuFeO_2$ in a rhombohedral geometry (3R-$CuFeO_2$) was structurally relaxed using the Quantum ESPRESSO package.[15–17] The lattice constants for the primitive unit cell were a = b = 3.0349 Å and c = 17.1656 Å.[31] A Hubbard U value of 2 eV, a 300 Rydberg energy cutoff, and a 3 × 3 × 1 k -point grid were employed for the structural relaxation. The optimized geometry was used in the BSE calculations of the XUV ground-state reflectivity at the Fe $M_{2,}3$ X-ray edge using the OCEAN code.[26–29] The BSE equations were solved using a 6 × 6 × 6 k-point mesh, a dielectric constant of 21.8, a 0.7 scaling factor for the Slater G parameter, and a 300 Rydberg energy cutoff. A 4.0 Bohr screening radius and a 2 × 2 × 2 screening mesh were applied. A post-calculation broadening routine was implemented using a MATLAB script to match the linewidth broadening observed in the experiment.

B.5.2 Fe $M_{2,3}$ Edge Excited State Calculations

Excited state changes to the transient XUV spectra at the Fe $M_{2,3}$ edge of $CuFeO_2$ were modeled using a modification to the OCEAN package discussed previously.[3,25,27,29] The modifications to the OCEAN code enables state-blocking of core-to-valence X-ray transitions at different points in momentum space, which simulates state-filling of the valence and con-duction bands following 400 nm photoexcitation. The state-blocked population of electrons and holes forbids or allows XUV transitions to specific points in k-space but does not account for carrier density, therefore, we use the peak position and relative intensity of the modeled spectra to compare experiment to theory. We obtain the modeled excited-state XUV spectra by subtracting the calculated ground state spectrum from the

calculated excited state spectrum to calculate the differential absorption. **Figure 3.3A** in the main text demonstrates agreement between the BSE modeled 400 nm charge transfer state and experiment.

We semi-empirically model the transient effects of distortions caused by the polaron state and the anisotropic c-axis expansion using a framework described previously.[25] We model polarons using the bond distortion method in which we locally apply an expansion to Fe–O bonds at one iron octahedra in the $CuFeO_2$ supercell.[32] The anisotropic, local distortion of the polaron was modeled as an expansion of the iron octahedra bond lengths ranging from 2–8% and then applied to the OCEAN code to calculate the resulting core-valence spectrum. The resulting modeled differential spectrum plotted in **Figure 3.3** of the main text is from a 6% expansion of the local iron octahedra selected for polaron formation. We also model an overall 6% anisotropic lattice expansion on each of the lattice directions to establish which lattice direction is responsible for the signal we observe after 2 ps in our transient spectrum. When modeling the overall anisotropic lattice expansion, we selectively expanded the lattice constants based upon the chosen axis to model which best agreed with experiment. **Figure B.9** shows a plot of *a*-, *b*-, and *c*-axis expansions.

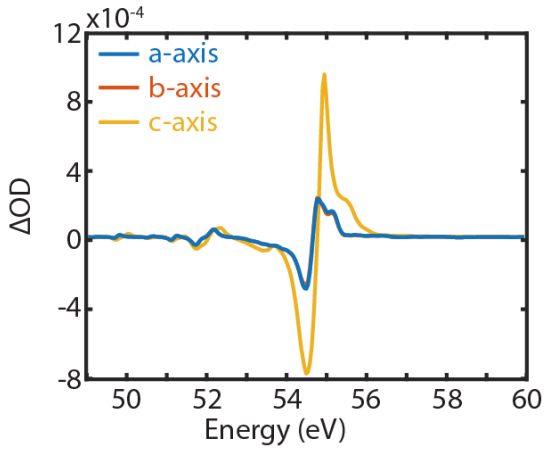

Figure B.9 DFT+BSE calculated lattice expansion and polaron distortion for an anisotropic *a*-axis (blue), *b*-axis (red), or *c*-axis (yellow) expansion

We find that the *c*-axis expansion best agrees with experiment. Particularly, the *c*-axis expansion is blue-shifted like the polaron feature, suggesting that expansion along the *c*-axis

contributes most to the convolved lattice expansion and polaron signal that we observe in our experimental transient XUV spectrum. The *c*-axis expansion has a much stronger contribution to the spectral signal than expansions along the other two axes. When convolved with the polaron feature, the *a*- and *b*-axis expansions would not result in the same spectral line shape.

B.6 Transient XUV Spectral Analysis

The ground state reflectivity of the $CuFeO_2$ thin film around the Fe $M_{2,3}$ edge is shown in **Figure B.10**. The static XUV reflectivity of $CuFeO_2$ is obtained by normalizing the measured static reflectivity spectrum of $CuFeO_2$ to the static reflectivity of a Si wafer, which does not have any absorption features below 100 eV. There is good agreement between the experimental ground state XUV reflectivity of $CuFeO_2$, and our BSE calculated ground state (**Fig. B.10**).

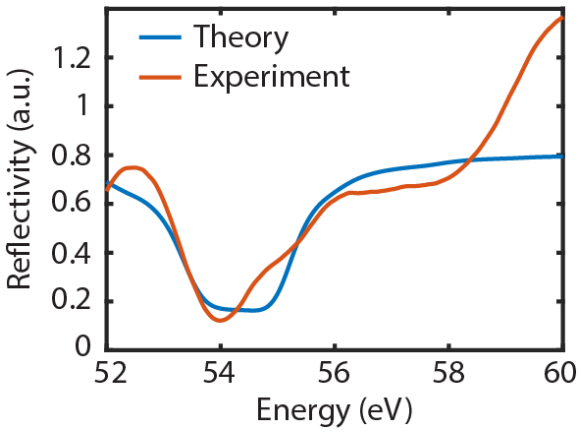

Figure B.10 Static XUV reflectivity (orange) and BSE calculated ground state (blue) spectra of $CuFeO_2$ thin film.

Figure B.11 shows an exponential fit of the spectral blue shift associated with photoexcited polaron formation at the Fe $M_{2,3}$ edge was performed. A single exponential function following the equation $a*exp(-x/b) + c$ results in a time constant of 90 ± 20 fs. The spectral shift was measured to have a magnitude of 0.7 ± 0.1 eV.

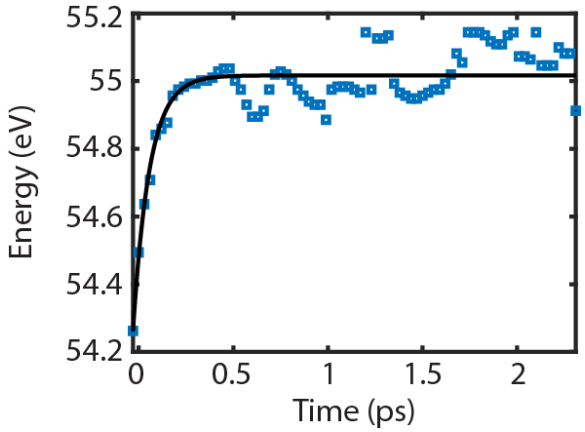

Figure B.11 Exponential fit of the spectral shift at the Fe $M_{2,3}$ edge of $CuFeO_2$.

Singular value decomposition (SVD) of the transient spectrum was performed to confirm independent spectral features and their kinetics and to ascribe weights to each independent spectral feature with respect to time. In the SVD analysis, we factorize the two-dimensional matrix of the transient spectrum by rotating (U), scaling (S), and then again rotating (V) the matrix. The scaling matrix contains the singular values along its diagonal, which we refer to as the number of components. This results in 3 singular values being necessary to adequately reconstruct the transient XUV spectrum (**Fig. B.12**). Each singular value corresponds to the three kinetic states that we observe in our transient spectrum. We ascribe the first singular value to the charge transfer state at 30 fs, the second to the polaron state at 180 fs, and the third to the convolved polaron and *c*-axis lattice expansion at 2 ps. We find that the inclusion of three singular values in our decomposition is adequate to reconstruct our transient spectra.

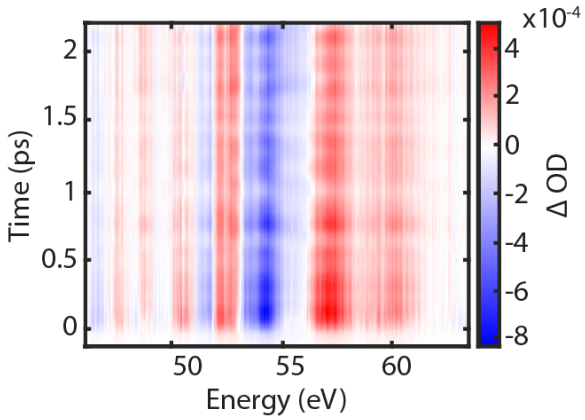

Figure B.12 Reconstructed transient spectrum based upon the singular value decomposition of the transient XUV at the Fe $M_{2,3}$ edge. The vectors employed for the SVD are shown in **Figure 3.3A** corresponding to the charge transfer state (blue, left), the polaron state (green, middle), and the lattice expansion and polaron state (red, right).

To confirm that three singular values are necessary to accurately describe the kinetic processes that take place in $CuFeO_2$ following 400 nm photoexcitation, we also measure the transient XUV response out to 1 ns. The long timescale measurements of thin film $CuFeO_2$ can be seen in **Figure B.13A** and do not experience any additional phenomena out to 1 ns. Further, the long timescale measurement demonstrates that the convolved polaronic and lattice expansion feature lives out to nanoseconds. We also include a kinetic plot of the contributions of the singular value decomposition components out to 1 ns (**Fig. B.13B**).

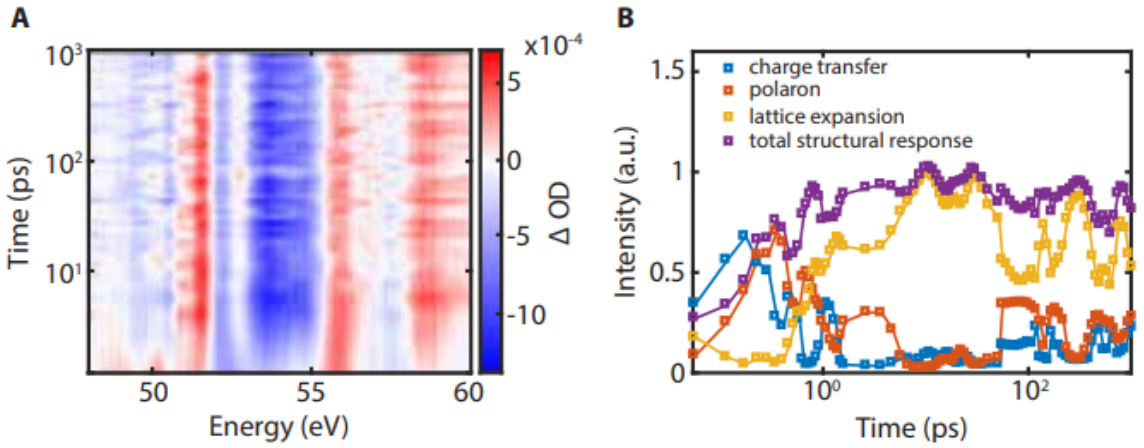

Figure B.13 (A) Long timescale transient measurement of thin film $CuFeO_2$ at the Fe $M_{2,3}$ edge. **(B)** Singular value decomposition of long timescale dynamics.

We apply best fit lines to the individual SVD components as shown in **Figure B.14**. The charge transfer and polaronic states are fit with exponential decays, for which the charge transfer state has a time constant of 50 ± 40 fs and the polaron state has a time constant of 790 ± 370 fs. The lattice expansion state is fit with a linear regression. The residuals for the line of best fit for each component of the SVD analysis can be found on the right-hand side of **Figure B.14**. Oscillations are present in the residuals for each SVD component; however these oscillations lack coherence. These are likely due to spectral noise and the convolution of all oscillations in the spectra through this SVD analysis. Because the SVD analysis only considers three components, energy dependent coherent oscillatory effects will be convolved. To deconvolve spectral oscillations at specific energies, **Figure 3.3** in the main text Fourier transforms the spectral oscillations at the negative absorption feature in the XUV spectrum at ~55 eV. **Figure B.15** shows sinusoidal fits for the two dominant coherent oscillations observed in the Fourier transform. **Figure B.15A** shows a 1.4 THz sinusoidal fit, **Figure B.15C** shows a 5.3 THz sinusoidal fit, and **Figure B.15E** shows a combined 1.4 and 5.3 THz fit. The residuals for each fit can be seen in the right panels. Some residual oscillations exist, which agrees with the Fourier transform in **Figure 3.3** of the main text in which there is an envelope of modes below the two dominant peaks at 1.4 and 5.3 THz. However, we see qualitative agreement with the combined 1.4 and 5.3 THz fit in **Figure B.15E**.

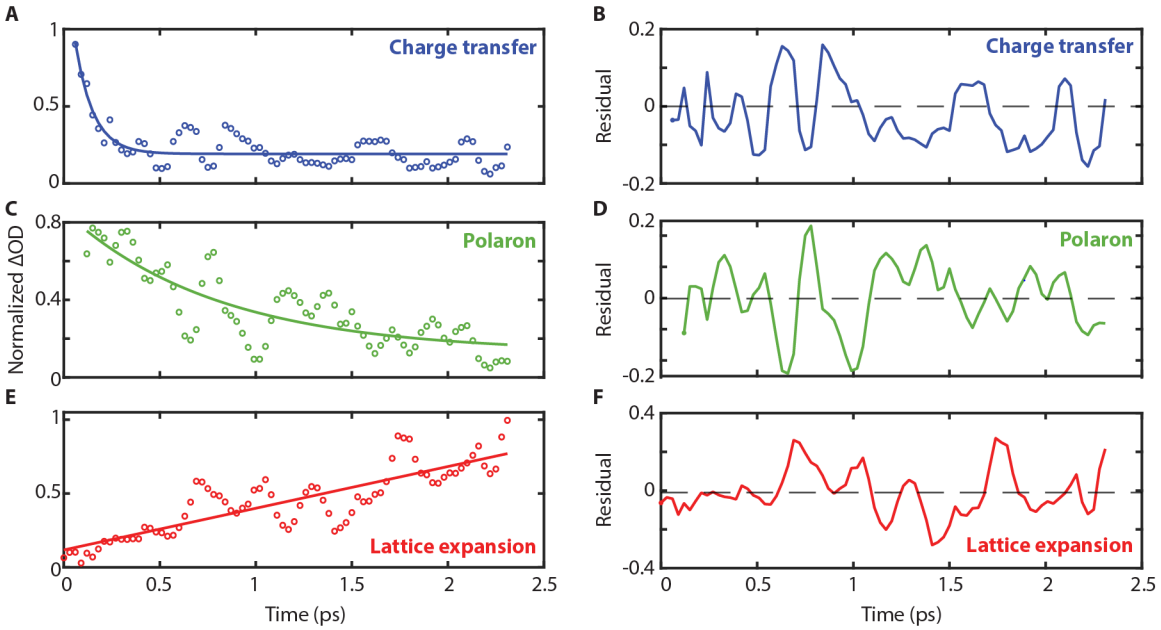

Figure B.14 Singular value decomposition components that are assigned to the charge transfer state **(A)**, the polaron state **(C)** and the delocalized lattice expansion **(E)**. The SVD components are normalized for comparison of relative contributions to the spectra. A monoexponential decay is fit to the charge transfer and polaronic components, while a linear regression is fit to the lattice expansion component. The residuals of each fit can be seen in the plots to the right **(B, D,** and **F)**.

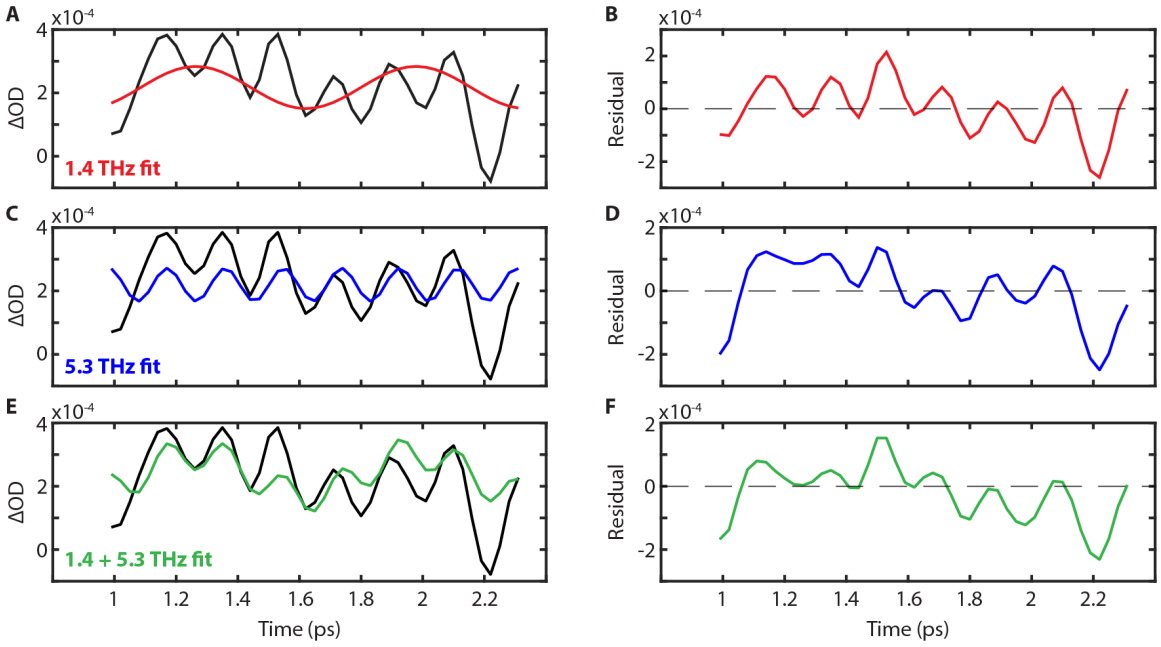

Figure B.15 Sinusoidal fits at 1.4 THz (**A**, red), 5.3 THz (**C**, blue), and a combined fit with 1.4 and5.3 THz components (**E**, green) of the main negative feature at ~55 eV in main text **Figure 3.2A** label 3 (black). The residuals of each fit (right) show some additional oscillations that are not accounted for in the fits (left).

B.7 Quantum Dynamics Simulation of Polaron Formation

The Holstein Hamiltonian[33] has been widely invoked to understand polaron formation and transport in materials ranging from organic crystals to transition metal dichalco-genides.[34,35] While the traditional Holstein Hamiltonian considers interactions between electronic excitations (charge carriers or excitons) and single phonon mode on each lattice site, we adopt the dispersive Holstein model,[36] which couples a carrier on a given site to phonons spanning a distribution of phonon frequencies, consistent with the variety of phonon modes observed in Raman spectra of materials. Th e dispersive Holstein Hamiltonian takes the form:

$$\hat{H} = \sum_i^N \epsilon_i \hat{n}_i + \sum_{\langle ij \rangle}^N v_{ij} \hat{a}_i^\dagger \hat{a}_j + \frac{1}{2}\sum_\alpha \left[\hat{P}_{i,\alpha}^2 + \omega_{i\alpha}^2 \hat{X}_{i,\alpha}^2\right] + \sum_\alpha c_{i,\alpha} \hat{X}_{i,\alpha} \hat{n}_i \qquad \textbf{(B.2)}$$

Here, $\hat{a}_j$ ($\hat{a}_i^\dagger$) is the annihilation (creation) operator for a charge carrier at lattice site *i*, and $\hat{n}_i = \hat{a}_i^\dagger \hat{a}_j$. $\hat{X}_{i,\alpha}(\hat{P}_{i,\alpha})$ is the dimensionless position (momentum) operator for the α-th phonon mode connected with the *i*-th lattice site. The first term in the Hamiltonian (Eq. B.2) represents the on-site energy of the carrier, and the second term is responsible for carrier hopping. The angular brackets $\langle \cdots \rangle$ guarantee the nearest-neighbor hopping. We take all lattice sites to be degenerate ($\epsilon_i = 0$), and assume a uniform site-hopping parameter ($v_{ij} = v =$ 300 cm^{-1}) consistent with previous studies on calculations of the hopping integral *v* in hematite and other iron-containing transition metal oxides.[37,38] The third term in **Equation B.2** constitutes the site-specific phonon baths, and the last term indicates on-site carrier–phonon coupling, which is linear in the local phonon bath coordinates and is responsible for the fluctuation of the on-site energies, ultimately resulting in small polaron formation.

We describe the carrier-phonon interaction with a spectral density:

$$J_i(\omega) = \frac{\pi}{2}\sum_\alpha \frac{c_{i,\alpha}^2}{\omega_{i\alpha}} \delta(\omega - \omega_{i\alpha}) \qquad \textbf{(B.3)}$$

choose these to be equivalent across all sites, and employ a sum of Lorentzians to model their distributions:

$$J(\omega) = \sum_{i=1}^{N_m} 4\lambda_i \frac{\Omega_i^2 \gamma_j \omega}{(\omega^2 - \Omega_i^2)^2 + 4\gamma_i^2 \omega^2} \quad \textbf{(B.4)}$$

Here, N_m denotes the number of Lorentzian distributions (also known as Brownian oscillator densities) we use in our model, Ω_i and γ_i denote the position of the peak and the width of the i-th Lorentzian distribution, and the coefficient λ_i scales the spectral density to the correct reorganization energy λ. For any spectral density $J(\omega)$, the total reorganization energy is defined as:

$$\lambda = \frac{1}{\pi} \int d\,\omega \frac{J(\omega)}{\omega} = \sum_i \lambda_i \quad \textbf{(B.5)}$$

To parameterize the spectral densities for $CuFeO_2$, we adopt values obtained in previous calculations and inferred from experiment. Specifically, we select the Lorentzian parameters (peak height and width) to align with clusters of experimentally observed Raman peaks in $CuFeO_2$.[39] For the reorganization energies, we consider previous work on α-Fe_2O_3, which has shown that $\lambda/\nu \approx 9$, with $\lambda_{Fe2O3} \approx 2984$ cm^{-1}.[37] In contrast, experimental evidence in $CuFeO_2$ suggests a possible reduction in the reorganization energy. To reflect this, we adopt a reduced ratio of $\lambda/\nu \approx 5$ for $CuFeO_2$. Hence, $\lambda_{CuFeO2} \approx 1500$ cm^{-1}. **Table B.3** summarizes the parameters we employ in this study.

TABLE B.3 Parameters for Lorentzian spectral densities in **Equation B.4**. For all three cases, we fix the total reorganization energy $\lambda = 1500$ cm^{-1}. All units are in cm^{-1}.

Region	Ω_i	λ_i	γ_i	Raman peaks
Low-frequency	545	1500	180	352, 509, & 652
High-frequency	1100	1500	100	1000, 1050, & 1171
Both	545 & 1100	900 & 600	180 & 100	352, 509, 652, 1000, 1050, & 1171

We simulate the quantum dynamics of polaron formation by invoking the Non-Interacting Blip Approximation (NIBA), a second-order perturbative theory valid when $\nu/\lambda \ll 1$.S40

This condition holds in our system. Under NIBA, the carrier population $P_n(t)$ of each site evolves according to a simple integrodifferential equation:

$$\frac{dP_n(t)}{dt} = \sum_{m=1}^{N} \int_0^t d\tau K_{nm}(t,\tau) P_m(\tau) \qquad \textbf{(B.6)}$$

Here, the kernel $K(t)$ arises from a second order expansion in the hopping integral v, with non-perturbative, multiphonon treatment of the carrier-phonon coupling. With $\epsilon_i = 0$, the elements of the kernel, $K(t)$, simplify thus,

$$K_{n\neq m}(t,\tau) = 2|v_{nm}|^2 exp[-Q_2(t-\tau)] cos\left[Q_1(t-\tau) - (1+\tfrac{\delta_n+\delta_m}{2})(Q_1(t)-Q_1(\tau))\right] \textbf{(B.7)},$$

and $K_{nm}(t,\tau) = \sum_{m\neq n} K_{mn}(t,\tau)$. The bath correlation function $Q(t) = Q_2(t) + iQ_1(t)$, is defined as:

$$Q(t) = 2\pi \int_0^\infty d\omega \frac{J(\omega)}{\omega^2}\left\{\coth\left(\frac{\beta\omega}{2}\right)[1-\cos(\omega t)] + isin(\omega t)\right\} \qquad \textbf{(B.8)}$$

The shift parameter δ arises from the initial bath conditions. For simulations starting from an unpolarized initial condition, δ = 0 for all sites, whereas, for those with polarized initial conditions, δ = −1 for the initial site and δ = 0 for all other sites.

We validate our NIBA-based dynamics by comparing against numerically exact results obtained using the Hierarchical Equations of Motion (HEOM).[41] Because HEOM becomes prohibitively computationally expensive for this strong carrier-phonon coupling limit when using multi-peaked spectral densities, we perform this comparison using a single-peak Lorentzian spectral density with parameters equivalent to those of the low-frequency component in **Table B.3**. Following Ref. [42], we performed HEOM simulations for both polarized and unpolarized initial conditions. **Figure B.16A** displays the HEOM results, while panel (B) shows the corresponding NIBA dynamics. Although NIBA captures the quantum dynamics for both initial conditions only semi qualitatively, it predicts the correct polaron formation timescale, i.e., the timescale corresponding to the place where the nonequilibrium dynamics arising from these initial conditions start to agree. The vertical dashed lines in both panels of **Figure B.16** indicate the polaron formation timescale. In summary, although NIBA

is an approximate, perturbative theory, it accurately captures polaron formation timescales compared against numerically exact methods.

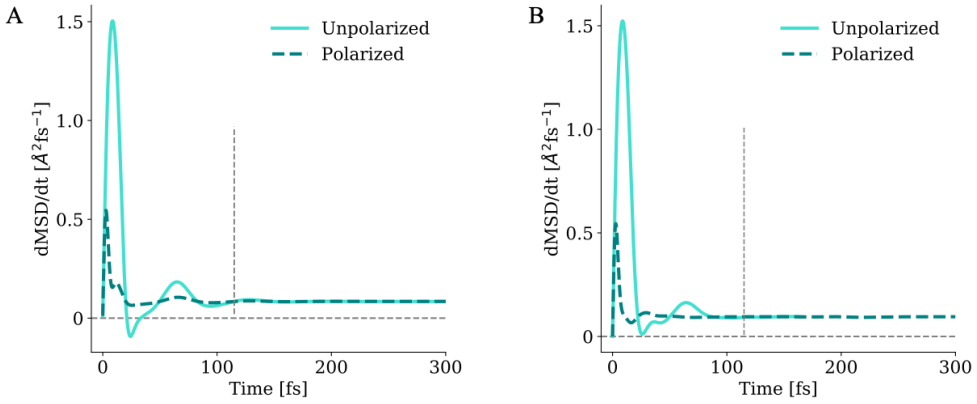

Figure B.16 Derivative of the mean squared displacement of polarons in the dispersive Holstein lattice obtained using **(A)** the numerically exact HEOM and **(B)** the perturbative NIBA. Both methods show qualitative agreement and, crucially, predict similar polaron formation timescales (within ±15 fs error).

To lower the cost of our quantum dynamics simulations and ensure that we can reach the thermodynamic limit of polaron formation free of finite-size effects, we adopt our space-time local generalized master equation (STL-GME) framework.[43] The STL-GME recognizes that systems like small polaron formers have finite spatial memory. We exploit this short-ranged memory to enable more efficient simulation of the quantum dynamics. This only entails moving from the time-nonlocal formulation in **Equation B.6** to a time-local and integrated one:

$$C_{n,m}(t+\delta t) = \sum_k U_{n,k}(t) C_{k,m}(t) \qquad \textbf{(B.9)}$$

where U is the dynamical generator for the spread of population dynamics. This quantity equilibrates to a finite value at short times, over which time a polaron can only spread over a finite spatial extent. As such, its form in an even larger space remains the same, enabling us to perform the quantum dynamics simulation of polaron formation over a large space using only a small reference calculation over a smaller space. In our current calculations, adopting the STL-GME reduces the memory cost by about an order of magnitude: a 15-site NIBA calculation with a 330 fs simulation time requires ~80 GB of memory, while the STL-

GME reduces the cost to that of a 9-site calculation with a ∼200 fs simulation time, requiring only about ∼ 10 GB of memory. We achieve convergence between NIBA and STL-GME in the derivative of the MSD, with an average error of ∼ 1.5%. For all MSD calculations, we employ a lattice distance of 5 Å.

We conclude our discussion with a short analysis of the conditions on the spectral density that determine relative speeds of polaron formation. In particular, we interrogate the seemingly counterintuitive result that adding a fast Lorentzian component to the spectral density in our model of $CuFeO_2$ slows polaron formation – a finding that contrasts earlier studies demonstrating that a faster Debye bath correlates to faster polaron formation.[36] We argue that this apparent contradiction is an artifact of the Debye spectral density, which conflates the characteristic frequency of the coupling distribution (its maximum) with its width into one parameter, ω_c. Instead, the Lorentzian spectral density disentangles the characteristic frequency of the coupling distribution, **Ω**, from the width of the distribution, γ, allowing us to test the effect of characteristic bath speed separately from the breadth of the phonon energies that are accessible.

To demonstrate this decoupling argument in the Lorentzian spectral density, we analyze the dynamics arising from a wide range of Lorentzian distributions by varying both **Ω** and γ. **Figure B.17** reports the polaron formation timescale as a function of **Ω** and γ. We find that these timescales are highly sensitive to the width, γ, but largely insensitive to the peak position, **Ω**. Physically, this is because polaron formation occurs faster when the phonon energies span a broad range, enabling more distributed energy dissipation. To understand the contrast between the Lorentzian and Debye spectral densities, we consider the overdamped limit of γ >> **Ω**, where one can approximate the Lorentzian distribution as a Debye

$$J(\omega) = \frac{2\lambda(2\gamma)}{\omega^2+(2\gamma)^2} \qquad \textbf{(B.10)}$$

with $\omega_c \rightarrow 2\gamma$. For Debye spectral densities, ω_c is the characteristic phonon frequency that dictates both the peak position and the width of the peak, and hence the decay timescale of the exponential of $Re\ Q(t) = Q_2(t),\ Exp[-Q_2(t)]$, which dictates the dissipative behavior of

the NIBA kernel *K(t)*. Indeed, under this overdamped condition, we find that increasing γ makes the polaron formation timescale shorter (see **Fig. B.17**), showing that our present results are in agreement with our previous observations.[36]

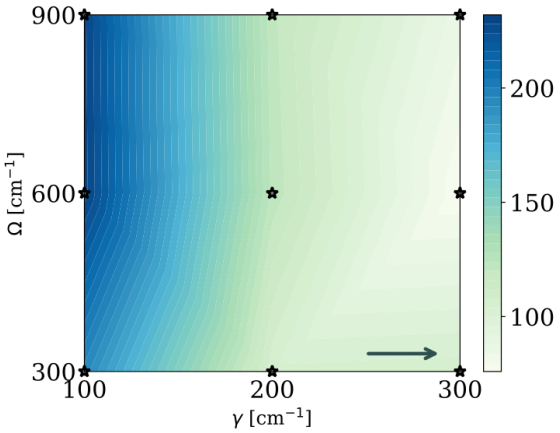

Figure B.17 Polaron formation time as a function of the Lorentzian peak position, Ω, and peak width, γ. The arrow shows that the decrease in polaron formation times observed at fixed Ω as γ increases mirrors the decrease in polaron formation times observed with increasing characteristic frequency, ω_c, in the Debye spectral density, consistent with our previous results detailed in Ref. [36].

We are now in a position to illustrate how the addition of the fast but narrow Lorentzian spectral density can yield slower polaron formation timescales than a slow but broad spectral density. Specifically, we focus on the decay behavior of $Exp[-Q_2(t)]$. For the case with only low-frequency phonon modes, $Exp[-Q_2(t)]$ shows a smooth decay, while for the case with only high-frequency contributions, $Exp[-Q_2(t)]$ initially shows a decay, but later shows a recurrence pattern, as evident in **Figure B.18**. A similar behavior in terms of polaron formation timescales is evident in **Figure B.17**, where increasing γ correlates strongly with shorter polaron formation timescales.

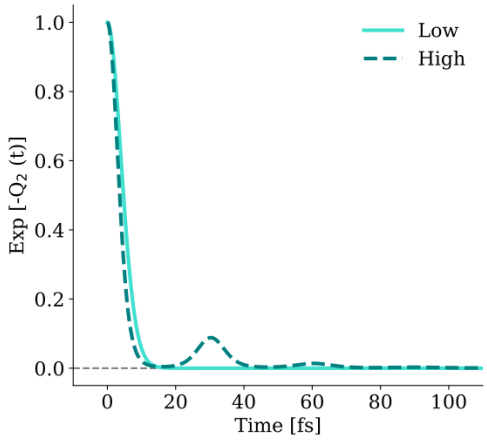

Figure B.18 Comparison of the dissipative component of the NIBA kernel, $Exp[-Q_2(t)]$, for the Lorentzian spectral density in the presence of low-frequency versus high-frequency modes.

Table B.4 Parameters for the doubly peaked Lorentzian spectral densities considered in the four cases discussed in the text. All units are in cm^{-1}.

Cases	Low-frequency region: Ω	Low-frequency region: γ	High-frequency region: Ω	High-frequency region: γ
Case 1	545	180	1100	100
Case 2	545	180	1100	180
Case 3	545	180	1100	180
Case 4	545	180	1400	100

Having shown that the available phonon density is the main factor that dictates the polaron formation timescale for singly peaked Lorentzian densities, we turn to doubly peaked counterparts that are reminiscent of the division between acoustic and optical phonon modes in solid-state materials. In particular, we consider three paradigmatic cases specified in **Table B.4**. Case 1 refers to the distribution where the low-frequency peak has a broad phonon distribution and the high-frequency region has a narrow distribution. Case 2 corresponds to the opposite scenario with a broad high-frequency region and a narrow low-frequency one. In case 3, both low- and high-frequency regions have the same breadth.

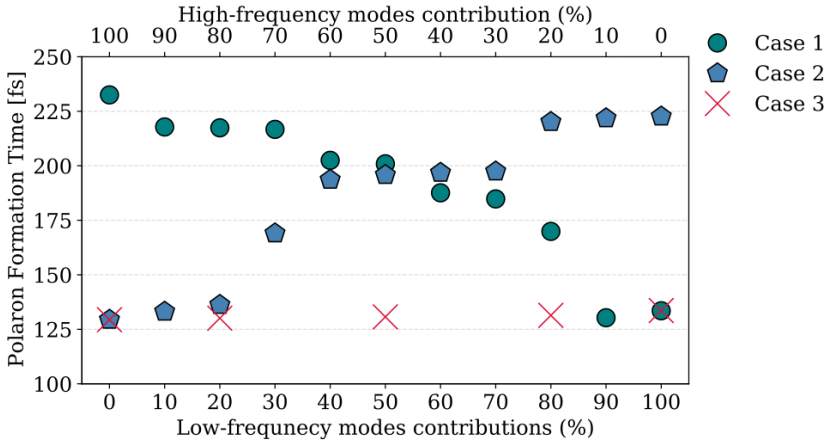

Figure B.19 Polaron formation times observed as we vary the balance of reorganization energies distributed between the low- and high-frequency regions for the different cases mentioned in **Table B.4**.

Given that the width of the spectral density dictates polaron formation timescales, one might anticipate that the total polaron formation timescale in the doubly peaked case might be dominated by the faster timescale set by the broader spectral distribution. However, we find that it is instead close to a weighted average of the two timescales, with the weights being determined by the reorganization energy of each spectral density peak. To illustrate this point, we calculate the polaron formation timescales for each of the three cases with doubly peaked Lorentzian distributions while varying the distribution of reorganization energy between low- and high-frequency regions (see **Fig. B19**). We find that shifting the reorganization energy to the narrow-width region (cases 1 and 2) increases the polaron formation timescale. If both low- and high-frequency regions have similar widths, the polaron formation timescale is independent of the reorganization energy distribution among regions (see case 3). We also consider a fourth case analogous to case 1 with a single difference: we separate the high- and low-frequency regions of the spectral density even further. This case allows us to test the effect of the central frequency of each of the two Lorentzian contributions to the spectral density We find the polaron formation timescale does not change significantly in this case (see **Fig. B.20**) This result reinforces the idea that the distribution of reorganization energy between the narrow and wide regions of the spectral density plays a decisive role in determining polaron formation timescales.

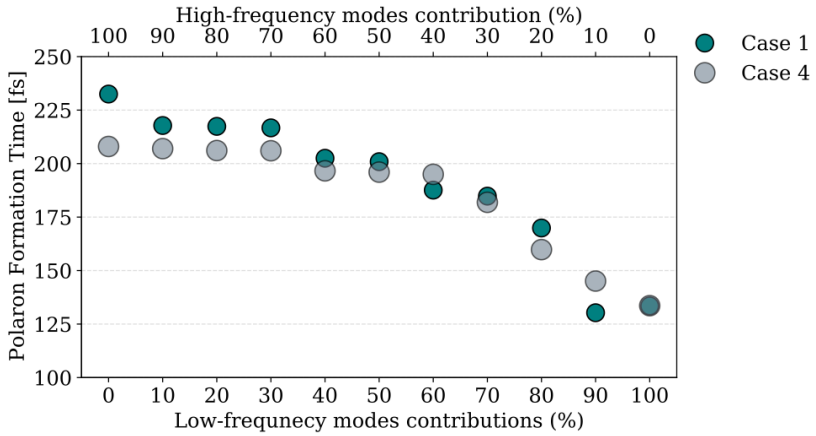

Figure B.20 Overall agreement in the polaron formation times observed across cases 1 and 4, mentioned in **Table B.4**, as we vary the balance of reorganization energies distributed between their low- and high-frequency regions. Importantly, the only difference between cases 1 and 4 is the center frequency of the high- and low-frequency contributions. This agreement reiterates the insight that the factors that largely determine polaron formation timescales are the breadth of polaron distributions and their weights determined by their respective reorganization energies.

To further support our argument that the narrow high-frequency region in the spectral density is primarily responsible for slowing down polaron formation, we show a comparison of three specific spectral density configurations and their corresponding polaron formation timescales. First, we consider the 'low' case from **Table B.3**, where the total reorganization energy is concentrated in the low-frequency region (**Fig. B.21A**). This results in a polaron formation timescale of ~ 130 fs. In the second case, we redistribute the reorganization energy between the low- and high-frequency regions in a 3:2 ratio (**Fig. B.21C**). In this case, the timescale increases to ~ 185 fs. Finally, we remove the high-frequency contribution entirely and reduce the total reorganization energy accordingly (**Fig. B.21E**), leading to a polaron formation timescale of ~ 140 fs.

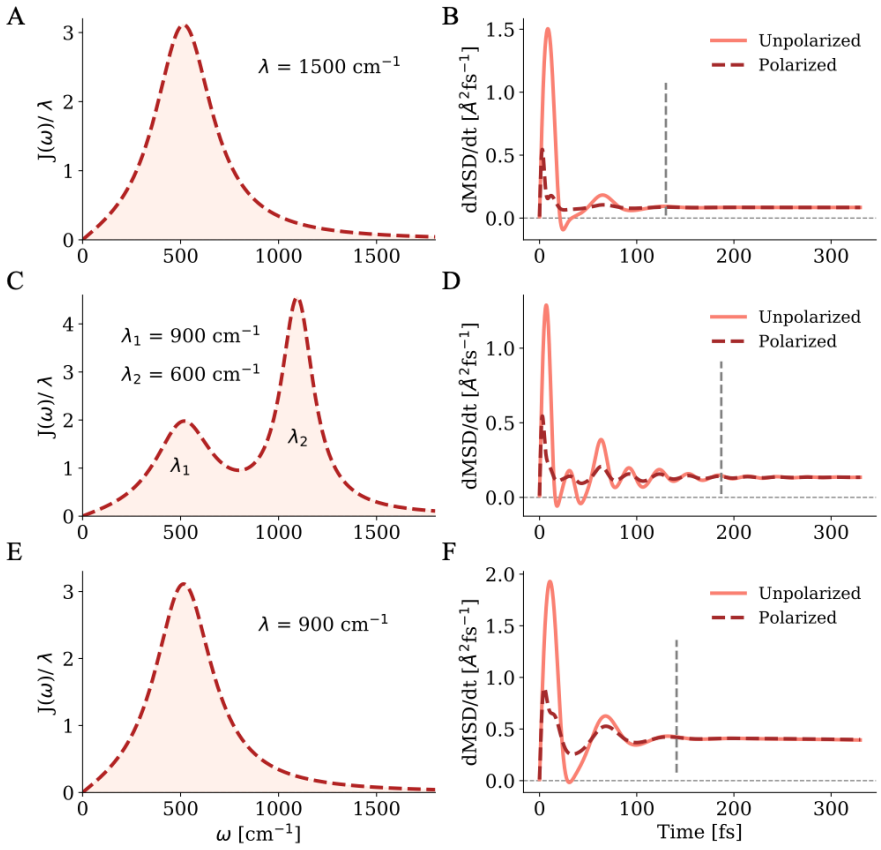

Figure B.21 Comparison of polaron formation times for three types of spectral density. The spectral density in panel **(A)** consists of only a single low-frequency peak with the full reorganization energy, $\lambda = 1500\ cm^{-1}$. Panel **(B)** shows that this spectral density leads to a polaron formation time of~ 130 fs. The spectral density in panel **(C)** consists of a low- and high-frequency contribution with the reorganization energy distributed in a 3:2 ratio, respectively. Panel **(D)** reveals that this spectral density leads to a polaron formation time of ~ 180 fs. In panel **(E)**, we adopt the same spectral density as in panel **(A)**, albeit with a reduction in its reorganization energy consistent with that of the low-frequency peak in the spectral density of panel **(B)**, i.e., $\lambda = 900\ cm^{-1}$. Panel **(F)** shows that this spectral density leads to a polaron formation time of ~ 140 fs. These results show how varying the portion of reorganization energy across the high- and low-frequency regions of the spectral density tunes polaron formation timescale.

These results clearly demonstrate that the presence of a narrow-breadth, high-frequency component, primarily associated with optical phonon modes, significantly slows down polaron formation. Therefore, by engineering or suppressing these narrow high-frequency modes, it may be possible to reduce the polaron formation timescale. In summary, this section emphasizes that both the width of the spectral density (i.e., phonon density) and the distribution of reorganization energy among these phonon modes are key factors in

determining the polaron formation timescale. Adjusting either parameter offers a pathway to control and potentially accelerate or decelerate polaron formation.

B.8 References

(1) Makula, P.; Pacia, M.; Macyk, W. How To Correctly Determine the Band Gap Energy of Modified Semiconductor Photocatalysts Based on UV–Vis Spectra. *J. Phys. Chem. Lett.* **2018**, *9*, 6814–6817.

(2) Pavunny, S. P.; Kumar, A.; Katiyar, R. S. Raman Spectroscopy and Field Emission Characterization of Delafossite $CuFeO_2$. *J. Appl. Phys.* **2010**, *107*, 103522. https://doi.org/10.1063/1.3284160.

(3) Liu, H.; Michelsen, J. M.; Mendes, J. L.; Klein, I. M.; Bauers, S. R.; Evans, J. M.; Zakutayev, A.; Cushing, S. K. Measuring Photoexcited Electron and Hole Dynamics in ZnTe and Modeling Excited-State Core–Valence Effects in Transient Extreme Ultraviolet Reflection Spectroscopy. *J. Phys. Chem. Lett.* **2023,** *14*, 2106–2111.

(4) Kim, Y.-J.; Mendes, J. L.; Michelsen, J. M.; Shin, H. J.; Lee, N.; Choi, Y. J.; Cushing, S. K. Coherent Charge Hopping Suppresses Photoexcited Small Polarons in $ErFeO_3$ by Antiadiabatic Formation Mechanism. *Sci. Adv.* **2024**, 10. https://doi.org/10.1126/sciadv.adk4282.

(5) de Roulet, B. R.; Drescher, L.; Sato, S. A.; Leone, S. R. Initial Electron Thermalization in Metals Measured by Attosecond Transient Absorption Spectroscopy. *Phys. Rev. B* **2024**, *110*, 174301.

(6) Zürch, M.; Chang, H.-T.; Borja, L. J.; Kraus, P. M.; Cushing, S. K.; Gandman, A.; Kaplan, C. J.; Oh, M. H.; Prell, J. S.; Prendergast, D.; Pemmaraju, C. D.; Neumark, D. M.; Leone, S. R. Direct and Simultaneous Observation of Ultrafast Electron and Hole Dynamics in Germanium. *Nat. Commun.* **2017**, *8*, 15734.

(7) Cushing, S. K.; Lee, A.; Molesky, I. J. P.; Carneiro, L. M.; Chang, H.-T.; Zürch, M.; Leone, S. R. Differentiating Photoexcited Carrier and Phonon Dynamics in the Δ, L, and Γ Valleys of Si(100) with Transient Extreme Ultraviolet Spectroscopy. *J. Phys. Chem. C* **2019**, *123*, 3343–3352.

(8) Géneaux, R.; Chang, H.-T.; Schwartzberg, A. M.; Marroux, H. J. B. Source Noise Suppression in Attosecond Transient Absorption Spectroscopy by Edge-Pixel Referencing. *Opt. Express* **2021**, *29*, 951.

(9) Perdew, J. P.; Burke, K.; Ernzerhof, M. Generalized Gradient Approximation Made Simple. *Phys. Rev. Lett.* **1996,** *77*, 3865–3868.

(10) Blöchl, P. E. Projector Augmented-Wave Method. *Phys. Rev. B* **1994**, *50*, 17953–17979.

(11) Ferri, M.; Elliott, J.; Farnesi Camellone, M.; Fabris, S.; Piccinin, S. Thermodynamic Stability and Native Point Defects of $CuFeO_2$ Photocathodes in Dry and Electrochemical Environments. *J. Phys. Chem. C* **2019**, *123*, 29589–29598.

(12) Naveas, N.; Pulido, R.; Marini, C.; Hernández-Montelongo, J.; Silván, M. M. First-Principles Calculations of Hematite (α-Fe_2O_3) by Self-Consistent DFT+U+V. *iScience* **2023**, *26*, 106033.

(13) Timrov, I.; Marzari, N.; Cococcioni, M. HP—A Code for the Calculation of Hubbard Parameters Using Density-Functional Perturbation Theory. *Comput. Phys. Commun.* **2022**, *279*, 108455.

(14) Cococcioni, M.; de Gironcoli, S. Linear Response Approach to the Calculation of the Effective Interaction Parameters in the LDA + U Method. *Phys. Rev. B* **2005**, *71*, 035105.

(15) Giannozzi, P.; Baroni, S.; Bonini, N.; Calandra, M.; Car, R.; Cavazzoni, C.; Ceresoli, D.; Chiarotti, G. L.; Cococcioni, M.; Dabo, I.; Dal Corso, A.; de Gironcoli, S.; Fabris, S.; Fratesi, G.; Gebauer, R.; Gerstmann, U.; Gougoussis, C.; Kokalj, A.; Lazzeri, M.; Martin-Samos, L.; Marzari, N.; Mauri, F.; Mazzarello, R.; Paolini, S.; Pasquarello, A.; Paulatto, L.; Sbraccia, C.; Scandolo, S.; Sclauzero, G.; Seitsonen, A. P.; Smogunov, A.; Umari, P.; Wentzcovitch, R. M. QUANTUM ESPRESSO: A Modular and Open-Source Software Project for Quantum Simulations of Materials. *J. Phys.: Condens. Matter* **2009**, *21*, 395502.

(16) Giannozzi, P.; Andreussi, O.; Brumme, T.; Bunau, O.; Buongiorno Nardelli, M.; Calandra, M.; Car, R.; Cavazzoni, C.; Ceresoli, D.; Cococcioni, M.; Colonna, N.; Carnimeo, I.; Dal Corso, A.; de Gironcoli, S.; Delugas, P.; DiStasio, R. A.; Ferretti, A.; Floris, A.; Fratesi, G.; Fugallo, G.; Gebauer, R.; Gerstmann, U.; Giustino, F.; Gorni, T.; Jia, J.; Kawamura, M.; Ko, H.-Y.; Kokalj, A.; Küçükbenli, E.; Lazzeri, M.; Marsili, M.; Marzari, N.; Mauri, F.; Nguyen, N. L.; Nguyen, H.-V.; Otero-de-la Roza, A.; Paulatto, L.; Poncé, S.; Rocca, D.; Sabatini, R.; Santra, B.; Schlipf, M.; Seitsonen, A. P.; Smogunov, A.; Timrov, I.; Thonhauser, T.; Umari, P.; Vast, N.; Wu, X.; Baroni, S. Advanced Capabilities for Materials Modelling with Quantum ESPRESSO. *J. Phys.: Condens. Matter* **2017**, *29*, 465901.

(17) Giannozzi, P.; Baseggio, O.; Bonfà, P.; Brunato, D.; Car, R.; Carnimeo, I.; Cavazzoni, C.; de Gironcoli, S.; Delugas, P.; Ferrari Ruffino, F.; Ferretti, A.; Marzari, N.; Timrov, I.; Urru, A.; Baroni, S. Quantum ESPRESSO toward the Exascale. *J. Chem. Phys.* **2020**, *152*. DOI: 10.1063/5.0005082.

(18) Wang, V.; Xu, N.; Liu, J.-C.; Tang, G.; Geng, W.-T. VASPKIT: A User-Friendly Interface Facilitating High-Throughput Computing and Analysis Using VASP Code. *Comput. Phys. Commun.* **2021**, *267*, 108033.

(19) Medeiros, P. V. C.; Stafström, S.; Björk, J. Effects of Extrinsic and Intrinsic Perturbations on the Electronic Structure of Graphene: Retaining an Effective Primitive Cell Band Structure by Band Unfolding. *Phys. Rev. B* **2014**, *89*, 041407.

(20) Medeiros, P. V. C.; Tsirkin, S. S.; Stafström, S.; Björk, J. Unfolding Spinor Wave Functions and Expectation Values of General Operators: Introducing the Unfolding-Density Operator. *Phys. Rev. B* **2015**, *91*, 041116.

(21) Iraola, M.; Mañes, J. L.; Bradlyn, B.; Horton, M. K.; Neupert, T.; Vergniory, M. G.; Tsirkin, S. S. IrRep: Symmetry Eigenvalues and Irreducible Representations of Ab Initio Band Structures. *Comput. Phys. Commun.* **2022**, *272*, 108226.

(22) Xu, H.; Wu, R.; Zhang, J.-Y.; Han, W.; Chen, L.; Liang, X.; Haw, C. Y.; Mazzolini, P.; Bierwagen, O.; Qi, D.-C.; Zhang, K. H. L. Revealing the Electronic Structure and Optical Properties of $CuFeO_2$ as a *p*-Type Oxide Semiconductor. *ACS Appl. Electron. Mater.* **2021**, *3*, 1834–1841.

(23) Maouhoubi, A.; Ouzaroual, L.; Toual, Y.; Mouchou, S.; Mezzat, F.; Azouaoui, A.; Ez-Zahraouy, H.; Hourmatallah, A.; Bouslykhane, K.; Benzakour, N. Structural, Electronic and Magnetic Properties of the $CuFeO_2$ Multiferroic Compound. *Arab. J. Chem.* **2024**, *17*, 105437.

(24) Upadhyay, D.; Pratap, A.; Jha, P. K. Computational Insights into the Electronic and Optical Properties of Newly Predicted Delafossite $CuFeO_2$. *AIP Conf. Proc.* **2020**, *2265*, 030613.

(25) Klein, I. M.; Liu, H.; Nimlos, D.; Krotz, A.; Cushing, S. K. Ab Initio Prediction of Excited-State and Polaron Effects in Transient XUV Measurements of α-Fe_2O_3. *J. Am. Chem. Soc.* **2022**, *144*, 12834–12841.

(26) Vinson, J.; Rehr, J. J.; Kas, J. J.; Shirley, E. L. Bethe-Salpeter Equation Calculations of Core Excitation Spectra. *Phys. Rev. B* **2011**, *83*, 115106.

(27) Vinson, J. Advances in the OCEAN-3 Spectroscopy Package. *Phys. Chem. Chem. Phys.* **2022**, *24*, 12787–12803.

(28) Gilmore, K.; Vinson, J.; Shirley, E.; Prendergast, D.; Pemmaraju, C.; Kas, J.; Vila, F.; Rehr, J. Efficient Implementation of Core-Excitation Bethe–Salpeter Equation Calculations. *Comput. Phys. Commun.* **2015**, *197*, 109–117.

(29) Shirley, E. L.; Vinson, J.; Gilmore, K. The OCEAN Suite: Core Excitations. In *International Tables for Crystallography, Volume I: X-ray Absorption Spectroscopy and Related Techniques*; Chantler, C. T., Boscherini, F., Bunker, B., Eds.; International Union of Crystallography: Chester, U.K., 2024; Vol. I, Chapter 6.17, pp 809–815.

(30) Troullier, N.; Martins, J. L. Efficient Pseudopotentials for Plane-Wave Calculations. *Phys. Rev. B* **1991**, *43*, 1993–2006.

(31) Jiang, C.-M.; Reyes-Lillo, S. E.; Liang, Y.; Liu, Y.-S.; Liu, G.; Toma, F. M.; Prendergast, D.; Sharp, I. D.; Cooper, J. K. Electronic Structure and Performance Bottlenecks of $CuFeO_2$ Photocathodes. *Chem. Mater.* **2019**, *31*, 2524–2534.

(32) Pham, T. D.; Deskins, N. A. Efficient Method for Modeling Polarons Using Electronic Structure Methods. *J. Chem. Theory Comput.* **2020**, *16*, 5264–5278.

(33) Holstein, T. Studies of Polaron Motion. *Ann. Phys.* **1959**, *8*, 325–342.

(34) Ortmann, F.; Bechstedt, F.; Hannewald, K. Theory of Charge Transport in Organic Crystals: Beyond Holstein's Small-Polaron Model. *Phys. Rev. B* **2009**, *79*, 235206.

(35) Bhattacharyya, S.; Sayer, T.; Montoya-Castillo, A. Nonequilibrium Relaxation Exponentially Delays the Onset of Quantum Diffusion. *Proc. Natl. Acad. Sci. U.S.A.* **2025**, 122. https://doi.org/10.1073/pnas.2424582122.

(36) Bhattacharyya, S.; Sayer, T.; Montoya-Castillo, A. Anomalous Transport of Small Polarons Arises from Transient Lattice Relaxation or Immovable Boundaries. *J. Phys. Chem. Lett.* **2024**, *15*, 1382–1389.

(37) Ahart, C. S.; Blumberger, J.; Rosso, K. M. Polaronic Structure of Excess Electrons and Holes for a Series of Bulk Iron Oxides. *Phys. Chem. Chem. Phys.* **2020**, *22*, 10699–10709.

(38) Ahart, C. S.; Rosso, K. M.; Blumberger, J. Electron and Hole Mobilities in Bulk Hematite from Spin-Constrained Density Functional Theory. *J. Am. Chem. Soc.* **2022**, *144*, 4623–4632.

(39) Chen, H.-W.; Huang, C.-Y.; Shu, G.-J.; Liu, H.-L. Temperature-Dependent Optical Properties of $CuFeO_2$ through the Structural Phase Transition. *RSC Adv.* **2021**, 11, 40173–40181.

(40) Dekker, H. Noninteracting-Blip Approximation for a Two-Level System Coupled to a Heat Bath. *Phys. Rev. A* **1987**, *35*, 1436–1437.

(41) Tanimura, Y.; Kubo, R. Time Evolution of a Quantum System in Contact with a Nearly Gaussian-Markoffian Noise Bath. *J. Phys. Soc. Jpn.* **1989**, *58*, 101–114.

(42) Li, T.; Yan, Y.; Shi, Q. A Low-Temperature Quantum Fokker–Planck Equation that Improves the Numerical Stability of the Hierarchical Equations of Motion for the Brownian Oscillator Spectral Density. *J. Chem. Phys.* **2022**, 156. https://doi.org/10.1063/5.0082108.

(43) Bhattacharyya, S.; Sayer, T.; Montoya-Castillo, A. Space-Local Memory in Generalized Master Equations: Reaching the Thermodynamic Limit for the Cost of a Small Lattice Simulation. *J. Chem. Phys.* **2025**, *162*, 091102.

Appendix C

SUPPORTING INFORMATION FOR CHAPTER 4: COHERENT CHARGE HOPPING SUPPRESSES PHOTOEXCITED SMALL POLARONS IN ERFEO$_3$ BY ANTIADIABATIC FORMATION MECHANISM

This appendix contains supporting information for **Chapter 4** and is adapted with permission from:

Kim, Y.-J.; **Mendes, J. L.**; Michelsen, J. M.; Shin, H. J.; Lee, N.; Choi, Y. J.; Cushing, S. K. Coherent Charge Hopping Suppresses Photoexcited Small Polarons in $ErFeO_3$ by Antiadiabatic Formation Mechanism. *Sci. Adv.* **2024**, *10* (12), eadk4282. https://doi.org/10.1126/sciadv.adk4282

C.1 Synthesis of Single-Crystalline $ErFeO_3$

[Adapted from Sci. Rep. 10, 11825 (2020) (32) Springer Nature].

Single crystals of $ErFeO_3$ were grown by the flux method utilizing PbO, PbF_2, PbO_2, and B_2O_3 fluxes in a high-temperature furnace. Er_2O_3 and Fe_2O_3 powders were prepared in a stoichiometric ratio and mixed with the flux compound. The mixture was heated to 1290 °C in a platinum crucible for 16 h until it was completely dissolved. Then, it was cooled slowly to 850 °C at a rate of 2 °C/h, and further cooled to 23°C at a rate of 100 °C/h. Large $ErFeO_3$ crystals with a cuboid shape and a length up to approximately 1 cm on one side were obtained. The crystallographic structure of the $ErFeO_3$ crystals was confirmed using an X-ray diffractometer (D/Max 2500, Rigaku Corp.). The oxygen vacancy of the ErFeO3 crystals was measured utilizing a WDS (Wavelength Dispersive X-ray Spectrometer) in an EPMA (Electronic Probe MicroAnalyzer, JEOL JXA-8530F). The incident electron beam was applied with an acceleration voltage of 15 kV and a current of 20 nA. The composition ratio was determined by analyzing the characteristic X-rays of each element measured in the four WDS channels with different wavelength ranges. The temperature (T) and magnetic-field (H) dependences of the DC magnetization were measured using a vibrating sample magnetometer at T = 2–150 K and H = -9– 9 T with a Physical Properties Measurement

System (PPMS, Quantum Design, Inc.). The T dependence of specific heat was measured with the standard relaxation method in the PPMS. The T and H dependences of the dielectric constant were observed at f = 500 kHz using an LCR meter (E4980, Agilent).

C.2 Ab Initio Electronic Structure Simulations

C.2.1 Calculation of Ground-State Electronic Structure

Geometry optimization and electronic structure calculations were conducted using the Quantum Espresso package for density-functional theory (DFT), an on-site Hubbard U correction was implemented for accurate band gap estimation (DFT+U, U = 1 eV).[2] Calculations were carried out on a unit cell of $ErFeO_3$ at 293 K based on the crystallographic information listed in **Table C.1**. Norm-conserving pseudopotentials are adopted to describe electron–ion interactions, and the Perdew–Burke–Ernzerho (PBE) functional under the generalized gradient approximation (GGA) is used to describe electron–electron exchange and correlation effects.[3,4] Fritz-Haber-Institute (FHI) pseudopotentials from the NNIN Virtual Vault database were utilized for the Fe^{3+} and O^{2-} ions, while a Vanderbilt pseudopotential from the Pseudo Dojo database was adopted for the Er^{3+} ion. The plane wave energy and charge density cut-offs were 100 and 500 Ry, respectively. A 6 × 6 × 2 Monkhorst–Pack k-point grid was used to sample the Brillouin zone with a total of 150 bands, and a Gaussian smearing of 0.003 eV in the Methfessel–Paxton scheme was utilized in the optimizations. The starting magnetization was set to a sum of zero for the Fe^{3+} ions. All the structures are fully relaxed and self-consistent calculations were performed to a convergence of 10^{-8} eV/atom with the forces on ions under 10^{-2} eV/Å. A calculated projected density of states and band structure are displayed in **Figures 4.1B** and **C** in the main text, and **Figure C.2**.

C.2.2 Modelling of Excited-State XUV Spectra

The modified X-ray absorption simulation package, OCEAN (Obtaining Core Excitations from the Ab initio electronic structure and the NIST BSE solver, version 3.0.2), was employed to qualitatively model the excited-state differential absorption spectra of $ErFeO_3$.

The calculation procedures adhered to the methodologies outlined in Refs. [5,6]. The OCEAN BSE calculation uses a screening mesh of 2 × 2 × 2, a dielectric constant of 25 at 293 K, a 4.0 Bohr screening radius, and a 0.7 scaling factor for the Slater G parameter. The spectral broadening factor was set to 0.5 for all the calculations. The calculated bandgap (approximately 1.8 eV) from DFT+U (U = 1 eV) in **Section C.2.1** was directly adopted without correction due to its close agreement with the experimental bandgap (1.83 ± 0.09 eV) (fig. S3). **Figure C.5** shows the calculated ground-state absorption spectra **(A)** of $ErFeO_3$ at the Fe $M_{2,3}$ edge. The pseudopotentials employed in the DFT calculations were utilized for OCEAN calculations as well. The modified OCEAN package allows for selective occupation of the conduction and valence bands (state filling) with electrons and holes, respectively, at different momentum k-points.[12] Because $ErFeO_3$ exhibits a direct bandgap, bands at the primary Γ point were filled with photoinduced electrons and holes. The calculation was performed on a 6 × 6 × 6 k-point grid. The calculated differential absorption spectra shown in **Figure 4.2B** were derived by subtracting the calculated ground-state absorption spectrum from the calculated excited-state absorption spectra obtained at various lattice configurations corresponding to the charge-transfer, Fe^{3+}–Fe^{2+} hopping, and polaron states based on the singular value decomposition vectors. This configuration involved a 10% axial elongation of the FeO_6 octahedron, accompanied by a contraction in the bond length of equatorial Fe^{3+} ions. This configuration accounts for the Jahn-Teller effects and crystal field splitting of the octahedral complex. The modified OCEAN package inherently exhibits an overestimation of lattice expansion. As a result, it is capable of only qualitatively calculating the changes in the crystal structure over time. By increasing the number of photoinduced electrons and holes in each band to accommodate varying photoexcitation fluence, i.e., charge carrier density, different electronic configurations were evaluated. This led to a noticeable increase in the absorption feature around 52 eV, as observed in **Figure C.7**. This closely resembles the absorption feature observed in the measured spectra (**Fig. 4.2** and **Fig. C.5**), which can be attributed to the Fe^{2+} state. For the calculation of the polaron state with the incorporation of the thermal expansion effects from electron-phonon couplings in several picoseconds, six Fe–O bonds in the octahedron were expanded with the concurrent enlargement of a single unit cell in all axes by 5 to 15% and the resulting spectrum was

averaged and subtracted from the same excited-state spectra. By incorporating the lattice expansion into the ground-state spectrum, the enhanced binding energy between the electrons in the Fe 3d orbital and the core level holes in the Fe 3p band is considered.[7-9] This provides an explanation for the hypsochromic shift of the negative-amplitude feature around 54 eV and the gradual increase in the amplitude of the spectral feature around 55 eV. This is primarily attributed to the elongation of bonds, resulting in a substantial decrease in covalency and an increase in the effective Madelung potential at the Fe^{3+} sites.[10]

C.3 Experimental Details for Transient XUV Reflection-Absorption Spectroscopy

The measurements were conducted using photoexcitation from a ~50 fs, 400 nm frequencydoubled output of a BBO crystal with p-polarization, pumped by an 800 nm, 1 kHz regeneratively amplified Ti:Sapphire laser (Legend Elite Duo, Coherent). The optical excitation fluence was set to 3 mJ/cm^2. Transient reflectance and differential absorption signals were measured by varying delay times between the excitation and probe pulses using an optomechanical delay stage (**Fig. C.4**). The photoexcited electronic dynamics were probed with XUV pulses produced by high-harmonic generation in an argon gas medium with an s-polarized few-cycle white light pulse (<6 fs, 550–950 nm). The residual white light beam was removed with a 200 nm thick aluminum filter (Lebow). The generated XUV continuum was used to probe the Fe $M_{2,3}$ absorption edge around 54 eV. A typical XUV spectrum around the Fe $M_{2,3}$ edge is shown in the inset of **Figure C.4**. An edge-pixel referencing scheme was used to reduce the contribution of intensity fluctuations by referencing to signal-free spectral regions.[11] The reflection measurement used a 10° grazing incidence geometry (80° from normal incidence). The ground-state static XUV reflectivity of $ErFeO_3$ shown in **Figure C.5** was obtained by normalizing the measured static reflectance spectrum of $ErFeO_3$ by that of a silicon wafer, which does not have any absorption features in the energy region of interest. Neon gas was used for spectral calibration. A detailed description of the setup is reported in Ref. [12].

C.4 Fitting Analysis of the Kinetic Model for the Relaxation Dynamics

To fit the temporal evolution of each state's population, a system of differential equations was numerically integrated.[13,14] These differential rate equations, **Equations C.1** to **C.3**, included in the three-component sequential kinetic scheme with a pseudo-first-order behavior (**Fig. 4.3B** and **Fig. C.8**), describe the rate of population change for each species and depend on the fitted parameters k_1 and k_2.

$$\frac{dN_{\mathrm{CT}}}{dt} = -k_1 \cdot N_{\mathrm{CT}}(t) \qquad \textbf{(C.1)}$$

$$\frac{dN_{\mathrm{Hopping}}}{dt} = k_1 \cdot N_{\mathrm{CT}}(t) - k_2 \cdot N_{\mathrm{Hopping}}(t) \qquad \textbf{(C.2)}$$

$$\frac{dN_{\mathrm{Polaron}}}{dt} = k_2 \cdot N_{\mathrm{Hopping}}(t) \qquad \textbf{(C.3)}$$

By solving these differential equations, the populations of the charge-transfer state, charge hopping between Fe^{3+}–Fe^{2+} sites, and small polaron state ($N_{\mathrm{CT}}(t)$, $N_{\mathrm{Hopping}}(t)$, and $N_{\mathrm{Polaron}}(t)$, respectively) for a specific set of k_1 and k_2 are obtained. The fits for the kinetic traces obtained from the multivariate regression analysis are obtained by numerical convolution with a Gaussian instrument response function to account for the instrument response function, the width of which is a variable within the fit. The time-dependent population of each species was solved analytically to yield the fractional population of each state as a function of time with **Equations C.4** to **C.6**:

$$[N_{\mathrm{CT}}(t)] = [N_{\mathrm{CT}}(0)]e^{-k_1 t} \qquad \textbf{(C.4)}$$

$$[N_{\mathrm{Hopping}}(t)] = \frac{[N_{\mathrm{CT}}(0)]k_1}{k_2 - k_1}[e^{-k_1 t} - e^{-k_2 t}] \qquad \textbf{(C.5)}$$

$$[N_{\mathrm{Polaron}}(t)] = [\mathrm{N_{CT}}(0)][1 - \frac{1}{k_2 - k_1}(k_2 e^{-k_1 t} - k_1 e^{-k_2 t})] \qquad \textbf{(C.6)}$$

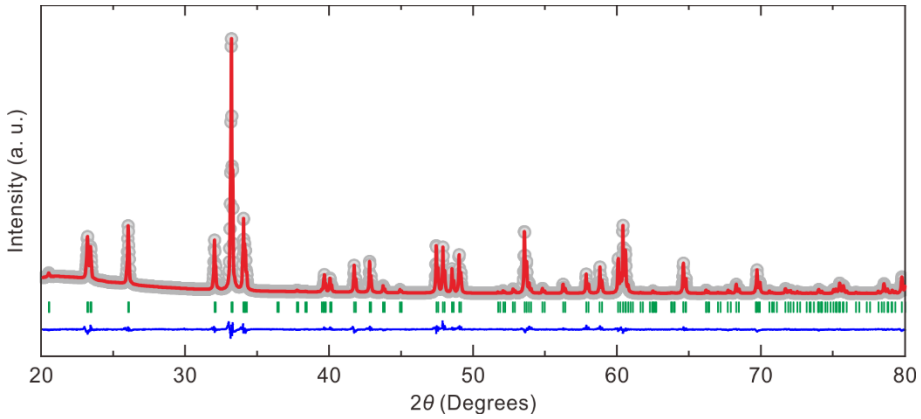

Figure C.1 X-ray diffraction pattern of single-crystalline $ErFeO_3$. Observed (grey circles) and calculated (red solid line) powder X-ray diffraction patterns for the ground-state $ErFeO_3$ single crystals at 293 K. The blue curve represents the intensity difference between the observed and calculated patterns. The short green lines denote the Bragg positions. Adapted from *Sci. Rep.* 10, 11825 (2020) (*32*) Springer Nature.[1]

Table C.1 Crystallographic information of $ErFeO_3$. Adapted from *Sci. Rep.* 10, 11825 (2020) (*32*) Springer Nature.[1]

Structure	Orthorhombic
Space group	*Pbnm*
Lattice parameters (Å)	$a = 5.2611$ [1]
	$b = 5.5835$ [1]
	$c = 7.5915$ [2]
	$c/a = 2.732$
R-factors (%)	$R_p = 6.95$
	$R_{wp} = 6.39$
	$R_{exp} = 3.52$
χ^2	3.29
Er (x, y, z)	(0.98127, 0.06922, 0.25)
Fe (x, y, z)	(0, 0.5, 0)
O_1 (x, y, z)	(0.1139, 0.4588, 0.25)
O_2 (x, y, z)	(0.695, 0.3085, 0.0597)

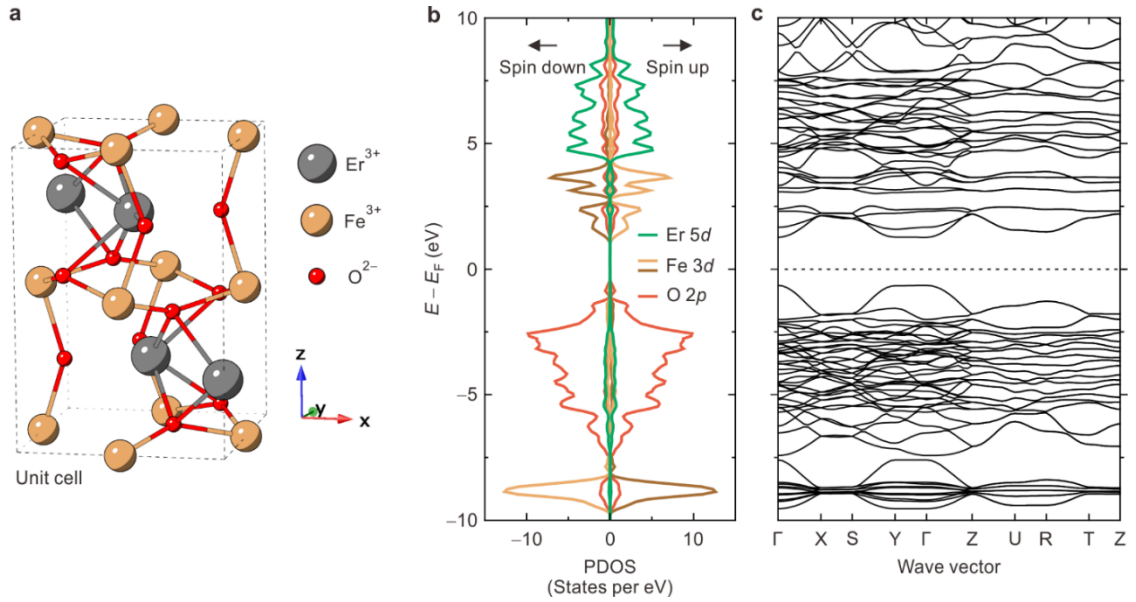

Figure C.2 Calculated ground-state electronic structure of $ErFeO_3$. (A) The crystal structure of the $ErFeO_3$ unit cell. *X* (*a*), *y* (*b*), and *z* (*c*), directions denote [001], [010], and [001] crystal axes, respectively, in the *Pbnm* space group. **(B)** Projected density of states (PDOS) onto each element computed using DFT for two opposite spin states. Er, Fe, and O are colored in green, brown, and red, respectively. Positive (negative) values stand for spin up (down). E_F denotes the Fermi energy. **(C)** Calculated band structure with an extended energy range compared to **Figure 4.1C** in the main text.

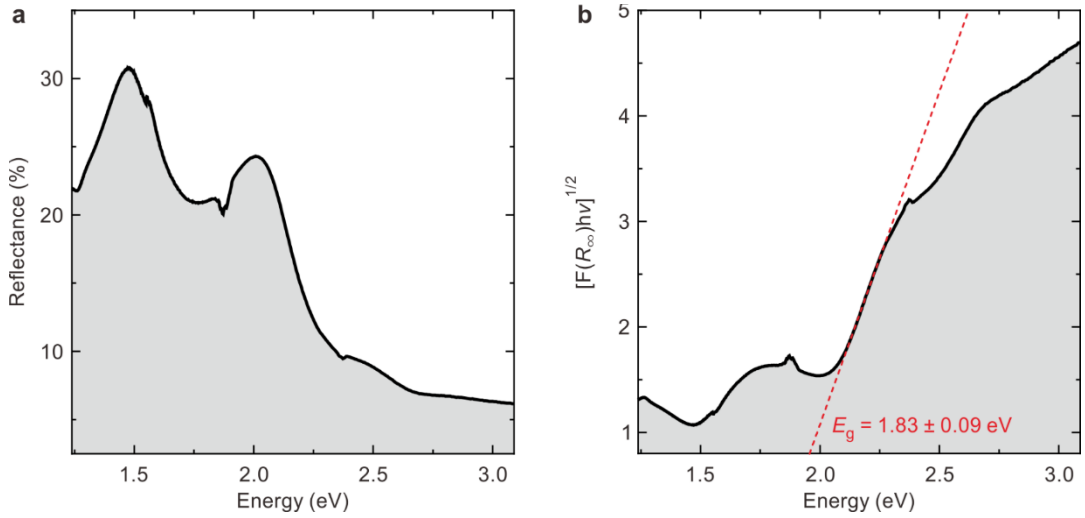

Figure C.3 Steady-state reflectance spectrum of $ErFeO_3$ and bandgap measurement. (A) Diffuse reflectance spectrum of the $ErFeO_3$ powder. **(B)** Kubelka-Munk-transformed reflectance spectrum. The bandgap (E_g) is determined to be 1.83 ± 0.09 eV, similar to the reported valued.[15,16] The peak feature around 1.7 eV is attributed to background noise.

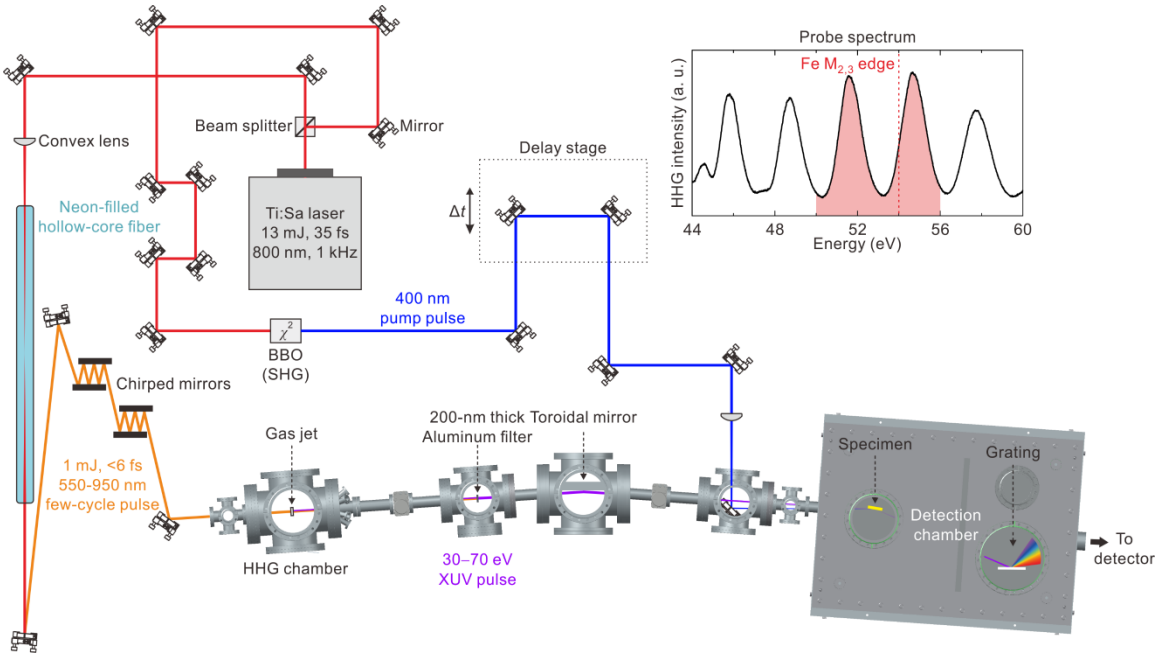

Figure C.4 Instrumental layout of the transient XUV reflection-absorption spectrometer. Using the nonlinear pulse-shortening approach with a gas (neon)-filled hollow-core fiber, a few-cycle white light fundamental pulse with high pulse energy (~1 mJ) is generated. Nonlinear high-harmonic generation is achieved by focusing the intense fundamental beam into an argon-filled gas jet inside a vacuum chamber. XUV probe pulses spanning the energy range of 30–70 eV are focused onto the sample as reflected in the toroidal mirror. A 400 nm pump pulse is also noncolinearly focused onto the specimen as reflected in the recombination mirror inside the chamber. The vacuum pressure for the measurement was 1×10^{-3} Torr.

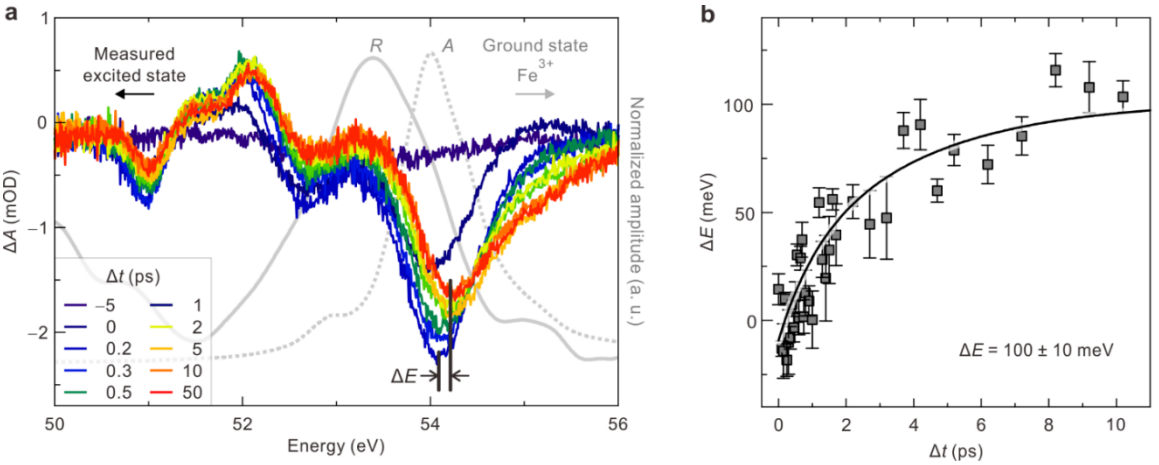

Figure C.5 Transient XUV spectra and ultrafast small polaron formation. (A) Time-resolved differential absorption spectra of $ErFeO_3$ for selected time delays (Δt) following photoexcitation at a fluence of 3 mJ/cm2. Corresponding Δt in picoseconds are indicated at the left bottom of the panel. Measured reflection (R) and unbroadened calculated absorption (A) spectra both in the ground state are overlaid as thick solid and dotted lines, respectively, presented in arbitrary units. **(B)** The spectral shift (ΔE) of the feature at ~54 eV in panel a plotted with time. A bi-exponential fit curve is overlaid as a guide for the eye.

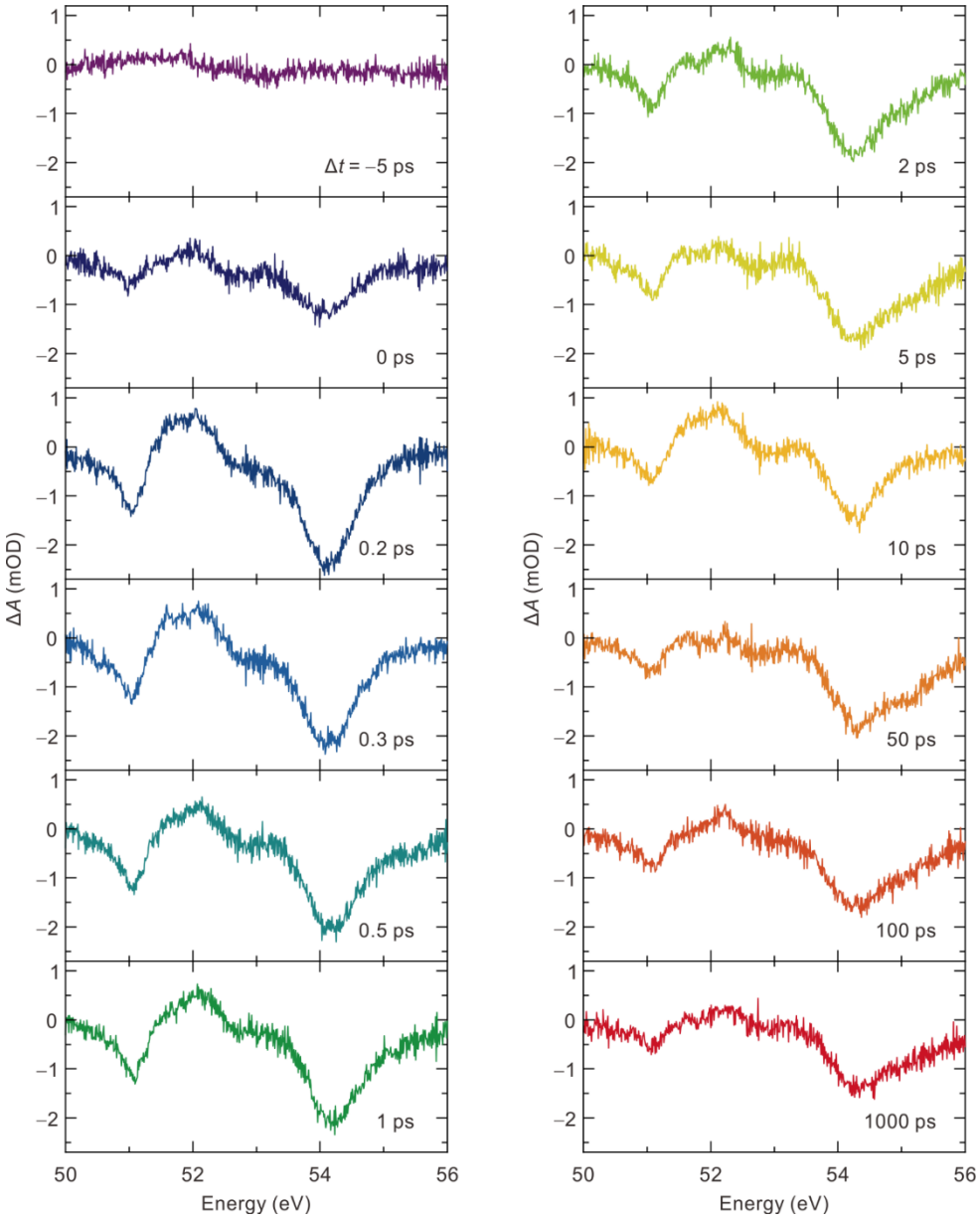

Figure C.6 Relaxation dynamics of $ErFeO_3$ at a long timescale. Dynamics become steady-state out to 1000 ps at a fluence of 3 mJ/cm^2. The main spectral features remain the same with reduced amplitudes. This set of data was measured separately from the one shown in **Figure 4.2A** in the main text.

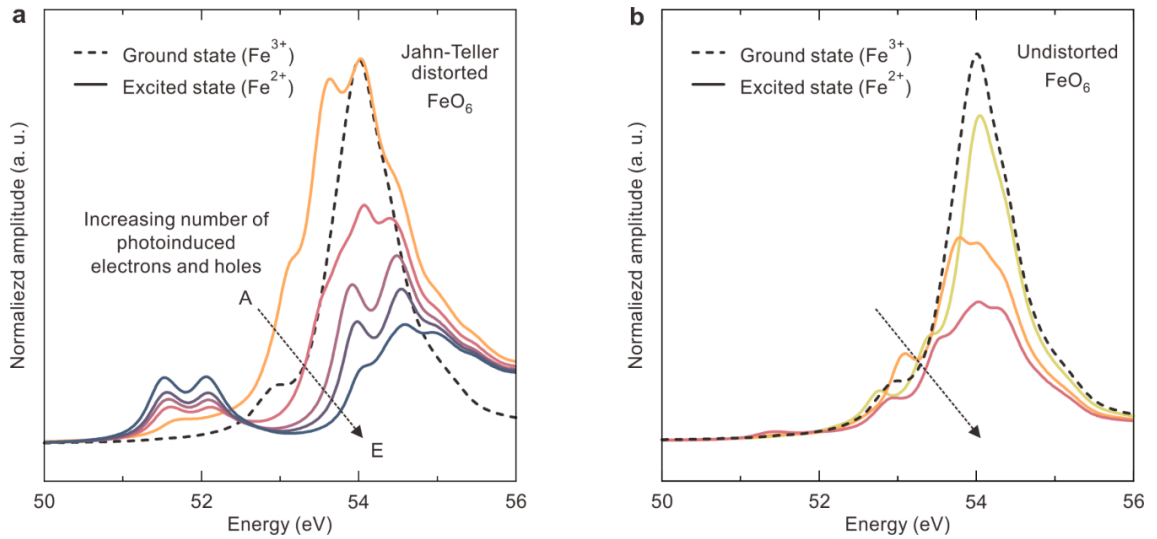

Figure C.7 Calculated core-level absorption spectra under different band filling conditions. (A) The simulated excited-state absorption spectra of the Fe $M_{2,3}$ edge at the CT state with a Jahn-Teller distorted FeO_6 octahedron. As the number of photoexcited electrons and holes increases in the conduction and valence bands at the primary Γ point, from A to E, respectively, the spectral amplitude of the corresponding feature around 52 eV is observed to increase. **(B)** Simulated excited-state absorption spectra of the same edges at the CT state without a Jahn-Teller distortion. In contrast to the expanded configuration shown in panel **a**, the undistorted FeO_6 octahedron does not exhibit any spectral features around 52 eV. This observation suggests that the observed spectral features in $ErFeO_3$ originate from the expansion and distortion of the octahedron upon photoexcitation.

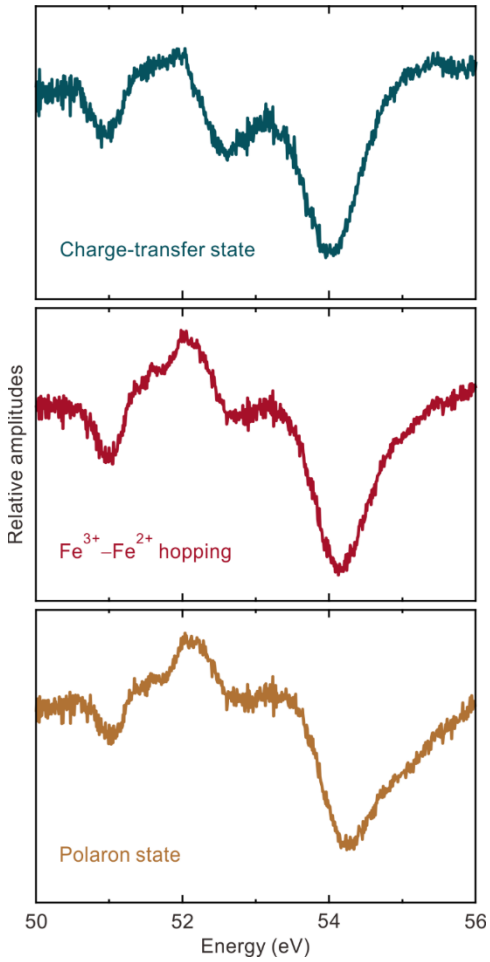

Figure C.8 Singular value decomposition vectors for the three-state kinetic model. The three spectral vectors were derived from the experimental data set. These vectors were combined linearly and used in a multivariate regression analysis. The purpose was to determine the time-dependent population of each state. Specifically, the states examined were the charge-transfer (hundreds of femtoseconds), the Fe^{3+}–Fe^{2+} hopping (less than a few picoseconds), and the small polaron states (several picoseconds). The mathematical description provided in **Section C.4** was used for this analysis. It is important to note that the charge hopping state is seen as an intermediate step connecting the charge-transfer and the polaron states.

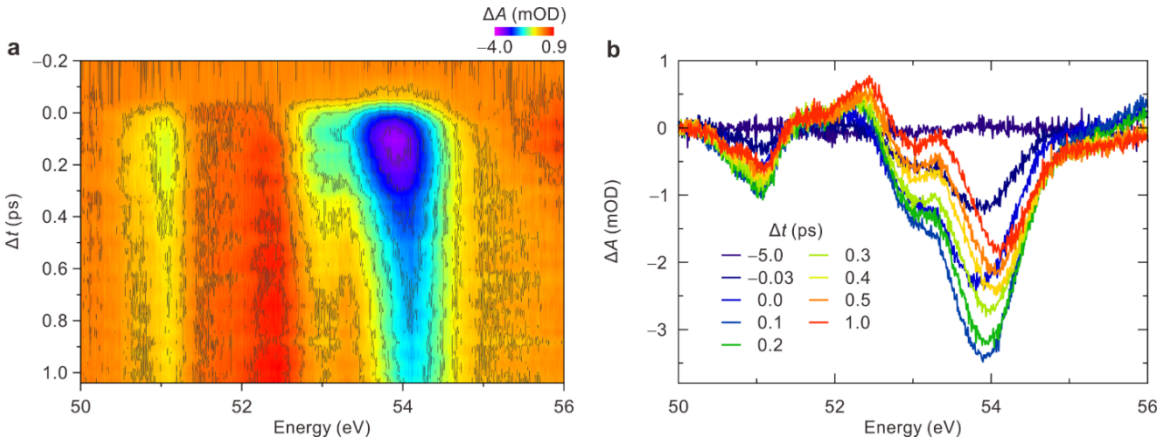

Figure C.9 Time-resolved differential absorption spectra with fine time steps. A separate measurement was performed at the same fluence of 3 mJ/cm², employing fine time steps, in order to check the reproducibility and analyze the observed oscillatory feature. **(A)** Two-dimensional false color plot of the time-resolved differential absorption spectra. **(B)** Time-resolved differential absorption spectra. Corresponding time delays are indicated inside the panel.

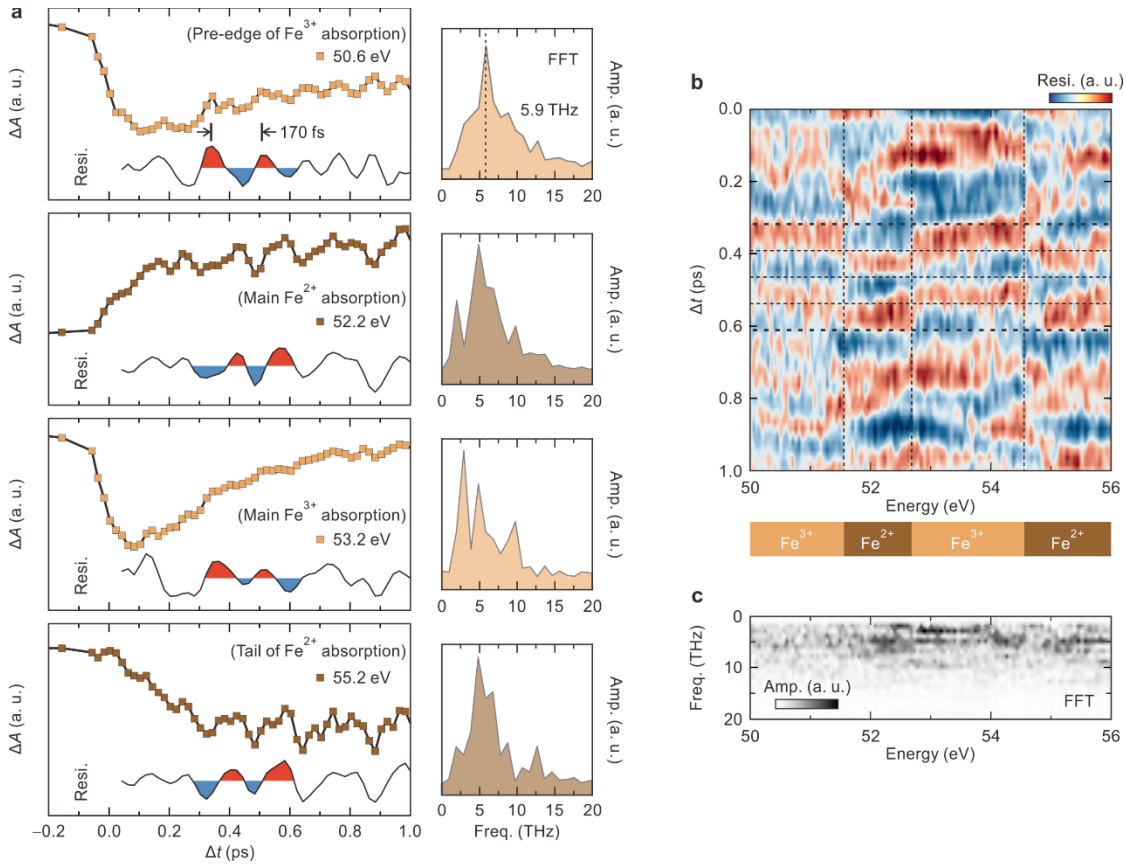

Figure C.10 Coherent charge hopping between Fe^{3+} and Fe^{2+}. (A) (Left) kinetic profiles at different probe energies obtained at a fluence of 3 mJ/cm². Probe energies are indicated inside each panel. Residual traces (Resi.) in each panel are obtained by subtracting a multi-exponential fit from each kinetic profile to highlight the oscillation feature for clarity. (Right) Fast Fourier transform (FFT) of the residuals. The main oscillation

frequency (Freq.) lies between 4.9–5.8 THz regardless of the probe region. **(B)** Two-dimensional false color plot of the residuals over the probe range (50–56 eV). The marked region with horizontal dotted lines is where the out-of-phase oscillatory behavior between the Fe^{3+} and Fe^{2+} states is apparent. Regarding the spectral assignment, the main decrease in absorption observed at 52.8–54.7 eV is indicative of the depletion of the initial Fe^{3+} state, while the main increase in absorption in the red-shifted region of 51.5–52.8 eV signifies the formation of the Fe^{2+} state upon photoexcitation. This assignment aligns with the well-established findings in previous studies of α-Fe_2O_3,[7,17,18] and it is also consistent with our calculation results (**Fig. C.7**). The two additional features observed at 50.0–51.5 eV and 54.7–56.0 eV, exhibiting the negative and positive absorption, share the same phase as the main spectral features of the Fe^{3+} and Fe^{2+} states, respectively, implying they belong to each state. The former could arise from the pre-edge absorption of the Fe^{3+} state, while the latter represents the tail of the Fe^{2+} absorption as also reflected in the calculated spectra (**Fig. C.7**). **(C)** Two-dimensional false color plot of the FFT profiles over the probe range. The main frequency is centered around 5 THz.

C.5 References

(1) Oh, D. G.; Kim, J. H.; Shin, H. J.; Choi, Y. J.; Lee, N. Anisotropic and Nonlinear Magnetodielectric Effects in orthoferrite $ErFeO_3$ Single Crystals. *Sci. Rep.* **2020,** *10,* 11825.

(2) Giannozzi, P.; Baroni, S.; Bonini, N.; Calandra, M.; Car, R.; Cavazzoni, C.; Ceresoli, D.; Chiarotti, G. L.; Cococcioni, M.; Dabo, I.; Dal Corso, A.; de Gironcoli, S.; Fabris, S.; Fratesi, G.; Gebauer, R.; Gerstmann, U.; Gougoussis, C.; Kokalj, A.; Lazzeri, M.; Martin-Samos, L.; Marzari, N.; Mauri, F.; Mazzarello, R.; Paolini, S.; Pasquarello, A.; Paulatto, L.; Sbraccia, C.; Scandolo, S.; Sclauzero, G.; Seitsonen, A. P.; Smogunov, A.; Umari, P.; Wentzcovitch, R. M. Quantum ESPRESSO: A Modular and Open-Source Software Project for Quantum Simulations of Materials. *J. Phys.: Condens. Matter* **2009,** *21,* 395502.

(3) van Setten, M. J.; Giantomassi, M.; Bousquet, E.; Verstraete, M. J.; Hamann, D. R.; Gonze, X.; Rignanese, G.-M. The PseudoDojo: Training and grading a 85 Element Optimized Norm-Conserving Pseudopotential table. *Comput. Phys. Commun.* **2018,** *226,* 39–54.

(4) Ernzerhof, M.; Scuseria, G. E. Assessment of the Perdew–Burke–Ernzerhof Exchange-Correlation Functional. *J. Chem. Phys.* **1999**, *110*, 5029–5036.

(5) Klein, I. M.; Liu, H.; Nimlos, D.; Krotz, A.; Cushing, S. K. *Ab Initio* Prediction of Excited-State and Polaron Effects in Transient XUV Measurements of α-Fe_2O_3. *J. Am. Chem. Soc.* **2022**, *144*, 12834–12841.

(6) Klein, I. M.; Krotz, A.; Lee, W.; Michelsen, J. M.; Cushing, S. K. *Ab Initio* Calculations of XUV Ground and Excited States for First-Row Transition Metal Oxides. *J. Phys. Chem. C* **2023**, *127*, 1077–1086.

(7) Husek, J.; Cirri, A.; Biswas, S.; Baker, L. R. Surface Electron Dynamics in Hematite (α-Fe_2O_3): Correlation between Ultrafast Surface Electron Trapping and Small Polaron Formation. *Chem. Sci.* **2017**, *8*, 8170–8178.

(8) Biswas, S.; Husek, J.; Baker, L. R. Elucidating Ultrafast Electron Dynamics at Surfaces Using Extreme Ultraviolet (XUV) Reflection-Absorption Spectroscopy. *Chem. Commun.* **2018**, *54*, 4216–4230.

(9) Rehr, J. J.; Ankudinov, A. L. Progress in the Theory and Interpretation of XANES. *Coord. Chem. Rev.* **2005**, *249*, 131–140.

(10) Datta, S.; Pandeya, R. P.; Dey, A. B.; Gloskovskii, A.; Schlueter, C.; Peixoto, T. R. F.; Singh, A.; Thamizhavel, A.; Maiti, K. Layer-Resolved Electronic Behavior in a Kondo Lattice System, $CeAgAs_2$. *J. Phys.: Condens. Matter* **2023**, *35*, 235601.

(11) Géneaux, R.; Chang, H.-T.; Schwartzberg, A. M.; Marroux, H. J. B. Source Noise Suppression in Attosecond Transient Absorption Spectroscopy by Edge-Pixel Referencing. *Opt. Express* **2021**, *29*, 951–960.

(12) Liu, H.; Michelsen, J. M.; Mendes, J. L.; Klein, I. M.; Bauers, S. R.; Evans, J. M.; Zakutayev, A.; Cushing, S. K. Measuring Photoexcited Electron and Hole Dynamics in ZnTe and Modeling Excited-State Core-Valence Effects in Transient Extreme Ultraviolet Reflection Spectroscopy. *J. Phys. Chem. Lett.* **2023**, *14*, 2106–2111.

(13) Biswas, S.; Husek, J.; Londo, S.; Fugate, E. A.; Baker, L. R. Identifying the Acceptor State in NiO Hole Collection Layers: Direct Observation of Exciton Dissociation and Interfacial Hole Transfer across a Fe_2O_3/NiO Heterojunction. *Phys. Chem. Chem. Phys.* **2018**, *20*, 24545–24552.

(14) Biswas, S.; Husek, J.; Londo, S.; Baker, L. R. Ultrafast Electron Trapping and Defect-Mediated Recombination in NiO Probed by Femtosecond Extreme Ultraviolet Reflection-Absorption Spectroscopy. *J. Phys. Chem. Lett.* **2018**, *9*, 5047–5054.

(15) Shen, H.; Feng, P.; Jiang, G.; Xian, Q. Synthesis of Mn-Doped $ErFeO_3$ with Enhanced Photo and Vibration Catalytic Activities. *J. Sol-Gel Sci. Technol.* **2020**, *95*, 230–238.

(16) Ravichandran, H.; Irusan, B.; Balaraman, S.; Govindasamy, M.; Krishnamoorthy, S.; Elayaperumal, M. Microwave Assisted Synthesis and Characterization of Fe^{3+}-O-Fe^{3+} Sublattice Magnetic Moment Influencing Ferromagnetism Exhibited Erbium Orthoferrite Sublattice ($ErFeO_3$) Perovskite Nanopowders. *J. Alloys Compd.* **2022**, *890*, 161825.

(17) Vura-Weis, J.; Jiang, C.-M.; Liu, C.; Gao, H.; Lucas, J. M.; de Groot, F. M. F.; Yang, P.; Alivisatos, A. P.; Leone, S. R. Femtosecond $M_{2,3}$-Edge Spectroscopy of Transition-Metal Oxides: Photoinduced Oxidation State Change in α-Fe2O3. *J. Phys. Chem. Lett.* **2013**, *4*, 3667–3671.

(18) Londo, S.; Biswas, S.; Husek, J.; Pinchuk, I. V.; Newburger, M. J.; Boyadzhiev, A.; Trout,A. H.; McComb, D. W.; Kawakami, R.; Baker, L. R. Ultrafast Spin Crossover in a Room-Temperature Ferrimagnet: Element-Specific Spin Dynamics in Photoexcited Cobalt Ferrite. *J. Phys. Chem. C* **2020**, *124*, 11368–11375.

A p p e n d i x D

SUPPORTING INFORMATION FOR CHAPTER 5: DYNAMIC COMPETITION BETWEEN HUBBARD AND SUPEREXCHANGE INTERACTIONS SELECTIVELY LOCALIZES ELECTRONS AND HOLES THROUGH POLARONS

This appendix contains supporting information for **Chapter 5** and is adapted with permission from:

Mendes, J. L.; Shin, H. J.; Seo, J. Y.; Lee, N.; Choi, Y. J.; Varley, J. B.; Cushing, S. K. Dynamic Competition Between Hubbard and Superexchange Interactions Selectively Localizes Electrons and Holes Through Polarons. *J. Am. Chem. Soc.* **2025**, *147* (19), 16018–16026. https://doi.org/10.1021/jacs.4c16837

D.1 $GdFeO_3$ Characterization

D.1.1 Ground State Optical Characterization

The band gap of single-crystal $GdFeO_3$ was determined using UV-Visible reflection spectroscopy (Cary 5000, Agilent Technologies). Scans were collected in a range of 250-1200 nm in reflectivity mode. For a Tauc plot analysis, the reflectance spectra were transformed using the Kubelka–Munk function using **Equation D.1**:

$$F(R_\infty) = \frac{(1-R_\infty)^2}{2R_\infty} \quad \textbf{(D.1)}$$

where $R_\infty = R_{sample}/R_{standard}$.[1] The direct band gap of $GdFeO_3$ was measured as ~1.43 eV and the indirect band gap was measured to be ~1.39 eV.

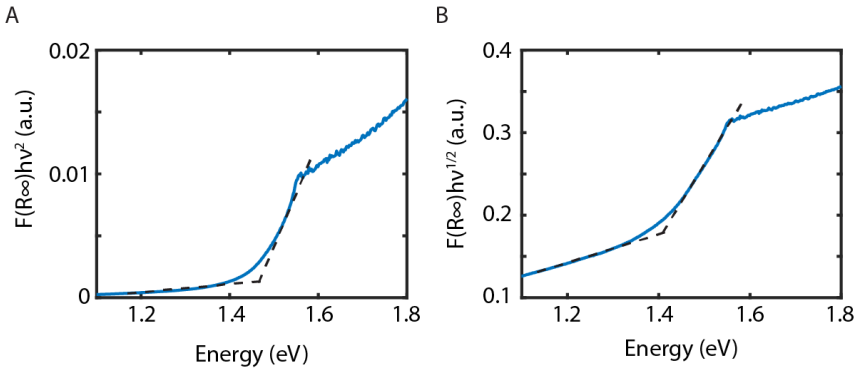

Figure D.1 Tauc plot from the measured optical ground state reflectivity of $GdFeO_3$ with $(\alpha h\nu)^{1/r}$ plotted as r = ½ for a direct allowed band gap transition **(A)** and r = 2 for an indirect allowed band gap transition **(B)**. The direct band gap is found to be ~1.43 eV and the indirect band gap is found to be ~1.39 eV.

D.1.2 Structural Characterization

The crystallographic structure and absence of a second phase were checked by the Rietveld refinement using the FullProf program for the power X-ray diffraction data. The data were obtained with a Rigaku D/Max 2500 powder X-ray diffractometer using Cu-K_α radiation. The result suggests that the $GdFeO_3$ forms an orthorhombic perovskite with the *Pbnm* space group. The lattice constants are found to be a = 5.3464 Å, b = 5.5996 Å, and c = 7.6623 Å with the reliability factors; χ^2 = 1.64, R_p = 2.29 %, R_{wp} = 3.03 %, and R_{exp} = 2.37 %. Further details of crystallographic data are summarized in **Table D.1**.

Table D.1 Crystallographic information of $GdFeO_3$. Unit cell parameters, reliability factors and position parameters for $GeFeO_3$.

Structure	Orthorhombic
Space group	*Pbnm*
Lattice parameters (Å)	$a = 5.3464(1)$ $b = 5.5996(1)$ $c = 7.6623(2)$ $c/a = 1.433$
R-factors (%)	$R_p = 2.29$ $R_{wp} = 3.03$ $R_{exp} = 2.37$
χ^2	1.64
Gd (x, y, z)	(1.0159, 0.0605, 0.25)
Fe (x, y, z)	(0.5, 0, 0)
O_1 (x, y, z)	(0.4219, 0.9627, 0.25)
O_2 (x, y, z)	(0.7107, 0.2988, 0.0455)

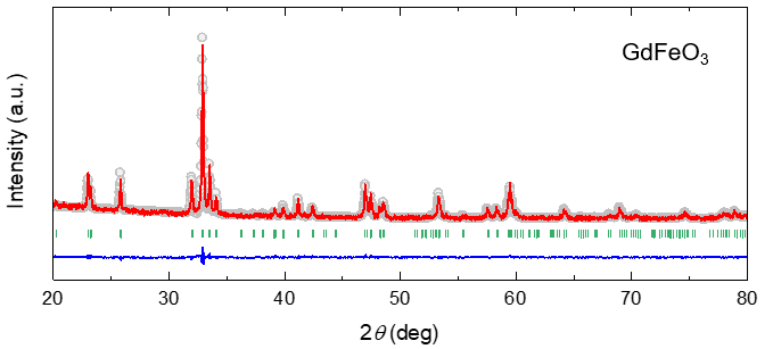

Figure D.2 X-ray diffraction pattern of single-crystalline $GdFeO_3$. The observed (gray circles) and calculated (red solid line) powder X-ray diffraction patterns for a $GdFeO_3$ single crystal at 293 K. The blue curve denotes the difference in intensity between the observed and calculated patterns, while the short green ticks indicate the Bragg reflection positions.

D.1.3 Fluorescence Lifetime

The fluorescence lifetime of $GdFeO_3$ was measured using a Stellaris Falcon Fluorescence Lifetime Imaging Microscope (FLIM, Leica Microsystems). Measurements were performed with the 10x dry lens objective. A CW 405 nm, 0.5 mW laser excites the $GdFeO_3$ single-crystal, and the resulting fluorescence was measured. The Stellaris Falcon employs TauSense software to gate the PMT detectors with 0.1 ns steps when using CW excitation. Similarly, a 790 nm, 80 MHz beam with 0.5 mW of average power was used to measure fluorescence lifetime. Fitting of lifetimes was conducted using the Leica LAS X software that deconvolves the instrument response function from resulting spectra. The n-exponential reconvolution employed by the Leica LAS X software is shown in **Equation D.2**:

$$y(t) = \{IRF(t + Shift_{IRF}) + Bkgr_{IRF}\} \otimes \left\{\sum_{i=0}^{n-1} A[i] e^{\left(-\frac{t}{\tau[i]}\right)} + Bkgr\right\} \quad \textbf{(D.2)}$$

where n is the number of exponential components, A is the amplitude of exponential pre-factors, τ is the lifetime, IRF is the instrument response function, $Bkgr$ is the tail offset correction for the background, $Shift_{IRF}$ is the correction for the IRF displacement, $Bkgr_{IRF}$ is a correction for the IRF background, i are the intensities associated with each exponential component.

The raw spectra, IRF, and resulting n-exponential reconvolutions for each wavelength can be found in **Figure D.3**. The resulting radiative lifetimes calculated using the Leica LAS X software were <100 ps for 790 nm versus 1.2 ± 0.4 ns for 405 nm. We would like to note that the Leica LAS X software calculates a lifetime below 100 ps following 790 nm excitation for the given raw spectra and instrument response function, however, given the limited number of time points in the fluorescence lifetime spectra following 790 nm excitation we refer to it qualitatively as <100 ps.

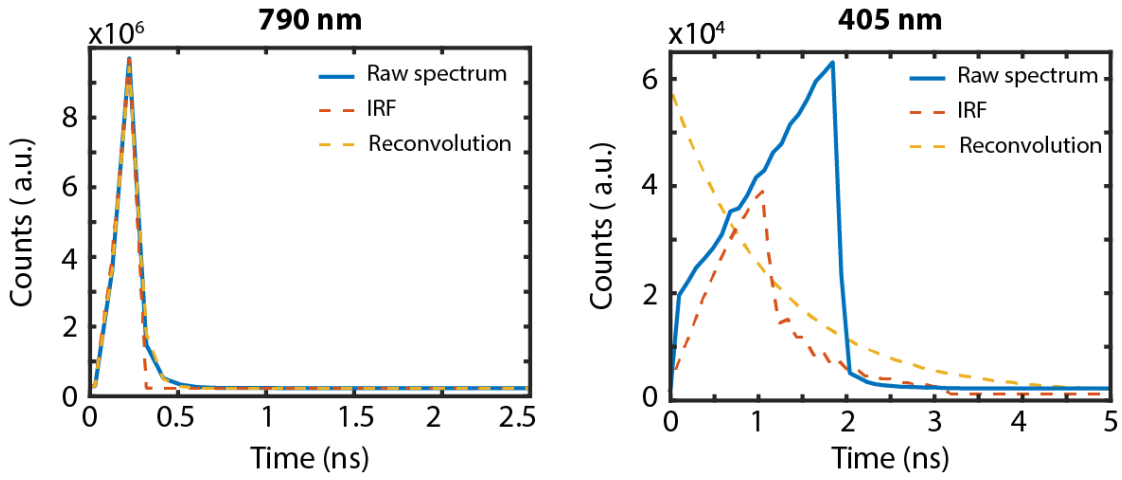

Figure D.3 Raw fluorescence spectra of $GdFeO_3$ following 790 nm (left) and 405 nm (right) excitation (blue). The red trace denotes the IRF for each wavelength and the yellow trace represents the reconvolution calculated by the Leica LAS X software for the 790 nm and 405 nm.

D.2 Experimental Setup: Transient Extreme Ultraviolet Reflectivity Spectrometer

The transient extreme ultraviolet (XUV) reflectivity spectrometer is described previously.[2,3] Briefly, a Legend Elite Duo laser system (Coherent Inc.) with 35 fs, 13 mJ, 1 kHz pulses centered at 800 nm is split by a 75:25 beam splitter with ~3 mJ being used to generate a few-cycle white light beam (<6 fs, 550-900 nm) for high harmonic generation (HHG) and ~10 mJ used for the pump path. The pump path uses both a p-polarized 800 nm beam and the 400 nm frequency doubled output of a BBO crystal with p-polarization, pumped with the 800 nm output of the Ti:Sapphire laser. The optical excitation fluence used in these experiments was ~11 mJ/cm^2 for both 400 nm and 800 nm pumped samples. Transient reflection is measured at a 10° grazing incidence (80° from normal incidence) geometry and measures the varying delay times between the pump and probe pulses by an optomechanical delay stage. The

photoexcited dynamics were probed with an XUV pulse produced with an s-polarized few-cycle white light pulse by HHG in argon. The residual white light beam is removed with a 200 nm thick Al filter (Luxel). The generated XUV continuum is used to probe the Fe $M_{2,3}$ absorption edges at ~54 eV. An edge-pixel referencing scheme was used to denoise the spectra due to intensity fluctuations and used signal-free spectral regions.[4]

D.2.1 Ground State Reflectivity and Long Timescale Dynamics

The ground state sample reflectivity at the Fe $M_{2,3}$ edge is shown in **Figure D.4**. The experimental spectrum (**Fig. D.4**, orange line) was smoothed using a moving average filter with a span of 2.0% of the pixels in the CCD image. The static XUV reflectivity of $GdFeO_3$ is obtained by normalizing the static XUV reflectivity spectrum of the sample by the static reflectivity of a Si wafer, which should not absorb the XUV beam below the Si K edge at ~100 nm. The spectrometer was calibrated using the photoionization continuum of neon gas.[5]

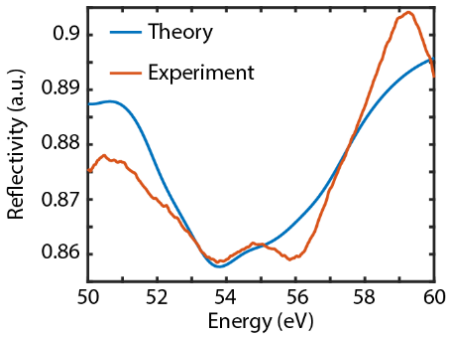

Figure D.4 Experimental ground state XUV reflectivity spectrum (orange) and DFT+BSE theory calculated ground state reflectivity (blue).

The transient spectra presented in the main text (**Figs. D.2A and D.4**) capture the relevant ultrafast features of charge transfer, polaron formation, and the superexchange induced spin crossover on Fe^{2+} centers. Additionally, we present here representative spectra of long timescale dynamics measured at the Fe $M_{2,3}$ X-ray edge following 800 and 400 nm photoexcitation to understand thermalization in the spectra. **Figure D.5A** and **D.5B** presents logarithmic spectra collected out to 1 ns. We compare the long timescale 800 and 400 nm pumped spectra to our DFT+BSE treatment of thermal expansion of the $GdFeO_3$ crystal

lattice (**Fig. D.5C** and **D.5D**) and to our modeled charge transfer and polaron states. The polaron state dominates the 800 nm pumped $GdFeO_3$ spectra out to 1 ns (**Fig. D.5C**), which suggests that thermal expansion of the lattice plays a minimal role in the observed spectral features. Similarly, the DFT+BSE modeled 400 nm charge transfer state (**Fig. D.5D**) continues to dominate the 400 nm pumped transient XUV spectrum, out to 1 ns. This suggests that the free carriers in the charge transfer state dominate the 400 nm pumped spectrum out to our temporal measurement limit.

Figure D.5E and **F** contain exponential fits of the intensity change with respect to time. The exponential model for both plots followed the equation: f(x) = a*exp(-x./b)+c. The resulting non-radiative recombination lifetime for the 800 nm exponential fit was 150±30 ps and for 400 nm excitation it was >1 ns. The radiative lifetime of the 400 nm pumped $GdFeO_3$ discussed in **D.1.3** exceeds the 1 ns temporal limit of our XUV spectrometer, resulting in an exponential fit that poorly describes the recombination lifetime of carriers in the 400 nm XUV spectrum.

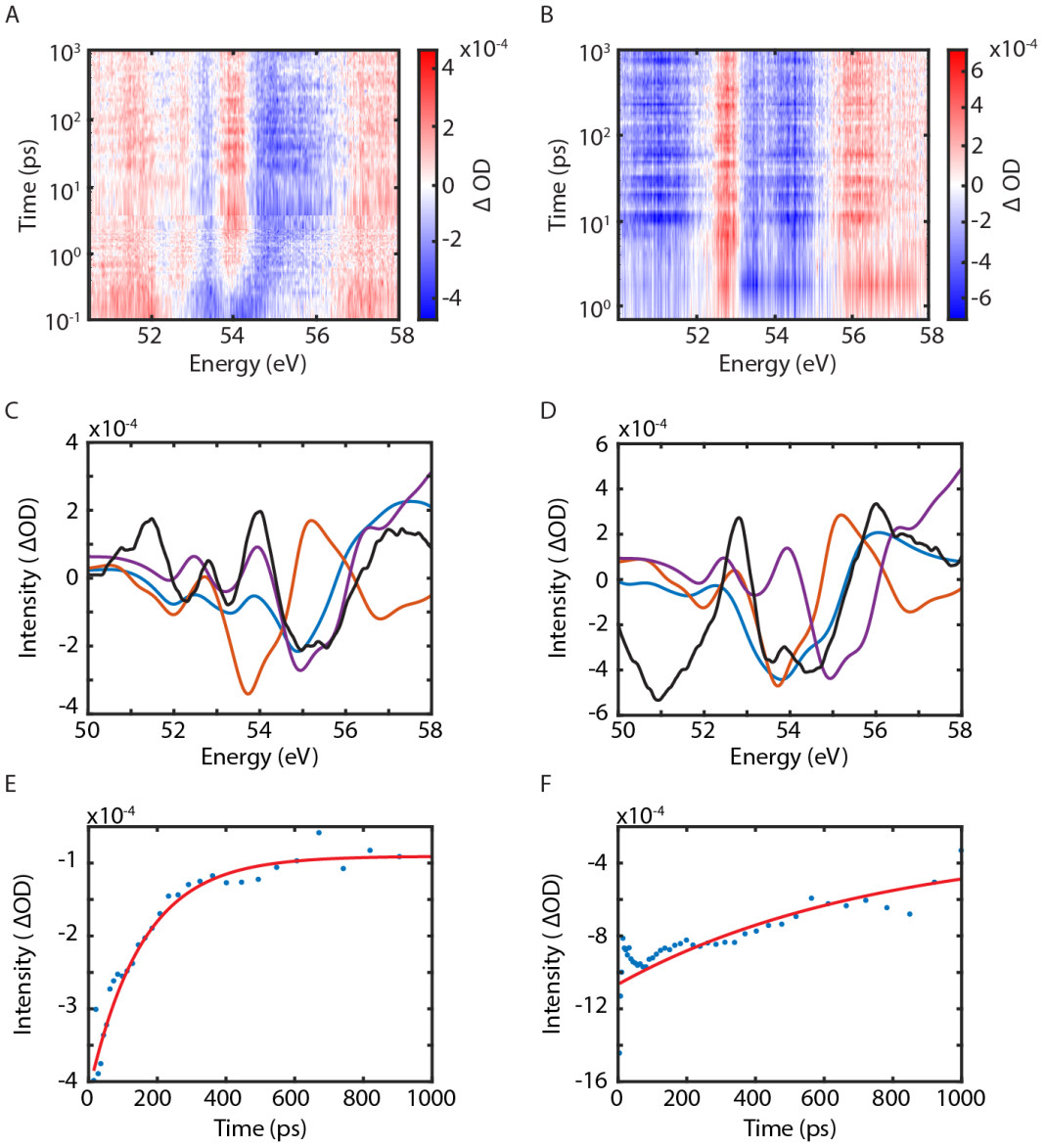

Figure D.5 Long timescale measurements of $GdFeO_3$ following 800 nm **(A)** and 400 nm **(B)** photoexcitation are plotted on a logarithmic time axis. Experimental lineouts 1 ns after 800 nm (**C**, black) and 400 nm (**D**, black) photoexcitation are compared to DFT+BSE modeled 800 and 400 nm charge transfer states (blue), the convolved electron and hole polaron state (purple), and a modeled 350 K thermal expansion of the crystal lattice (red). For the 800 nm spectrum **(C)** the polaron state best agrees with the 1 ns experimental trace, while the 400 nm spectrum **(D)** agrees well with the 400 nm charge transfer state. Exponential fits of the change in intensity over time for the 800 nm pumped spectrum **(E)** and the 400 nm pumped spectrum **(F)**.

D.2.2 Experimental Photoexcited Carrier Density Approximation

The photoexcited carrier density was calculated assuming that for each photon absorbed by the $GdFeO_3$ single crystal, one electron-hole pair is excited.[6–8] The number of photoexcited

carriers (N_e) generated by both excitation wavelengths can be approximated by **Equation D.3**:

$$N_e = \frac{F}{\hbar\upsilon} * \frac{1-R}{D}(1 - \exp(-\alpha D))\big(1 + R\exp(-\alpha D)\big) \quad \textbf{(D.3)}$$

where F is the pump fluence (~11 mJ/cm^2), $\hbar\upsilon$ is the excitation energy, R is the reflectivity coefficient,[9] D is the probe depth (~2 nm), and α is the absorption coefficient.[10] In the case of 800 nm photoexcitation, this results in a photoexcited carrier density of ~7.3x10^{20} cm^{-3}, and for 400 nm excitation a carrier density of ~3.7x10^{20} cm^{-3}. The DFT calculated unit cell of $GdFeO_3$ has a volume of ~2.4x10^{-22} cm^3 and given that each unit cell contains 4 iron atoms, there are approximately ~1.6x10^{22} Fe atoms/cm^3. This would result in ~4.5% and ~2.3% of iron atoms excited following 800 nm and 400 nm photoexcitation, respectively.

D.3 Spectral Analysis

The spectral shift associated with polaron formation in the 800 nm pumped XUV spectra and the decrease in intensity associated with thermalization of hot carriers at the Fe $M_{2,3}$ edge in the 400 nm pumped spectra were fit with single exponential functions following the equation: a*exp(-x./b)+c. The plots of each can be found in **Figures D.6** and **5.2C** in the main text, respectively. The polaron shift resulted in an exponential fit with a time constant of 250 ± 40 fs and a formation rate of ~4 ps. The spectral shift was measured to have a magnitude of 420 ± 150 meV.

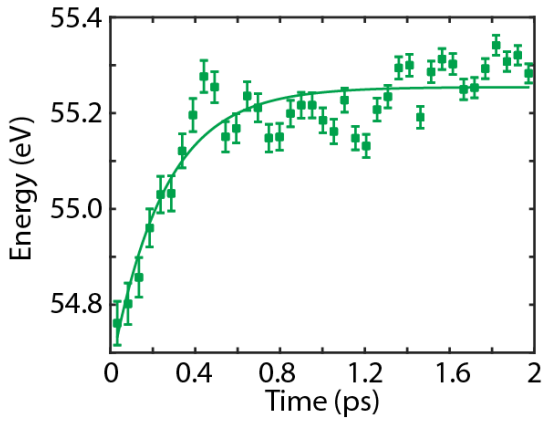

Figure D.6 A fit of the spectral shift at the Fe $M_{2,3}$ edge following 800 nm photoexcitation. The fitting was performed by finding the minima of the averaged spectral intensity between 54.0 – 55.0 eV.

Additionally, to confirm independent spectral features and kinetics of the resulting phenomena in both 800 and 400 nm pumped XUV spectra, we performed singular value decomposition (SVD). The SVD analysis factorizes the two-dimensional matrix of the transient spectra by rotating (U), scaling (S), and then again rotating (V) the matrix. The scaling matrix contains the singular values along its diagonal, which we refer to as the number of components. The number of singular values or components in the scaling matrix is selected to minimize the total number of singular values.

In the case of 800 nm photoexcitation, two singular values well reproduce the kinetics and spectral features of the transient spectra (**Fig. D.7A**). Adding additional singular values to the SVD of the 800 nm transient spectra results in components that look identical to earlier components, but with lower intensity contributions, suggesting that two is sufficient and any additional components are negligible. The SVD components for the 800 nm spectra plotted in **Figure D.7A** agree well with both the polaron state (component 1) and the MMCT state (component 2). To visualize the kinetics of the components, **Figure 5.5C** in the main text, plots the components associated with the MMCT state and the polaron state as a function of time using the experimental 800 nm transient spectrum.

For the SVD of the 400 nm pumped XUV spectra, one component is sufficient to successfully reproduce the transient spectrum. Suggesting that one process dominates the spectra and kinetics of the plot. The component in **Figure D.7B** agrees well with the 400 nm LMCT state, suggesting that aside from carrier thermalization, this state dominates the 400 nm transient kinetics.

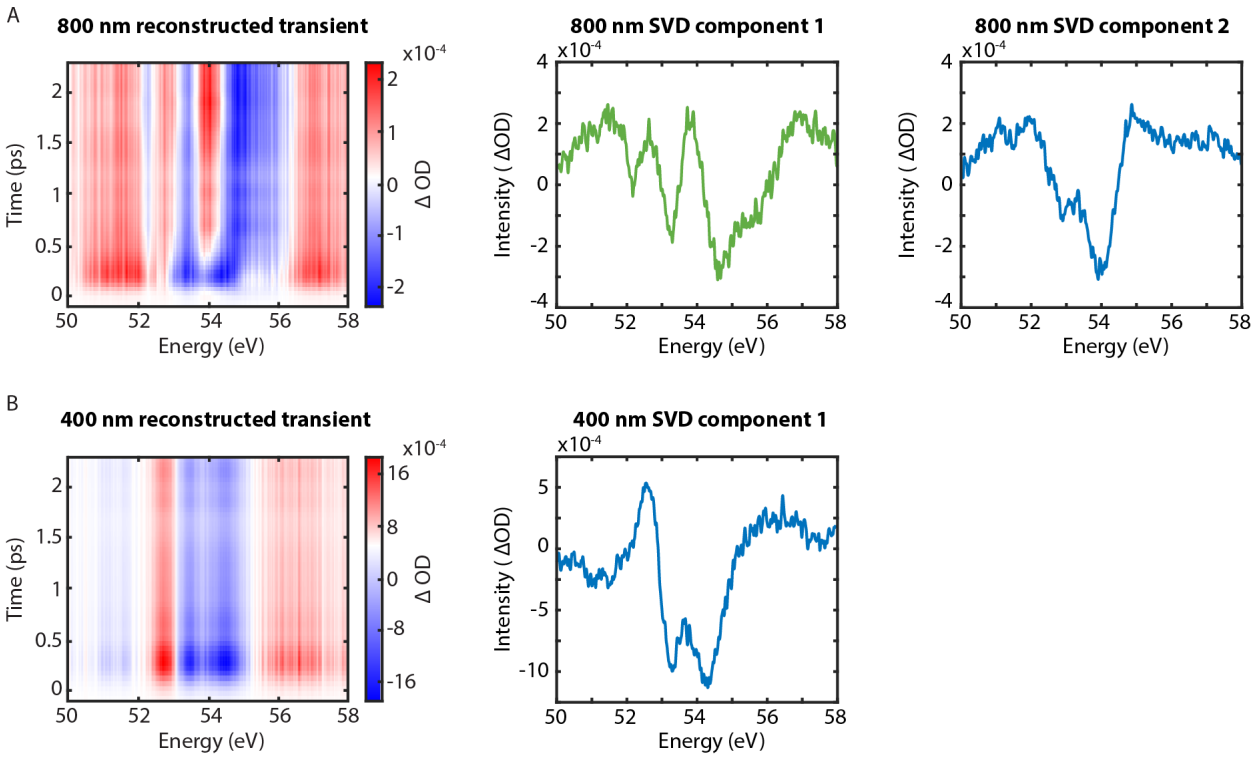

Figure D.7 Singular value decomposition analysis of 800 nm **(A)** and 400 nm **(B)** pumped XUV spectra. Decomposing the 800 nm pumped XUV spectra into two components results in a reconstruction of the transient spectra (**A**, left) that agrees well with the experimental spectra. The first component of the 800 nm SVD analysis (**A**, middle) agrees well with the polaron state, and the second component (**A**, right) agrees well with the 800 nm MMCT state. The 400 nm pump spectra can be reconstructed (**B**, left) in good agreement with the experimental spectra using only one component (**B**, right), which agrees well with the 400 nm LMCT state.

D.4 Theoretical Methods: Ground State and Excited State Core-Level Spectra

D.4.1 Density Functional Theory Calculations

Geometry optimization and density functional theory (DFT) were conducted using the Quantum ESPRESSO package with norm-conserving general gradient approximation (GGA), Perdew–Burke–Ernzerhof (PBE) pseudopotentials.[11–13] Geometry optimizations employed an input $GdFeO_3$ unit cell containing 20 atoms and based upon the experimental crystallographic information listed in **Table D.1**. A 250 Rydberg kinetic energy cutoff and an 11 × 10 × 7 Monkhorst–Pack k-mesh sampling of the first Brillouin zone was used to sample 200 bands. The starting magnetization was set to a sum of zero for Fe^{3+} ions to represent the antiferromagnetic orientation of neighboring spins at 293 K.[9] A Hubbard *U* parameter of 4 eV and 5 eV was applied to Fe and Gd atoms respectively for DFT and

DFT+BSE calculations. The structures employed in the DFT and DFT+BSE calculations described below were fully relaxed and calculations were performed to a convergence of 10^{-8} eV/atom with the forces on ions under 10^{-3} eV/Å.

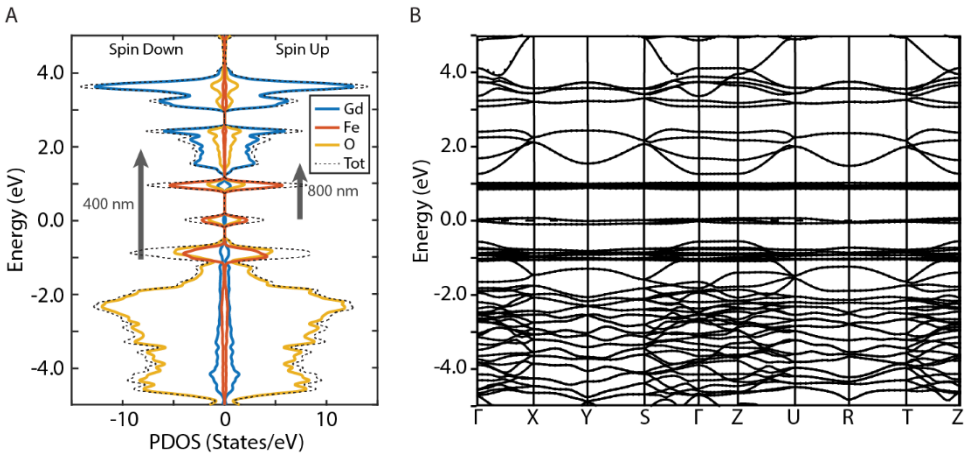

Figure D.8 DFT+U calculated projected density of states **(A)**, and band structure **(B)** used for DFT+BSE calculations of core-level spectra.

D.4.2 Defect Supercell Calculations of Polarons

Hole and electron polarons were modeled within a supercell approach,[14] using a 2 × 2 × 1 repetition of the optimized unit cells (160-atom supercells) calculated for an antiferromagnetic spin ordering ground state. The defect supercell calculations with pSIC and hybrid functionals were performed using the VASP code version 5.4,[15] using the HSE06 screened hybrid functional,[16,17] the implemented pSIC approach,[18,19] and the projector augmented wave (PAW) approach with the VASP4 PAW_PBE potentials (Fe_pv : 14 valence electrons, Gd: 18 valence electrons, and O: 6 valence electrons).[20,21] All supercell simulations adopted a plane-wave energy cutoff of 400 eV, and evaluated energies with a single special *k*-point at 0.25, 0.25, 0.25. Simulations with DFT+U with pSIC adopted a Hubbard *U* value only for the Fe d states with a value of 5.3 as based on default parameters used for the Materials Project database.[22,23] All initial structures were optimized from unit cells with an antiferromagnetic ground state with magnetic moments of 4.8 and 7.2 for the Fe and Gd, respectively, with final moments of approximately 4 and 7 obtained for the bulk for the studied levels of theory. The lattice constants for the supercells with self-consistency

determined for each level of theory, with the impact of the fraction of exact change on the electronic band included in **Figure D.9**.

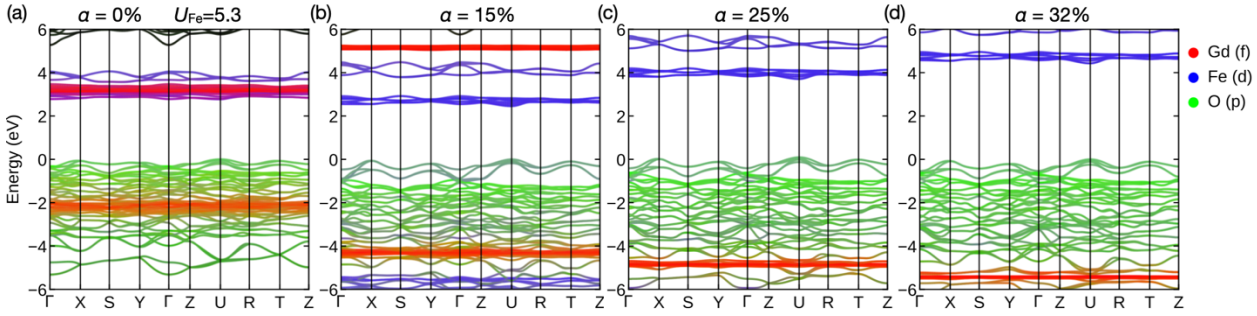

Figure D.9 Summary of variations in the electronic structure for $GdFeO_3$, shown at different levels of theory from PBE+U **(A)** to HSE06 with different levels of exact exchange such as 15% **(B)**, 25% **(C)** and 32% **(D)**. The primary impact of exact exchange is widening of the band gap between the upper valence band (Fe and O derived) and the localized Fe-d derived band, with the separation between the latter band and a higher-lying conduction band (Fe and Gd derived) remaining largely ~ 1 eV higher, independent of the exact exchange.

D.4.3 Fe $M_{2,3}$ Edge Ground State Calculation

The fully relaxed parameters used in the DFT+U calculations for $GdFeO_3$ discussed in **D.4.1** were applied to the DFT+BSE calculations of the $GdFeO_3$ ground state reflectivity at the Fe $M_{2,3}$ X-ray edge. The BSE calculation employed a screening mesh of 2 × 2 × 2, a dielectric constant of 4.28 at 293 K,[9] a 4.0 Bohr screening radius, and a 0.7 scaling factor for the Slater G parameter. A spectral broadening of 0.25 eV was applied for all calculated spectra. The calculated ground state reflectivity of $GdFeO_3$ is plotted in **Figure D.4** and is compared to the experimentally measured XUV ground state at the Fe $M_{2,3}$ X-ray edge. As shown in **Figure D.4**, the DFT+BSE calculated ground state agrees well with the measured ground state reflectivity of the $GdFeO_3$ sample.

D.4.4 Fe $M_{2,3}$ edge Excited and Thermal State Calculations

Excitation-wavelength-dependent changes to the transient XUV spectra of $GdFeO_3$ were calculated using a modification to the OCEAN package described previously.[3,24–26] Effectively, the modification to the OCEAN code enables us to selectively allow or forbid core-to-valence X-ray transitions to valence and conduction bands at different points in

momentum space, to simulate state-filling of electrons and holes following photoexcitation. We modeled our charge transfer state by populating the conduction band with electrons either at 1.55 eV (800 nm) or 3.1 eV (400 nm) above the valence band maximum (VBM) and similarly populating the valence band with holes to model the movement of carriers following photoexcitation. This population of electrons and holes effectively forbids or allows XUV transitions to specific points in k-space but does not account for carrier density, therefore, the modeled peak position and relative intensity is used to compare experiment to theory. We model our transient XUV spectra by subtracting the calculated ground state spectrum from the calculated excited state spectra to calculate the differential absorption. **Figures 5.2 and 5.5** in the main text demonstrate agreement between DFT+BSE modeled 400 nm and 800 nm charge transfer states, respectively.

A thermal isotropic expansion of the $GdFeO_3$ unit cell was modeled to determine if thermal effects were present in the experimental spectra and is described previously.[27] We isotropically expanded the $GdFeO_3$ unit cell to model temperatures from 293 K up to 500 K.[28] The spectrum of a modeled 350 K expansion can be seen in **Figure D.5C** and **D**. We find no significant contributions of thermal isotropic lattice expansion to 800 nm or 400 nm excited transient XUV spectra.

D.4.5 Fe $M_{2,3}$ Edge DFT+BSE Polaron State Calculations

Our semi-empirical method for modeling transient effects of photoexcited polaron formation on XUV core-level spectra is achieved using our DFT+BSE framework and has been described previously.[27] Electron polarons are modeled using the bond distortion method,[29] locally applying an expansion to Fe-O bonds at one iron octahedra in the $GdFeO_3$ unit cell. Similarly, hole polarons on iron atoms are modeled by applying a local contraction to the Fe–O bonds in an FeO_6 octahedra. **Figure D.10** demonstrates the change in intensity between a modeled electron polaron and hole polaron centered on an iron atom. Both polarons were modeled with a 1-8% isotropic distortion of the local FeO_6 octahedra, with a 5% distortion agreeing best with experimental spectra. The electron polaron has a higher spectral intensity than the more dispersive hole polaron. We also simultaneously model electron and hole

polarons with the bond distortion method at neighboring iron sites by employing an expansion and contraction to consider spectrally convolved electron and hole polarons at the Fe $M_{2,3}$ edge (**Fig. D.10**). The electron and hole polarons on iron centers are spectrally convolved at the Fe $M_{2,3}$ edge, and occur at the same energy alignment, which is shifted to higher energy relative to both the LMCT and MMCT states. These anisotropic distortions to the $GdFeO_3$ unit cell are then applied to our DFT+BSE method and the resulting XUV spectrum is treated similarly to our excited state calculation detailed in **D.4.4** to generate a differential absorption spectrum (**Fig. D.10**).

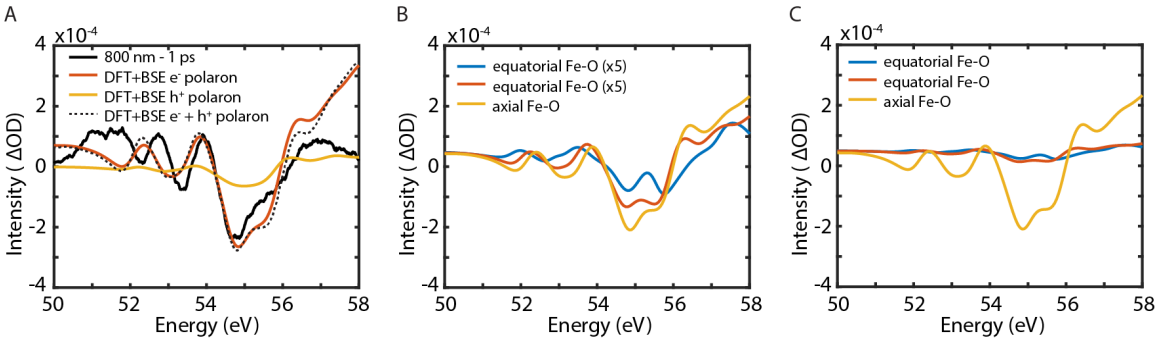

Figure D.10 (A) Experimental lineout (black solid) 1 ps after 800 nm photoexcitation compared to DFT+BSE modeled electron (red) and hole (yellow) polarons and compared to a convolved DFT+BSE electron and hole polaron at neighboring iron atoms (black dashed). The DFT+BSE modeled hole polaron is much weaker than the electron polaron due to its delocalized nature, and when convolved together the electron polaron dominates the predicted dynamics. **(B)** A DFT+BSE modeled electron polaron for an anisotropic expansion of either the equatorial (blue and red) or axial (yellow) Fe–O bonds. The equatorial lineouts are each scaled by 5 times to be compared to the axial distortion. The equatorial ligand expansion is significantly weaker than the axial ligand expansion as plotted in **(C)** and demonstrates that axial distortions dominate the spectral signature of polaron formation.

Additionally, we model an anisotropic polaronic distortion to stimulate the Jahn–Teller effect. To achieve this distortion, we selectively distort equatorial or axial ligands in the FeO_6 octahedra. **Figure D.10B and C** shows that an anisotropic polaronic expansion results in different spectral contributions to the signature of the polaron. We find that axial distortions have a greater effect on the spectral intensity of the polaronic feature in the transient XUV spectrum, which agrees with our findings that the polaronic distortion induces a Jahn–Teller type distortion in the lattice.

D.4.6 Fe $M_{2,3}$ Edge pSIC+DFT+BSE Polaron State Calculations

In addition to our semi-empirical modeling of polaronic distortions, we apply the polaronic distortions obtained from the ab initio defect supercell calculations discussed in **D.4.2** to our DFT+BSE approach, which we refer to as pSIC+DFT+BSE. The distortion acts as the input for OCEAN and enables us to simulate the excited state X-ray edges that result from the ab initio electron and hole polaron distortions calculated using the defect supercell method.

D.5 Ligand-Field Multiplet Theory Calculations

Ligand-field multiplet theory calculations (CTM4XAS) were conducted to model the XUV absorption of oxidation and spin states of different iron species.[30] The different oxidation states were modeled by designating the final state of the initial Fe^{3+} state to be either Fe^{2+} or Fe^{4+}. Spin configurations of the photoexcited Fe^{2+} and Fe^{4+} states were modeled by varying the cubic crystal field splitting (10Dq) and the exchange energy (*J*) for either configuration. The Fe^{3+} high-spin ground state was subtracted from the Fe^{2+} and Fe^{4+} excited states to generate predicted difference spectra following photoexcitation. **Figure D.11** compares these difference spectra with the experimental 400 nm LMCT, 800 nm MMCT, and 800 nm polaron states. The ground state bleach of the Fe^{3+} high-spin feature was shifted to align with experimental bleach at the Fe $M_{2,3}$ edge. The 400 nm LMCT state agrees with a high-spin Fe^{2+} state (**Fig. D.11A**) and the 800 nm polaron state (**Fig. D.11C**) agrees well with a Fe^{2+} low-spin and Fe^{4+} high-spin configuration.

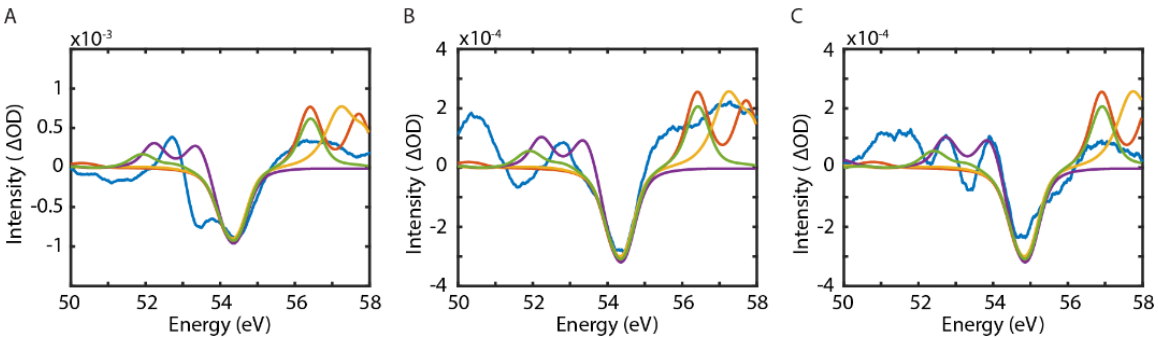

Figure D.11 (A) 400 nm LMCT state, **(B)** 800 nm MMCT state, **(C)** 800 nm polaron state. Experimental (blue), Fe^{4+} high-spin state (yellow), Fe^{4+} low-spin state (red), Fe^{2+} high-spin state (green), Fe^{2+} low-spin state (purple).

D.6 References

(1) Makuła, P.; Pacia, M.; Macyk, W. How to Correctly Determine the Band Gap Energy of Modified Semiconductor Photocatalysts Based on UV–Vis Spectra. *J. Phys. Chem. Lett.* **2018,** *9,* 6814–6817. https://doi.org/10.1021/acs.jpclett.8b02892.

(2) Kim, Y.-J.; Mendes, J. L.; Michelsen, J. M.; Shin, H. J.; Lee, N.; Choi, Y. J.; Cushing, S. K. Coherent Charge Hopping Suppresses Photoexcited Small Polarons in $ErFeO_3$ by Antiadiabatic Formation Mechanism. *Sci. Adv.* **2024,** *10,* eadk4282. https://doi.org/10.1126/sciadv.adk4282.

(3) Liu, H.; Michelsen, J. M.; Mendes, J. L.; Klein, I. M.; Bauers, S. R.; Evans, J. M.; Zakutayev, A.; Cushing, S. K. Measuring Photoexcited Electron and Hole Dynamics in ZnTe and Modeling Excited State Core-Valence Effects in Transient Extreme Ultraviolet Reflection Spectroscopy. *J. Phys. Chem. Lett.* **2023,** *14,* 2106–2111. https://doi.org/10.1021/acs.jpclett.2c03894.

(4) Géneaux, R.; Chang, H.-T.; Schwartzberg, A. M.; Marroux, H. J. B. Source Noise Suppression in Attosecond Transient Absorption Spectroscopy by Edge-Pixel Referencing. *Opt. Express* **2021,** *29,* 951. https://doi.org/10.1364/OE.412117.

(5) Codling, K.; Madden, R. P.; Ederer, D. L. Resonances in the Photo-Ionization Continuum of Ne I (20-150 eV). *Phys. Rev.* **1967,** *155,* 26–37. https://doi.org/10.1103/PhysRev.155.26.

(6) de Roulet, B. R.; Drescher, L.; Sato, S. A.; Leone, S. R. Initial Electron Thermalization in Metals Measured by Attosecond Transient Absorption Spectroscopy. *Phys. Rev. B* **2024,** *110,* 174301. https://doi.org/10.1103/PhysRevB.110.174301.

(7) Zürch, M.; Chang, H.-T.; Borja, L. J.; Kraus, P. M.; Cushing, S. K.; Gandman, A.; Kaplan, C. J.; Oh, M. H.; Prell, J. S.; Prendergast, D.; Pemmaraju, C. D.; Neumark, D. M.; Leone, S. R. Direct and Simultaneous Observation of Ultrafast Electron and Hole Dynamics in Germanium. *Nat. Commun.* **2017,** *8,* 15734. https://doi.org/10.1038/ncomms15734.

(8) Cushing, S. K.; Lee, A.; Porter, I. J.; Carneiro, L. M.; Chang, H.-T.; Zürch, M.; Leone, S. R. Differentiating Photoexcited Carrier and Phonon Dynamics in the Δ, L, and Γ Valleys of Si(100) with Transient Extreme Ultraviolet Spectroscopy. *J. Phys. Chem. C* **2019,** *123,* 3343–3352. https://doi.org/10.1021/acs.jpcc.8b10887.

(9) Zhu, X.-H.; Xiao, X.-B.; Chen, X.-R.; Liu, B.-G. Electronic Structure, Magnetism and Optical Properties of Orthorhombic $GdFeO_3$ from First Principles. *RSC Adv.* **2017,** *7,* 4054–4061. https://doi.org/10.1039/C6RA25259A.

(10) Husain, S.; Keelani, A. O. A.; Khan, W. Influence of Mn Substitution on Morphological, Thermal and Optical Properties of Nanocrystalline $GdFeO_3$ Orthoferrite. *Nano-Struct. Nano-Objects* **2018,** *15,* 17–27. https://doi.org/10.1016/j.nanoso.2018.03.002.

(11) Perdew, J. P.; Burke, K.; Ernzerhof, M. Generalized Gradient Approximation Made Simple. *Phys. Rev. Lett.* **1996,** *77,* 3865–3868. https://doi.org/10.1103/PhysRevLett.77.3865.

(12) Giannozzi, P.; Baroni, S.; Bonini, N.; Calandra, M.; Car, R.; Cavazzoni, C.; Ceresoli, D.; Chiarotti, G. L.; Cococcioni, M.; Dabo, I.; Corso, A. D.; Gironcoli, S. de; Fabris, S.; Fratesi, G.; Gebauer, R.; Gerstmann, U.; Gougoussis, C.; Kokalj, A.; Lazzeri, M.; Martin-Samos, L.; Marzari, N.; Mauri, F.; Mazzarello, R.; Paolini, S.; Pasquarello, A.; Paulatto, L.; Sbraccia, C.; Scandolo, S.; Sclauzero, G.; Seitsonen, A. P.; Smogunov, A.; Umari, P.; Wentzcovitch, R. M. QUANTUM ESPRESSO: A Modular and Open-Source Software Project for Quantum Simulations of Materials. *J. Phys. Condens. Matter* **2009,** *21,* 395502. https://doi.org/10.1088/0953-8984/21/39/395502.

(13) Giannozzi, P.; Andreussi, O.; Brumme, T.; Bunau, O.; Buongiorno Nardelli, M.; Calandra, M.; Car, R.; Cavazzoni, C.; Ceresoli, D.; Cococcioni, M.; Colonna, N.; Carnimeo, I.; Dal Corso, A.; de Gironcoli, S.; Delugas, P.; DiStasio, R. A.; Ferretti, A.; Floris, A.; Fratesi, G.; Fugallo, G.; Gebauer, R.; Gerstmann, U.; Giustino, F.; Gorni, T.; Jia, J.; Kawamura, M.; Ko, H.-Y.; Kokalj, A.; Küçükbenli, E.; Lazzeri, M.; Marsili, M.; Marzari, N.; Mauri, F.; Nguyen, N. L.; Nguyen, H.-V.; Otero-de-la-Roza, A.; Paulatto, L.; Poncé, S.; Rocca,

D.; Sabatini, R.; Santra, B.; Schlipf, M.; Seitsonen, A. P.; Smogunov, A.; Timrov, I.; Thonhauser, T.; Umari, P.; Vast, N.; Wu, X.; Baroni, S. Advanced Capabilities for Materials Modelling with Quantum ESPRESSO. *J. Phys. Condens. Matter* **2017,** *29,* 465901. https://doi.org/10.1088/1361-648X/aa8f79.

(14) Freysoldt, C.; Grabowski, B.; Hickel, T.; Neugebauer, J.; Kresse, G.; Janotti, A.; Van de Walle, C. G. First-Principles Calculations for Point Defects in Solids. *Rev. Mod. Phys.* **2014,** *86,* 253–305. https://doi.org/10.1103/RevModPhys.86.253.

(15) Kresse, G.; Furthmüller, J. Efficiency of Ab-Initio Total Energy Calculations for Metals and Semiconductors Using a Plane-Wave Basis Set. *Comput. Mater. Sci.* **1996,** *6,* 15–50. https://doi.org/10.1016/0927-0256(96)00008-0.

(16) Heyd, J.; Scuseria, G. E.; Ernzerhof, M. Hybrid Functionals Based on a Screened Coulomb Potential. *J. Chem. Phys.* **2003,** *118,* 8207–8215. https://doi.org/10.1063/1.1564060.

(17) Paier, J.; Marsman, M.; Hummer, K.; Kresse, G.; Gerber, I. C.; Angyan, J. G. Screened Hybrid Density Functionals Applied to Solids. *J. Chem. Phys.* **2006,** *124,* 154709.

(18) Sadigh, B.; Erhart, P.; Åberg, D. Variational Polaron Self-Interaction-Corrected Total-Energy Functional for Charge Excitations in Insulators. *Phys. Rev. B* **2015,** *92,* 075202. https://doi.org/10.1103/PhysRevB.92.075202.

(19) Zhou, F.; Sadigh, B.; Erhart, P.; Åberg, D. Ab Initio Prediction of Fast Non-Equilibrium Transport of Nascent Polarons in SrI_2: A Key to High-Performance Scintillation. *npj Comput. Mater.* **2016,** *2,* 1–7. https://doi.org/10.1038/npjcompumats.2016.22.

(20) Kresse, G.; Joubert, D. From Ultrasoft Pseudopotentials to the Projector Augmented-Wave Method. *Phys. Rev. B* **1999,** *59,* 1758–1775. https://doi.org/10.1103/PhysRevB.59.1758.

(21) Blöchl, P. E. Projector Augmented-Wave Method. *Phys. Rev. B* **1994,** *50,* 17953–17979. https://doi.org/10.1103/PhysRevB.50.17953.

(22) Ong, S. P.; Richards, W. D.; Jain, A.; Hautier, G.; Kocher, M.; Cholia, S.; Gunter, D.; Chevrier, V. L.; Persson, K. A.; Ceder, G. Python Materials Genomics (Pymatgen): A Robust, Open-Source Python Library for Materials Analysis. *Comput. Mater. Sci.* **2013,** *68,* 314–319. https://doi.org/10.1016/j.commatsci.2012.10.028.

(23) Jain, A.; Ong, S. P.; Hautier, G.; Chen, W.; Richards, W. D.; Dacek, S.; Cholia, S.; Gunter, D.; Skinner, D.; Ceder, G.; Persson, K. A. Commentary: The Materials Project: A Materials Genome Approach to Accelerating Materials Innovation. *APL Mater.* **2013,** *1,* 011002. https://doi.org/10.1063/1.4812323.

(24) Vinson, J. Advances in the OCEAN-3 Spectroscopy Package. *Phys. Chem. Chem. Phys.* **2022,** *24,* 12787–12803. https://doi.org/10.1039/D2CP01030E.

(25) Gilmore, K.; Vinson, J.; Shirley, E. L.; Prendergast, D.; Pemmaraju, C. D.; Kas, J. J.; Vila, F. D.; Rehr, J. J. Efficient Implementation of Core-Excitation Bethe–Salpeter Equation Calculations. *Comput. Phys. Commun.* **2015,** *197,* 109–117. https://doi.org/10.1016/j.cpc.2015.08.014.

(26) Vinson, J.; Rehr, J. J.; Kas, J. J.; Shirley, E. L. Bethe–Salpeter Equation Calculations of Core Excitation Spectra. *Phys. Rev. B* **2011,** *83,* 115106. https://doi.org/10.1103/PhysRevB.83.115106.

(27) Klein, I. M.; Liu, H.; Nimlos, D.; Krotz, A.; Cushing, S. K. Ab Initio Prediction of Excited-State and Polaron Effects in Transient XUV Measurements of α-Fe_2O_3. *J. Am. Chem. Soc.* **2022,** *144,* 12834–12841. https://doi.org/10.1021/jacs.2c03994.

(28) Chavan, S. V.; Tyagi, A. K. Nanocrystalline $GdFeO_3$ via the Gel-Combustion Process. *J. Mater. Res.* **2005,** *20,* 2654–2659. https://doi.org/10.1557/JMR.2005.0337.

(29) Pham, T. D.; Deskins, N. A. Efficient Method for Modeling Polarons using Electronic Structure Methods. *J. Chem. Theory Comput.* **2020,** *16,* 5264–5278. https://pubs.acs.org/doi/10.1021/acs.jctc.0c00374.

(30) Stavitski, E.; de Groot, F. M. F. The CTM4XAS Program for EELS and XAS Spectral Shape Analysis of Transition Metal L Edges. *Micron* **2010,** *41,* 687–694. https://doi.org/10.1016/j.micron.2010.06.005.

Appendix E

SUPPORTING INFORMATION FOR CHAPTER 7: EXPERIMENTALLY MAPPING THE PHASE DIAGRAMS OF PHOTOEXCITED SMALL POLARONS

E.1 Uncertainties in the Polaron Parameterization from Experimental Measurements

To understand the uncertainties associated with approximating the phase diagrams from experimental observables, we include reported experimental uncertainties for the polaron energy. These experimental uncertainties are propagated through the approximation for $E_{polaron}$ as half of the experimental spectral shift. Several data points from literature do not have reported uncertainties and cannot be statistically analyzed.

We further include reported experimental uncertainties for the experimentally determined exchange energy per spin. In the case where error bars are reported in literature from inelastic neutron scattering experiments, we include those error bars. However, several of the iron oxides studied did not have reported error bars. In the case of these materials, we consider both reported inelastic neutron scattering (INS) and Raman scattering experiments to develop statistics. We also consider theoretically modeled exchange energy where necessary. **Table E.1** shows these statistics for several of the material systems under investigation. We note α-FeOOH has only one experimentally determined value for J in the literature. a-TiO_2 and $BiVO_4$ both have $3d^0$ ground state electronic configurations and therefore do not exhibit spin exchange on their transition metal sites.

Table E.1 Exchange energies from inelastic neutron and Raman scattering experiments and theory. All values are in units of eV. J is approximated as exchange energy per spin. "–" denotes no known literature value for one of the necessary parameters.

	J (INS)	J (Raman)	J (theory)	Average J value	Standard deviation
α-Fe_2O_3	0.0097 ± 0.0031 [1,2]	–	–	0.0097 [1,2]	0.0031 [1,2]
$CuFeO_2$	0.017,[3] 0.014,[4] 0.043[5]	–	–	0.025	0.018
$ErFeO_3$	0.38 ± 0.16 [7]	–	–	0.38 [7]	0.16 [7]

$BiFeO_3$	0.16,[8] 0.24,[9] 0.14,[10] 0.12 [11]	–	–	0.17	0.05
α-FeOOH	–	0.19 [12]	–	–	
$GdFeO_3$	0.10 [13]	–	0.16 [14]	0.13	0.04

Density functional theory (DFT) is known to have systematic uncertainties associated with calculating energies for transition metals. For example, DFT is notorious for underestimating band gaps of transition metal oxides under both the local density approximation (LDA) and the generalized gradient approximation (GGA). Several methods have emerged to calculate band gaps which agree with experimentally measured values, including the use of an on-site repulsion term (Hubbard U) or the use of hybrid pseudopotentials.[15] Generally though, density functional theory experiences systematic differences depending on the functionals and methods being applied

Bandwidths were all approximated using the generalized gradient approximation (GGA). On the other hand, phonon dispersions were calculated using different exchange-correlation functionals, ranging from the local density approximation (LDA) to Perdew-Burke-Ernzerhof functionals within the GGA.

E.2 Singular Value Decomposition Kinetic Models

Singular value decomposition (SVD) was employed to extract the spectral weights of different contributions to the transient XUV spectra. The resulting temporal weights of the SVD components were fit with rate equation models, as described previously, to elucidate the kinetics of the singular values.[16,17] Briefly, a generalized sequential kinetic model is applied to the weighted SVD components of the transient XUV spectra. Here, the sequential kinetic model is always initiated by a charge transfer state (S_{CT}) that evolves through one or more intermediate states (S_n) before the carrier relaxes. Schematically, this can be understood by **Equation E.1**:

$$S_{CT} \overset{k_1}{\rightarrow} S_1 \overset{k_2}{\rightarrow} S_2 \ldots \overset{k_n}{\rightarrow} S_n \quad \textbf{(E.1)}$$

The rate equations that correspond to these states are dependent upon the number of intermediate states, where in the case of α-Fe_2O_3 and $GdFeO_3$, there are only charge transfer (S_{CT}) and polaron (S_P) states. In the case of $CuFeO_2$ there is initially a charge transfer state (S_{CT}), followed by an intermediate polaron state (S_P), and finally a *c*-axis lattice expansion state ($S_{Lattice}$). In the case of $ErFeO_3$, there is again an initial charge transfer state (S_{CT}), an intermediate Fe^{3+}–Fe^{2+} charge hopping state (S_{Hop}), followed by the polaron state (S_P). **Equations E.2–4** encompass the rate equations for states S_0 through S_n:

$$\frac{dN_0}{dt} = -k_1 N_0(t) \quad \textbf{(E.2)}$$

$$\frac{dN_i}{dt} = k_i N_{i-1}(t) - k_{i+1} N_i(t) \text{ where } 1 \leq i \leq n-1 \quad \textbf{(E.3)}$$

$$\frac{dN_n}{dt} = k_n N_{n-1}(t) \quad \textbf{(E.4)}$$

where Ni(t) is the time-dependent population of state Si. The lines of best fit in **Figure 7.2** of the main text are numerical solutions of the differential equations in **Equations E.2–4**, convolved with a Gaussian instrument response function. The resulting convolved populations were scaled by independent amplitudes and offsets to fit the experimentally determined SVD weights.

E.3 References

(1) Hill, A. H.; Jacobsen, H.; Stewart, J. R.; Jiao, F.; Jensen, N. P.; Holm, S. L.; Mutka, H.; Seydel, T.; Harrison, A.; Lefmann, K. Magnetic Properties of Nano-Scale Hematite, α-Fe_2O_3, Studied by Time-of-Flight Inelastic Neutron Spectroscopy. *J. Chem. Phys.* **2014**, *140* (4), 044709. https://doi.org/10.1063/1.4862235.

(2) Samuelsen, E. J.; Shirane, G. Inelastic Neutron Scattering Investigation of Spin Waves and Magnetic Interactions in α-Fe_2O_3. *Phys. Status Solidi B* **1970**, *42* (1), 241–256. https://doi.org/10.1002/pssb.19700420125.

(3) Ye, F.; Fernandez-Baca, J. A.; Fishman, R. S.; Ren, Y.; Kang, H. J.; Qiu, Y.; Kimura, T. Magnetic Interactions in the Geometrically Frustrated Triangular Lattice Antiferromagnet $CuFeO_2$. *Phys. Rev. Lett.* **2007**, *99* (15), 157201. https://doi.org/10.1103/PhysRevLett.99.157201.

(4) Terada, N.; Khalyavin, D. D.; Manuel, P.; Asai, S.; Masuda, T.; Saito, H.; Nakajima, T.; Osakabe, T. Elastic and Inelastic Neutron Scattering Experiments under High Pressure in the Frustrated Antiferromagnet $CuFeO_2$. *Phys. Rev. B* **2024**, *110* (2), 024406. https://doi.org/10.1103/PhysRevB.110.024406.

(5) Nakajima, T.; Suno, A.; Mitsuda, S.; Terada, N.; Kimura, S.; Kaneko, K.; Yamauchi, H. Magnons and Electromagnons in a Spin-Lattice-Coupled Frustrated Magnet $CuFeO_2$ as Seen via Inelastic Neutron Scattering. *Phys. Rev. B* **2011**, *84* (18), 184401. https://doi.org/10.1103/PhysRevB.84.184401.

(6) Schmidt, W.; Brotzeller, C.; Geick, R.; Schweiss, P.; Treutmann, W. Magnon-Phonon Coupling in Fe_2SiO_4. *J. Magn. Magn. Mater.* **1992**, *104–107*, 1049–1050. https://doi.org/10.1016/0304-8853(92)90484-6.

(7) Koshizuka, N.; Ushioda, S. Inelastic-Light-Scattering Study of Magnon Softening in $ErFeO_3$. *Phys. Rev. B* **1980**, *22* (11), 5394–5399. https://doi.org/10.1103/PhysRevB.22.5394.

(8) Jeong, J.; Goremychkin, E. A.; Guidi, T.; Nakajima, K.; Jeon, G. S.; Kim, S.-A.; Furukawa, S.; Kim, Y. B.; Lee, S.; Kiryukhin, V.; Cheong, S.-W.; Park, J.-G. Spin Wave Measurements over the Full Brillouin Zone of Multiferroic $BiFeO_3$. *Phys. Rev. Lett.* **2012**, *108* (7), 077202. https://doi.org/10.1103/PhysRevLett.108.077202.

(9) Matsuda, M.; Fishman, R. S.; Hong, T.; Lee, C. H.; Ushiyama, T.; Yanagisawa, Y.; Tomioka, Y.; Ito, T. Magnetic Dispersion and Anisotropy in Multiferroic $BiFeO_3$. *Phys. Rev. Lett.* **2012**, *109* (6), 067205. https://doi.org/10.1103/PhysRevLett.109.067205.

(10) Xu, Z.; Wen, J.; Berlijn, T.; Gehring, P. M.; Stock, C.; Stone, M. B.; Ku, W.; Gu, G.; Shapiro, S. M.; Birgeneau, R. J.; Xu, G. Thermal Evolution of the Full Three-Dimensional Magnetic Excitations in the Multiferroic $BiFeO_3$. *Phys. Rev. B* **2012**, *86* (17), 174419. https://doi.org/10.1103/PhysRevB.86.174419.

(11) Delaire, O.; Stone, M. B.; Ma, J.; Huq, A.; Gout, D.; Brown, C.; Wang, K. F.; Ren, Z. F. Anharmonic Phonons and Magnons in $BiFeO_3$. *Phys. Rev. B* **2012**, *85* (6), 064405. https://doi.org/10.1103/PhysRevB.85.064405.

(12) M. V. Abrashev, V. G. Ivanov, B. S. Stefanov, N. D. Todorov, J. Rosell, V. Skumryev; Raman Spectroscopy of alpha-FeOOH (goethite) Near Antiferromagnetic to Paramagnetic Phase Transition. *J. Appl. Phys.* **2020,** *127* (20): 205108. https://doi.org/10.1063/5.0006352

(13) Sakata, T.; Enomura, A. Studies of the Rare Earth–Iron Interactions in the Orthoferrites $GdFeO_3$ and $HoFeO_3$. *Phys. Status Solidi A* **1979**, *52* (1), 311–314. https://doi.org/10.1002/pssa.2210520134.

(14) Zhu, X.-H.; Xiao, X.-B.; Chen, X.-R.; Liu, B.-G. Electronic Structure, Magnetism and Optical Properties of Orthorhombic $GdFeO_3$ from First Principles. *RSC Adv.* **2017**, *7* (7), 4054–4061. https://doi.org/10.1039/C6RA25259A.

(15) Weng, M.; Pan, F.; Wang, L.-W. Wannier–Koopmans Method Calculations for Transition Metal Oxide Band Gaps. *Npj Comput. Mater.* **2020**, *6* (1), 33. https://doi.org/10.1038/s41524-020-0302-0.

(16) Kim, Y.-J.; Mendes, J. L.; Michelsen, J. M.; Shin, H. J.; Lee, N.; Choi, Y. J.; Cushing, S. K. Coherent Charge Hopping Suppresses Photoexcited Small Polarons in $ErFeO_3$ by Antiadiabatic Formation Mechanism. *Sci. Adv.* **2024**, *10* (12), eadk4282. https://doi.org/10.1126/sciadv.adk4282.

(17) Carneiro, L. M.; Cushing, S. K.; Liu, C.; Su, Y.; Yang, P.; Alivisatos, A. P.; Leone, S. R. Excitation-Wavelength-Dependent Small Polaron Trapping of Photoexcited Carriers in α-Fe_2O_3. *Nat. Mater.* **2017**, *16* (8), 819–825. https://doi.org/10.1038/nmat4936.